LOCKHEED MARTIN ENERGY RESEARCH LIBRARIES

3 4456 0510965 5

ORNL-5753

ornl

OAK
RIDGE
NATIONAL
LABORATORY

UNION
CARBIDE

Gas-Cooled Reactor Programs

High-Temperature Gas-Cooled Reactor Technology Development Program

Annual Progress Report for Period Ending December 31, 1980

F. J. Homan
Paul R. Kasten

OAK RIDGE NATIONAL LABORATORY
CENTRAL RESEARCH LIBRARY
CIRCULATION SECTION
4500N ROOM 175
LIBRARY LOAN COPY
DO NOT TRANSFER TO ANOTHER PERSON
If you wish someone else to see this report, send in name with report and the library will arrange a loan.
UCN-7969 (3 9-77)

GAS-COOLED REACTOR PROGRAMS
SCIENCE ENGINEERING TECHNOLOGY

OPERATED BY
UNION CARBIDE CORPORATION
FOR THE UNITED STATES
DEPARTMENT OF ENERGY

Printed in the United States of America. Available from
National Technical Information Service
U.S. Department of Commerce
5285 Port Royal Road, Springfield, Virginia 22161
NTIS price codes—Printed Copy: A15 Microfiche A01

This report was prepared as an account of work sponsored by an agency of the United States Government. Neither the United States Government nor any agency thereof, nor any of their employees, makes any warranty, express or implied, or assumes any legal liability or responsibility for the accuracy, completeness, or usefulness of any information, apparatus, product, or process disclosed, or represents that its use would not infringe privately owned rights. Reference herein to any specific commercial product, process, or service by trade name, trademark, manufacturer, or otherwise, does not necessarily constitute or imply its endorsement, recommendation, or favoring by the United States Government or any agency thereof. The views and opinions of authors expressed herein do not necessarily state or reflect those of the United States Government or any agency thereof.

ORNL-5753
Distribution
Category UC-77

Contract No. W-7405-eng-26

GAS-COOLED REACTOR PROGRAMS

HIGH-TEMPERATURE GAS-COOLED REACTOR TECHNOLOGY DEVELOPMENT PROGRAM
ANNUAL PROGRESS REPORT FOR PERIOD ENDING DECEMBER 31, 1980

F. J. Homan, Base Technology Program Manager
Paul R. Kasten, Program Director

Date Published: August 1981

OAK RIDGE NATIONAL LABORATORY
Oak Ridge, Tennessee 37830
operated by
UNION CARBIDE CORPORATION
for the
DEPARTMENT OF ENERGY

LOCKHEED MARTIN ENERGY RESEARCH LIBRARIES
3 4456 0510965 5

CONTENTS

FOREWORD ix

SUMMARY xiii

1. HTGR CHEMISTRY 1
   1.1 SORPTION OF IODINE ON LOW-CHROMIUM ALLOY STEEL 1
   1.2 IODINE SORPTION AND DESORPTION FROM GRAPHITE 4
      1.2.1 Description of the Experimental System 5
         1.2.1.1 Graphite Specimens 6
         1.2.1.2 Range of Test Data 6
      1.2.2 Adsorption Isotherms for Grade H451 Graphite . . . 9
      1.2.3 Desorption from Graphite 10
      1.2.4 Conclusions 12
   1.3 SILVER DIFFUSION IN H451 GRAPHITE 12
   1.4 PLUTONIUM AND URANIUM DIFFUSION IN GRAPHITE 15
   1.5 REFERENCES 16

2. FUELED GRAPHITE DEVELOPMENT 19
   2.1 INTRODUCTION 19
      2.1.1 Irradiation Testing 19
      2.1.2 Development Work 20
      2.1.3 Project Work Statement Activities 21
      2.1.4 Equipment Maintenance and Development 21
   2.2 IRRADIATION EXPERIMENTS 21
      2.2.1 High Flux Isotope Reactor Target Capsules 22
         2.2.1.1 Capsule HT-34 22
         2.2.1.2 Capsule HT-35 23
      2.2.2 HRB Capsules 27
         2.2.2.1 HRB-13 27
         2.2.2.2 Capsule HRB-14 28
         2.2.2.3 Capsule HRB-15b 31
         2.2.2.4 Capsule HRB-15a 32
         2.2.2.5 Capsule HRB-16 38
   2.3 DEVELOPMENT WORK 38
      2.3.1 Pyrocarbon Coating by CO_2 Dilution 42
      2.3.2 Silicon Carbide Characterization and Testing . . . 43
         2.3.2.1 Silicon Carbide Microstructure Characterization 44
         2.3.2.2 Correlation of Silicon Carbide Microstructures with Deposition Conditions . . 44
         2.3.2.3 Interaction with Fission Product Elements 45
         2.3.2.4 Kinetic Studies 47
      2.3.3 Dense UCO Fuel Kernel Development 48
   2.4 PROJECT WORK STATEMENT ACTIVITIES 49
      2.4.1 PWS FD-10 49
      2.4.2 PWS FD-12 49
      2.4.3 PWS FD-13 63
      2.4.4 PWS FD-18 69
      2.4.5 PWS FD-20 70

2.5 EQUIPMENT DEVELOPMENT AND MAINTENANCE 71
2.5.1 Irradiated Microsphere Gamma Analyzer 71
2.5.2 Postirradiation Gas Analyzer 75
2.5.3 X-Ray Micrographic Facility 80
2.6 FOREIGN ASSIGNMENT 80
2.6.1 $(Th,U)O_2$ Performance Assessment 82
2.7 SERVICE WORK FOR GENERAL ATOMIC COMPANY 83
2.7.1 Electron Microprobe Studies for General Atomic Company 83
2.7.2 PGA Studies for General Atomic Company 84
2.7.3 IMGA Studies for General Atomic Company 84
2.8 REFERENCES 91

3. PRESTRESSED CONCRETE PRESSURE VESSEL DEVELOPMENT 95
3.1 INTRODUCTION 95
3.2 ANALYSIS METHODS 95
3.2.1 Revisions to the Endochronic Concrete Constitutive Relations 95
3.2.1.1 Base Model Constitutive Relations 96
3.2.1.2 Refined Model Constitutive Relations . . . 98
3.2.1.3 Cracking 99
3.2.1.4 Strain Subdivisions 100
3.2.1.5 Modulus of Elasticity 101
3.2.1.6 Investigation Conclusions 103
3.2.2 Finite-Element Computation of Creep Effects in Concrete Structures 103
3.2.2.1 Background 103
3.2.2.2 Approach 104
3.2.2.3 Results to be Provided 106
3.3 CONCRETE PROPERTIES IN A NUCLEAR ENVIRONMENT 106
3.3.1 Review of Concrete Property Data 107
3.3.2 Concrete Multiaxial Material Testing System 108
3.3.2.1 Concrete Multiaxial Material Test System Performance Specification 109
3.3.2.2 Test System Enclosure 111
3.4 INSTRUMENTATION EVALUATION AND DEVELOPMENT 113
3.5 STRUCTURAL MODEL TESTS 120
3.5.1 Review of PCRV-Related Model Tests 120
3.5.2 Development of Model Testing Techniques 120
3.5.2.1 Fibrous Concrete Evaluations 121
3.5.2.2 PCRV Model Technique Validation Studies . 130
3.6 LINER AND PENETRATION STUDIES 136
3.7 REFERENCES 146

4. STRUCTURAL MATERIALS 149
4.1 INTRODUCTION 149
4.2 MECHANICAL PROPERTIES OF HTGR ALLOYS, WELDMENTS, AND CERAMICS 150
4.2.1 Creep and Tensile Testing of Metallic Materials . . 150
4.2.2 Aging Studies 157
4.2.3 Fatigue and Fatigue Crack Growth 157
4.2.4 Creep Crack Growth 164
4.2.5 Testing of Ceramics 167

4.3 CORROSION OF HTGR ALLOYS 168
4.3.1 Steam Corrosion of Engineering Alloys 168
4.3.2 Oxidation-Carburization-Vaporization in HTGR Helium 171
4.3.2.1 Variability of Carbon Potential of Flowing HTGR Helium in Retorts 172
4.3.2.2 Effects of P_{H_2O} on Carburization 174
4.3.2.3 Oxidation and Vaporization 174
4.3.3 Mechanical Property-Corrosion Interactions 174
4.3.4 Gas Composition Studies 180
4.4 JOINING TECHNOLOGY 182
4.4.1 Weldability of Modified Inconel 617 Alloys 182
4.4.2 Welding of Cast Nickel-Base Superalloys 184
4.4.3 Laser and Electron Beam Welding of Oxide-Dispersion-Strengthened Alloy MA956 190
4.5 STRUCTURAL CERAMICS 194
4.5.1 Characterization of Fibrous Insulations 194
4.5.2 Depressurization Testing 195
4.5.3 Characterization of Dense Ceramics 197
4.5.4 Environmental Testing of Ceramics 199
4.6 FISSION PRODUCT—MATERIALS INTERACTIONS 200
4.6.1 Evaluation of Existing Data and Specimens 200
4.6.2 High-Temperature Exposure of Hastelloy X and Inconel 617 in Tellurium-Cesium Environments . . . 200
4.6.3 Strain-Cycle Tests in Tellurium-Cesium Environments 201
4.7 REFERENCES 202

5. HTGR GRAPHITE STUDIES 205
5.1 GRAPHITE IRRADIATIONS 205
5.1.1 Creep Capsule OC-4 205
5.1.2 Design of 1200°C Creep Capsule OC-X 207
5.1.3 Graphite Irradiations in HFIR 208
5.2 IRRADIATION RESULTS 209
5.2.1 Behavior of Graphite Grade TSX 209
5.2.2 Examination of German Reflector Graphites 218
5.3 GRAPHITE CORROSION STUDIES 218
5.3.1 Corrosion Tests 218
5.3.2 Catalytic Effects on Graphite Corrosion 221
5.3.3 Electrical Conductivity as a Measure of Oxidation Gradients 224
5.3.4 Characterization of German Grade ASR—1RG 230
5.3.5 Mechanical Properties of Oxidized Grade 2020 . . . 233
5.3.6 BET Surface Area Measurements 238
5.4 REFERENCES 242

6. HTR CORE EVALUATION 245
6.1 REFERENCES 246

7. HTR PHYSICS STUDIES 247
7.1 HTR METHODS DEVELOPMENT 247
7.2 PEBBLE-BED HTR CORE ANALYSIS 248
7.3 PRISMATIC HTR CORE ANALYSIS 250
7.4 REFERENCES 251

8. HTR SHIELDING STUDIES 253
8.1 REFERENCES 255

9. APPLICATION AND PROJECT ASSESSMENTS 257
9.1 HTR REFORMER AND PROCESS HEAT MODELING STUDIES 257
9.1.1 Characterization of Chemical Heat Pipe System . . . 257
9.1.2 Process Heat Reactor Dynamics Studies 269
9.1.2.1 Steam-Methane Reformer Simualtion 270
9.1.2.2 CHP Pipeline Dynamics 271
9.1.2.3 Methanator Simulation 271
9.2 HTR APPLICATION ASSESSMENTS OF FOSSIL CONVERSION PROCESSES 271
9.3 PROJECT AND PRIORITY ASSESSMENTS 273
9.3.1 Objective 273
9.3.2 Progress This Reporting Period 273
9.3.3 Summary of Analysis Results 274
9.3.4 Approach and Assumptions 274
9.3.5 Parametric Studies 276
9.3.5.1 Plant Lifetime 276
9.3.5.2 Plant Scheduling 277
9.3.5.3 Discount Factor 278
9.3.5.4 End Year of Comparison 280
9.3.5.5 Research and Development and First-of-a-Kind Costs 281
9.3.5.6 Plant Costs 282
9.4 REFERENCES 283

10. HTR CFTL STUDIES 285
10.1 INTRODUCTION 285
10.2 INITIAL SCOPE OF THE STUDIES 285
10.3 CORE SUPPORT PERFORMANCE TEST 287
10.3.1 The Loop Configuration 288
10.3.2 The CSPT Test Vessel 292
10.3.3 Loop Limitations 292
10.3.4 Test Assembly 293
10.3.5 Operating Limitations 294
10.4 EVALUATION OF PARAMETERS AT THE TEST ASSEMBLY 295
10.5 IMPURITY MEASUREMENT AND CONTROL 297
10.6 TESTING OF HEAT EXCHANGE EQUIPMENT 297
10.6.1 Intermediate Heat Exchanger 298
10.6.1.1 Objectives 298
10.6.1.2 Method 299
10.6.1.3 Test Configuration 299
10.6.1.4 Scheduling 301

10.6.2 Steam Generator 302
10.6.3 Core Auxiliary Heat Exchanger 302
10.6.4 Reformer and Methanator 302
10.7 OTHER PRIMARY LOOP COMPONENTS 303
10.7.1 Thermal Barrier 303
10.7.2 Intracore Components 303
10.8 CONCLUSIONS 304
10.9 REFERENCES 304

FOREWORD

During this past year the High-Temperature Gas-Cooled Reactor (HTR) Technology Development Program at Oak Ridge National Laboratory (ORNL) has expanded into new areas: HTR physics and shielding studies, application and project assessments, and component testing associated with heat transfer and fluid flow in an HTR helium environment. Since other changes have occurred previously, it is appropriate to summarize the history of the ORNL Thermal Gas-Cooled Reactor Program and to review the program changes through the years.

The origins of the present Gas-Cooled Reactor Programs (GCRP) go back to about September 1957; at that time the U.S. Atomic Energy Commission (AEC) undertook a comprehensive study of gas-cooled reactors (GCRs) for power production; individual studies were made by Kaiser Engineers, Hanford, and ORNL. The intent was to present to the Congress a specific set of conclusions about the possible role of GCRs in the United States together with a set of recommendations, which would constitute a national program for GCR development. This led to the establishment of the GCRP at ORNL in 1958, with R. A. Charpie as program director, and adoption of the Experimental Gas-Cooled Reactor (EGCR) project by the AEC.

With a view toward early construction of a reactor, the AEC requested ORNL, along with Kaiser Engineers, to complete initial GCR design studies by April 1958. The concept was to be based largely on existing technology; the principal variations from the Magnox GCR as developed in Great Britain were the use of stainless-steel-clad fuel elements, enriched UO_2 fuel, and helium as the cooling gas. It was also considered important to look at the future potential of GCRs; to this end ORNL undertook various experimental studies to explore the prospects of using alternate materials, which would simplify the design and significantly improve the performance of enriched-fuel GCRs.

In the 60-MW(e) EGCR project, ORNL was responsible for design review, development of fuel, control rods, control rod drives, experimental facilities, and development work on reactor components; Oak Ridge Operations Office was responsible for reactor construction and design; Kaiser Engineers was the principal architect-engineer; Allis-Chalmers was responsible for the core, including the fuel design, the moderator, blowers, heat transfer-fluid flow design, and the neutronics design; Tennessee Valley Authority was to be the operator. ORNL also became involved in the reactor physics and reactor design studies; experimental investigation of heat transfer and fluid flow behavior; materials development including fuel, graphite and structural metals; out-of-pile testing of components; and in-pile-loop testing of fuels.

In addition to the EGCR project, the early GCR program included studies of advanced gas-cooled reactors (AGRs), particularly of pebble-bed reactors (PBRs). In 1958 Sanderson and Porter developed a PBR design; also, Battelle-Columbus was working on coated-particle fuels. In 1959 the AEC asked ORNL to evaluate this PBR work as part of its GCRP. During 1960

two PBR design studies were carried out, and experimental work was initiated on coated-particle fuel development and performance. The design studies led to plans for a PBR experiment (PBRE). However, because the General Atomic Company was developing the High-Temperature Gas-Cooled Reactor (HTGR) with support from both the AEC and utilities, it was eventually determined that the PBRE was not cost-effective, and the project was terminated in 1963. However, the coated fuel development and fission product behavior efforts started under that program were continued as part of the GCRP.

W. D. Manly was director of the GCRP from 1961 until 1964. During this period the EGCR project proceeded into the construction phase, the emphasis on coated-particle-fueled reactors shifted from PBRs to the HTGR, and studies were initiated on the Gas-Cooled Fast Breeder Reactor (GCFR). Starting in 1961 a cooperative program was initiated with the European Organization for Economic Cooperation and Development (OECD) Dragon Project for HTR development (this continued until the termination of the Dragon Project in 1974). In 1964 the GCRP was split into three parts: G. D. Whitman was named director of the EGCR program, D. B. Trauger became director of the AGR program, and Myer Bender became responsible for the GCFR work. Soon thereafter the GCFR effort was merged into the AGR program. This latter program also included the foreign exchanges on GCR technology other than the EGCR agreements with the United Kingdom.

From 1964 to 1966 construction of the EGCR continued and reached the stage of being ready for fuel insertion, with fuel on site. However, the project was terminated in January 1966 on the basis that the EGCR was not competitve with light water reactors. Subsequently, the previous AGR program became the GCRP, emphasizing HTGR development, with D. B. Trauger as director. Reactor physics efforts were reoriented to allow ORNL participation in the Peach Bottom HTGR Zero Power Commissioning Program. (After the Peach Bottom HTGR started power operation, ORNL participated in surveillance of the circulating activity in the reactor coolant circuit.) ORNL cooperated closely with the General Atomic Company in calculating the predicted nuclear properties of the reactor. Also in early 1966, ORNL studies of large HTGRs (started about 1965) were expanded to include evaluation of design and fuel cycle performance. The GCRP also continued work on fueled graphite development, associated fission product behavior, PBR-type spherical fuel elements [under the Arbeitsgemeinschaft Versuchs-Reaktor (AVR) Memorandum of Understanding], investigations of moderator materials, and HTGR analysis. Prestressed-concrete reactor vessel development (PCRV)(a new technology area) was also initiated in 1966 and has continued until the present. In 1967 and 1968 additional component development was initiated, which included rotating seal development, properties of nickel alloy weldments for HTGR steam generators, and review of HTGR steam generator designs. The mid-1960 work on materials was the beginning of the current HTR materials development effort. Although separate from the GCRP, other HTGR work was also carried out at ORNL, including work under the safety program and fuel recycle studies under the Thorium Utilization Program.

In 1970 the Thorium Utilization Program became part of the GCRP, and P. R. Kasten was named director. At that time the HTGR portion of the GCRP consisted of coated-particle—based fuel development, fission product release and transport studies, materials studies, PCRV development, a coordinated program with HTGR safety studies, and HTGR fuel recycle development involving head-end reprocessing and fuel refabrication. During the 1970s the reactor technology portion of the program expanded into the HTGR safety area, and in 1975 the safety work included both development and licensing-supported activities. After 1975 the HTGR safety program activities decreased, and subsequently the remaining safety studies were transferred to the Nuclear Regulatory Commission safety program at ORNL. The graphite development program was initiated in 1974 and has continued since that time. Starting in 1971, the AEC and the Nuclear Research Establishment at Jülich (KFA-Jülich), Federal Republic of Germany (FRG), signed an information exchange agreement covering HTR base technology, with ORNL interacting with KFA-Jülich. In 1977 the U.S.-FRG Umbrella Agreement covering gas-cooled reactor technology was implemented; ORNL—KFA-Jülich information exchange continues today under the Umbrella Agreement.

The HTGR fuel recycle development work also enlarged during the 1970s, performing expanded fuel recycle technology development and carrying out planning studies for recycle pilot plant implementation and for commercialization studies. However, the recycle effort decreased after HTGRs were withdrawn from the commercial market, and in 1978 the HTGR fuel recycle program became part of the Consolidated Fuel Recycle Program at ORNL. During 1978 studies were reinitiated on the fuel cycle performance of PBRs, and an overall evaluation of pebble- and prism-fueled reactors was completed in 1980.

During this last year the new areas listed at the beginning of this foreword were started so that the HTR program now covers fission product and coolant chemistry, fuel development, PCRV studies, materials studies, graphite development, reactor physics and shielding studies, application assessments and evaluations, and HTR component testing. The ORNL effort is integrated with the national HTR program under the direction of the U.S. Department of Energy, and close cooperation is maintained with other program participants, particularly with General Atomic Company, Gas-Cooled Reactor Associates, and General Electric Company. In its areas of participation, ORNL contributes special and unique facilities to the national HTR program and provides objective expertise to assist in bringing the HTR toward useful and important applications.

Paul R. Kasten

SUMMARY

1. HTGR CHEMISTRY

Sorption of Iodine on Low-Chromium-Alloy Steel

Iodine sorption tests on low-alloy steel were concentrated initially on the 400°C isotherm. At iodine pressures ranging from 10^{-1} to 10^{-2} Pa (10^{-6} to 10^{-7} atm) and a temperature of 400°C, loading increase with partial pressure evidently results from FeI_2 formation. Between 10^{-2} and 10^{-5} Pa (10^{-7} and 10^{-10} atm), we observed a variability of from one to two orders of magnitude in the loading, which was clearly related to changes in the surface condition. The lowest loadings were obtained with specimens that appeared to be corroded; the highest loadings, which in this range were constant at 5 μg/cm^2, evidently represent monolayer coverage on the bare steel surface. A steep decline in loading was observed below 10^{-5} Pa (10^{-10} atm), with a value of about 0.05 μg/cm^2 typical at 10^{-6} Pa (10^{-11} atm). As with graphite, iodine desorption rates were determined in tests involving either a drop in the iodine partial pressure or an increase in the specimen temperature.

Iodine Sorption and Desorption from Graphite

Iodine sorption tests on grade H451 graphite were conducted from 250 to 1000°C. At each temperature, we found a linear relationship between the logarithm of iodine loading (microgram per gram of graphite) and the logarithm of the iodine partial pressure. At 1000°C the iodine loading ranged from 10^{-5} μg/g at an iodine partial pressure of 5×10^{-6} Pa (5×10^{-11} atm) to 2×10^{-4} μg/g at a partial pressure of 8×10^{-3} Pa (8×10^{-8} atm). Equilibrium iodine loadings increased with decreasing temperature, although not at a uniform rate. At the lowest test temperature (250°C), iodine loadings ranged from 2×10^{-2} μg/g to 1.2 μg/g for the same range of iodine concentrations in the helium. In addition to equilibrium tests, the rate of iodine desorption was measured by two other types of tests: desorption caused by a rapid drop in iodine partial pressure and desorption caused by a temperature rise.

Silver Diffusion in H451 Graphite

Silver diffusion profiles were measured for two different sample configurations. In the first, hollow graphite cylinders were partially filled with silver-laden graphite powder and sealed with a graphite end-cap. For the second set of experiments, solid graphite cylinders were used. The cylinders were surrounded by a graphite foil loaded with the silver source. The foils had a paper-like consistency and were wrapped tightly around the samples. The isothermal diffusion anneals were performed in a small tube furnace. Although most experiments were performed in a vacuum, some were run in inert and reducing atomospheres. After the diffusion anneal, the samples were radially sectioned by a small precision lathe. The amount of radioactive silver in each section was measured by placing the collected graphite powder in a sodium iodide detector.

Two features are apparent for all the diffusion profiles. A high-concentration, slow or nonmoving silver component occurs near the surface. Away from the surface, a low-concentration, faster moving component occurs. This behavior is similar to results previously seen for cesium diffusion in graphite. We are currently analyzing our results in a diffusion-with-trapping model as presented by Evans et al. However, this model does not cover the behavior of the tightly bound surface layer.

Plutonium and Uranium Diffusion in Graphite

An investigation has been initiated to study the vapor pressure and diffusion properties of plutonium in graphite. The experimental procedures used in the work will be tested first by using uranium as a stand-in for plutonium. Two types of diffusion experiments are planned: (1) a two-block contact method in which graphite blocks with embedded uranium will be contacted with other graphite blocks that are initially uranium free (these experiments are currently in progress) and (2) a method employing a simulated fuel stick bonded to graphite, in which the matrices in the fuel sticks used will contain low concentrations of uranium.

2. FUELED GRAPHITE DEVELOPMENT

The Fueled Graphite Development Program at ORNL continues as part of the national HTGR fuel development effort being conducted in cooperation with the General Atomic Company (GA). The ORNL portion of the program centers around irradiation testing and specialized postirradiaiton examination (PIE) techniques and equipment. General Atomic's portion of the program includes interface with core designers and with the licensing activity and responsibility for the fuel performance model development. At the end of the current reporting period, the task of screening candidate fuels is essentially completed. The remaining work is the selection and qualification for licensing of a reference fuel. Our role in the qualification effort will be to continue providing services for the assembly and monitoring of irradiation capsules, special examinations of irradiated fuel, and assistance in interpreting the results of the examinations.

The major focus of the Fueled Graphite Development Program work during this reporting period has been on the examination of fuels from capsules HRB-14 and HRB-15b by use of the irradiated microsphere gamma analyzer (IMGA) and the postirradiation gas analyzer (PGA) systems. These capsules contained candidate fissile fuels being considered in the reference fuel selection process. Fuel from capsule HRB-15a will also be considered; this capsule was irradiated during 1980.

In addition to cooperating with GA under the national HTGR fuel development program, cooperation with the German Nuclear Research Center at Jülich [Kernforschungsanlage (KFA) Jülich] is in progress. The cooperation with KFA is part of the formal agreement between the U.S. and German governments for gas-cooled reactor development. Areas of work under the ORNL/KFA cooperation include fuel PIE techniques and procedures. Also

included in the cooperation is a personnel exchange. A report of work performed during this reporting period by the ORNL assignee to KFA is included in Chap. 2.

The Fueled Graphite Development Program continues to be organized around four subtasks: (1) Irradiation Testing, (2) Development Work, (3) Project Work Statement (PWS) Activities, and (4) Equipment Development and Maintenance. Highlights of work under each of these subtasks are

Irradiation Testing

- Completed final topical reports on HT-34 and HRB-13 experiments. The major conclusion reached from the HT-34 work is that considerable within-batch variation exists in the irradiation behavior of the pyrocarbon (PyC) coatings on Biso-coated fertile particles. Batches, which were gastight before irradiation, became permeable during irradiation, with the degree of permeability varying greatly. This behavior is probably the result of a wide variation in the coating conditions of the particles, caused by their random movement within the coater. The major objective of the HRB-13 experiment was to determine the influence on irradiation performance of deviations from spherical form for weak-acid-resin (WAR)-derived fissile particles. The presence of chlorine in the particles compromised this objective, which caused all test specimens to perform poorly.

- Partially completed the PIE on fuel specimens irradiated in capsules HRB-14 and HRB-15b. The most significant observations from the HRB-14 fuel examination was the loss of both gaseous and metallic fission products. Postirradiation examination of the ORNL fuel irradiated in capsule HRB-15b has not proceeded to the point that definitive conclusions can be reached. However, PGA work on GA Triso-coated particles showed good performance relative to fission gas retention.

- Completed irradiation of capsule HT-35. This irradiation was completed at the end of 1980, but no examinations have yet taken place.

- Partially completed irradiation of capsule HRB-15a. This capsule contains only fuel fabricated by GA. We operated this capsule as a service to GA during FY 1980, with funds coming from the ORNL program. In FY 1981 this arrangement was changed slightly so that U.S. Department of Energy (DOE) funds designated for GA irradiation service work were included in the ORNL program. Beginning in FY 1981, this work is covered under a separate task and will be reported under that task in the 1981 annual report.

- Completed planning for the HRB-16 experiment. This work was done in conjunction with GA and will be included in the GA irradiation service task beginning in FY 1981.

Development Work

- Completed studies on PyC deposited by use of CO_2 dilution of the coating gas. The only work remaining to be completed on this subtask is the examination of fuel with CO_2-diluted PyC coatings irradiated in capsule HT-35. These studies have shown no advantage from CO_2 dilution over conventional coating recipes for PyC deposition. More sophisticated PIE techniques applied to fuel from batch OR-2013 (formerly thought to be gastight after irradiation) showed these particles to have become gas-permeable during irradiation in capsule HT-34. It was the perceived excellent performance of batch OR-2013 in earlier HT capsules that led to these additional studies of PyC coating by using CO_2 dilution.

- Completed the silicon carbide (SiC) characterization phase of the SiC development subtask. Correlations have been established between deposition parameters and SiC microstructure, based on transmission electron microscopy (TEM), x-ray diffraction, and small-angle x-ray scattering (SAXS) measurements.

- Completed laboratory-scale studies on dense UCO kernel fabrication. Microspheres of dense UCO with the desired UO_2 + UC_2 content have been produced by using a two-step sintering process. The sintering was done at 1500°C, which is considered an advantage over conventional sintering recipes that require temperatures as high as 1900°C. Atmospheres of argon plus small percentages of carbon monoxide are used to control the chemical composition of the microspheres.

Project Work Statement Activities

- Work was completed on PWS FD-12. On the basis of examination of Biso-coated particles irradiated in HT-34 and HRB-14, we concluded that coatings vary considerably within a batch in their ability to remain gastight during irradiation. From these results we conclude that it is probably not possible to produce Biso-coated fuel that will meet rigid performance specifications. The recent selection of a Triso-Triso system for the reference low-enriched uranium (LEU) fuel cycle was well advised.

- Work was completed on PWS FD-13. This comparison of IMGA with postirradiation annealing and autoradiography (PIAA) showed the ORNL-developed IMGA system to be more effective in measuring both failed-particle fractions and retaining fission products in irradiated coated-particle fuels.

Equipment Maintenance and Development

- A new particle handler was fabricated for IMGA. The new handler, which is more versatile than was the old one, is designed for remote maintenance. This feature will preclude the time-consuming cell decontamination required for maintenance of the old handler.

- Much work was done with the cold-particle-breaking feature of the PGA system. Development of the capability for hot-particle breaking continued. We tried to establish the capability for making an Ne-He measurement on Biso-coated particles that have been irradiated, but this feature is not yet operational.

- Construction of the remote x-radiography unit was completed, and the equipment is now operational.

3. PRESTRESSED CONCRETE PRESSURE VESSEL DEVELOPMENT

Techniques are being developed under the analysis methods development task to improve the accuracy and efficiency of modern finite-element codes. Two areas are currently under investigation: revisions to the endochronic concrete constitutive relations and computations of creep effects in concrete structures. Although the theory represents a potentially powerful tool for use in the analaysis of prestressed concrete pressure vessels (PCRVs), results of the investigation of the endochronic theory indicate that the relations are of limited use until methods for determining creep and cracking effects are implemented and more control of the shape of the concrete stress-strain curve is obtained. By using the principle of superposition and a rate-type creep law with internal variables corresponding to a Maxwell chain model, a set of FORTRAN IV subroutines is being developed to provide a finite-element program for creep calculations of concrete structures.

Evaluation of concrete material properties in a nuclear environment included both an updated review of available data and a performance specification for a concrete multiaxial testing system. Results of the review of concrete properties indicate that:

- Data needs exist for concrete behavior under multiaxial, elevated-temperature, and irradiation loadings.
- The applicability of high-strength concrete to current designs needs to be assessed.
- Alternative construction material systems such as fibrous concrete should be evaluated for their potential to provide improved PCRV performance at reduced cost.

A draft performance specification has been prepared for a concrete multiaxial material-testing system that, when fabricated, will provide data representative of PCRV concrete behavior under normal and postulated accident conditions. Covered in the specification are requirements for specimen configuration, static load capability, fatigue loading capability, load frame assembly, hydraulic actuators, load transducers, loading platens, hydraulic supply system, environmental chamber, specimen displacement instrumentation, interactive computer control, data acquisition and analysis, and acceptance testing.

A cylindrical (1200-mm-long, 991-mm-OD, 152-mm-thick wall) ASTM A 508 class 2 steel specimen containing a longitudinal surface flaw was monitored

by acoustic emission (AE) under the instrumentation evaluation and development task while the vessel was subjected to a thermal shock. During AE monitoring 780 valid events were recorded over the entire surface of the vessel, with 286 of the events occurring within ±100 mm of the flaw. Event activity was so intense (occurrance and peak voltages) during small extensions of the vessel flaw that the AE system locked itself out to activity similar to that during leakage of a vessel (continuous noise). Although the test was conducted at relatively low amplifier gains (~65 dB), results show that, because of the energy associated with the flaw growth, future tests should be conducted at much lower amplifier gains.

Under the structural models task an overview of PCRV-related model tests was conducted, and techniques were initiated for development of wire-winding and nonleak liner systems for PCRV models. Contained in the summary of model tests is information on (1) requirements for PCRV model tests, (2) model testing methods, (3) structural model types, (4) materials for structural models, (5) size effects, (6) instrumentation for model tests, (7) hydraulic versus pneumatic pressure loading of models, and (8) review of PCRV-related model tests. We are investigating the feasibility of modifying a commercial concrete pipe wire-winding facility so that closer wire spacings and wire layering can be used for PCRV models. The use of flanged heads to which a skirt section of 12-gauge AISI 1008 drawing quality steel is joined is being evaluated as a candidate PCRV liner material. These techniques and a relatively new construction material (fibrous concrete) will be evaluated by testing an approximately 1/30-scale fibrous concrete model.

The liners and penetrations task activities tested weldments for the steel penetrations and closures of the liner system for the PCRV for an HTGR. Drop-weight, dynamic precracked Charpy, and compact tests of the weld metal and heat-affected zones (HAZs) of W-3 weldment material are presented. Results obtained from testing a 1 *T* compact specimen from plate P2, using a recently developed computerized *J*-integral unloading compliance system, are presented and compared with previously published fracture toughness data.

4. STRUCTURAL MATERIALS

Work at ORNL on HTGR structural materials is directed toward development of the materials technology necessary for designing and licensing HTGR systems.

Mechanical Properties

Long-term creep tests, many exceeding 30,000 h, on a number of candidate HTGR alloys have continued to show relatively little effect of HTGR helium on creep rates but have shown measureable deterioration of fracture strains. Much emphasis has been on the creep behavior of weldments, particularly Hastelloy X and Inconel 617. Hastelloy X weldments prepared with Hastelloy S filler metal exhibited very good properties.

A number of alloys have reached aging exposures exceeding 20,000 h. Postexposure testing includes tensile, impact, creep-rupture, fatigue, and

crack growth. Inconel 618 has been found to have thermal stability much superior to that of Inconel 617, Hastelloy X, and HD556. Low-cycle fatigue tests on Hastelloy X and Inconel 617, including materials aged at 538 to 871°C up to 20,000 h, have shown that the effect of aging is relatively minor and generally beneficial, although both aging time and temperature affect cyclic life. Investigation of fatigue crack propagation in aged and unaged Hastelloy X and Inconel 617 continued, and work began on creep crack growth in alloy 800H.

Mechanical testing of ceramics was initiated, high-precision compressive creep results were obtained on fused silica, four-point bend tests were started on silicon nitride, and a system was designed and constructed for stress relaxation testing.

Corrosion

Steam corrosion testing of alloys was terminated after 28,000 h because of the loss of access to the exposure facility. A report summarizing all the data obtained has been prepared.

A wide variability of carburization rates has been observed under HTGR-helium exposure conditions considered to be equivalent. This has been explained on the basis of flow direction and specimen position variability of carbon potential and H_2O supply rates. Alloys carburized in HTGR helium under zero applied stress were found to dilate up to 1% as a result of carburization-induced surface stresses. Finally, data were obtained showing that H_2O is probably the most important factor in controlling the carburization of alloys in HTGR helium.

Joining

Three modified Inconel 617 alloys were welded satisfactorily, and preliminary results indicated good weldment properties. Welding evaluation of cast nickel-base alloys has shown that high-energy density welding processes such as laser and electron beam have promise for making acceptable fusion welds in alloy 713LC. These techniques have also been employed to join oxide-dispersion-strengthed alloy MA956, and tests of weldments produced are in progress.

Structural Ceramics

Experiments to determine the effects of aging on the resilience of fibrous insulations were initiated. Depressurization testing of several insulations and dense ceramics was completed. One material, a Masrock fused silica, disintegrated in the test, but all others survived without readily discernable effects. Specimens of Corning 7941 fused silica were examined before and after creep testing. Devitrification had not occurred in 2000 h at 982°C, and the only visible change in structure was a coalescence of porosity.

Fission Product Interactions

Examination of nickel-base alloys exposed to low concentrations of tellurium for 6000 h at 700°C has confirmed that tellurium diffuses selectively along grain boundaries and results in severe intergranular embrittlement. This effect is minimized in alloys containing about 1% Nb.

5. HTGR GRAPHITE STUDIES

Irradiations in ORR

After considerable difficulty in procuring components, the second 600°C compressive creep experiment (capsule OC-4) was inserted into the ORR on November 25, 1980. Because of changes in the core configuration, the experiment tended to run hot but operated well with a 10% reduction in reactor power. By December 31, 33 d of a minimum 110-d exposure had been completed. Design of the 1200°C creep capsule is now being refined on the basis of the successfully completed bench test runs.

Irradiations in HFIR

Two irradiation experiments were or are in progress in the High Flux Isotope Reactor (HFIR). One (HTK-4) under the U.S.-Federal Republic of Germany (FRG) Umbrella Agreement is due out of the reactor in April 1981. The other experiment, conducted for and supported by United Nuclear Company, investigated the behavior of TSX graphite in the N-Reactor at Hanford. This experiment is of sufficient importance to the HTGR program that the results are reported here in some detail. Grade TSX is quite similar to the H327 graphite used in the Fort St. Vrain Reactor. The major conclusions were (1) all mechanical properties remain "safe" at the fluence usually defined as "end-of-life" and (2), at least at 600°C, results from HFIR correctly predict graphite behavior in a power reactor over an approximate 50-fold flux difference.

Oxidation Experiments

Catalytic oxidation has now been observed in HTGR graphite grades H451, 2020, and German grade ASR-1RG. We take as evidence of catalysis either "inside-out" oxidation or, more directly, pinhole oxidation around observable high-atomic-weight inclusion. If these observed phenomena are attributed to iron, calculations show that the ORNL oxidation apparatus operates at impurity concentrations in the range where the oxidation potential permits $Fe \rightleftharpoons Fe(II)$ to proceed.

In other experiments, nondestructive measurement of electrical conductivity by eddy-current techniques has been demonstrated to be an excellent qualitative measure of burn-off level and profile. Quantitative measures are in progress. A growing body of data now exist on the German reflector graphite ASR-1RG. The material exhibits catalytic pinhole oxidation. Mechanical property data are somewhat clouded by the large particle size, which is incommensurate with our sample geometries, but the general behavior is identical to that of the U.S. graphites.

6. HTR CORE EVALUATION

A comparative technical and economic evaluation of pebble-bed and prismatic-fueled high-temperature reactors (HTRs) considered outlet coolant temperatures of 750, 850, and 950°C and reactor power levels of 3000 and 1000 MW(t). Important differences between the two reactor core systems were identified, such as those associated with the PCRV and containment building, the control and control rod systems, the fuel performance and fission product release, the fuel cycle cost and nuclear performance, reactor availability, and research and development costs. Cost estimates were based on probability distributions, and a decision methodology was employed, which utilized these cost probability distributions. We concluded that, on the basis of the results of this study, the United States should continue to develop the prismatic-fueled HTGR.

7. HTR PHYSICS STUDIES

Physics studies were performed to support the pebble-bed and prismatic-fueled HTR core assessment. Of special interest were the control requirements of the pebble-bed core, its susceptibility to xenon-driven oscillation, and its performance in regard to fuel utilization and fuel temperature distributions. Continued development of analysis methods has brought enhanced neutronics, fuel management, and thermal hydraulic capability into routine use.

8. HTR SHIELDING

The HTR Shielding Program began in FY 1981, and initial activities involved finding a suitable cross section set and planning a major shielding experiment. An HTGR design problem was calculated with two ORNL cross section libraries, and the results were compared with GA results. For one of the ORNL libraries, a satisfactory comparison could be achieved by choosing graphite data processed with the appropriate temperature. Although substantial disagreement existed in some regions, agreement in regions of interest for the experiment was good. Consequently, this cross section set was selected for HTR shielding analysis.

Planning for the shielding experiment began in November 1980 in a meeting between ORNL and GA personnel.

9. APPLICATION AND PROJECT ASSESSMENTS

High-Temperature Reactor Reformer and Process Heat Modeling Studies

The chemical heat pipe (CHP) flowsheet as previously presented by General Electric Company (GE) was evaluated, and a number of errors in mass flow rate and in energy balances were determined. The work performed provides an understanding for evaluating the current reference CHP system flowsheet being developed by GE and GA.

Dynamic response modeling of HTR-process heat distribution systems is being performed. Initial emphasis has been on the CHP systems, including the reactor, intermediate-heat exchanger (IHX), reformer, pipeline, and methanator systems. Dynamic simulation models have been developed or obtained for the reactor, the reformer, the pipeline, and the methanator systems. These codes still need to be integrated.

High-Temperature Reactor Application Assessments for Fossil Conversion Processes

During our participation in the HTR Process Applications Work Group meetings, the Exxon catalytic coal gasification (ECCG) process was selected for primary emphasis in 1981. Comments on Bechtel's draft economic ground rules, literature references on the ECCG process, and an estimate of the distribution of the high-temperature heat requirements of the ECCG process were provided.

Project and Priority Assessments

Six reactor applications were evaluated relative to their total commercialization cost per barrel of crude oil equivalent produced and/or saved. One application represents the steam cycle HTR with an outlet-coolant temperature of 750°C, and five applications include the use of an HTR with an outlet coolant temperature of 850 to 950°C as a high-temperature heat source to a reformer.

The most promising applications were identified, and parametric studies were carried out to show the effects of changing (1) plant lifetime, (2) plant scheduling, (3) discount factor, (4) end-year-of comparison, (5) research and development (R&D) and first-of-a-kind (FOAK) costs, and (6) plant costs.

The six plant applications, unit costs, and total commercialization cost of both product energy and crude oil saved/produced were obtained. The HTR steam cycle and HTR reformer for oil shale processing were the most cost-effective and were significantly lower in cost than the CHP and the coal liquefaction/gasification applications studied. However, the shale oil syncrude needs further processing to be comparable with the other products.

10. HTR CFTL STUDIES

The Component Flow Test Loop (CFTL) has been evaluated for testing HTGR components. The Stage Alpha version of this loop is being constructed with Gas-Cooled Fast Reactor (GCFR) Program funds. Unique characteristics of this loop and supporting facilities include the ability to circulate relatively large volumes of helium at HTGR operating temperatures and pressure, the potential for executing rapid and controlled transients involving both flow and power input, the availability of a sophisticated data acquision system, and the availability of large amounts of electrical power (40 MW and more). Initial study indicates that application of the CFTL is pertinent to performance testing of the HTGR core

support structure, to determining the performance characteristics and structural response of various heat exchange components and systems, and to evaluating the core spatial fluid flow and temperature behavior under various reactor conditions.

Of the various applications, the test that appeared to have the most favorable attributes for early resolution with the Stage Alpha CFTL was a performance test of the HTGR core support structure. Preliminary evaluation of the associated test requirements indicates that the coolant flow range required is well within the capacity of the CFTL circulators and that appropriate flow conditions can be produced in a test piece having the needed geometries. Hardware acquired under the GCFR program but not installed in the Stage Alpha design can be used to fabricate an appropriate test vessel. A controlled power supply of approximately 1.5 MW will be needed; although this power is available from the installed transformers, additional controls for about 1 MW will be needed. Planning for the core support performance test (CSPT) is proceeding on the basis that it will be the first test carried out in the CFTL.

1. HTGR CHEMISTRY

R. P. Wichner

1.1 SORPTION OF IODINE ON LOW-CHROMIUM ALLOY STEEL — M. F. Osborne and R. B. Briggs

The primary objective of these tests was to determine the equilibrium sorptive capacity of 2-1/4 Cr-1 Mo steel (which comprises most of the cooler regions of HTGR coolant circuit) under conditions representative of normal operation. The data will be used to improve the capability for predicting iodine desorption as functions of temperature and location in the primary circuit.

Previous studies of iodine sorption on steel were carried out at relatively high iodine partial pressures, usually above 10^{-2} Pa (10^{-7} atm), compared with less than 10^{-7} Pa (10^{-12} atm) expected in the HTGR. Many of the early measurements were obtained under conditions in which large fractions of the available iodine existed as iron iodides (primarily FeI_2) in condensed and/or gaseous form. Conversely, thermodynamic calculations[1] show that, under normal operating conditions, the dominant gaseous species will be hydrogen iodide followed by monoatomic iodine, with no significant amount of FeI_2 present. Therefore, we attempted to determine the equilibrium loadings at the lowest possible iodine partial pressures, with realistic hydrogen pressures added to the helium.

An apparatus and a procedure were developed to conduct the experiments under conditions that could be related to those in the HTGR coolant as follows:

Parameter	Test condition	HTGR condition
Atmosphere	Helium + 500 vpm* H_2	Helium + 10 vpm* H_2
Total pressure	1×10^5 Pa (1.0 atm)	4.8×10^6 Pa (48 atm)
Iodine partial pressure	10^{-6} to 10^{-2} Pa (10^{-11} to 10^{-7} atm)	$<10^{-5}$ Pa ($<10^{-10}$ atm)
Metal temperature	200 to 800°C	~300 to 800°C

In the test apparatus, a low partial pressure of iodine was added to the helium stream by passing helium through a vessel containing elemental

*vpm = volume parts per million.

iodine that was maintained at a controlled low temperature (−80 to −50°C). The helium, containing iodine traced with ^{131}I, passed over the metal specimens mounted in a quartz furnace tube. Rectangular arrays of thin plates were used to provide relatively high surface area—low mass adsorption specimens to facilitate continuous monitoring of the radioactive ^{131}I with mobile NaI(Tl) detectors. In conducting the experiment, stable conditions were maintained for several days until the counting data indicated that the iodine loading on the 2-mm-long primary specimen was at or near equilibrium. Either the temperature or iodine partial pressure was changed, and a new equilibrium loading was sought. Thus, a series of measurements was made on each specimen over a period of several weeks.

In this series of tests, emphasis was on determining the 400°C isotherm. We discovered that iodine sorption was reduced by specimen oxidation; therefore, we sought to minimize this effect both by reducing the level of oxidizing impurities in the helium and by adding hydrogen. Our data at 400°C are presented as the solid symbols in Fig. 1.1. Data at 400°C reported by Neill[2] (open triangles) and by Milstead et al.[3] (open circles) are shown for comparison. As is readily apparent, we found a

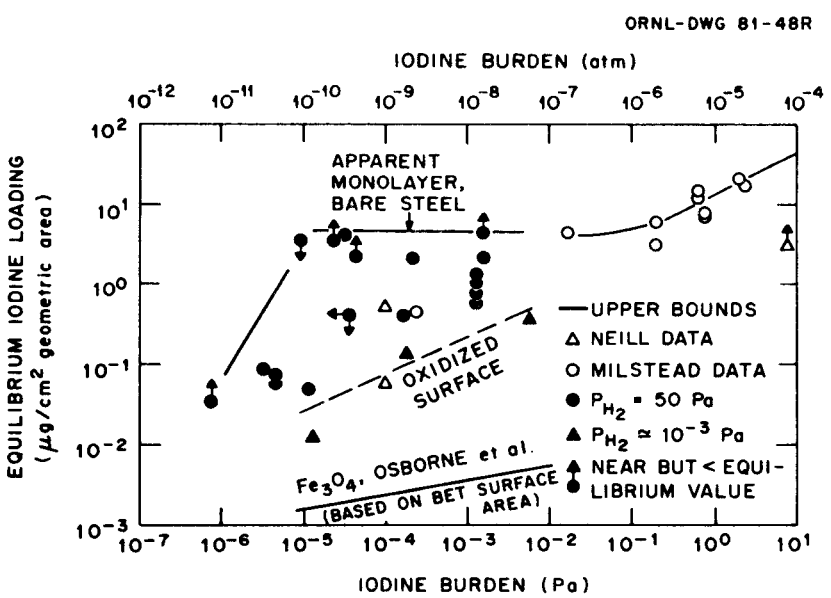

Fig. 1.1. Comparison of all measurements of iodine sorption on steel at 400°C. 1 bar = 10^{-5} Pa.

range of equilibrium iodine loadings at iodine pressures of 10^{-5} to 10^{-3} Pa, depending on the extent of oxidation. Compared with equilibrium loadings on bare metal (~4 μg I/cm^2 geometric area) in this iodine pressure range, heavy oxidation reduced the loading by factors of 10 to 100. At lower iodine pressures ($<10^{-5}$ Pa), the iodine loading decreased approximately linearly with pressure. At 500 to 800°C, equilibrium loadings declined with increasing temperature at all iodine pressures investigated, but the data were not sufficient to define the isotherms.

Although uncertainties exist in the true surface areas available for gas adsorption on the various specimens, comparison on the basis of geometric area (Fig. 1.1) appears to be reasonably consistent. A monolayer of iodine or hydrogen iodide was about 4 μg I/cm^2 geometric area for our specimens, which were determined to have a ratio of true surface area to geometric area of about 50. This large ratio resulted from the combination of surface roughness and crack formation during fabrication. Comparison of these data with the theoretically estimated value of 0.086 μg I/cm^2 for monolayer chemisorption on iron by Compere et al.[4] yielded adequate agreement (i.e., 4/0.086 = 47).

From the limited experimental information reported by Neill[2] and by Milstead et al.,[3] we assume that their specimens were oxidized to some extent and that most of Milstead's data reflect the behavior of FeI_2 primarily, rather than that of iodine or hydrogen iodide. Depending on mass transfer effects, much higher iodine loadings are possible where $FeI_2(s)$ is stable, as shown in Fig. 1.1 and discussed by Hoinkis.[5] However, this reaction is condensation, rather than chemisorption. The equilibrium loadings of iodine or hydrogen iodide were reduced by the presence of oxide on the specimens, approximately to the extent predictable from previous studies of iodine sorption on pure Fe_3O_4 by Osborne et al.[6] (Because these Fe_3O_4 data are based on true surface area, the curve should be shifted upward by a factor of about 50 for direct comparison.) At iodine pressures of 2×10^{-6} to 1×10^{-3} Pa, the higher temperature data indicated consistently lower iodine loadings, as expected.

1.2. IODINE SORPTION AND DESORPTION FROM GRAPHITE — R. A. Lorenz and R. L. Towns

Tests have been performed on the sorptive behavior of iodine on type H451 graphite, the selected core graphite. The determination of equilibrium sorptive capacities at very low iodine partial pressures is emphasized in this work. Toward this goal, our test procedures allow on-line determination of the sorptive capacity down to iodine partial pressures of about 10^{-6} Pa ($\sim 10^{-11}$ atm) in helium at a total pressure of 0.1 MPa (1 atm). The apparatus employed is of the helium flow-through type. Detectors monitor the degree of sorption on specimens and traps, which, together with the helium flow rate and source vapor pressure, yields a continuous determination of iodine mass transport.

For these tests, temperatures ranged from 250 to 1000°C. At each temperature, we found a linear relationship between the logarithm of iodine loading (microgram per gram of graphite) and the logarithm of the iodine partial pressure. At 1000°C, the iodine loading ranged from 10^{-5} μg/g at an iodine partial pressure of 5×10^{-6} Pa (5×10^{-11} atm) to 2×10^{-4} μg/g at a partial pressure of 8×10^{-3} Pa (8×10^{-8} atm). Equilibrium iodine loadings increased with decreasing temperature, although not at a uniform rate. At the lowest test temperature (250°C), iodine loadings ranged from 2×10^{-2} μg/g to 1.2 μg/g for the same range of iodine concentrations in the helium. In addition to equilibrium tests, the rate of iodine desorption was measured by two other types of tests: desorption caused by a rapid drop in iodine partial pressure and desorption caused by a temperature rise.

The principal purpose of this study was to improve the capability for predicting the locations of iodine deposition in the primary circuit by providing improved sorptivity data. Primary-circuit partial pressures are expected to be about 10^{-9} Pa (10^{-14} atm). In our experiments we have therefore sought to achieve as low iodine pressures as possible; the lowest we have thus far achieved is 10^{-6} Pa (10^{-11} atm).

Only a few sorptivity studies on graphite relate to HTGR conditions because of the commonly held belief that the inherently low sorptivity by graphite makes holdup on it unimportant. However, using published values

for graphite sorptivity of iodine, such as those of Osborne et al.,[6] one can readily show that the large internal surface available within the graphite more than compensates for its low sorptivity. No measurements have been made on the reference core graphite material (grade H451). In addition, earlier studies in the low partial pressure range[6] were performed on fragmentized material (<250-μm particles) that could yield uncharacteristically high sorptivities.

A second objective of this study was to measure rates of iodine desorption from graphite under conditions that may aid in accident-consequence determination. Toward this goal, desorption rates have been determined by diminution of iodine partial pressure at a constant temperature and by stepwise increase in temperature at a constant iodine pressure. The first method approximates depressurization conditions (wherein iodine partial pressures are reduced as the total pressure falls) as closely as possible in a 1-atm apparatus. The second desorption procedure approximates core heatup conditions and is also useful in determining the range of desorption activation energies. The analysis and interpretation of the data are still in an early stage. Therefore, all conclusions presented here that involve data analysis and interpretation are preliminary.

1.2.1 Description of the Experimental System

The apparatus is the continuous-flow type in which radioactively traced elemental iodine in a refrigerated U-tube is slowly evaporated into flowing purified helium. The concentration of iodine in the atmospheric-pressure system is controlled by the refrigerator temperature and by the addition of helium through a separate line. This dilution helium is used to provide the clean helium sweep for desorption tests.

A calibrated NaI gamma scintillation counter monitors the amount of ^{131}I tracer collected on the graphite sample. A second similar counting system is used to measure the iodine activity on the charcoal filter downstream of the graphite sample. Because the charcoal filter is essentially a perfect collector of iodine, the concentration of iodine in the helium flowing in the system can be calculated. An additional measurement of iodine concentration in the helium is obtained periodically by

diverting the entire flow stream through a bypass line into a removable charcoal cartridge. A conventional tube furnace is used to control the graphite test specimen in the usual test range of 250 to 1000°C.

1.2.1.1 Graphite Specimens

The graphite specimens were formed from grade H451, which is currently the reference core graphite selected by General Atomic Company (GA). This material is made from a near isotropic mix of calcined coke filler particles with diameters of less than 500 μm to which are added graphite fines. The filler plus pitch binder are extruded into 50.8-cm-diam cylinders, baked, impregnated once, and graphitized at 2800°C. The product is purified, using a halogen gas to diminish the content of iron and other metals that form volatile halides. The specimens used in these tests were annular cylinders closed at one end (cup-shaped). Iodine-laden helium flowed into the open end and passed through the walls of the specimen. The specimen was 2.54 cm long and had a diameter of 1.7 cm and a wall thickness of 0.60 cm. Vigorous cleansing methods were applied to remove dust and adsorbed moisture after the specimen was machined. Additional treatment before the start of a sorption run included degassing for about 24 h in an approximately 0.7-Pa ($\sim 7 \times 10^{-6}$ atm) vacuum and heating at 1000°C in helium.

The measured surface BET area varies somewhat, depending on the specimen and the measurement technique. Generally, measurements ranged between 0.33 and 1.08 m^2/g, with an average value of about 0.8 m^2/g. The average helium density of the specimens tested was 2.05 g/cm^3. A list of impurities found in four specimens in concentrations of at least 1 ppm is given in Table 1.1.

1.2.1.2 Range of Test Data

The range of test conditions for the five test runs performed on grade H451 graphite are summarized in Table 1.2. Initially, in runs 3 and 4, the specimen temperature was held constant, whereas the iodine partial pressure was increased in a stepwise manner after equilibrium loading was achieved. The procedure was altered for subsequent runs in order to minimize the number of changes required in setting the iodine saturator conditions. Although the performance of the iodine saturator was satisfactory

Table 1.1. Impurities in grade H451 graphite in concentrations of at least 1 ppm found by neutron activation analysis

Impurity	Range found in four samples (ppm)
Na	1.0 to 1.6
Mg	3.0 to 12
Al	0.7 to 2.4
Cl	3.0 to 14
K	0.5 to 1.5
Ti	1.6 to 2.7
V	6.0 to 6.5
Cr	2.4 to 2.8
Fe	3.4 to 33
Cu	0.2 to 3.0
Zn	1.0 to 7.8
Mo	0.9 to 1.0

Table 1.2. Range of conditions for iodine sorption tests on grade H451 graphite

Run	Graphite temperature range (°C)	Range of iodine pressure (Pa)	Range of iodine loadings (μg/g)
3	428	2×10^{-4}–5×10^{-2}	0.023–0.4
4	600	2×10^{-4}–2×10^{-2}	8×10^{-4}–0.045
5	250–1000	1.5×10^{-2}	2×10^{-4}–1.2
6	250–1000	1.5×10^{-4}	6.5×10^{-5}–0.09
7	250–1000	9×10^{-6}–3×10^{-2}	3.3×10^{-5}–0.6

overall, it was occasionally erratic for unknown reasons, especially following changes in refrigerator temperatures. Therefore, runs 5 and 7 were performed with minimal changes in iodine saturator conditions. Equilibrium loadings were measured by progressively lowering the specimen temperature at a constant iodine pressure.

Figure 1.2 illustrates the course of a typical 42-d test (run 5). The ordinate signifies the measured iodine loadings (microgram per gram of graphite) during the run as determined from the on-line gamma detector

ORNL DWG 80-1569

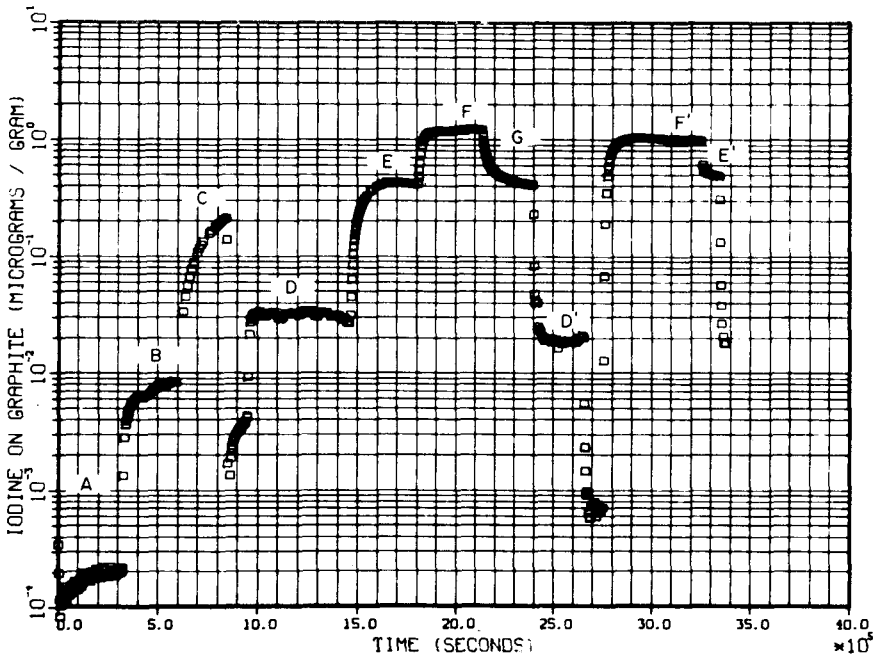

Fig. 1.2. Logarithm of graphite sorption-desorption run 5.

reading. The initial segment (*A*) illustrates the approach to an equilibrium loading of 2.0×10^{-4} μg/g at 1000°C in about 3 d. Subsequently, the specimen temperature was reduced to 800°C, and segment *B* illustrates the approach to equilibrium, again in about 3 d. The following segment (*C*) was a time of test disruption by a power failure beginning 6.0×10^5 s after the start of the run. On recovery, equilibrium loadings were obtained at 600°C (*D*), 400°C (*E*), and 250°C (*F*). An isothermal desorption test was performed at about 21.0×10^5 s (segment *G*), where the iodine partial pressure was reduced to zero for about 3 d; during this time the loading diminished from about 1.1 μg/g to 0.4 μg/g. Subsequently, the reproducibility of loadings obtained earlier in the run was determined in segments *D′* (600°C), *F′* (250°C), and *E′* (400°C). As shown, the loadings obtained with repeated conditions deviated from those initially obtained by approximately −50, −10, and +25% for these three cases. This is a far more consistent behavior than is normally observed for the steel specimens.

1.2.2 Adsorption Isotherms for Grade H451 Graphite

The equilibrium sorption data for all the test runs thus far conducted on graphite are plotted in Fig. 1.3. The uncertainties in the loading are quite large at 1000°C, caused mainly by poor counting statistics at the low levels involved. The limit of resolution for the current test arrangement is about 10^{-5} μg/g. Except for the 428°C isotherm, all of the equilibrium adsorption isotherms shown were acquired by using data from three or four different graphite compacts. The consistency of the data (except for a single point at 250°C) indicates that the equilibrium loadings are not strongly affected by the individual sample characteristics, although our samples were all cut from the same block.

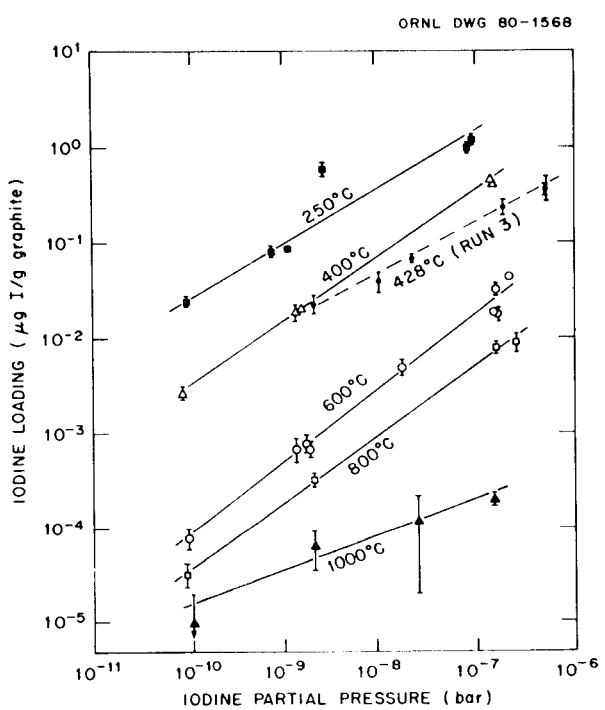

Fig. 1.3. Equilibrium iodine levels in grade H451 graphite. 1 bar = 10^{-5} Pa.

The equilibrium loadings shown in Fig. 1.3 are substantially lower than those previously observed by Osborne et al.[6] for grade H327 graphite. Direct comparisons are given in Table 1.3 for two temperatures, each at

Table 1.3. Comparison of observed equilibrium loadings in grade H451 graphite with previous study[a] using pulverized grade H327 graphite.

Temperature (°C)	Iodine pressure (Pa)	Data of Osborne[a] for pulverized grade H327 (atoms/cm^2)	Pulverized H327 loading, assuming 0.8-m^2/g surface (μg/g)	H451 loading, this study (μg/g)	Pulverized H327[a] / H451
600	10^{-4}	10^{11}	0.17	5×10^{-4}	340
	10^{-5}	3.5×10^{10}	0.058	9×10^{-5}	640
400	10^{-4}	4.2×10^{11}	0.70	0.015	47
	10^{-5}	1.8×10^{11}	0.30	3.2×10^{-3}	94

[a]M. F. Osborne, E. L. Compere, and H. J. de Nordwall, *Studies of Iodine Adsorption and Desorption on HTGR Coolant Circuit Materials* ORNL/TM-5094 (April 1976).

two iodine pressures. Currently measured iodine loadings in graphite are 47 to 640 times less than predicted by the previous study. Undoubtedly, use in the earlier study of pulverized graphite specimens contributed to the higher observed loadings. In addition, the experimental technique differed: the previous tests were performed in a static system at high vacuum, whereas the current tests were conducted in flowing helium at atmospheric pressure. We plan to repeat our measurements by employing the helium flow-through technique with grade H327 to clarify the reason for this significant difference in observed loading.

1.2.3 Desorption from Graphite

Two types of desorption runs were performed: (1) isothermal desorption, achieved by reducing the iodine pressure to zero, and (2) temperature-induced desorption, obtained by stepwise elevations of sample temperatures at a constant iodine pressure. Figure 1.2, illustrating the course of run 5, shows both types of desorption tests. Segment *G* pertains to an isothermal desorption from an equilibrium loading at 250°C, whereas segments *D′* and *E′* represent temperature-induced desorptions.

Table 1.4 is a summary of the isothermal desorption test results. The initial desorption rate depended primarily on the graphite temperature and also on the value of the initial loading and the helium flow rate. The highest desorption rate observed occurred at 800°C, where an initial fractional rate of 0.45%/s was measured. Table 1.5 lists the results of the

Table 1.4. Summary of isothermal desorption rate tests on graphite

Run	Temperature (°C)	Initial loading (μg/g)	Helium flow rate (cm^3/m)	Initial fractional release rate (s^{-1})	Time to desorb 50% of initial loading (s)
3	428	0.41	19	8.4×10^{-6}	1.7×10^5
3	429	0.39	15	5.3×10^{-6}	2.9×10^5
5	250	0.21	71	4.3×10^{-6}	
5	600	0.020	52	1.27×10^{-3}	4.6×10^2
6	400	0.015	68	5.7×10^{-5}	5.5×10^4
6	250	0.080	73	3.1×10^{-6}	9.6×10^5
7	800	7.5×10^{-3}	71	4.50×10^{-3}	1.5×10^2

Table 1.5. Iodine desorption from graphite by increasing temperature (run 7)

Temperatures, °C[a]		Initial loading (μg/g)	Initial fractional release rate (s^{-1})
Initial	Final		
250	250[b]	0.48	3.4×10^{-6}
250	300	0.47	3.9×10^{-5}
300	400	0.44	1.6×10^{-4}
400	500	0.33	6.4×10^{-4}
500	600	0.13	1.7×10^{-3}
600	700	6.2×10^{-3}	2.6×10^{-3}

[a]Temperatures held for 50 min at each level.

[b]Iodine pressure reduced to zero at start of test.

temperature-induced desorptions performed during run 7 with the iodine partial pressures reduced to zero. The initial observed rates are comparable to the values obtained at the corresponding temperatures by the isothermal method. These desorptions were performed by forcing the helium flow through the graphite specimen, a standard rate being about 70 cm^3/min at STP. Therefore, purely thermally induced desorption rates (for example, caused by accidental core heatup with no pressure loss) would be substantially less. Hence, tests approximate more closely conditions during graphite outgassing following a depressurization event. In any

case, iodine desorption from a large graphite mass is a complex process involving (1) the intrinsic rate of desorption of the surface, (2) the rate of iodine convection caused by bulk helium flow through the pores, and, finally, (3) diffusion from blind pores and small capillaries that are not significantly reached by the helium flow.

1.2.4 Conclusions

Tests were performed to determine the equilibrium loadings of iodine on grade H451 graphite in the temperature range of 250 to 1000°C and iodine partial pressure range of about 10^{-2} to 10^{-6} Pa ($\sim 10^{-7}$ to 10^{-11} atm). In addition, rates of iodine desorption were determined under a variety of conditions of two different types: (1) under isothermal conditions having a drop in iodine partial pressure and (2) desorption from step increases in specimen temperature. All tests were performed at atmospheric pressure in a flowing helium system.

The measurements of equilibrium loadings on grade H451 graphite were far more consistent and reproducible than were those for steel. As shown in Fig. 1.3, the logarithm of the loading varied linearly with the logarithm of the iodine partial pressure throughout the experimental range of temperatures and partial pressures. Where direct comparison is possible, these iodine loadings fall significantly below previous determinations by Osborne et al.[6] This finding is most likely a result of the use of a crushed graphite sample in the earlier study in which an abnormally high concentration of active sites would be expected. The extent to which the graphite affected this difference (grade H327 in the earlier tests) will be determined in future tests.

Iodine sorption rates were determined in two types of tests: desorption caused by reduction in iodine partial pressure at constant temperature and desorption caused by step elevations in temperature. These data are summarized in Tables 1.2 through 1.4. The latter method is useful in determining the range of available chemisorption sites.

1.3 SILVER DIFFUSION IN H451 GRAPHITE — R. A. Causey*

The isotope ^{110m}Ag, produced by the neutron activation of the fission product ^{109}Ag, plays a significant role in determining the primary circuit

---

*Consultant, University of Virginia, Charlottesville.

activity of an HTGR under normal operation, especially for fuel employing lower enrichment and higher burnup. This combination leads to more plutonium fissions, for which the silver yield is much higher. We summarize the work performed during the first two years of a three-year study on silver diffusion in graphite. The graphite used is Great Lakes grade H451, which is a slightly anisotropic, coarsely grained graphite having an average density of approximately 1.76 g/cm^3.

Silver diffusion profiles were measured for two different sample configurations. In the first, hollow graphite cylinders were partially filled with silver-laden graphite powder and sealed with a graphite end-cap. For the second set, solid graphite cylinders were used. The cylinders were surrounded by a graphite foil loaded with the silver source. The foils had a paper-like consistency and were wrapped tightly around the samples.

The isothermal diffusion anneals were performed in a small tube furnace. Although most experiments were performed in a vacuum, some were run in inert and reducing atmospheres. After the diffusion anneal, the samples were radially sectioned by a small precision lathe. The amount of radioactive silver in each section was measured by placing the collected graphite powder in a sodium iodide detector.

Diffusion profiles for silver in H451 graphite were measured from 490°C to 800°C. Silver concentrations were varied from 10 ng/g to 1 μg/g. Representative profiles are shown in Figs. 1.4 and 1.5.

Two features are apparent for all the diffusion profiles. A high-concentration, slow or nonmoving silver component occurs near the surface. Away from the surface, a low-concentration, faster moving component occurs. This behavior is similar to results previously reported for cesium diffusion in graphite.[7,8]

The silver near the surface appears to be only adsorbed material on the rough graphite surface. Runs at even the highest temperatures did not show an appreciable movement of this component. This adsorption likely occurs both on active carbon sites created during sample machining and on machining powders left on the surface.

The faster diffusing component inside the sample is likely to be the part that is able to escape the outer active region. The rate at which

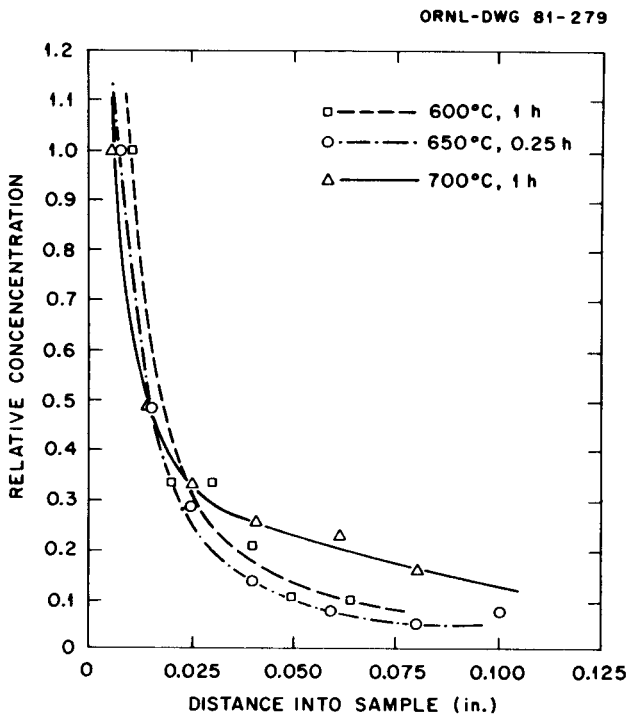

Fig. 1.4. Silver diffusion into solid graphite cylinders. 1 in. = 25.4 mm.

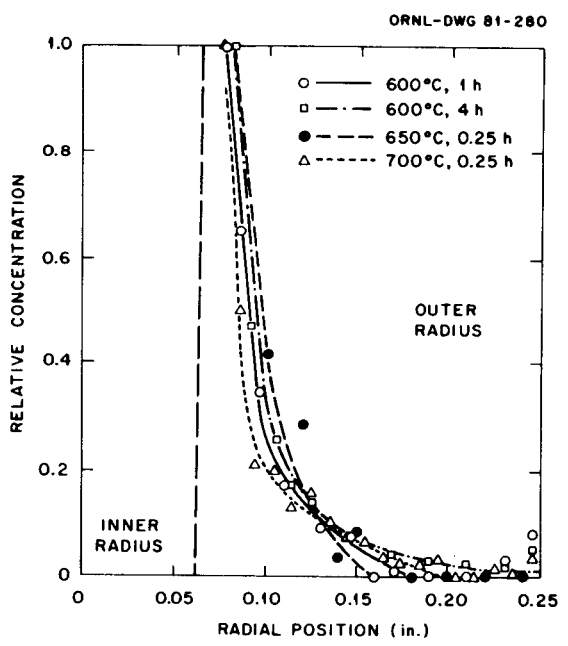

Fig. 1.5. Silver diffusion out of hollow graphite cylinders. 1 in. = 25.4 mm.

this material diffuses suggests that it is diffusing along connecting pore surfaces. Preliminary data for longer anneal times show the possibility of some trapping even deep into the sample. Figure 1.6 shows the Arrhenius plot for the diffusion coefficients determined for the hollow cylinder data. This plot is for the fast component and does not include the effect of trapping.

At present we are analyzing our results in terms of a diffusion-with-trapping model as presented by Evans et al.[8] However, this model does not cover the behavior of the tightly bound surface layer.

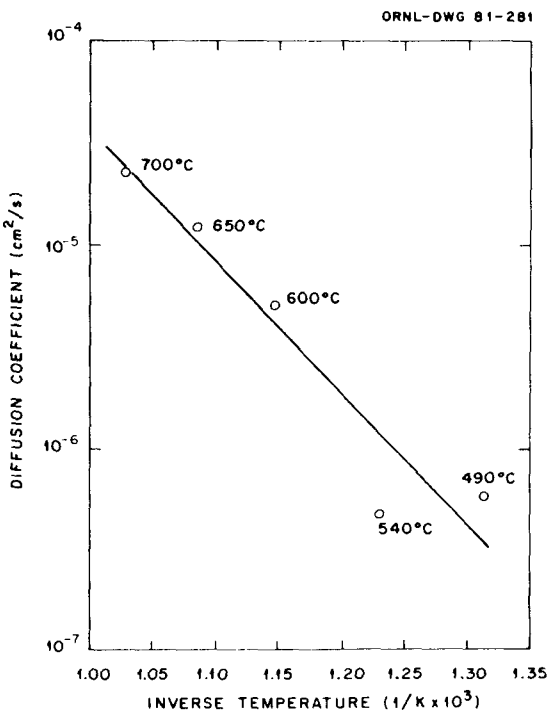

Fig. 1.6. Arrhenius plot for ^{110m}Ag in H451 graphite.

1.4. PLUTONIUM AND URANIUM DIFFUSION IN GRAPHITE — O. K. Tallent and P. C. Arwood

An investigation has been initiated on the vapor pressure and diffusion properties of plutonium in graphite. The experimental procedures used in the work will be tested first by using uranium as a stand-in for

plutonium. Two types of diffusion experiments are planned: (1) a two-block contact method in which graphite blocks with embedded uranium will be contacted with other graphite blocks that are initially uranium free (these experiments are currently in progress) and (2) a method employing a simulated fuel stick bonded to graphite, in which the matrices in the fuel sticks used will contain low concentrations of uranium. Purposes for use of the first method include (1) relatively fast experimental startup and data acquisition; (2) provision of samples for testing scanning electron microscope, x-ray fluorescence, and radioautograph analytical methods; (3) determination of approximate temperature (400 to 1500°C) and concentration effects; and (4) ease of transfer of experiments into an alpha glove box for plutonium work. The second method is designed to simulate as closely as practical actual reactor conditions. This method will require the use of relatively complex equipment and special attention to sample preparation and experimental detail. An attempt will be made to relate mathematically data obtained by the two methods, with the objective of limiting the number of the second type of experiments required. Essentially the same apparatus used in the second method will also be used for plutonium vapor pressure measurements.

Initial experiments using the two-block contact method are currently in progress. First results from 6-h tests at 800°C show less than 1 ppm U transfer from graphite surfaces containing approximately 500 ppm UO_2 to clean graphite surfaces.

1.5 REFERENCES

1. T. M. Besmann, *SOLGASMIX-PV, a Computer Program to Calculate Equilibrium Relationships in Complex Chemical Systems,* ORNL/TM-5775 (1977).
2. F. H. Neill, *Adsorption and Desorption of Iodine on Mild Steel,* ORNL/TM-2763 (1970).
3. C. E. Milstead, W. E. Bell, and J. H. Norman, "Deposition of Iodine on Low Chromium-Alloy Steel," *Nucl. Appl. Technol.* 7: 360–66 (1968).
4. E. L. Compere, M. F. Osborne, and H. J. de Nordwall, *Iodine Behavior in an HTGR,* ORNL/TM-4744 (1975).

5. E. Hoinkis, *A Review of the Adsorption of Iodine on Metals and Its Behavior in Loops*, ORNL/TM-2916 (1970).
6. M. F. Osborne, E. L. Compere, and H. J. de Nordwall, *Studies of Iodine Adsorption and Desorption on HTGR Coolant Circuit Materials*, ORNL/TM-5094 (1976).
7. D. Chandra and J. M. Norman, *J. Nucl. Mater.* 62: 298–310 (1976).
8. R. B. Evans, W. D. Davis, and A. L. Sutton, Jr., *Cesium Diffusion in Graphite*, ORNL-5648 (May 1980).

2. FUELED GRAPHITE DEVELOPMENT

F. J. Homan

2.1 INTRODUCTION

The Fueled Graphite Development Program at ORNL continues to be organized around four subtasks. Highlights of the work accomplished during 1980 are given below.

2.1.1 Irradiation Testing

- Completed final topical reports on HT-34 and HRB-13 experiments. The major conclusion reached from the HT-34 work is that considerable within-batch variation exists in the irradiation behavior of the pyrocarbon (PyC) coatings on Biso-coated fertile particles. Batches that were gastight before irradiation became permeable during irradiation, with the degree of permeability varying greatly. This behavior is probably the result of a wide variation in the coating conditions of the particles, caused by their random movement within the coater. The major objective of the HRB-13 experiment was to determine the influence on irradiation performance of deviations from spherical form for weak-acid resin (WAR)-derived fissile particles. The presence of chlorine in the particles compromised this objective, which caused all test specimens to perform poorly.
- Partially completed the postirradiation examination (PIE) of fuel specimens irradiated in capsules HRB-14 and HRB-15b. The most significant observation from the HRB-14 fuel examination was the loss of both gaseous and metallic fission products. Postirradiation examination on the ORNL fuel irradiated in capsule HRB-15b has not proceeded to the point that definitive conclusions can be reached. However, Postirradiaiton Gas Analyzer (PGA) work on General Atomic Company (GA) Triso-coated particles showed good performance relative to fission gas retention.
- Completed irradiation of capsule HT-35. This irradiation was completed at the end of 1980, but no examinations have yet taken place.

- Partially completed irradiation of capsule HRB-15a. This capsule contains only fuel fabricated by GA. We operated this capsule as a service to GA during FY 1980, with funds coming from the ORNL program. In FY 1981 this arrangement was changed slightly so that Department of Energy (DOE) funds designated for GA irradiation service work were included in the ORNL program. Beginning in FY 1981, this work is covered under a separate task and will be reported under that task in the 1981 annual report.

- Completed planning for the HRB-16 experiment. This work was done in conjunction with GA and will be included in the GA irradiation service task beginning in FY 1981.

2.1.2 Development Work

- Completed studies on PyC deposited, using CO_2 dilution of the coating gas. The only work remaining to be completed on this subtask is the examination of fuel with CO_2-diluted PyC coatings irradiated in capsule HT-35. These studies have shown no advantage from CO_2 dilution over conventional coating recipes for PyC deposition. More sophisticated PIE techniques applied to fuel from batch OR-2013 (formerly thought to be gastight after irradiation) showed these particles to have become gas-permeable during irradiation in capsule HT-34. It was the perceived excellent performance of batch OR-2013 in earlier HT capsules that led to these additional studies of PyC coating using CO_2 dilution.

- Completed the silicon carbide (SiC) characterization phase of the SiC development subtask. Correlations have been established between deposition parameters and SiC microstructure, based on transmission electron microscopy (TEM), x-ray diffraction, and small-angle x-ray scattering (SAXS) measurements.

- Completed laboratory-scale studies on dense UCO kernel fabrication. Microspheres of dense UCO with the desired UO_2 + UC_2 content have been produced by a two-step sintering process. The sintering was done at 1500°C, which is considered an advantage over conventional sintering recipes, which require temperatures as high as 1900°C.

Atmospheres of argon plus small percentages of carbon monoxide are used to control the chemical composition of the microspheres.

2.1.3 Project Work Statement Activities

- Work was completed on PWS FD-12. From examination of Biso-coated particles irradiated in HT-34 and HRB-14, we concluded that coatings vary considerably within a batch in their ability to remain gastight during irradiation. From these results, we conclude that it is probably not possible to produce Biso-coated fuel that will meet rigid performance specifications. The recent selection of a Triso-Triso system for the reference low-enriched uranium (LEU) fuel cycle was well advised.
- Work was completed on PWS FD-13. This comparison of the irradiated microsphere gamma analyzer (IMGA) with postirradiation annealing and autoradiography (PIAA) showed the ORNL-developed IMGA system to be more effective in measuring failed-particle fractions and retained fission products in irradiated coated-particle fuels.

2.1.4 Equipment Maintenance and Development

- A new particle handler was fabricated for IMGA. The new handler, which is more versatile than was the old one, is designed for remote maintenance. This feature will obviate the time-consuming cell decontamination required for maintenance of the old handler.
- Much work was done with the cold-particle-breaking feature of the PGA system. Development of the capability for a hot-particle-breaking system continued. We tried to establish the capability for making an Ne-He measurement on Biso-coated particles that have been irradiated.
- Construction of the remote x-radiography unit was completed, and the equipment is now operational.

2.2 IRRADIATION EXPERIMENTS — F. J. Homan

During this reporting period two irradiation capsules were assembled and irradiated. Capsule HT-35 completed four cycles in the High Flux

Isotope Reactor (HFIR) in November 1980, and capsule HRB-15a will complete eight cycles of irradiation in HFIR in January 1981.

The irradiation program at ORNL moved into a new phase during 1980. The reference fresh fuel selection is scheduled for September 1981. After selection, the remaining work is associated with fuel qualification and licensing, which involves proof testing of large quantities of fuel made in production-scale equipment to a reference fuel product specification. ORNL does not have production-scale capability and therefore will no longer be involved in the fuel fabrication phase of the work. The fuel for future irradiation experiments will be fabricated by GA. We will continue the assembly work and monitoring of the capsules while they are in the reactor. A major portion of the PIE and performance assessment work will be done at ORNL.

The irradiation program in the near future will feature one HRB capsule per year. Because the HT capsules are primarily for screening purposes, none are scheduled beyond HT-35.

2.2.1 High Flux Isotope Reactor Target Capsules — F. J. Homan

The final topical report on capsule HT-34 was completed during this reporting period. Capsule HT-35 was assembled and irradiated. Postirradiation examination and data analysis on this capsule will be reported next year.

2.2.1.1 Capsule HT-34 — T. N. Tiegs

The design, fabrication, and PIE results of capsule HT-34 have been reported.[1-4] During the past reporting period a topical report[5] was completed, the abstract of which follows.

> Irradiation experiment HT-34 was designed to correlate HTGR Biso- and Triso-coated-particle performance with fabrication parameters. Gamma analysis of the irradiated Triso-coated ThO_2 particles showed that the SiC deposited at the highest coating rate performed best. Similar analysis of the irradiated Biso-coated ThO_2 particles showed no performance differences that could be related to coating conditions, but all the particles showed a significant loss of cesium (>50%) at the higher temperatures. Fission gas content measurements at room temperature showed that Biso particles from all

batches, except one batch, had become permeable during irradiation. A partial or complete loss of fission gas from a few particles from a sample of particles inferred that significant coating property variations exist within any given batch. A possible source of uncertainty in interpreting the permeability results may have been introduced because the Biso particles did not receive a postcoating anneal. Biso particles from a batch that had been prepared by using a CO_2 diluent and that had shown outstanding performance in earlier experiments were found to have become permeable during irradiation in HT-34. In contrast, inert gas intrusion measurements on Biso-coated inert (carbon) particles showed, without exception, a marked decrease in permeability.

2.2.1.2 Capsule HT-35 — T. N. Tiegs, I. I. Siman-Tov, and M. J. Kania

The objectives and description of capsule HT-35 have been reported.[6] This experiment was a cooperative effort between ORNL and GA. Specimens prepared at ORNL occupied about 75% of the available test space for fertile particles; the remainder of the test space for fertile particles was occupied by GA specimens. In addition to the fertile particles, ORNL tested Triso-coated LEU fissile particles in the driver rod positions.

Descriptions of the ORNL Biso- and Triso-coated particles are given in Tables 2.1 and 2.2, respectively.

Capsule HT-35 was inserted into the target position of the HFIR on August 17, 1980. It was removed from the reactor on November 19, 1980, after 2140.56 h of total accumulated time at reactor full power. A tabulation of fast fluence values and burnups is given in Table 2.3.

The capsule was disassembled in December 1980 without problem. The GA portions of the experiment were stored in appropriately identified containers for future examination at ORNL. The ORNL fertile particles were unloaded from their graphite crucibles and visually examined. For the most part the particles were in excellent condition; however, a few broken particles (less than four particles in each case) were observed with batches A-762HT, A-765HT, and A-785HT in the high-temperature region and with A-762HT in the low-temperature region. Further examination of these particles will be made with the IMGA and PGA systems to determine quantitatively their irradiation performance.

The driver fuel rods containing the Triso-coated LEU particles are currently being electrolytically deconsolidated to obtain individual

Table 2.1. Location and characterization data for Biso-coated particles in HT-35

Batch[a]	Positions	Dimensions[b]		LTI[c] depostion		LTI[c] density		LTI[c] open porosity (%)	Ne/He permeability	Defective fraction[d]
		Buffer (μm)	LTI (μm)	Temp. (°C)	Rate (μm/min)	Observed gradient (Mg/m^3)	Corrected gradient (Mg/m^3)			
A-762HT	11, 33	69.7	71.4	1225	3.3	1.962	1.904	2.96	0.36	1.3×10^{-5}
A-765HT	4, 29	79.3	78.6	1350	3.1	1.915	1.858	2.99	0.34	1.8×10^{-5}
A-780HT	1, 5, 30	76.3	78.2	1350	4.0	1.864	1.773	4.92	0.37	4.2×10^{-6}
A-785HT	10, 32	83.9	76.3	1225	3.1	1.872	1.815	3.02	0.32	8.6×10^{-7}
A-898HT	13, 17	82.5	79.1	1275	3.2	1.954	1.874	4.1	0.21	4.1×10^{-6}
A-899HT	18, 40	85.2	91.3	1300	3.0	1.953	1.874	4.1	0.21	1.2×10^{-4}
A-901HT	14, 27	90.6	67.7	1200	3.2	1.957	1.826	6.7	0.24	2.4×10^{-5}
A-914HT	20, 41, 42	86.5	81.0	1300	3.6	1.889	1.804	4.5	0.26	6.4×10^{-5}
A-915HT	21, 43	86.2	77.6	1300	4.1	1.928	1.844	4.4	0.23	5.7×10^{-6}
A-919HT	23, 45	90.9	78.5	1325	4.0	1.960	1.861	5.1	0.31	3.2×10^{-5}
A-935HT	24, 48	82.8	70.8	1275	3.8	1.955	1.867	4.52	ND[e]	6.3×10^{-5}
A-961HT	26, 49	76.6	68.8	1275	3.2	1.976	1.906	3.55	0.23	2.0×10^{-6}
J-489	35	81.4	77.7	1375	5.8	1.90	1.79	5.84	0.28	1.5×10^{-6}

[a]A-762, -765, -780, -785 irradiated previously in HT-34; J-489 is a reference batch irradiated in HT-30 and OF-2; A-901 prepared using mixed gas; remaining Biso coatings prepared using propylene-argon-CO_2 gas mixtures. All kernels are nominally 500 μm in diameter.

[b]Mean values.

[c]LTI = low-temperature isotropic.

[d]Standard 2-h chlorine leach at 1500°C.

[e]Not determined

Table 2.2. Location and characterization data for Triso-coated particles in HT-35

Batch	Position	Dimensions,[a] μm				SiC		OLTI density, Mg/m^3		OLTI open porosity (%)
		Buffer	ILTI[b]	SiC	OLTI[c]	Deposition rate (μm/min)	Density (Mg/m^3)	Observed gradient	Corrected gradient	
					UCO kernels[d]					
OR-2884H	1, 14	54.6	37.9	32.8	45.8	0.94	3.200	2.061	1.983	3.79
OR-2885H	6, 19	54.6	37.9	35.9	43.1	0.72	3.204	2.054	1.946	5.27
OR-2886H	12, 25, 39, 52	54.6	37.9	31.6	43.2	0.45	3.198	2.056	1.947	5.32
OR-2887H	9, 22, 37, 50	54.6	37.9	53.0	44.8	0.48	3.197	2.062	1.982	3.88
OR-2888H	3, 16	54.6	37.9	42.5	43.2	0.24	3.194	1.939	1.888	2.61
A-976	28, 31, 34, 41 44, 47	60.7	40.7	34.6	35.7	0.33	[e]	[e]	[e]	[e]
					Inert kernels[f]					
OR-2879H	Bottom-1, -2	94.4	76.6	38.7	37.1	1.11	3.198	2.077	1.993	4.05
OR-2880H	Top-3, -4	94.4	76.6	38.8	44.7	0.78	3.195	2.072	2.025	2.27
OR-2881H	Bottom-3, -4	94.4	76.6	38.5	44.7	0.55	3.196	2.071	2.013	2.79
OR-2882H	Bottom-1, -2	94.4	76.6	30.7	42.2	0.28	3.205	2.067	1.972	4.60

[a]Average values.

[b]ILTI = inner low-temperature isotropic.

[c]OLTI = outer low-temperature isotropic.

[d]Kernel derived from weak-acid resins except for batch A-976. Kernels for batch A-976 are dense UCO prepared by external gelation process.

[e]To be determined.

[f]Triso inert particles are contained in magazine end plugs. Bottom end plugs of magazines 1 (top) and 2 contain General Atomic Company fission product transport experiments.

Table 2.3. Fast fluence[a] and burnup data for fuel specimens in capsule HT-35

Capsule position	Burnup, % FIMA			Fast fluence $E > 29$ fJ (neutrons/m^2)
	^{235}U	^{238}U	^{232}Th	
1P[b], 52P	84.3	7.6	3.3	3.95×10^{25}
1, 52	84.4	8.0	3.5	4.21
2, 51			3.7	4.47
3, 50	84.6	8.7		4.81
4, 49			4.1	4.99
5, 48			4.3	5.22
6, 47	84.9	9.8		5.48
7, 46			4.7	5.71
8, 45			5.0	5.93
9, 44	85.1	11.1		6.17
10, 43			5.4	6.39
11, 42			5.7	6.61
12, 41	85.3	12.2	5.9	6.83
13, 40			6.2	6.99
13P, 40P				
14P[b], 39P	85.5	13.3	6.6	7.55
14, 39			6.8	7.82
15, 38	85.6	14.0		7.96
16, 37			7.2	8.08
17, 36			7.4	8.23
18, 35	85.7	14.8		8.32
19, 34			7.7	8.41
20, 33			7.8	8.49
21, 32	85.8	15.5		8.57
22, 31			8.1	8.64
23, 30			8.2	8.68
24, 29	85.9	15.9		8.72
25, 28			8.3	8.75
26, 27	85.9	16.1	8.3	8.79
26P, 27P				

[a]Fluence data based on axial flux distribution used for HT-30 (ORNL-5274, pp. 227 and 232).

[b]End plug position.

particles. Further examinations of those particles will also be made with the IMGA system to determine quantitatively their fission product inventories.

2.2.2 HRB Capsules — F. J. Homan

During this reporting period the final topical report on capsule HRB-13 was completed. Most of the PIE was completed on capsules HRB-14 and HRB-15b. These capsules contained fuel from both ORNL and GA, and some examinations were performed on GA fuel. The examinations of GA fuel are reported in Sect. 2.7. Capsule HRB-15a was assembled and irradiated. This capsule contained only GA-produced fuel. Capsule HRB-16 was planned during 1980, and the scheduled insertion date is June 1981.

2.2.2.1 HRB-13

Descriptions of the capsule design, fabrication, operation, and PIE have been reported.[7-10] During the past reporting period a topical report[11] was written, the abstract of which follows.

> Irradiation capsule HRB-13 tested High-Temperature Gas-Cooled Reactor (HTGR) fuel under accelerated conditions in the High Flux Isotope Reactor (HFIR) at Oak Ridge National Laboratory (ORNL). Irradiation space was shared by ORNL and Los Alamos Scientific Laboratory; however, the current report is concerned with only the ORNL portion of the experiment. The ORNL portion of the capsule was designed to provide definitive results on how variously misshapen kernels affect the irradiation performance of weak-acid-resin (WAR)-derived fissile fuel particles.
>
> Two batches of WAR fissile fuel particles were Triso-coated and shape-separated into four different fractions, depending on their deviation from sphericity, which ranged from 9.6 to 29.7%.
>
> The fissile particles were irradiated for 7721 h. Heavy-metal burnups ranged from 80 to 82.5% fraction of initial heavy-metal atoms (FIMA). Fast neutron fluences (>0.18 MeV) ranged from 4.9×10^{25} to 8.5×10^{25} neutrons/m^2.
>
> The postirradiation examination (PIE) showed that the two batches of fissile particles contained chlorine, presumably introduced during deposition of the SiC coating. This resulted in chemical attack of the SiC coating by heavy-metals and fission products and subsequent release of volatile fission products such as ^{137}Cs. The attack apparently was strictly temperature dependent. Although some correlation of particle

failure fraction with deviation from sphericity was evident, the results are inconclusive as a result of SiC corrosion. Even the "best" particles in the experiment showed unacceptable failure fractions.

2.2.2.2 Capsule HRB-14

Descriptions of the fabrication, operation, and initial PIE of the HRB-14 capsule have been reported.[12–14] During the past reporting period, all the ORNL planchets were electrolytically deconsolidated to recover the individual coated particles for examination with the IMGA and PGA systems. Selected particle batches from loading zones 1, 2, 5, 6, 9, and 10 were examined. In the following summary results from examination of planchets 1, 37, and 73 are presented. Results from other planchets will be presented later.

Planchets 1, 37, and 73 contained fertile particle batch A-770 and, as reported previously,[14] were severely debonded when the capsule was disassembled. Metallography of the fertile particles (Fig. 2.1) confirmed that they had failed because of fast-neutron damage to the pyrocarbon coatings, even at lowest fluence position. Batch A-770 had a low-temperature isotropic (LTI) optical Bacon anisotrophy factor (BAF_o) of 1.107, and these particles were expected to fail during irradiation. They were part of a series of tests to establish the upper limit for BAF_o.

Results on the IMGA examination of the Biso-coated ThO_2 particle batches are given in Tables 2.4 through 2.6. At present we are using the $^{137}Cs/^{106}Ru$ activity ratio to determine the extent of any cesium release during irradiation. As shown, the only particle batches that showed no average ^{137}Cs loss were the ones at the very ends of the capsule at the lowest burnup positions. All the other batches showed some degree of ^{137}Cs loss. The greatest releases were observed with particles in loading zones 5 and 6 and not in the highest burnup positions (i.e., loading zones 9 and 10). Thermal analysis indicated that the temperatures in loading zones 5 and 6 were higher than in the other loading zones. We therefore believe we are seeing a temperature effect. Similar results were indicated in the gamma scans of the empty graphite sleeve,[14] which showed that the highest gamma activities were associated with the 5 and 6 loading zones. As reported[14] the activity was caused by ^{137}Cs, ^{134}Cs, ^{110m}Ag, ^{140}Ba, ^{140}La, and ^{154}Eu.

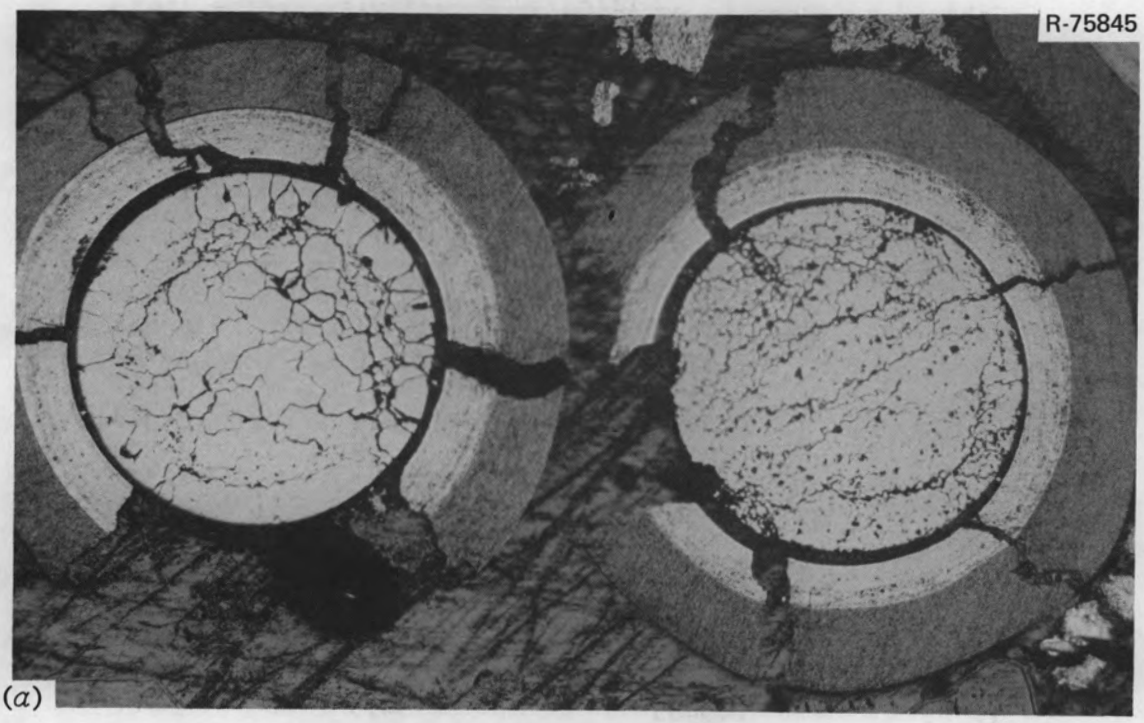

(*a*)

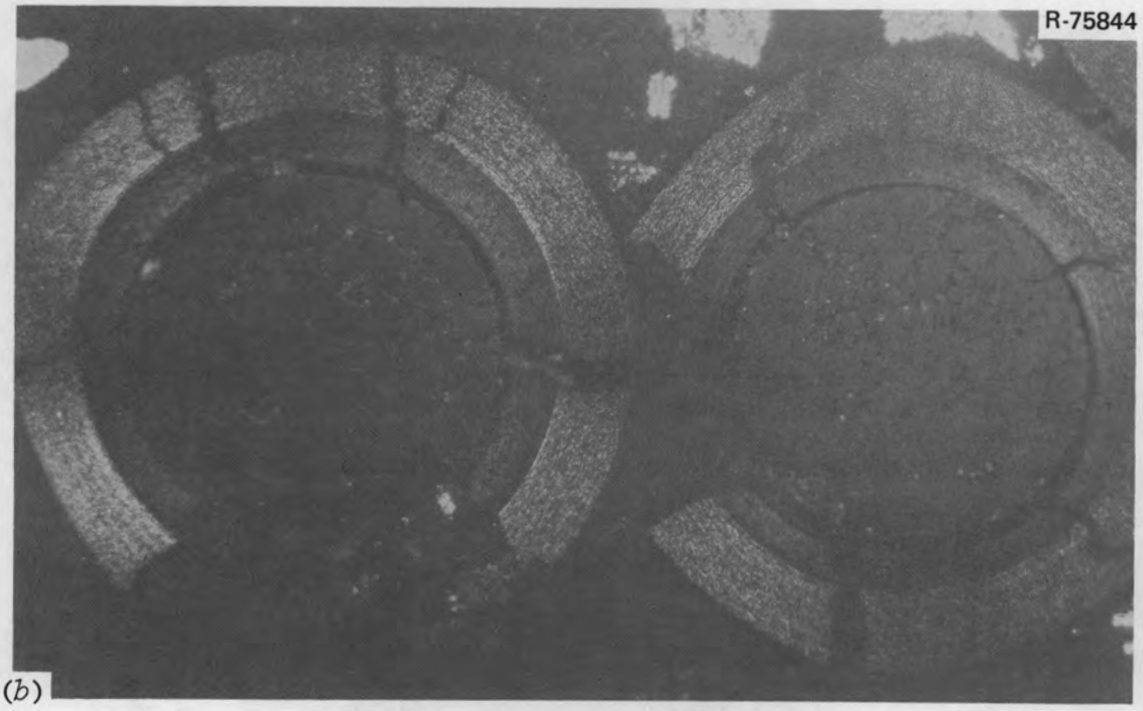

(*b*)

Fig. 2.1. Biso-coated ThO_2 (batch A-770) irradiated in planchet 1 of HRB-14. Failure of the coating is caused by fast neutron damage. (*a*) Bright field. (*b*) Polarized light. (125×)

Table 2.4. Results on $^{137}Cs/^{106}Ru$ activity ratios from Biso-coated ThO_2 particles from loading zones 1 and 2 of HRB-14

Planchet	Average $^{137}Cs/^{106}Ru$ measured activity ratio	Calculated $^{137}Cs/^{106}Ru$ (%)	Particle batch
2	1.058	106.0	A-804
4	1.039	104.1	J-655
5	1.027	103.0	A-762
6	0.9180	92.1	J-647
7	0.9563	96.1	J-649
8	0.9245	92.8	A-803
10	0.9369	94.2	A-785
11	0.8267	83.1	J-651
12	0.8968	90.2	A-787
13	0.8633	87.0	A-771
14	0.9334	94.0	A-786
15	0.8288	83.6	A-784
16	0.8230	83.0	A-758
17	0.9405	94.9	A-782
18	0.8257	83.4	A-766

Table 2.5. Results on $^{137}Cs/^{106}Ru$ activity ratios from Biso-coated ThO_2 particles from loading zones 5 and 6 of HRB-14

Planchet	Average $^{137}Cs/^{106}Ru$ measured activity ratio	Calculated $^{137}Cs/^{106}Ru$ (%)	Particle batch
38	0.8866	90.5	A-804
39	0.7576	77.3	J-641
40	0.7236	73.9	J-655
41	0.7672	78.4	A-762
42	0.5856	59.9	J-647
43	0.5273	53.9	J-649
44	0.6319	64.7	A-803
45	0.6692	68.6	A-765
46	0.6718	68.8	A-785
47	0.4533	46.5	J-651
48	0.6280	64.4	A-787
49	0.5415	55.6	A-771
50	0.6415	65.9	A-786
51	0.6482	66.6	A-784
52	0.6085	62.6	A-758
53	0.8017	82.5	A-782

Table 2.6. Results on $^{137}Cs/^{106}Ru$ activity ratios from Biso-coated ThO_2 particles from loading zones 9 and 10 of HRB-14

Planchet	Average $^{137}Cs/^{106}Ru$ measured activity ratio	Calculated $^{137}Cs/^{106}Ru$ (%)	Particle batch
74	0.7913	82.1	A-804
75	0.6349	65.9	J-641
76	0.7142	74.1	J-655
77	0.7130	74.0	A-762
78	0.5496	57.1	J-647
79	0.5360	55.6	J-649
80	0.5500	57.1	A-803
81	0.6276	65.2	A-765
82	0.6519	67.8	A-785
83	0.5293	55.0	J-651
85	0.6329	65.8	A-771
86	0.7186	74.7	A-786
87	0.7871	81.8	A-784
88	0.6752	70.3	A-758
89	0.7776	80.9	A-782
90	0.7773	80.9	A-766

In conjunction with IMGA analysis of the fertile particles, postirradiation fission gas measurements were also made. These measurements are part of the work scope of PWS-FD-12; consequently, the results are summarized in Sect. 2.4.2.

In addition to the IMGA analysis of the ThO_2 particles, the Triso-coated UCO particles supplied by GA were also examined. Since these were medium-enriched uranium (MEU) particles, detailed measurements were made of the ^{110m}Ag inventories. Analysis of these particles is in progress and will be reported later.

2.2.2.3 Capsule HRB-15b

The objectives, fabrication, operation, and disassembly of capsule HRB-15b have been reported.[15-17] All the GA particles, which comprised about two-thirds of the total irradiation space, were packaged and shipped to GA for detailed examination. (See also Sect. 2.7 for additional work on GA HRB-15b particles at ORNL.)

The ORNL particles were either Biso- or Triso-coated ThO_2. No ORNL fissile particles were irradiated. Visual examination of the particles in their trays showed no failures; however, a few particles were mechanically broken during the disassembly and storage operations.

The ORNL paticles have been removed from the graphite trays and stored in appropriate containers. The particles are now awaiting examination of selected batches by the IMGA and PGA systems.

2.2.2.4 Capsule HRB-15a — I. I. Siman-Tov and M. J. Kania

Capsule HRB-15a contained fuel specimens supplied by GA (no ORNL fuel). The capsule was designed, assembled, and operated at ORNL. Assembly was completed in July 1980, and irradiation began on July 26, 1980. This capsule will complete its scheduled eight-cycle irradiation period on January 28, 1981. The capsule will be discharged from the reactor and stored in the HFIR pool to allow short-lived fission products to decay to an acceptable level before shipment to GA.

The operating history of capsule HRB-15a in Table 2.7 includes anticipated operation data for the last irradiation cycle (203). The

Table 2.7. Capsule HRB-15a reactor operating history

HFIR cycle	Cycle schedule				Irradiation time,[a] h	
	Begin		End			
	Date	Time	Date	Time	In cycle	Total accumulated
196	7/26/80	0200	8/16/80	2200	524	524
197	8/17/80	1805	9/8/80	1435	523	1047
198	9/9/80	2230	10/1/80	2000	525	1572
199	10/3/80	2300	10/25/80	2036	525	2097
200	10/26/80	1724	11/7/80	0700[b]		
	11/9/80	1130	11/19/80	0948	514	2611
201	11/20/80	1710	12/12/80	0935	520	3131
202	12/15/80	2144	1/6/81	1300	520	3651
203	1/7/81	1550	1/29/81[c]		~521	~4172

[a]Irradiation time is given in equivalent hours at 100 MW.

[b]Irregular (scheduled) reactor shutdown during cycle 200. The reactor also operated at reduced power on several occasions during some cycles because of weather conditions.

[c]Expected shutdown date for cycle 203.

total operating time is expected to be 4172 ± 5 h at a full reactor power of 100 MW, resulting in a peak accumulated fast fluence of 7.25×10^{25} neutrons/m^2 $(E > 29\ fJ)_{HTGR}$. The actual versus design fuel rod loadings[18] for HRB-15a are presented in Table 2.8. The deviation in the actual loadings from those used in the design calculations contributed to the problem of maintaining time-averaged fuel centerline temperatures at 1250°C without exceeding a maximum of 1350°C. Preliminary temperature histories of fuel specimens located adjacent to thermocouple positions for the first four irradiation cycles are shown in Figs. 2.2 through 2.9.

Table 2.8. ^{235}U and Th contents of the General Atomic Company fuel rods for capsule HRB-15a

Rod position	^{235}U content (g/m)	^{235}U design (g/m)	Difference (%)	Th content (g/m)	Th design (g/m)	Difference (%)
1	1.795	1.925	− 6.7	33.876	37.257	−9.1
2	1.353	1.581	−14.4	30.647	30.455	+0.6
3	1.160	1.358	−14.6	27.634	26.838	+3.0
4	1.241	1.205	+ 3.0	25.503	24.486	+4.1
5	1.149	1.097	+ 4.7	24.757	22.794	+8.6
6	0.793	1.021	−22.3	21.093	21.523	−2.0
7	0.935	0.967	− 3.3	20.720	20.567	+0.7
8	0.863	0.932	− 7.4	20.242	19.880	+1.8
9	0.769	0.912	−15.7	19.938	19.450	+2.5
10	0.925	0.909	+ 1.8	19.067	19.364	−1.5
11	0.943	0.908	+ 3.9	20.106	19.287	+4.2
12	0.805	0.920	−12.5	20.241	19.460	+4.9
13	0.903	0.950	− 5.0	19.770	19.987	−1.1
14	0.856	1.001	−14.5	20.542	20.941	−1.9
15	0.945	1.078	−12.3	21.634	22.422	−3.5
16	1.260	1.189	+ 6.0	24.797	24.541	+1.0
17	1.606	1.529	+ 5.0	30.353	30.198	+0.5
18	1.900	1.805	+ 5.3	32.390	32.840	−1.4

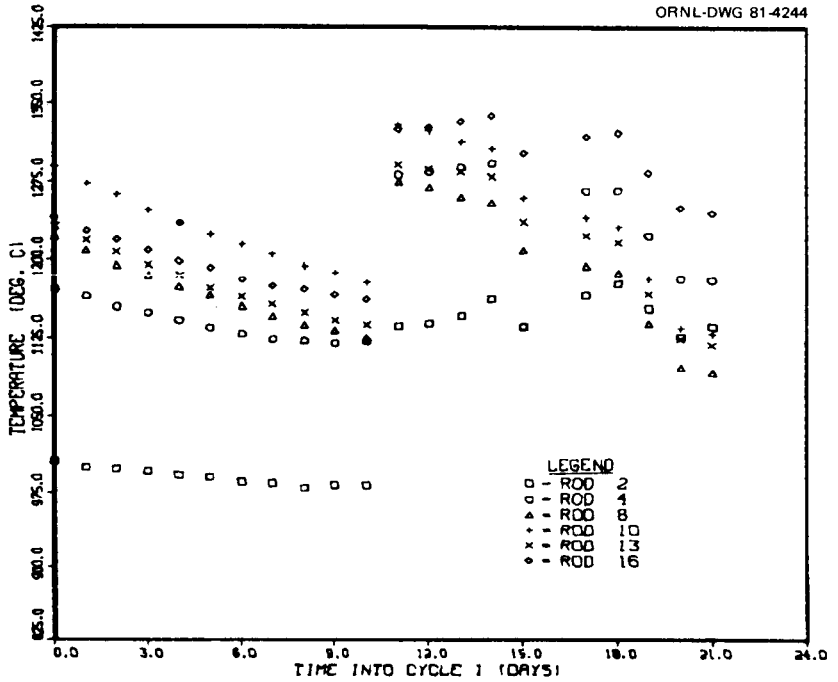

Fig. 2.2. Calculated fuel rod centerline temperatures during first cycle of operation for capsule HRB-15a.

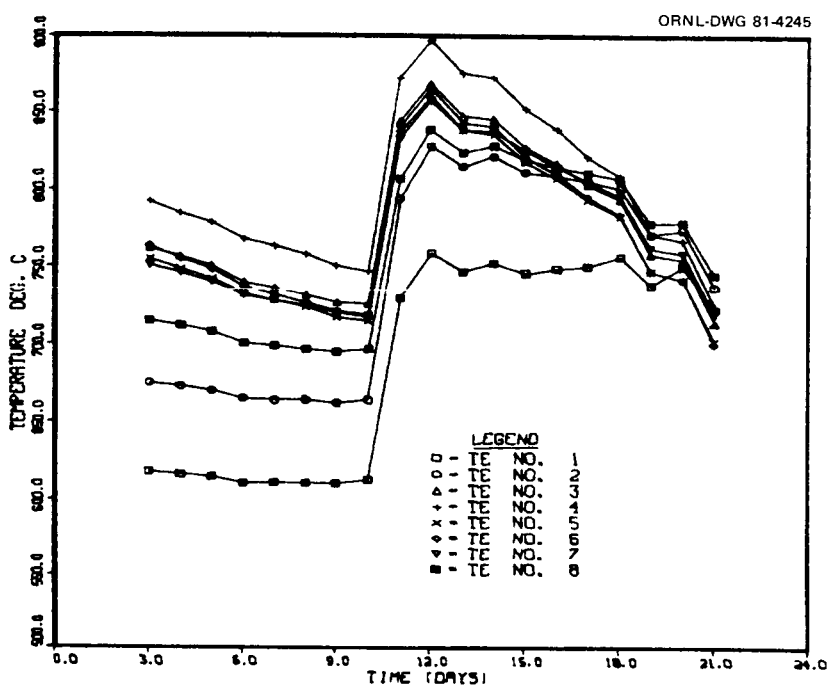

Fig. 2.3. Measured graphite sleeve midwall temperatures during first cycle of operation for capsule HRB-15a.

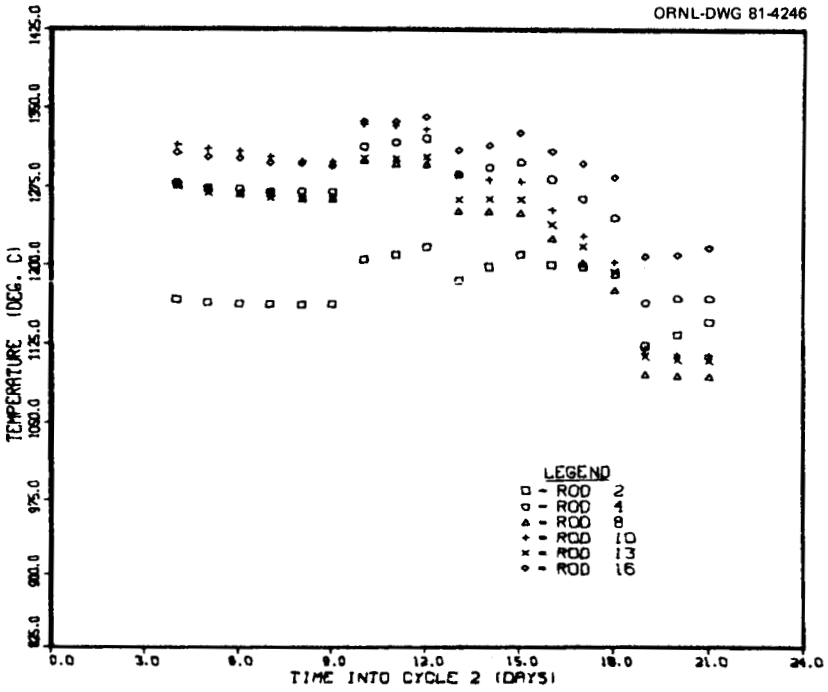

Fig. 2.4. Calculated fuel rod centerline temperatures during second cycle of operation for capsule HRB-15a.

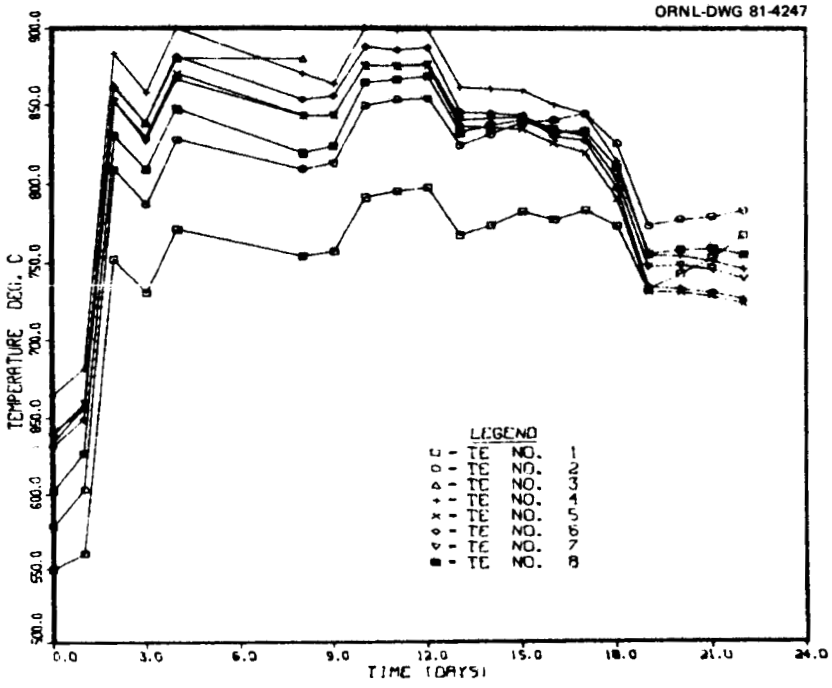

Fig. 2.5. Measured graphite sleeve midwall temperatures during second cycle of operation for capsule HRB-15a.

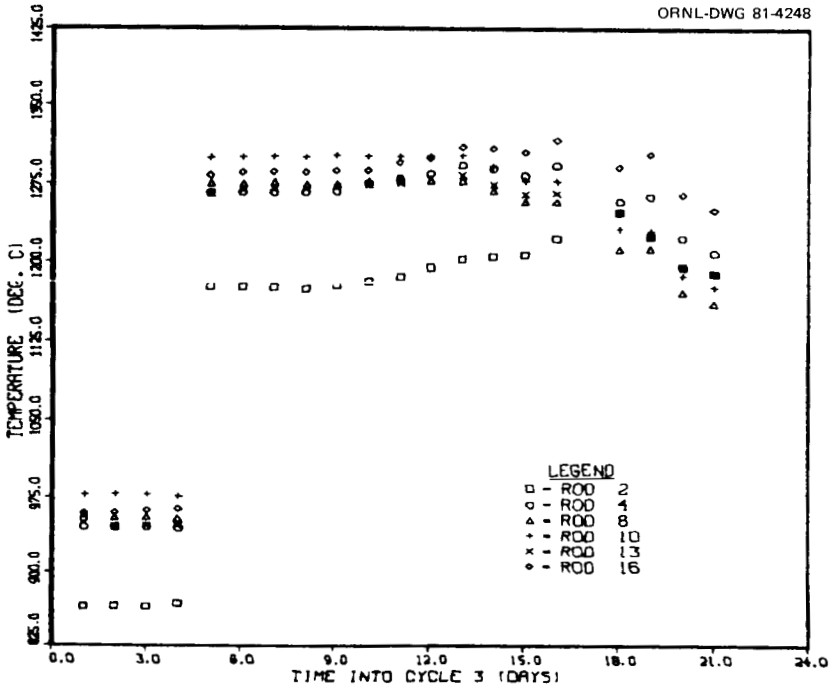

Fig. 2.6. Calculated fuel rod centerline temperatures during third cycle of operation for capsule HRB-15a.

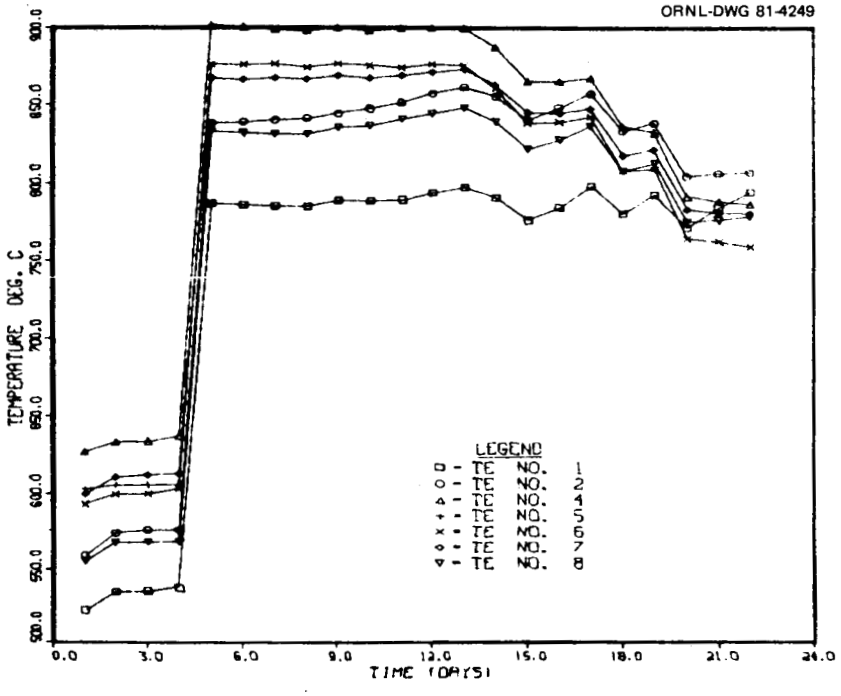

Fig. 2.7. Measured graphite sleeve midwall temperatures during third cycle of operation for capsule HRB-15a.

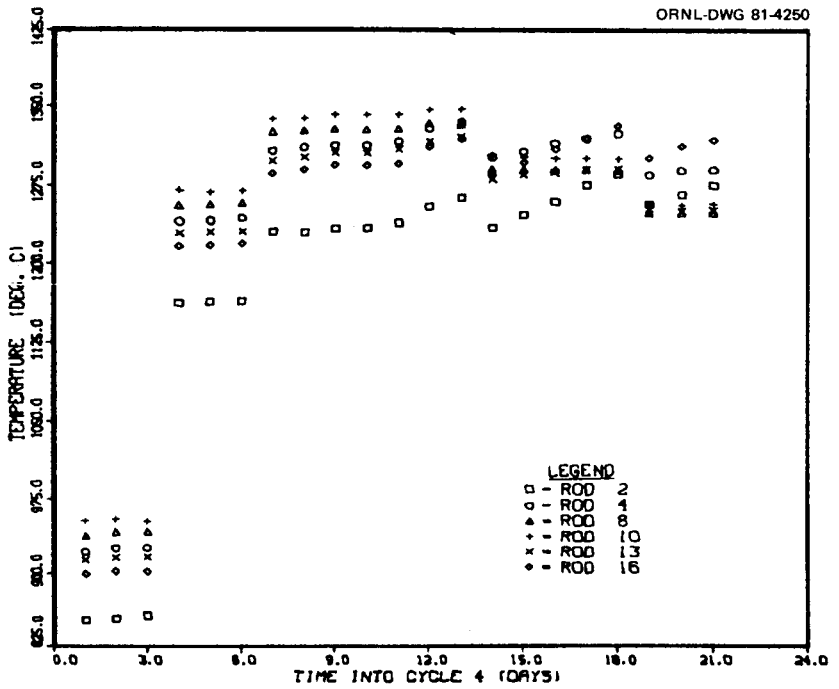

Fig. 2.8. Calculated fuel rod centerline temperatures during fourth cycle of operation for capsule HRB-15a.

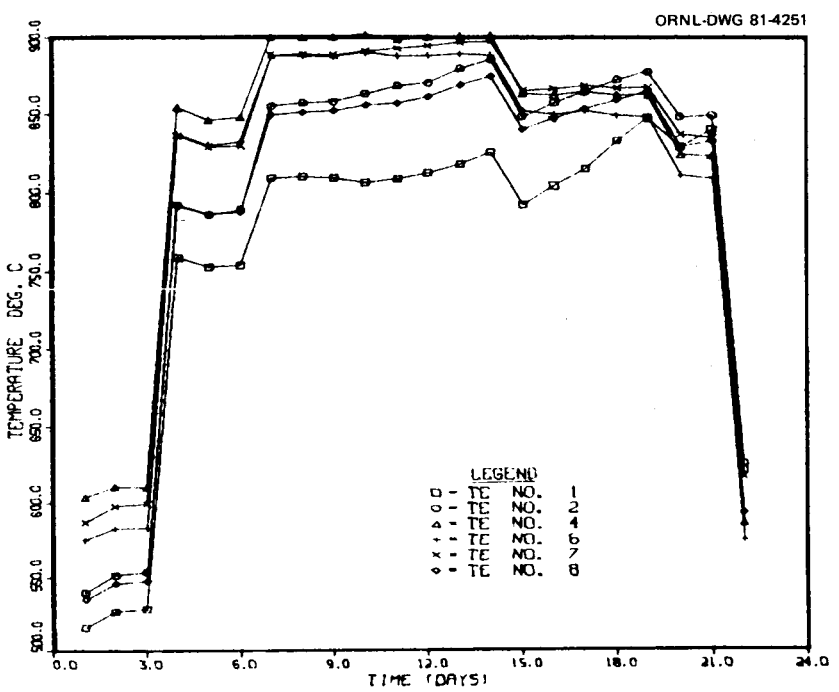

Fig. 2.9. Measured graphite sleeve midwall temperatures during fourth cycle of operation for capsule HRB-15a.

Each figure contains calculated centerline temperatures and recorded thermocouple temperatures for each of the four cycles. Fuel specimen and thermocouple correlation for fuel rods 2, 4, 8, 10, 13, and 16 are listed below.

Fuel specimen	Thermocouple
2	1
4	2
8	3
10	4, 5, and 6
13	7
16	8

Data summarizing the ratios of fission gas release to birth rate (R/B) for the first four irradiation cycles are presented in Table 2.9 Calculated burnup and accumulated fast fluence for fuel specimens during the total irradiation period are given in Table 2.10. Calculations to determine similar data for the remaining irradiation cycles are under way and will be forwarded to GA when completed.

2.2.2.5 Capsule HRB-16 — I. I. Siman-Tov and M. J. Kania

Capsule HRB-16 will contain fuel specimens fabricated at GA and will be assembled and irradiated at ORNL. Fuel loading calculations performed at ORNL were supplied to GA for fuel specimen preparation. These calculations for each fuel specimen position are shown in Table 2.11; thorium and ^{235}U contents are presented. This capsule will contain fuel rods and particle trays holding loose particles. Beginning of irradiation is scheduled for June 1981. Because of the similarity of configuration, rod dimension, and composition with HRB-15a, the loadings were calculated on the basis of HRB-15a design loadings.

2.3 DEVELOPMENT WORK — F. J. Homan

Development activities have been centered in three areas:

- Pyrocarbon coating by using CO_2 dilution. This work is essentially complete except for the evaluation of specimens prepared for

Table 2.9. Capsule HRB-15a R/B[a] data

Sample	Date taken	Accumulated irradiation time (h)	^{85m}Kr	^{87}Kr	^{88}Kr	^{135}Xe	^{133}Xe
1	7/28/80	60.0	6.45×10^{-6}	4.28×10^{-6}	3.97×10^{-6}	4.67×10^{-6}	1.89×10^{-5}
2	8/5/80	251.15	4.00×10^{-6}	3.02×10^{-6}	1.56×10^{-6}	0.99×10^{-6}	0.92×10^{-5}
3	8/12/80	418.45	3.82×10^{-6}	2.70×10^{-6}	2.67×10^{-6}	1.13×10^{-6}	0[b]
4	8/25/80	711.45	5.06×10^{-6}	3.21×10^{-6}	3.40×10^{-6}	1.32×10^{-6}	3.14×10^{-5}
5	8/29/80	805.2	15.00×10^{-6}	9.85×10^{-6}	5.45×10^{-6}	10.82×10^{-6}	14.33×10^{-5}
6	9/2/80	903.3	14.09×10^{-6}	9.19×10^{-6}	5.04×10^{-6}	7.72×10^{-6}	7.97×10^{-5}
7	9/16/80	1168.0	16.11×10^{-6}	9.60×10^{-6}	7.83×10^{-6}	7.18×10^{-6}	20.38×10^{-5}
8	9/23/80	1307.6	17.60×10^{-6}	12.02×10^{-6}	8.95×10^{-6}	12.35×10^{-6}	10.16×10^{-5}
9	10/10/80	1583.0	7.33×10^{-6}	5.76×10^{-6}	3.99×10^{-6}	3.18×10^{-6}	6.59×10^{-5}
10	10/13/80	1656.5					
11	10/17/80	1750.9	19.61×10^{-6}	12.39×10^{-6}	10.24×10^{-6}	12.52×10^{-6}	20.87×10^{-5}
12	10/24/80	1919.4	15.07×10^{-6}	10.47×10^{-6}	7.87×10^{-6}	6.97×10^{-6}	6.78×10^{-5}
13	10/31/80	2044.8	12.83×10^{-6}	8.69×10^{-6}	6.59×10^{-6}	5.02×10^{-6}	3.37×10^{-5}

[a]R/B = Ratio of fission gas release to birth rate.

[b]No release rate available.

Table 2.10. Calculated burnup and damage fluence for specimens in capsule HRB-15a at end of irradiation

Rod	Calculated burnup (% FIMA)[a]			Fluence, neutrons/m^2 (E > 29 fJ) HTGR
	^{235}U	^{238}U	^{232}Th	
1	78.5	8.7	2.5	4.11×10^{25}
2	80.6	10.5	3.1	4.58
3	82.3	13.0	4.0	5.25
4	83.2	14.9	4.8	5.68
5	83.7	16.4	5.3	6.13
6	84.0	17.6	5.8	6.57
7	84.3	18.9	6.4	6.92
8	84.5	19.8	6.7	7.10
9	84.9	20.1	6.9	7.15
10	84.7	20.4	7.0	7.25
11	84.5	19.8	6.8	7.15
12	84.5	19.5	6.6	7.10
13	84.3	18.9	6.4	6.77
14	84.0	17.6	5.8	6.37
15	83.8	16.7	5.5	5.90
16	82.9	14.1	4.5	5.25
17	81.7	11.8	3.6	4.51
18	80.8	10.7	3.2	4.11

[a]FIMA = fissions per initial (heavy) metal atom.

Table 2.11. Fuel rod loadings for HRB-16

Fuel rod[a]	^{235}U (g/m)	Th (g/m)
1	2.037	46.014
2	1.617	35.344
3	1.382	30.646
4	1.206	27.424
5	1.098	25.433
6	1.014	23.786
7	0.964	22.779
8	0.926	21.906
9	0.911	21.535
10	0.910	21.466
11	0.909	21.391
12	0.929	21.752
13	0.965	22.513
14	1.033	23.966
15	1.087	24.970
16	1.211	27.962
17	1.438	32.644
18	1.817	37.841

[a]Rod 1 is at the top of the capsule.

irradiation in capsule HT-35. Work during this reporting period has shown no particular advantage for PyC coatings deposited by using CO_2 dilution of the coating gas. Further, additional studies on batch OR-2013 (see Sect. 2.4.2) have shown that the performance of this batch in earlier irradiation experiments was not as exceptional as was originally thought. It was this perceived exceptional performance that launched the additional studies on PyC deposited by using CO_2 dilution.

- SiC characterization and testing. This work is aimed at producing SiC coatings that can retain fission product silver yet resist chemical attack from fission product palladium. Three phases of the work have been in progress during this reporting period: (1) the characterization of SiC and correlation of the microstructures observed with deposition parameters, (2) the testing of coatings in out-of-reactor thermal gradient heating tests to correlate performance

with microstructure, and (3) kinetic and thermodynamic studies aimed at establishing the time dependence of palladium attack and potential performance improvements through kernel chemistry changes. The first phase of the work is complete; the second and third phases are in progress. Kernels that were "doped" (some with silver, some with palladium) have been Triso-coated and are now being heated. Examination after heating will determine how effectively silver has been retained and how well the coatings resisted palladium attack. The most promising microstructure will be identified and studied further for additional performance improvements.

Dense UCO fuel kernel development. Dense UCO is one of four fissile kernel candidates being considered for the reference MEU fuel concept. The work at ORNL has been directed at fabrication of UCO kernels with high density and controlled chemical composition (relative amounts of UO_2 and UC_2). This work is an important input to the fuel production considerations of the reference fuel selection. The laboratory phase of this work is essentially completed. Dense UCO kernels have been fabricated, using feed material from both the internal and the external gelation flowsheets. The kernels produced have been of high density and have had chemical compositions in the desired range. The technique developed used a two-step sintering process and temperatures in the range of 1550°C. This procedure offers several advantages over conventional sintering techniques, which require temperatures in the range of 1900°C. The work that remains under this subtask is the scaleup studies necessary for large-scale production. These studies will be accomplished with equipment at GA.

2.3.1 Pyrocarbon Coating by CO_2 Dilution — D. P. Stinton

During the past year, the effort to produce and characterize CO_2-diluted coatings was completed. However, only irradiation testing of these coatings can determine the actual value of CO_2 dilution. Irradiation testing of eight CO_2-diluted batches is well under way in HT-35 (see Sect. 2.2.1.2). A report was written summarizing this work,[19] the abstract of which follows.

A Biso-coated fuel particle for the High-Temperature Gas-Cooled Reactor consists of a 500-μm-diam ThO_2 kernel, an 85-μm-thick layer of low-density carbon, and a 75-μm-thick layer of high-density pyrocarbon. The purpose of the coatings is to contain fission products generated during irradiation. During the past ten years, the permeability and anisotropic properties of the pyrocarbon layers have been optimized for good irradiation performance. Even those coatings whose properties were optimized for anisotropy and permeability sometimes fail during irradiation. However, one batch of particles produced in 1973 by depositing the highly dense pyrocarbon layer from a mixture of propylene and CO_2 has shown good performance in several irradiation tests. Because of these encouraging results, this experiment was undertaken to determine carefully the effect of CO_2 dilution on pyrocarbon coatings.

Coatings produced from mixtures of 50% propylene, 25% CO_2, and 25% Ar were found to be more gastight than coatings produced from mixtures of pyropylene and argon, helium, or H_2. Higher concentrations of CO_2 in the gas mixture caused severe oxidation of graphite components in the coating furnace. The permeability of these coatings was found to depend on the deposition temperature. Low deposition temperatures produced more gastight coatings. It was also determined that CO_2 had little or no effect on the anisotropy of the coating. Irradiation testing of CO_2-diluted coatings is under way.

2.3.2 Silicon Carbide Characterization and Testing — R. J. Lauf, T. B. Lindemer, and D. N. Braski

The purpose of the SiC development program is to improve our understanding of the relation of the microstructural details of the coatings to process variables and to irradiation behavior (specifically fission product retention). This information is needed to develop appropriate specifications for coatings so that fission product release will be minimized.

The current work involves a number of activities: (1) several characterization techniques were evaluated to determine their suitability for studying the structures and defects in SiC coatings; (2) these techniques were used to observe the way in which coating microstructures vary as the deposition parameters are systematically changed; (3) coatings of each experimental type were exposed out of reactor to attack by the fission product elements silver and palladium; and (4) coatings deposited under similar conditions to some of those studied here were irradiated in HFIR capsule HT-35 and will be examined during 1981.

2.3.2.1 Silicon Carbide Microstructure Characterization — R. J. Lauf and D. N. Braski

A topical report on characterization of SiC microstructures[20] was completed in September 1980 and will be issued in 1981. An abstract of this report follows.

> Fuel particles for the HTGR contain a layer of pyrolytic SiC to act as a pressure vessel and fission product barrier. The SiC is deposited by thermal decomposition of methyltrichlorosilane (CH_3SiCl_3 or MTS) in an excess of hydrogen. Coatings deposited at temperatures from 1500 to 1700°C and coating rates from 0.4 to 1.2 μm/min have been studied by transmission electron microscopy, small-angle x-ray scattering, x-ray diffraction, optical microscopy, density measurements, scanning electron microscopy, and microhardness measurements. Transmission electron microscopy has the necessary resolution to provide crystallographic information on small coating defects. Major defects were voids, stacking faults, and dislocations. Small-angle x-ray scattering was used to measure the void size distribution; voids were generally from 20 to 80 nm in diameter. X-ray diffraction indicates that SiC coatings are predominantly cubic β-SiC. However, the high stacking fault density in some coatings can give rise to both x-ray and electron diffraction effects. In some small areas the faulted structure resembles one or more polytypes of α-SiC. The evidence indicates, though, that this is a consequence of rapid growth and not a two-phase "α + β" mixture in the thermodynamic sense. Reflected-light microscopy can be used quantitatively to measure average grain size and shape but cannot resolve most coating defects. Density measurement can be used to differentiate between coatings that exhibit extremes in performance but cannot be used to detect small variations in quality. Scanning electron microscopy shows that deposition variables affect coating surface morphology, but these features are difficult to quantify and do not bear a simple relationship to internal coating defects. Microhardness was a very insensitive indicator of coating quality.

2.3.2.2 Correlation of Silicon Carbide Microstructures with Deposition Conditions — R. J. Lauf

A topical report on the relation between SiC microstructures and deposition conditions[21] was issued in May 1980. The abstract of this report appeared in the HTGR annual report for 1979.

Work is continuing in this area, with the addition of three German coating batches and two batches from the large coater at GA. Transmission

electron microscopy and SAXS will be used to compare the coatings with those studied earlier. Also, by obtaining scattering curves for the German coatings in the ORNL 10-m SAXS camera, we can correlate our SAXS results with the German work.[22]

2.3.2.3 Interaction with Fission Product Elements — R. J. Lauf and T. B. Lindemer

The results of out-of-reactor annealing of Triso-coated UO_2 microspheres doped with silver and palladium were reported[23] in July 1980. An abstract of this report follows.

> Fuel particles for the High-Temperature Gas-Cooled Reactor contained a layer of pyrolytic silicon carbide, which acts as a pressure vessel and provides containment for metallic fission products. The SiC layer is deposited by the thermal decomposition of methyltrichlorosilane (CH_3SiCl_3 or MTS) in an excess of hydrogen. Certain fission products, notably silver and palladium, can cause degradation of the SiC during irradiation. The purpose of this study is to develop a quantitative data base to better understand noble-metal attack as well as to evaluate the relationship between SiC deposition conditions and noble-metal release.
>
> The interaction between SiC and noble-metal fission product elements was investigated in the temperature range 1200 to 1500°C. Simulated high-burnup Triso-coated fuel particles were fabricated by impregnating UO_2 microspheres with metallic Ag or Pd followed by coating them under systematically varied conditions. The coated particles were mounted in carbon disks and were annealed for 2000 h in a thermal gradient of 27.5°C/mm.
>
> Metallographic examination revealed three modes of interaction: local attack of the SiC associated with nodules of Ag or Pd, presence of free metal particles partway through the coating thickness where no visible penetration path existed, and accumulation of free metal along circumferential striations in coatings deposited at or below 1550°C.
>
> The rates of attack of SiC by Ag and Pd are strongly temperature dependent. The Pd attack rate increases slightly with increasing SiC coating rate, while SiC deposition temperature has little effect. Since the Pd attack rates during out-of-reactor annealing agree with rates measured in irradiated particles, it is likely that attack is controlled by grain boundary diffusion.

In addition, a workshop on fission product interactions with SiC was hosted by GA on October 21—23, 1980. This workshop was attended by

R. J. Lauf, T. B. Lindemer, and T. N. Tiegs of ORNL; H. Grubmeier of KFA Jülich; P. Brown of AERE Harwell; and D. Hanson, J. Kaae, F. Montgomery, C. Young, B. Meyers, and others of the GA staff. Craig Smith, who chaired the meeting, provided the following text of the synopsis prepared by the participants:

> Core design studies conducted at GA have shown that fuel failure and fission product release associated with fission product—SiC reactions in Triso fissile fuels may limit the allowable range of core outlet temperatures for an HTGR. Reactions between fission products and SiC result in a decrease in SiC thickness. Silicon carbide failure via this mechanism is defined as the reduction in thickness that would result in Cs release from a coated particle during normal reactor operation. Because of the potential impact on reactor design, a workshop was held at GA. Primary goals of the workshop were to (i) combine experimental observations into a common data base for use by all participating organizations, (ii) develop a consensus for one concurrent understanding of fission product reactions with SiC, and (iii) recommend directions for future experimental programs.
>
> The meetings began with a description of items needed by an HTGR core designer to predict the impact of fission product—SiC reactions during reactor operation. This was followed by a series of prepared presentations that covered (i) characterization of the SiC layer, (ii) observations of fission product—SiC reactions in fission product doped, unirradiated samples, and (iii) observations of reactions in irradiated HTGR fuels. In addition, Ag diffusion in SiC was addressed in some of the presentations. The presentations were followed by general discussions that were intended to give one current understanding of fission product reactions with SiC and provide direction for future programs.
>
> The conclusion and recommendations of the participants are as follows:
>
> Fission Product—SiC Reactions
>
> - Rates of reaction are independent of kernel composition and enrichment.
> - Available data are consistent with a rate model that assumes square root time dependence for temperatures below 1500°C and with a model that is linear with time above ~1700°C.
> - Specific areas not adequately addressed include (i) impact of CO and Cl on reaction rate, (ii) reactions in Triso ThO_2, and (iii) development of SiC failure criteria.

- Longer term programs should allow for in-pile model verification and accident condition testing of fuels that have experienced varying degrees of fission product—SiC reaction.

Ag Diffusion in SiC

- Maintenance doses associated with Ag release are predicted to be somewhat higher than those from Cs release.
- Current experimental observations suggest that the total core inventory of Ag released by diffusion through "intact" SiC at 1000—1150°C in particles irradiated for one year will exceed the inventory released from all particles with failed coatings within the core.
- A program plan for study of Ag diffusion in SiC and development of models describing diffusive release of Ag through the SiC of Triso coatings (and graphite) is needed. It should show when models are needed, when they can be supplied using data collected from samples irradiated in planned fuel test capsules, and, if needed, when they can be supplied using data collected from alternative irradiation vehicles.

SiC Characterization

- The ongoing SiC characterization program is needed to support attempts to define and minimize the impact of SiC-fission product reactions and diffusion phenomena.
- In addition to the ongoing program, it is recommended that (i) coating bed temperatures be reported in all characterization studies and (ii) that two batches of coated material from the GA 240-mm-diameter coater be included in the program.

2.3.2.4 Kinetic Studies — T. B. Lindemer and R. L. Pearson

The main objective of this program has been to acquire an understanding of the fuel, fission product, and coating kinetic processes and thermodynamics of the system to the degree that permits identification and quantitative description of failure mechanisms and improved fuel performance by means of kernel chemical modification. A report[24] on this program was published in November 1980.

Work in progress consists primarily of heating Triso-coated particles with kernels containing simulated fission products known to interact with SiC. These include kernels of LaC_2, NdC_2, UO_2/UC_2 plus palladium, UO_2 plus palladium, and UO_2 plus silver. The primary objective is to determine whether the interaction with SiC below 1725 K

depends on time or on the square root of time. These particles are being heated to about 10,000 h in a temperature gradient of 28 K/mm.

2.3.3 Dense UCO Fuel Kernel Development — D. P. Stinton

A potential fissile particle for the HTGR is a highly dense microsphere with a composition of UO_2 plus UC_2. A procedure was developed to convert urania plus carbon microspheres produced by internal gelation to the desired composition. This process was described in a report,[25] the abstract of which follows.

> A process for the fabrication of uranium dioxide—uranium dicarbide microspheres for use as an advanced nuclear fuel is described. The U-C-O phase diagram was utilized extensively in applying thermochemical principles to the combined process of uranium carbide synthesis and kernel sintering. Variation of the partial pressure of carbon monoxide during the carbothermic reduction of urania plus carbon allowed the kernel composition and density to be controlled. X-ray diffraction, microstructural examination, and detailed chemical analyses were used to identify the kernel composition. A procedure was developed to convert urania plus carbon microspheres produced by a wet-chemical gelation process to a highly dense UO_2-UC_2 product at 1550°C. Kernels were first treated at 1550°C in Ar—1% CO for 4 h to produce high-density microspheres with a composition of $UO_2 + UC_xO_y$ ($x + y < 1.1$). These kernels were then processed at 1550°C for an additional 4 h in Ar—3% CO to shift the thermodynamic equilibrium from $UO_2 + UC_xO_y$ to the desired $UO_2 + UC_2$. Batches of material containing different initial amounts of carbon have been processed to produce high-density microspheres having specific UC_2 contents.

The process for the production of highly dense UO_2 and UC_2 was extended for use on particles produced by the external gelation process. The previous conversion schedule for material prepared by internal gelation was modified for use with material produced by external gelation. The modifications consisted of heating very slowly (50°C/h) from room temperature to 600°C plus an additional hold at 200°C for 2 h. This gentle rate allowed a very slow evolution of volatiles and prevented the cracking of particles during heatup. The sintering atmosphere was also changed during the first 1550°C sintering step to Ar—0.5% CO. A problem still exists because small voids are present in the particles prepared by

external gelation. These voids usually appear closed to the surface in cross section but are actually open to the surface. About 1 kg of external-gelation-derived kernels produced from 7%-enriched uranium was converted by this process for use in irradiation test HT-35. Photographs of these kernels are shown in Fig. 2.10.

2.4 PROJECT WORK STATEMENT ACTIVITIES — F. J. Homan

This work is being performed under the Fuel, Graphite, and Fission Product Subprogram, which falls under the auspices of the Umbrella Agreement between the United States and the Federal Republic of Germany (FRG), a government-to-government agreement. The fuel development work is being done by ORNL, GA, and KFA (Kernforschungsanlage) Jülich. The ORNL work is covered under five project work statements (PWSs): PWS FD-10, Optimization of SiC Microstructure for Retention of Metallic Fission Products; PWS FD-12, Quantification of Irradiation-Induced Permeability in Pyrocarbon Coatings; PWS FD-13, Comparison of IMGA and PIAA; PWS FD-18, Fuel Chemical Performance Modeling; and PWS FD-20, Evaluation of German Fuel Particles Using IMGA.

2.4.1 PWS FD-10 — F. J. Homan

Several letters and drafts concerning this PWS have been exchanged over the past three years. Extensive work is in progress at both ORNL and KFA. An informal exchange of reports and samples for characterization has existed for some time without the formalization required by a PWS. The most effective way to cooperate has not been established at this time, and no formal PWS exists. It was decided at the last Subprogram Manager's meeting (held at GA in September 1980) to defer formalization of this cooperation until definitive results are available at ORNL and KFA. During this reporting period small samples of SiC coating fragments were exchanged for SAXS experiments at both sites.

2.4.2 PWS FD-12 — M. J. Kania, J M Robbins, and E. L. Ryan

The purpose of PWS FD-12 is the quantification of irradiation-induced permeability in PyC coatings. Specific objectives are to

ORNL-PHOTO 2626-80

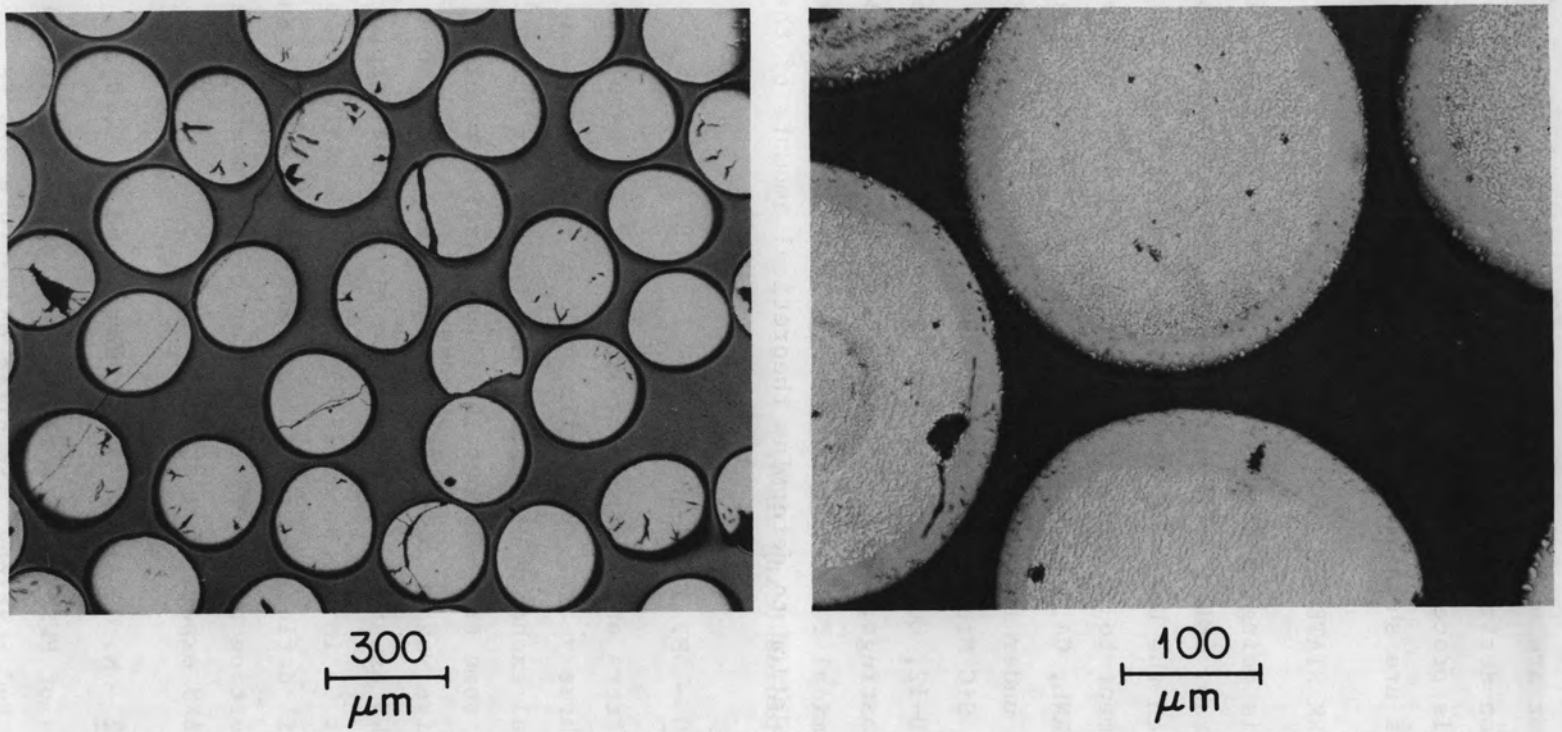

Fig. 2.10. About 1 kg of UO_2-UC_2 kernels was produced with correct stoichiometries; however, internal voids are present.

- establish temperature and fluence dependence of PyC coating permeability,
- establish influence of coating conditions and properties on irradiation-induced permeability in PyC coatings, and
- bring parallel work being done in the United States and FRG under one program.

To meet these objectives irradiated fuels from three experiments were chosen for investigation: one experiment from the FRG program, BR2-P12, and two from the U.S. program, HT-34 and HRB-14.

One requirement of this PWS is to investigate fission gas retention in irradiated coated particles from these three experiments. To achieve this, irradiated particles were selected and analyzed with the IMGA system to obtain a fission product inventory of prominent gamma emitters. These same particles were then broken in the PGA to measure the inventory of stable fission gases retained by the PyC coatings. The IMGA data together with neutronics information on the respective irradiation facility makes possible a calculation to determine theoretical amounts of these same stable fission gases that should be present in each particle. The ratio of the measured fission gas release from PGA to the calcualted fission gas inventory is then the "particle" fission gas release fraction. For PyCs that have retained their fission gases, this ratio will depend on the amount of gas that remains within the kernel microstructure. The amount of gas that would be released on measurement in the PGA system would be equal to the "kernel" fission gas release fraction. This does not include those fission gases remaining in the kernel. The kernel release fraction is dependent on kernel stoichiometry, irradiation temperature, fuel burnup, and irradiation time. For those particles that have lost their gas inventory, this ratio will approach zero, depending on the quantity of fission gas lost.

For the FRG-irradiated particles, PGA measurements for the stable krypton and xenon isotope inventories were reported previously.[26] For the irradiated particles from HT-34 (ref. 5), inventory measurements of the stable isotopes ^{83}Kr, ^{84}Kr, ^{86}Kr, ^{131}Xe, ^{132}Xe, and ^{136}Xe are presented in Table 2.12. Gas inventory data, in nanomoles, are reported for each of six particles for all particle batches of interest. Similar data for

Table 2.12. Results of fission-gas inventory measurements on particles from experiment HT-34

Position-particle	Batch	Quantity of gas, nmol									
		^{83}Kr	^{84}Kr	^{86}Kr	Σ Kr	^{131}Xe	^{132}Xe	^{134}Xe	^{136}Xe	Σ Xe	Xe/Kr
					High-temperature magazine						
27-1	A-765	0.46	3.36	4.20	8.02	2.62	9.83	10.10	19.44	42.00	5.23
27-2		0.52	3.96	4.84	9.33	3.06	11.45	11.88	22.86	49.25	5.28
27-3		0.49	3.65	4.58	8.72	2.78	10.22	10.60	20.45	44.04	5.05
27-4		0.63	4.64	5.84	11.12	3.51	13.23	13.60	26.15	56.49	5.08
27-5		0.01	0.01	0.02	0.04	0.01	0.03	0.01	0.04	0.09	2.25
27-6		0.49	3.80	4.50	8.80	2.75	10.15	10.78	20.78	44.46	5.05
29-1	A-780	0.46	3.20	3.95	7.61	2.59	9.24	9.65	18.57	40.05	5.26
29-2		0.49	3.73	4.50	8.72	2.82	10.19	10.57	20.61	44.20	5.07
29-3		0.54	3.75	4.61	8.90	3.01	10.75	11.31	22.09	47.17	5.30
29-4		0.63	4.49	5.51	10.63	3.62	13.07	13.55	25.76	56.01	5.27
29-5		0.69	4.74	5.70	11.14	3.77	13.85	14.60	27.85	60.06	5.39
29-6		0.66	4.56	5.60	10.82	3.62	13.20	14.37	27.23	58.42	5.40
30-1	A-785	0.40	2.92	3.45	6.77	2.16	7.97	8.05	15.67	33.85	5.00
30-2		0.54	3.61	4.42	8.56	2.79	10.11	10.40	20.23	43.54	5.08
30-3		0.48	3.73	4.59	8.81	2.89	10.76	10.95	21.69	46.30	5.25
30-4		0.52	3.93	4.81	9.27	2.92	10.96	11.16	21.66	46.70	5.04
30-5		0.50	3.74	4.62	8.86	2.99	10.90	11.12	21.67	46.68	5.27
30-6		0.57	4.15	5.06	9.76	3.09	11.47	11.57	22.65	48.77	4.98
32-1	A-806	0.08	0.33	0.50	0.92	0.36	1.01	0.95	2.08	4.40	4.79
32-2		0.16	0.84	1.17	2.17	1.03	2.46	2.50	4.94	10.93	5.04
32-3		0.21	0.90	1.20	2.31	0.87	2.36	2.67	5.23	11.13	4.81
32-4		0.10	0.51	0.70	1.32	0.47	1.41	1.44	2.92	6.24	4.72
32-5		0.43	2.63	3.07	6.14	2.12	6.57	7.07	13.30	29.07	4.73
32-6		0.08	0.31	0.56	1.02	0.35	0.91	0.94	1.82	4.03	3.94
33-1	A-762	0.61	4.07	5.31	9.99	3.45	11.51	12.11	23.28	50.35	5.04
33-2		0.49	3.44	4.41	8.35	2.73	9.70	10.11	19.78	42.32	5.07
33-3		0.02	0.07	0.07	0.16	0.05	0.12	0.16	0.28	0.61	3.81
33-4		0.57	3.64	4.72	8.92	3.07	10.61	10.96	21.42	46.06	5.16
33-5		0.47	3.25	4.00	7.73	2.80	9.45	9.95	19.17	41.36	5.35
33-6		0.57	4.11	4.89	9.57	3.37	11.52	12.44	24.06	51.39	5.37
35-1	A-782	0.53	3.41	4.09	8.04	2.92	9.83	10.46	20.32	43.53	5.41
35-2		0.54	3.41	4.20	8.15	2.86	9.54	10.13	20.27	42.80	5.25
35-3		0.54	3.36	4.34	8.24	2.71	9.45	9.88	19.62	41.66	5.06
35-4		0.50	3.39	4.19	8.09	2.93	9.82	10.15	19.98	42.88	5.30
35-5		0.39	2.73	3.30	6.43	2.21	7.57	7.99	15.32	33.10	5.15
35-6		0.42	2.84	3.52	6.79	2.35	8.31	8.52	16.39	35.58	5.24
36-1	A-786	0.56	3.56	4.69	8.81	3.11	10.49	10.75	21.02	45.38	5.15
36-2		0.48	3.39	4.13	8.01	2.79	9.53	9.77	19.10	41.19	5.14
36-3		0.47	3.33	3.85	7.65	2.80	9.49	9.93	19.42	41.65	5.45
36-4		0.62	3.93	4.55	9.09	3.32	11.18	12.03	23.03	49.56	5.45
36-5		0.67	4.22	5.25	10.14	3.58	12.59	13.42	26.10	55.69	5.49
36-6		0.49	3.46	4.28	8.23	2.76	9.85	9.95	19.51	42.08	5.11

Table 2.12. (continued)

Position-particle	Batch	Quantity of gas, nmol									
		^{83}Kr	^{84}Kr	^{86}Kr	Σ Kr	^{131}Xe	^{132}Xe	^{134}Xe	^{136}Xe	Σ Xe	Xe/Kr
38-1	A-787	0.53	3.11	3.90	7.55	2.84	9.69	10.41	20.47	43.41	5.75
38-2		0.59	3.70	4.75	9.04	3.34	11.32	12.13	23.63	50.42	5.57
38-3		0.25	1.30	1.73	3.28	1.28	3.59	4.18	8.10	17.15	5.23
38-4		0.53	3.35	4.31	8.19	3.12	10.33	11.02	21.56	46.03	5.61
38-5		0.57	3.50	4.52	8.60	2.96	10.19	10.85	21.28	45.29	5.26
38-6		0.59	3.62	4.64	8.84	3.29	10.96	12.13	23.49	49.89	5.64
39-1-1	OR-1975-T	0.42	2.92	3.88	7.22	2.33	8.14	8.20	15.91	34.58	4.79
39-1-2		0.65	3.91	5.17	9.73	3.30	11.29	11.84	23.10	49.53	5.09
39-1-3		0.49	3.26	4.33	8.09	2.64	9.35	9.35	18.14	39.49	4.88
39-1-4		0.41	2.94	3.91	7.26	2.31	8.19	8.13	15.90	34.53	4.75
39-1-5		0.51	3.46	4.58	8.55	2.64	9.67	9.62	18.90	40.83	4.78
39-1-6		0.53	3.58	4.75	8.87	2.98	10.20	10.76	21.08	45.03	5.08
39-2-1	OR-2013-T	0.47	3.15	3.63	7.25	2.37	8.16	8.26	16.48	35.27	4.86
39-2-2		0.09	0.34	0.56	0.99	0.30	0.62	0.87	1.66	3.46	3.47
39-2-3		0.54	3.56	4.58	8.68	2.87	9.68	9.94	19.70	42.20	4.86
39-2-4		0.14	0.45	0.75	1.34	0.43	0.89	1.27	2.56	5.15	3.84
39-2-5		0.68	4.29	5.47	10.45	3.61	12.44	13.11	25.46	54.63	5.23
39-2-6		0.57	3.84	5.04	9.46	3.19	10.91	10.92	21.63	46.65	4.93
				Low-temperature magazine							
40-1	A-765	0.28	1.23	1.74	3.25	1.03	3.41	3.61	7.38	15.43	4.73
40-2		0.42	2.36	3.13	5.91	1.91	6.29	6.92	13.70	28.82	4.88
40-3		0.16	0.98	1.28	2.43	0.80	2.70	2.86	5.73	12.09	4.98
40-4		0.31	2.03	2.60	4.94	1.70	5.44	5.77	11.28	24.20	4.89
40-5		0.42	2.59	3.34	6.36	2.19	7.10	7.76	15.07	32.13	5.05
40-6		0.38	1.98	2.55	4.91	1.62	5.66	5.95	11.88	25.12	5.12
42-1	A-780	0.40	2.22	2.84	5.45	1.72	5.37	5.90	11.60	24.58	4.51
42-2		0.41	2.06	2.64	5.12	1.56	5.27	5.65	11.34	23.83	4.65
42-3		0.35	1.91	2.48	4.74	1.49	4.65	5.08	10.15	21.38	4.51
42-4		0.48	2.35	3.23	6.07	1.83	6.11	6.64	13.20	27.77	4.58
42-5		0.43	2.00	2.61	5.05	1.52	5.07	5.75	11.16	23.49	4.65
42-6		0.46	2.02	2.90	5.38	1.58	5.25	5.68	11.34	23.85	4.44
43-1	A-785	0.38	1.96	2.50	4.83	1.54	5.80	5.46	10.92	23.00	4.76
43-2		0.40	1.92	2.48	4.80	1.65	4.91	5.40	10.63	22.60	4.71
43-3		0.40	2.08	2.72	5.20	1.67	5.41	5.87	11.60	24.55	4.72
43-4		0.09	0.52	0.76	1.38	0.44	1.50	1.57	3.23	6.74	4.89
43-5		0.38	2.03	2.58	5.00	1.60	5.12	5.63	11.22	23.57	4.72
43-6		0.13	0.74	1.00	1.88	0.59	1.93	2.07	4.31	8.90	4.73
45-1	A-806	0.14	0.78	1.02	1.94	0.61	1.99	2.08	4.39	9.08	4.68
45-2		0.37	2.09	2.64	5.10	1.73	5.32	5.93	11.61	24.61	4.82
45-3		0.39	1.91	2.48	4.78	1.49	4.65	5.03	10.61	21.34	4.46
45-4		0.13	0.71	0.97	1.81	0.61	1.93	2.01	4.20	8.75	4.82
45-5		0.15	0.88	1.20	2.23	0.73	2.38	2.52	5.18	10.81	4.84
45-6		0.39	2.00	2.57	4.96	1.69	5.05	5.72	11.27	23.73	4.78

Table 2.12. (continued)

Position-particle	Batch	Quantity of gas, nmol									
		^{83}Kr	^{84}Kr	^{86}Kr	Kr	^{131}Xe	^{132}Xe	^{134}Xe	^{136}Xe	Xe	Xe/Kr
46-1	A-762	0.32	1.52	1.88	3.72	1.38	4.26	4.74	9.55	19.93	5.35
46-2		0.32	1.59	2.01	3.92	1.54	4.39	4.88	9.75	20.57	5.25
46-3		0.32	1.62	2.07	4.02	1.40	4.35	4.78	9.51	20.04	4.98
46-4		0.31	1.51	1.95	3.78	1.42	4.42	4.88	9.65	20.36	5.39
46-5		0.28	1.33	1.79	3.41	1.17	3.84	4.17	8.52	17.71	5.19
46-6		0.12	0.60	0.83	1.56	0.48	1.53	1.70	3.53	7.25	4.65
48-1	A-782	0.08	0.23	0.40	0.71	0.24	0.66	0.76	1.61	3.28	4.60
48-2		0.27	1.23	1.65	3.15	1.04	3.07	3.32	6.80	14.23	4.51
48-3		0.36	1.59	2.02	3.97	1.26	3.73	4.16	8.33	17.48	4.40
48-4		0.31	1.47	1.82	3.61	1.20	3.61	4.01	8.08	16.90	4.68
48-5		0.29	1.40	1.79	3.48	1.09	3.26	3.70	7.29	15.35	4.41
48-6		0.56	2.89	1.47	4.92	2.74	5.17	8.08	13.24	29.24	5.94
49-1	A-786	0.05	0.25	0.46	0.76	0.22	0.71	0.68	1.55	3.15	4.16
49-2		0.22	0.74	1.08	2.05	0.65	1.89	2.14	4.38	9.06	4.43
49-3		0.29	1.32	1.85	3.46	1.02	3.14	3.47	7.06	14.70	4.24
49-4		0.45	1.91	2.58	4.94	1.39	4.36	4.73	9.72	20.20	4.09
49-5		0.36	1.25	1.78	3.40	0.99	3.18	3.37	6.98	14.52	4.27
49-6		0.16	0.70	0.94	1.80	0.57	1.69	1.92	3.90	8.09	4.49
52-1	OR-1975-T	0.09	0.46	0.66	1.22	0.37	1.02	1.26	2.65	5.36	4.40
52-2		0.08	0.36	0.56	1.01	0.32	0.86	0.92	2.09	4.25	4.21
52-3		0.19	0.60	0.96	1.75	0.56	1.60	1.79	3.79	7.74	4.41
52-4		0.03	0.15	0.23	0.42	0.14	0.35	0.39	0.81	1.69	4.05
52-5		0.12	0.43	0.70	1.24	0.34	1.09	1.22	2.64	5.28	4.24
52-6		0.06	0.21	0.37	0.64	0.19	0.59	0.63	1.41	2.82	4.40

irradiated particles of HRB-14 (ref. 12) are presented in Table 2.13. Here only particles from test sets 1, 3, and 5 were examined, and the data from five particles of each batch are shown. Some specific particle batches have missing PGA data, and the reasons for the missing data are presented.

For each particle examined, the number of fissions that occurred was calculated, based on the ^{106}Ru inventory measured during IMGA analysis. Appropriate fission product yields for ^{106}Ru, ^{137}Cs, and ^{86}Kr were generated by using the facility neutronics data, the irradiation history, and the CACA-2 computer code.[27] Using the ^{106}Ru yield, the total number of fissions was calculated for each particle. Once the number of fissions and their appropriate fission yields were known, theoretical inventories of ^{137}Cs and ^{86}Kr were easily calculated. To determine particle fission gas release fractions, the ratio of the PGA-measured inventory of ^{86}Kr to the calculated ^{86}Kr inventory was taken. The ^{86}Kr isotope was chosen because it does not have a large (n,γ) cross section and because its primary source is a result of fission. Particle release fractions for experiments HT-34 and HRB-14 are shown in Figs. 2.11 and 2.12, respectively. In each case the release fraction is plotted as a function of irradiation position in the capsule.

Also shown in each figure is a comparison between the measured particle release fraction and the predicted kernel release fraction. The predicted kernel release value is based on an empirically derived function for gas release[28] from previous krypton and xenon release measurements in irradiation capsules HT-12 through HT-15 (ref. 29). These values represent upper bounds of gas release and describe the temperature, irradiation time, and burnup dependencies as discussed earlier. The error bar shown for each position results from the uncertainty in burnup for each particle. This uncertainty arises from the unknown kernel diameter because the number of fissions is well known from the IMGA data. Burnups were calculated by considering a $\pm 2\sigma$ variation on a mean kernel diameter of 488.15 μm with a standard deviation of 14.37 μm. In both HT-34 and HRB-14 the particle release fractions are significantly lower than the predicted kernel release values.

Table 2.13. Results of fission gas inventory measurements on ORNL Biso-coated particle irradiated in experiment HRB-14

Planchet-particle	Batch	Quantity of gas, nmol								
		^{83}Kr	^{84}Kr	^{86}Kr	Σ Kr	^{131}Xe	^{132}Xe	^{134}Xe	^{136}Xe	Σ Xe
1- 1-1[a]	A-770									
1- 2-1	A-804	0.05	0.20	0.33	0.59	0.18	0.51	0.56	1.20	2.45
-2		0.08	0.27	0.44	0.79	0.23	0.69	0.73	1.54	3.19
-3		0.04	0.15	0.25	0.44	0.15	0.41	0.44	0.92	1.91
-4		0.50	0.14	0.21	0.40	0.14	0.37	0.42	0.84	1.77
-5		0.30	0.10	0.16	0.29	0.09	0.19	0.25	0.49	1.02
1- 3-1	J-641	0.03	0.04	0.08	0.15	0.05	0.11	0.14	0.30	0.60
-2		0.11	0.32	0.55	0.98	0.30	0.89	0.93	1.98	4.09
-3		0.03	0.07	0.14	0.23	0.09	0.21	0.20	0.48	0.99
-4		0.19	0.66	0.96	1.81	0.61	1.67	1.74	3.63	7.65
-5		0.18	0.64	0.91	1.73	0.58	1.56	1.63	3.43	7.20
1- 4-1	J-655	0.29	0.99	1.35	2.64	0.90	2.40	2.47	5.03	10.81
-2		0.10	0.37	0.61	1.09	0.24	0.65	0.66	1.47	3.03
-3		0.05	0.16	0.30	0.51	0.15	0.39	0.43	0.92	1.89
-4		0.27	0.93	1.27	2.47	0.77	2.39	2.35	4.88	10.40
-5		0.39	1.33	1.74	3.47	1.16	3.07	3.12	6.46	13.81
1- 5-1	A-762	0.13	0.46	0.68	1.28	0.42	1.09	1.18	2.41	5.09
-2		0.28	0.92	1.25	2.46	0.91	2.38	2.46	5.04	10.79
-3		0.26	0.88	1.20	2.34	0.81	2.29	2.34	4.90	10.34
-4		0.06	0.18	0.28	0.53	0.17	0.48	0.55	1.13	2.33
-5		0.14	0.47	0.71	1.33	0.43	1.22	1.25	2.64	5.54
1- 6-1	J-647	0.16	0.56	0.81	1.53	0.47	1.42	1.43	3.07	6.39
-2		0.44	1.59	2.06	4.09	1.52	3.93	4.04	8.17	17.66
-3		0.47	1.71	2.18	4.37	1.63	4.02	4.18	8.55	18.39
-4		0.36	1.21	1.58	3.16	1.09	2.92	3.05	6.23	13.29
-5		0.54	1.95	2.35	4.84	1.98	4.93	5.29	10.55	22.74
1- 7-1	J-649	0.09	0.36	0.60	1.06	0.33	1.04	1.05	2.25	4.66
-2		0.42	1.47	1.80	3.69	1.35	3.55	3.78	7.51	16.20
-3		0.37	1.35	1.71	3.44	1.11	3.15	3.23	6.66	14.16
-4		0.48	1.72	2.21	4.42	1.66	4.35	4.60	9.12	19.72
-5		0.50	1.81	2.31	4.62	1.78	4.58	4.87	9.69	20.93
1- 8-1	A-803	0.22	0.72	1.01	1.95	0.67	1.87	1.91	4.00	8.45
-2		0.34	1.18	1.56	3.08	1.17	3.10	3.15	6.39	13.82
-3		0.09	0.30	0.48	0.87	0.29	0.96	1.00	2.11	4.37
-4		0.32	1.14	1.49	2.96	1.08	2.96	2.99	6.08	13.11
-5		0.12	0.42	0.65	1.19	0.37	1.09	1.10	2.44	5.00
1- 9-1	A-765	0.11	0.42	0.64	1.17	0.36	1.25	1.26	2.64	5.51
-2		0.21	0.66	0.96	1.83	0.64	1.86	1.89	3.94	8.32
-3		0.30	1.12	1.49	2.91	1.07	2.88	2.90	6.07	12.92
-4		0.10	0.39	0.62	1.12	0.35	1.04	1.09	2.37	4.86
-5		0.23	0.78	1.07	2.08	0.72	2.15	2.13	4.44	9.44
2-10-1	A-785	0.27	1.02	1.31	2.59	0.87	2.66	2.73	5.54	11.80
-2		0.12	0.44	0.67	1.23	0.36	1.15	1.19	2.55	5.26
-3		0.19	0.71	0.99	1.90	0.64	1.80	1.89	3.86	8.19
-4		0.35	1.26	1.61	3.23	1.18	3.18	3.37	6.93	14.65
-5		0.17	0.67	0.93	1.78	0.56	1.65	1.73	3.60	7.55
2-11-1	J-651	0.37	1.31	1.72	3.41	1.16	3.30	3.35	6.99	14.80
-2		0.07	0.29	0.48	0.85	0.24	0.78	0.79	1.70	3.51
-3		0.40	1.43	1.87	3.70	1.30	3.58	3.70	7.53	16.12
-4		0.31	1.02	1.38	2.71	0.80	2.56	2.58	5.29	11.24
-5		0.38	1.40	1.77	3.55	1.20	3.52	3.54	7.36	15.63

Table 2.13. (continued)

Planchet-particle	Batch	Quantity of gas, nmol								
		^{83}Kr	^{84}Kr	^{86}Kr	Σ Kr	^{131}Xe	^{132}Xe	^{134}Xe	^{136}Xe	Σ Xe
2-12-1	A-787	0.09	0.39	0.60	1.08	0.33	1.11	1.14	2.43	5.02
-2		0.09	0.28	0.47	0.84	0.23	0.74	0.77	1.64	3.38
-3		0.08	0.32	0.51	0.91	0.26	0.85	0.90	1.90	3.91
-4		0.19	0.74	1.00	1.93	0.65	1.84	1.91	3.93	8.33
-5		0.32	1.12	1.47	2.91	1.00	2.90	2.95	6.08	12.94
2-13-1	A-771	0.18	0.64	0.90	1.71	0.52	1.59	1.63	3.39	7.13
-2		0.36	1.29	1.67	3.32	1.12	3.24	3.25	6.61	14.22
-3		0.33	1.16	1.49	2.98	0.97	2.90	2.90	5.92	12.68
-4		0.36	1.24	1.64	3.24	1.20	3.41	3.45	7.09	15.16
-5		0.24	0.95	1.24	2.43	0.78	2.33	2.34	4.88	10.33
2-14-1	A-786	0.29	1.10	1.45	2.84	0.97	2.80	2.79	5.64	12.21
-2		0.22	0.85	1.19	2.27	0.78	2.14	2.16	4.41	9.50
-3		0.07	0.27	0.45	0.79	0.21	0.67	0.72	1.53	3.14
-4		0.20	0.83	1.15	2.19	0.78	2.47	2.42	5.18	10.85
-5		0.16	0.57	0.80	1.53	0.46	1.50	1.52	3.18	6.66
2-15-1	A-704	0.40	1.56	1.95	3.91	1.42	4.05	4.17	8.50	18.14
-2		0.33	1.21	1.58	3.12	1.15	3.32	3.36	6.94	14.78
-3		0.19	0.77	1.08	2.04	0.63	1.91	1.92	4.06	8.52
-4		0.28	1.04	1.39	2.71	0.87	2.70	2.65	5.48	11.70
-5		0.58	2.16	2.81	5.55	2.10	5.78	6.08	12.28	26.24
2-16-1	A-758	0.14	0.52	0.78	1.44	0.44	1.33	1.35	2.91	6.02
-2		0.30	1.09	1.47	2.86	0.95	2.87	2.81	5.74	12.38
-3		0.38	1.34	1.75	3.46	1.20	3.45	3.45	7.06	15.16
-4		0.17	0.55	0.85	1.57	0.46	1.51	1.56	3.24	6.78
-5		0.11	0.45	0.69	1.25	0.40	1.20	1.22	2.62	5.45
2-17-1	A-782	0.33	1.32	1.66	3.31	1.16	3.41	3.41	6.89	14.88
-2		0.29	1.10	1.39	2.79	0.93	2.84	2.83	5.78	12.40
-3		0.19	0.72	1.02	1.93	0.60	1.81	1.84	3.81	8.06
-4		0.31	1.21	1.59	3.11	1.06	3.12	3.03	6.19	13.40
-5		0.32	1.16	1.56	3.04	1.07	3.13	3.07	6.24	13.52
2-18-1	A-766	0.14	0.43	0.70	1.27	0.42	1.20	1.22	2.67	5.51
-2		0.37	1.46	1.89	3.73	1.25	3.74	3.77	7.68	16.44
-3		0.40	1.76	2.18	4.34	1.37	4.70	4.61	9.24	19.92
-4		0.27	1.15	1.45	2.88	0.94	2.77	2.88	5.86	12.46
-5		0.30	1.40	1.72	3.42	1.08	3.68	3.72	7.37	15.86
5- 1-1[a]	A-770									
5- 2-1	A-804									
-2		0.55	2.60	3.23	6.38	2.00	6.81	6.73	13.48	29.02
-3		0.42	1.93	2.41	4.77	1.43	4.88	4.78	9.67	20.76
-4		0.49	2.19	2.70	5.38	1.66	5.61	5.66	11.26	24.20
-5		0.42	2.00	2.46	4.87	1.51	4.92	4.91	9.86	21.20
5- 3-1	J-641	0.63	3.03	3.64	7.30	2.38	8.29	8.05	15.90	34.62
-2		0.66	3.22	4.00	7.88	2.57	8.75	8.42	16.93	36.68
-3		0.45	2.24	2.62	5.32	1.73	5.80	5.65	11.17	24.36
-4		0.62	2.92	3.51	7.05	2.27	7.69	7.38	14.72	32.06
-5		0.54	2.65	3.25	6.44	2.19	7.16	7.08	13.79	30.22
5- 4-1	J-655	0.32	1.66	2.00	3.99	1.26	4.43	4.29	8.85	18.84
-2		0.40	1.95	2.45	4.81	1.50	5.13	4.91	9.93	21.47
-3		0.50	2.38	3.01	5.90	1.81	6.18	5.92	11.86	25.77
-4		0.07	0.19	0.32	0.59	0.25	0.49	0.77	1.19	2.70
-5		0.45	2.21	2.72	5.38	1.66	5.80	5.65	11.28	24.40

Table 2.13. (continued)

Planchet-particle	Batch	Quantity of gas, nmol								
		^{83}Kr	^{84}Kr	^{86}Kr	Σ Kr	^{131}Xe	^{132}Xe	^{134}Xe	^{136}Xe	Σ Xe
5- 5-1	A-762	0.47	2.29	2.78	5.54	1.66	5.63	5.49	11.08	23.86
-2		0.19	0.88	1.14	2.21	0.72	2.27	2.18	4.54	9.70
-3		0.40	1.92	2.36	4.69	1.36	4.74	4.51	9.20	19.80
-4		0.50	2.42	3.00	5.93	2.05	6.88	6.60	13.41	28.95
-5		0.56	2.56	3.22	6.34	2.16	7.06	7.01	14.16	30.38
5- 6-1	J-647	0.56	2.79	3.47	6.83	2.21	7.35	7.12	14.13	30.80
-2		0.71	3.40	4.42	8.55	2.75	9.22	8.98	18.03	38.99
-3		0.11	0.55	0.79	1.45	0.45	1.46	1.42	3.04	6.38
-4		0.79	3.80	4.92	9.52	3.23	10.66	10.60	21.31	45.81
-5		0.56	2.76	3.49	6.81	2.07	6.96	6.81	13.51	29.35
5- 7-1[b]	J-649	0.22	0.97	1.25	2.45	0.83	2.62	2.49	5.17	11.11
-2[b]		0.35	2.99	3.75	7.10	3.77	17.82	20.98	37.47	79.65
-3[b]		0.63	2.93	3.65	7.20	2.47	8.04	7.96	15.66	34.14
-4[b]		0.44	2.10	2.51	5.04	1.57	5.31	5.14	10.32	22.35
-5[b]		0.58	3.07	3.46	7.11	2.65	8.57	8.27	16.69	36.18
5- 8-1	A-803	0.44	2.14	2.62	5.20	1.72	5.59	5.39	10.98	23.69
-2		0.52	2.66	3.28	6.47	2.26	7.18	6.85	13.79	30.04
-3		0.65	3.15	4.00	7.81	2.82	9.07	8.86	17.62	38.36
-4		0.45	2.26	2.72	5.43	1.76	5.65	5.42	10.89	23.72
-5		0.56	2.78	3.48	6.81	2.26	7.38	7.14	14.32	31.09
3- 9-1	A-765	0.48	2.35	2.86	5.70	2.00	6.44	6.16	12.53	27.14
-2		0.37	1.80	2.12	4.29	1.39	4.67	4.46	9.01	19.53
-3		0.47	2.28	2.74	5.49	1.85	5.80	5.71	11.48	24.85
-4		0.44	2.20	2.72	5.36	1.71	5.59	5.44	10.10	23.85
-5		0.39	1.97	2.37	4.73	1.47	4.88	4.72	9.51	20.58
6-10-1	A-785	0.38	1.96	2.32	4.66	1.51	4.97	4.81	9.65	20.94
-2		0.42	2.12	2.52	5.05	1.64	5.52	5.38	10.79	23.33
-3		0.40	1.95	2.26	4.61	1.51	4.95	4.86	9.72	21.05
-4		0.39	1.69	2.17	4.25	1.37	4.70	4.29	9.16	19.53
-5		0.42	1.91	2.27	4.59	1.54	4.98	4.87	9.75	21.15
6-11-1	J-651	0.52	2.60	3.07	6.19	2.20	7.31	7.14	14.20	30.85
-2		0.54	2.52	3.09	6.15	2.10	7.07	7.05	14.02	30.24
-3		0.58	2.86	3.50	6.94	2.26	7.64	7.41	14.75	32.02
-4		0.50	2.48	3.03	6.01	2.00	6.84	6.50	13.10	28.44
-5		0.60	3.04	3.67	7.31	2.40	8.02	7.76	15.41	33.59
6-12-1	A-787	0.45	2.17	2.59	5.21	1.82	6.10	5.93	11.90	25.75
-2		0.20	0.99	1.22	2.41	0.73	2.86	2.61	5.41	11.62
-3		0.16	0.62	0.88	1.66	0.58	1.81	1.72	3.56	7.68
-4		0.51	2.50	3.03	6.05	2.11	7.06	6.80	13.57	29.55
-5		0.24	0.98	1.25	2.47	0.87	2.72	2.62	5.28	11.49
6-13-1	A-771	0.37	1.98	2.33	4.68	1.52	5.39	5.11	10.27	22.30
-2		0.41	2.07	2.44	4.92	1.75	6.17	5.94	11.92	25.78
-3		0.43	2.26	2.68	5.38	2.02	6.79	6.53	13.13	28.48
-4		0.39	1.94	2.34	4.68	1.57	5.22	5.06	10.15	22.00
-5		0.47	2.39	2.86	5.72	1.92	6.72	6.39	12.90	27.94
6-14-1	A-786	0.57	2.88	3.44	6.90	2.34	8.14	7.68	15.22	33.38
-2		0.43	2.18	2.67	5.28	1.71	5.80	5.56	11.11	24.18
-3		0.41	1.95	2.36	4.72	1.56	5.14	4.95	9.85	21.51
-4		0.32	1.68	1.95	3.94	1.19	4.27	4.03	8.14	17.63
-5		0.41	2.13	2.52	5.05	1.71	5.76	5.59	11.56	24.23

Table 2.13. (continued)

Planchet-particle	Batch	Quantity of gas, nmol								
		^{83}Kr	^{84}Kr	^{86}Kr	Σ Kr	^{131}Xe	^{132}Xe	^{134}Xe	^{136}Xe	Σ Xe
6-15-1	A-784	0.45	2.26	2.68	5.39	1.81	6.06	5.87	11.67	25.42
-2		0.31	1.67	2.00	3.98	1.19	4.36	4.02	8.20	17.77
-3		0.38	1.97	2.37	4.73	1.45	5.13	4.93	9.98	21.41
-4		0.37	1.85	2.19	4.41	1.38	4.79	4.61	9.25	20.03
-5		0.23	1.00	1.28	2.51	0.91	2.81	2.65	5.47	11.84
6-16-1	A-758	0.40	2.03	2.39	4.82	1.68	5.71	5.46	10.94	23.80
-2		0.39	1.81	2.20	4.40	1.39	4.79	4.58	9.28	20.04
-3		0.31	1.49	1.78	3.59	1.13	3.96	3.80	7.72	16.61
-4		0.38	2.00	2.48	4.87	1.58	5.45	5.25	10.46	22.74
-5[c]										
6-17-1	A-782	0.42	2.28	2.68	5.38	1.79	6.00	5.86	11.66	25.31
-2		0.53	2.74	3.31	6.58	2.21	7.32	7.00	14.04	30.57
-3		0.43	2.15	2.57	5.15	1.71	5.51	5.38	10.81	23.42
-4		0.39	2.09	2.47	4.95	1.64	5.54	5.25	10.36	22.78
-5		0.25	1.47	1.79	3.51	1.16	3.99	3.91	7.81	16.86
6-18-1	A-766	0.44	2.14	2.63	5.21	1.63	5.75	5.52	11.21	24.11
-2		0.36	1.92	2.30	4.58	1.41	4.97	4.63	9.46	20.48
-3		0.38	1.79	2.18	4.36	1.30	4.70	4.53	9.14	19.68
-4		0.34	1.73	2.17	4.24	1.25	4.41	4.32	8.63	18.61
-5		0.32	1.57	1.87	3.76	1.15	4.14	3.98	8.13	17.41
9- 1-1[a]	A-770									
9- 2-1	A-804	0.50	2.75	3.32	6.58	1.94	7.26	6.76	13.60	29.56
-2		0.36	1.93	2.34	4.63	1.29	5.26	5.03	10.51	22.09
-3		0.42	2.24	2.72	5.37	1.49	5.76	5.54	11.13	23.93
-4		0.29	1.90	2.09	4.28	1.32	5.15	4.88	10.21	21.56
-5		0.39	2.16	2.56	5.12	1.53	5.64	5.34	10.89	23.42
9- 3-1	J-641	0.23	0.88	1.21	2.31	0.75	2.58	2.55	5.25	11.14
-2		0.58	3.27	3.75	7.60	2.48	8.71	8.48	17.18	36.85
-3		0.56	3.14	3.68	7.37	2.42	8.60	8.33	16.60	35.95
-4		0.65	3.69	4.32	8.66	2.72	10.02	9.52	19.17	41.43
-5[b]		0.33	3.26	4.09	7.68	3.64	19.90	22.88	40.68	87.29
9- 4-1	J-655	0.54	2.96	3.41	6.91	2.20	8.02	7.79	15.33	33.34
-2		0.53	2.96	3.41	6.91	2.14	7.87	7.57	14.94	32.53
-3		0.47	2.79	3.14	6.40	2.05	7.49	7.19	14.49	31.22
-4		0.59	3.28	3.89	7.76	2.62	9.22	9.02	18.10	38.97
-5		0.17	0.74	0.97	1.89	0.59	2.19	2.10	4.18	9.06
9- 5-1	A-762	0.41	2.33	2.69	5.43	1.73	6.23	5.96	11.86	25.79
-2		0.38	2.12	2.44	4.94	1.62	5.85	5.73	11.34	24.54
-3		0.42	2.33	2.70	5.45	1.67	5.99	5.76	11.35	24.77
-4		0.38	2.21	2.55	5.15	1.61	6.09	5.89	11.61	25.20
-5		0.49	2.70	3.19	6.38	2.07	7.22	7.12	13.97	30.38
9- 6-1	J-647	0.59	3.17	3.81	7.57	2.70	9.47	9.13	18.00	39.29
-2		0.64	3.52	4.23	8.39	2.51	9.46	8.85	17.71	38.53
-3		0.68	3.67	4.40	8.75	2.71	9.92	9.56	19.07	41.25
-4		0.60	3.35	3.84	7.79	2.49	9.02	8.68	17.32	37.50
-5		0.63	3.42	4.09	8.14	2.55	9.54	9.05	18.17	39.32
9- 7-1	J-649	0.71	3.79	4.97	9.47	3.18	11.00	10.50	21.24	45.92
-2		0.62	3.56	4.41	8.59	2.60	9.45	8.72	17.55	38.34
-3		0.54	3.00	3.70	7.24	2.44	8.66	8.28	16.30	35.68
-4		0.52	2.81	3.44	6.76	2.23	7.94	7.28	14.59	32.04
-5		0.67	3.70	4.71	9.08	3.04	10.40	9.56	19.16	42.16

Table 2.13. (continued)

Planchet-particle	Batch	Quantity of gas, nmol								
		^{83}Kr	^{84}Kr	^{86}Kr	Σ Kr	^{131}Xe	^{132}Xe	^{134}Xe	^{136}Xe	Σ Xe
9- 8-1	A-803	0.10	0.50	0.75	1.36	0.48	1.42	1.36	2.93	6.21
-2		0.46	2.69	3.33	6.48	2.09	7.56	7.14	14.50	31.29
-3		0.47	2.47	3.10	6.03	1.93	6.96	6.51	13.02	28.43
-4		0.54	2.83	3.68	7.04	2.11	7.82	7.54	15.07	32.55
-5		0.47	2.53	3.21	6.21	1.87	7.00	6.43	13.10	28.41
9- 9-1	A-765	0.47	2.51	3.28	6.26	1.92	6.95	6.58	13.21	28.66
-2		0.47	2.51	3.18	6.14	2.06	7.38	7.10	14.21	30.75
-3		0.48	2.77	3.52	6.77	2.15	7.73	7.32	14.63	31.82
-4		0.46	2.38	2.86	5.70	1.82	6.69	6.11	12.83	27.44
-5		0.39	2.12	2.67	5.18	1.62	5.81	5.42	10.85	23.71
10-10-1	A-785	0.45	2.35	2.88	5.69	1.66	6.35	5.86	11.85	25.73
-2		0.52	2.85	3.68	7.06	2.21	7.99	7.57	14.99	32.75
-3		0.48	2.48	3.11	6.07	1.94	6.93	6.53	13.16	28.56
-4		0.51	2.61	3.26	6.38	2.05	7.05	6.90	13.44	29.45
-5		0.48	2.64	3.40	6.52	2.11	7.45	7.19	14.24	31.00
10-11-1	J-651	0.63	3.46	4.43	8.52	2.58	9.76	9.07	18.16	39.59
-2		0.59	3.36	4.37	8.32	2.57	9.22	8.72	17.70	38.21
-3		0.16	0.63	0.91	1.70	0.52	1.74	1.62	3.57	7.46
-4		0.58	3.26	4.21	8.05	2.44	8.88	8.37	16.42	36.10
-5		0.54	2.82	3.52	6.88	2.04	7.63	7.40	14.72	31.78
10-12-1	A-787	0.35	1.90	2.40	4.65	1.51	5.34	5.26	10.46	22.57
-2		0.35	2.05	2.55	4.96	1.55	5.47	5.24	10.64	22.91
-3		0.33	1.61	2.06	3.99	1.16	4.71	4.52	9.07	19.46
-4		0.38	1.92	2.43	4.74	1.39	5.35	5.22	10.55	22.51
-5		0.35	2.01	2.38	4.74	1.43	5.36	5.08	10.26	22.13
10-13-6	A-771	0.37	2.20	2.57	5.13	1.47	5.92	5.59	11.16	24.14
-7		0.40	2.15	2.56	5.11	1.47	5.88	5.58	11.08	24.02
-8		0.39	2.14	2.53	5.06	1.55	5.74	5.49	10.70	23.48
-9		0.44	2.40	2.84	5.69	1.83	6.72	6.42	12.80	27.77
-10		0.46	2.53	3.01	6.00	1.97	7.41	7.13	14.21	30.71
10-14-1	A-786	0.39	2.07	2.55	5.02	1.47	5.52	5.23	10.52	22.74
-2		0.49	2.62	3.17	6.28	1.97	6.99	6.60	13.27	28.85
-3		0.46	2.42	2.98	5.85	1.83	6.52	6.25	12.42	27.02
-4		0.32	1.89	2.24	4.45	1.38	5.04	4.82	9.55	20.80
-5		0.41	2.20	2.84	5.45	1.63	6.13	5.69	11.60	25.05
10-15-1	A-784	0.45	2.71	3.38	6.53	2.16	7.89	7.41	14.85	32.31
-2		0.30	1.83	2.21	4.34	1.34	5.05	4.87	9.84	21.08
-3		0.43	2.24	2.79	5.45	1.58	5.89	5.59	11.29	24.36
-4		0.49	2.87	3.56	6.92	2.17	8.28	7.76	15.59	33.82
-5		0.11	0.26	0.43	0.80	0.20	0.74	0.71	1.51	3.16
10-16-1	A-758	0.47	2.49	3.13	6.08	1.89	6.69	6.54	12.82	27.94
-2		0.40	2.23	2.77	5.40	1.70	6.18	5.77	11.51	25.18
-3		0.44	2.36	2.92	5.71	1.75	6.26	5.97	12.06	26.05
-4		0.40	2.06	2.58	5.04	1.44	5.54	5.25	10.56	22.79
-5		0.38	2.07	2.62	5.06	1.63	5.67	5.65	11.19	24.14
10-17-1	A-782	0.13	0.59	0.85	1.57	0.41	1.70	1.64	3.40	7.15
-2		0.37	1.98	2.49	4.84	1.43	5.55	5.29	10.65	22.92
-3		0.36	2.00	2.52	4.89	1.44	5.19	5.00	9.84	21.46
-4		0.42	2.26	2.79	5.46	1.57	6.16	5.69	11.42	24.84
-5		0.10	0.46	0.70	1.26	0.35	1.32	1.32	2.67	5.65

Table 2.13. (continued)

Planchet-particle	Batch	Quantity of gas, nmol								
		^{83}Kr	^{84}Kr	^{86}Kr	Σ Kr	^{131}Xe	^{132}Xe	^{134}Xe	^{136}Xe	Σ Xe
10-18-1	A-766	0.26	1.53	1.95	3.75	1.07	4.23	4.04	8.42	17.76
-2		0.42	2.34	2.90	5.66	1.63	6.24	5.76	11.67	25.31
-3		0.27	1.69	2.15	4.11	1.17	4.56	4.46	9.08	19.28
-4		0.45	2.56	3.16	6.17	1.86	6.99	6.40	12.90	28.15
-5[b]		0.29	3.05	4.02	7.35	3.35	19.75	22.34	39.77	85.20

[a]No particles were broken from batch A-770 because of the apparent large number of outer coating failures during irradiation.

[b]Gas release from particle indicated that fissile particle was crushed rather than particle from fertile particle batch indicated.

[c]Particle lost during postirradiation gas analyzer loading sequence.

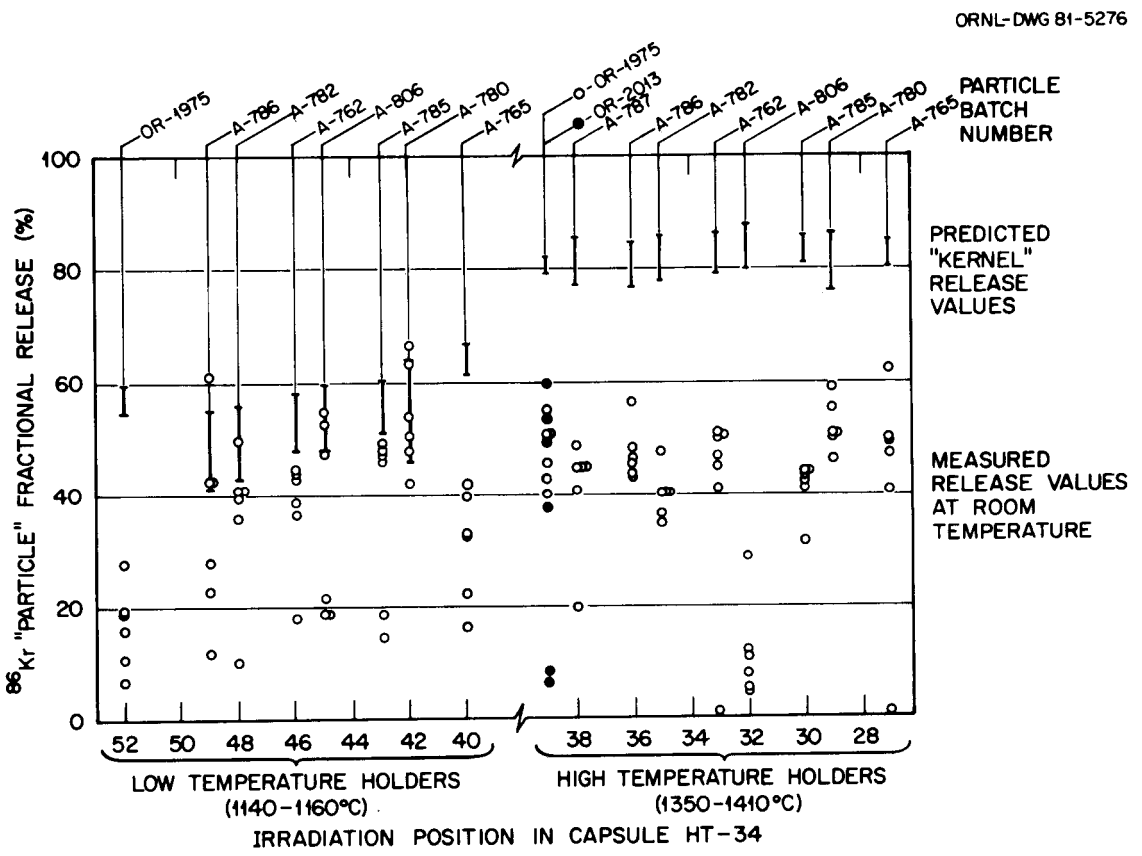

Fig. 2.11. Fraction release of ^{86}Kr fission gas measured in Biso-coated ThO_2 particles irradiated in capsule HT-34.

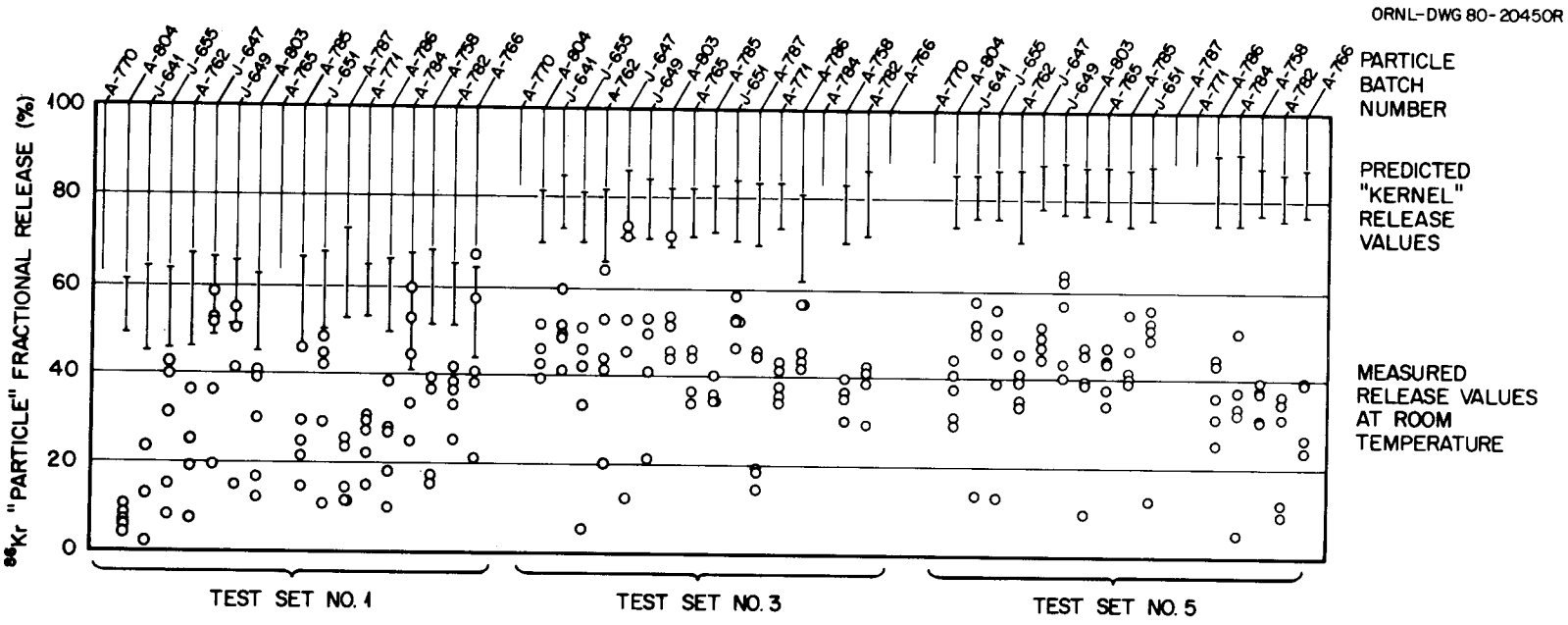

Fig. 2.12. Comparison of particle fission gas release measurements with predicted kernel release for Biso-coated ThO_2 particles irradiated in HRB-14.

Only particle batch A-780 of HT-34 in the low-temperature region had ^{86}Kr particle release fractions near the predicted kernel release values. In general the particle release fractions measured in both the low- and high-temperature regions had similar values of 40 to 60%. This similarity occurred despite a 200°C temperature difference and an approximate doubling of the accumulated neutron fluence in the high-temperature region as compared with the low-temperature region. Variations in ^{86}Kr release in a single batch are such that batch-to-batch comparisons based on coating properties are insignificant. It should also be noted that particle batch OR-2013, previously reported to be gastight,[30] had particle gas release fractions ranging from 10 to 60% compared with a predicted kernel release fraction of approximately 80%.

In experiment HRB-14 similar results to those shown for HT-34 were experienced. None of the 18 different particle batches examined from the three test sets had ^{86}Kr particle release fractions near the predicted kernel release values in all the five particles measured. The within-batch scatter of the data is highest for particles from test set 1 but also exists in the other test sets. Only about 6% of the particles examined had measured ^{86}Kr particle release fractions near the predicted kernel release. The within-batch variation appears to be more evident than in HT-34. This variation is much greater than the batch-to-batch variation that can be attributed to different coating conditions. No neutron fluence dependence is apparent in the particle gas release data comparing the three test sets. Test set 5 had the highest accumulated fluence, and test set 1 had the lowest.

A final report on the question of permeability of PyC coatings addressed in the PWS is now in preparation. Preliminary results indicate that the within-batch variation on gas release is such that batch-to-batch comparisons using as-deposited coating characterization data are meaningless.

2.4.3 PWS FD-13 — M. J. Kania

The objective of PWS FD-13 is to compare PIE techniques used in the United States and in the FRG to measure statistically significant failure fractions of irradiated coated particle fuels. This PWS specifically

calls for comparing results obtained using the IMGA system[31] at ORNL and the PIAA system[32] at KFA Jülich. Two particle batches were selected for comparison: (1) batch EO-819/820, a $(Th,U)O_2$ kernel with a Triso coating that was irradiated in experiment BR2-P21 of the FRG fuel development program, and (2) batch A-601, a WAR-derived UC_xO_{1-x} kernel with a Triso coating that was irradiated in experiment OF-2 of the U.S. program. In each irradiation experiment the particles were contained in fuel rods and were electrolytically deconsolidated to obtain the loose particles necessary for both procedures. From OF-2, fuel rod C-2-2 was used; from BR2-P21, fuel rods 3707 and 3735 were used.

Results of the IMGA examination to determine activity ratios $^{134}Cs/^{95}Zr$, $^{137}Cs/^{95}Zr$, and $^{134}Cs/^{137}Cs$ for each of the three fuel rods are shown in Table 2.14. Along with the activity ratios are presented the number of particles examined from each rod and the standard deviation of the activity ratio for the total particle population. Figure 2.13 compares graphically the $^{137}Cs/^{95}Zr$ activity ratio histograms for the three sets of particles examined. Each histogram is 50 channels wide. Quite noticeable is the difference in the histogram for batch A-601 versus the histograms for the two fuel rods 3707 and 3735 containing batch EO-819/820. The standard deviations about the mean $^{137}Cs/^{95}Zr$ ratio for the three histograms are 6.5, 26.6, and 16.3%, respectively. Within each set of data exists a "normal-like" looking distribution, which contains the largest percentage of the particles. To the left of this distribution are those particles with activity ratios indicative of low ^{137}Cs inventory. For the two FRG fuel rods there are a large number of particles with activity ratios to the left of the distribution; for the OF-2 fuel rod only two particles are indicated.

For the BR2-P21 particles an estimate was made of the number of particles having $^{137}Cs/^{95}Zr$ ratios significantly different from the mean value. This estimate was accomplished by assuming a symmetric distribution for the normal-like looking portion. The center of each was visually determined, and the distribution was folded back on itself (right to left). Those channels of the histogram that did not fall within were then assumed to contain particles that had lost significant amounts of ^{137}Cs. For fuel rod 3707, the channel numbers were 1 through 11 and represented 109 of the 977 particles examined, or 11.2%. For fuel rod 3735, the

Table 2.14. Selected activity ratios measured by irradiated microsphere gamma analyzer on standardized particle batches for PWS FD-13

Experiment/ fuel rod	Particle batch	Activity ratio	IMGA data[a]			Standard deviation (%)	Population size
			Minimum (Bq/Bq)	Maximum (Bq/Bq)	Mean (Bq/Bq)		
OF-2/C-2-2	A-601	$^{137}Cs/^{95}Zr$	4.606E-4	7.027E-2	5.451E-2	6.55	1281
BR2-P21/3707	EO 819/820	$^{137}Cs/^{95}Zr$	8.034E-2	5.479E-1	3.328E-1	26.65	977
BR2-P21/3735	EO 819/820	$^{137}Cs/^{95}Zr$	9.807E-2	4.795E-1	3.654E-1	16.33	927
OF-2/C-2-2	A-601	$^{134}Cs/^{95}Zr$	7.387E-4	1.457E-1	1.104E-1	7.52	1281
BR2-P21/3707	EO 819/820	$^{134}Cs/^{95}Zr$	1.147E-2	1.110E-1	6.759E-2	29.42	977
BR2-P21/3735	EO 819/820	$^{134}Cs/^{95}Zr$	1.355E-2	1.002E-1	7.615E-2	18.17	927
OF-2/C-2-2	A-601	$^{134}Cs/^{137}Cs$	1.607	2.182	2.023	2.45	1281
BR2-P21/3707	EO 819/820	$^{134}Cs/^{137}Cs$	1.343	2.102	1.993	7.88	977
BR2-P21/3735	EO 819/820	$^{134}Cs/^{137}Cs$	1.006	2.151	2.068	5.43	927

[a]IMGA data corrected back to discharge date from reactor for each experiment.

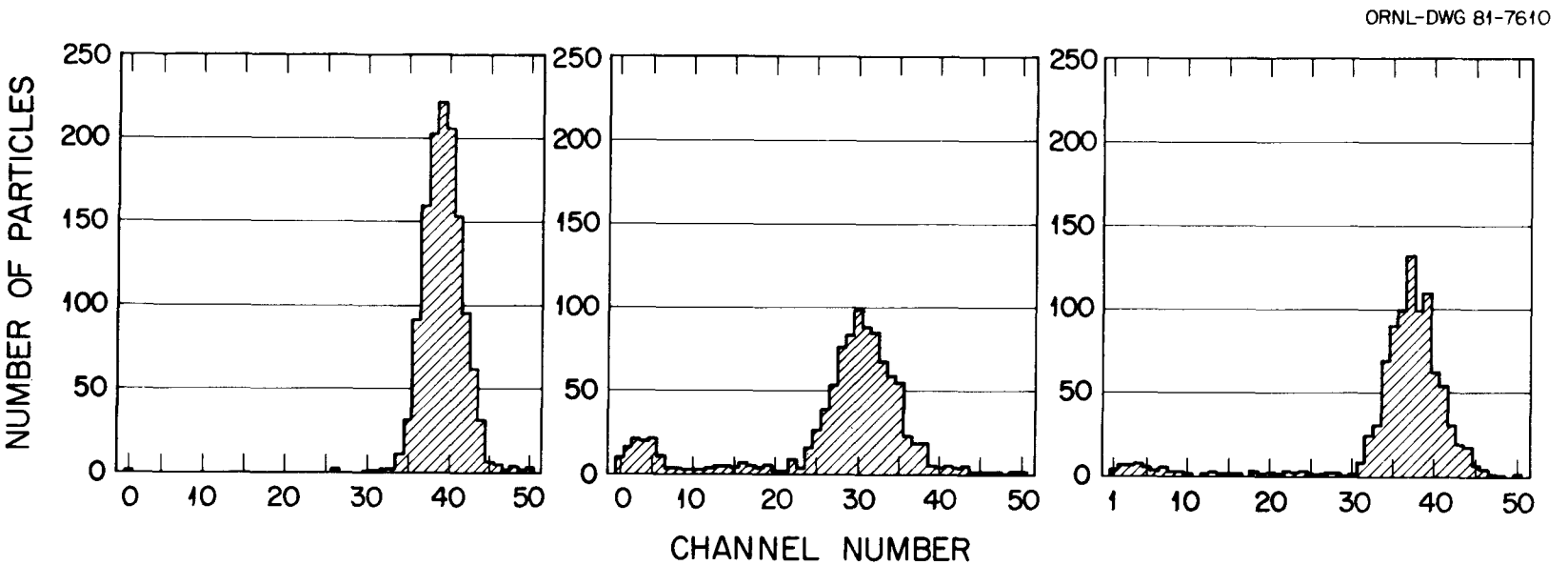

Fig. 2.13. Comparison of the $^{137}Cs/^{95}Zr$ activity ratio histograms measured during irradiated microsphere gamma analyzer examination. From left to right are the data from batch A-601 in OF-2 rod C-2-2, batch EO-819/820 rod 3707, and batch EO-819/820 in BR2-P21 rod 3735.

channel numbers were 1 through 22 and represented 58 of the 927 particles examined, or 6.3%. This same procedure was used on the OF-2 fuel rod; the channel numbers were 1 through 29, which accounted for 2 of the 1281 particles examined, or 0.16%.

It should be pointed out that these numbers are estimates based on the procedure outlined earlier. From previous work,[33] it is known that the distribution of activity ratio measurements on particles is not normal. Rather than being symmetric, it rises faster and falls off less rapidly than a normal distribution. Based on this, it appears that the previous estimates are actually underpredicting the number of particles with deficient cesium inventory. For comparison within this PWS, the number of defective particles generated earlier are quite sufficient. However, further statistical investigations would be necessary if actual fuel qualification were required. These investigations on other IMGA examinations are in process.

Before subjecting the particles to the PIAA examination, the particles were examined for fission gas release at KFA. These nondestructive measurements pass room-temperature helium over the loose particles, and any fission gases released from defective fuel are swept away with the helium. The sweep gas is then analyzed for activity. Such measurements are qualitative and do not present a good comparison for the number of failed particles except when similar fuels having nearly the same irradiation conditions are compared. This is the case for the two BR2-P21 fuel rods but not for the fuel from the OF-2 fuel rod. The results of the room-temperature gas release measurements, shown in Table 2.15, indicate that all three particle sets exhibit some activity in the sweep gas. The fuel from rods 3707 and 3735 have nearly the same activity, but the activity for the OF-2 fuel is 3 to 4 times lower.

In the PIAA examination, particles from batch EO-819/820 were first annealed at 300°C for 50 h and then at 1000°C for 5 h. Particles from batch A-601 were annealed at 300°C for 15 h before the final annealing at 1000°C for 5 h. In all cases the loose particles were contained in graphite trays with a capacity of about 320 particles per tray. During the annealing procedure a helium purge system was used to detect any fission gases released from particles.

Table 2.15. Comparison of failed particle determinations under PWS FD-13

Experiment/ fuel rod	Particle batch	Room temperature gas release[a]	PIAA[b]	IMGA
BR2-P21/ 3707	EO 819/820	8.5 CPS	53/954	109/977
BR2-P21/ 3735	EO 819/820	10.5 CPS	0/961	58/927
OF-2/ C-2-2	A-601	1.5 CPS	2/1196	2/1281

[a]Unpublished work of R. Duwe, Institut für Reaktorwerkstoffe, KFA Jülich. The data presented gives only the ^{85}Kr count rate (CPS, counts per second) recorded during the analysis.

[b]Unpublished work of J. Schunck, Institut für Reaktorwerkstoffe, KFA Jülich.

The results of the PIAA examination of each of the sets of particles are shown in Table 2.15 along with the IMGA and gas release measurement data. Beta autoradiography of the trays containing particles from fuel rod 3707 revealed a number of failed particles as shown in Fig. 2.14. The number of particles determined to be failed was 53, and all were found in one graphite tray. A visual examination of the particles in the tray neither showed any to be cracked nor indicated any mechanical damage to coatings. During the anneal, no fission gases were detected in the helium purge gas. No particles from fuel rod 3735 were determined to be failed from the beta autoradiography of the respective trays. For particles from the OF-2 fuel rod, two were determined to be failed from the graphite tray autoradiography. On visual examination of these two particles, cracked coatings were observed in both particles. Here again no fission gases were detected in the helium purge system during the anneal.

A comparison of the results shown in Table 2.15 indicates agreement between the PIAA and IMGA data for the particle batch A-601 from OF-2. However, the agreement for particle batch EO-819/820 in fuel rods 3707 and 3735 from experiment BR2-P21 is relatively poor. In both the PIAA and IMGA analysis of particles from rod 3707, failed particles were detected. The IMGA data suggests 109 failed, whereas the PIAA data suggests 53

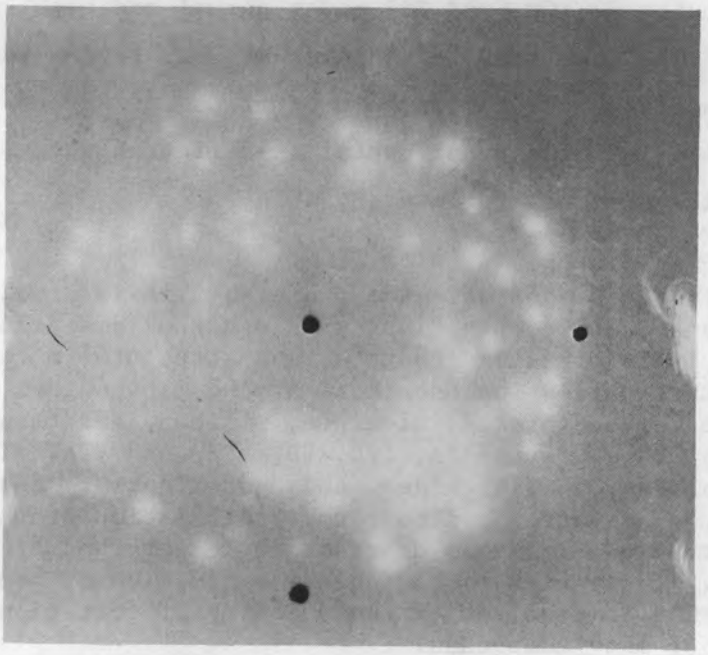

Fig. 2.14. Photograph of the beta autoradiograph showing detectable failed particles from fuel rod 3707 in experiment BR2-P21. A total of 53 particles were determined to be failed in this photograph. Photograph courtesy of KFA Jülich.

failed, a factor of 2 less. In the case of rod 3735, IMGA data suggest 58 defective particles, but the PIAA data suggest no failed particles. The gas release measurements suggest that the number of failed particles in both rods should be near the same because of the similar activity detected in the sweep gas. Quite clearly, from the $^{137}Cs/^{95}Zr$ activity ratio histograms in Fig. 2.13 a significant number of particles in both fuel rods have low $^{137}Cs/^{95}Zr$ ratios.

No further measurements on the fuel selected for this PWS are planned. A final report, including the results presented here and a more detailed comparison of the type of data and results obtained by using the IMGA and PIAA postirradiation techniques, is being prepared.

2.4.4 PWS FD-18 — T. B. Lindemer

This PWS, which was concluded this reporting period, is entitled "Fuel Chemical Performance Modeling." The long-term objective was to predict the chemical behavior of fuel, fission products, and containment

system (including Fe, Cr, and Ni) under normal and hypothetical accident conditions. This task resulted in a major ORNL review paper of the in-reactor thermochemistry of fission product Cs and Rb and of Li, Na, and K and their oxides.[34] The paper contains 43 figures and cities 270 references; the abstract follows.

> This paper considers the phase equilibria of alkali metal oxides and their combinations with other oxides relevant to nuclear fuels, fission products, and structural materials. These other oxides include those of the lanthanides, the actinides, iron, nickel, aluminum, silicon, and those of periodic table groups IIA, IVB, VB, VIB, and VIA. The alkali metal halides, chalcogenides, and hydroxides are also included. Techniques are developed to permit calculation of phase equilibria and Ellingham diagrams in ternary and higher order systems. These techniques include estimation of previously unknown 298.15 K values of the enthalpy of formation and the entropy of many compounds.

2.4.5 PWS FD-20 — M. J. Kania

The objective of this PWS on fuel development is the measurement of statistically significant failed-particle fractions on FRG fuels. Through this PWS, irradiated candidate HTR fuel specimens from the FRG fuel development program will be shipped to ORNL, where they will undergo postirradiation exmination. In particular, the IMGA system at ORNL will be used to measure failed-particle fractions, and the evaluation data collected with the IMGA will be provided.

Fuel from three irradiation experiments of the FRG program has been selected as the first samples to be examined under this PWS. The fuel selected is of one type, being a $(Th,U)O_2$ kernel with a high-temperature isotropic (HTI) Biso coating, derived from methane. The irradiation experiments chosen have similar operating temperatures but accumulated different levels of fast neutron fluence. General information regarding these fuel samples is listed below in Table 2.16. Using the IMGA system we can obtain fission product retention as a function of neutron fluence for these HTI Biso-coated particles. Shipping arrangements are under way, and the particles are expected at ORNL some time during 1981. The fuel elements have been deconsolidated and approximately 1200—2000 loose particles from each experiment will be shipped.

Table 2.16 FRG fuel specimens for PWS FD-20

Irradiation experiment	Particle batch	Irradiation temperature (°C)	Fast neutron fluence (E > 0.1 MeV)
FRJ2-P22, compact 1	E0–1232-1234	950–1100	$<1 \times 10^{25}$
R2-K10, sphere 3	E0–1084	900–1050	3.4×10^{25}
HFR-K1 sphere B2	E0–1232-1234	950–1100	5.0×10^{25}

2.5 EQUIPMENT DEVELOPMENT AND MAINTENANCE — F. J. Homan

Three major pieces of equipment for use with PIE of fuel from irradiation capsules have been developed over the past few years. These items of equipment are unique to the HTGR community in the United States, and in some cases the capabilities are unique in the world. Although this equipment is in routine use in the examination of HTGR fuel particles, we are continuing to develop and upgrade the capabilities to provide more and better quality information.

2.5.1 Irradiated Microsphere Gamma Analyzer — M. J. Kania, T. N. Tiegs, and G. A. Moore

The IMGA system operated throughout the report period without reoccurrence of problems in the automated particle handler. As an integral part of the PIE of HTGR candidate fuels, the IMGA system was used to determine fission product retention in irradiated coated particles from experiments HRB-14 and HRB-15b. The results from experiment HRB-14 are reported in Sect. 2.2.2.2, and the HRB-15b results were forwarded to GA.

For small numbers of loose irradiated particles from experiments HT-13, HT-14, HT-15, HT-34, HRB-14, and HRB-15b, the IMGA system was used to measure fission product inventories before gas inventory measurements in the PGA system. These data were then used to calculate the quantity of stable fission gases produced during the respective irradiation periods. Application of these data is discussed in more detail in Sect. 2.5.2.

During this report period fabrication of a new automated particle handler was completed. This new handler offers several advantages over the current particle handler, eliminates several design flaws, and will improve in-cell maintenance. In particular, the new handler provides

- Improved mechanical reliability through elimination of sample changer right-angle drive and replacement with a simplified Geneva drive mechanism. This changes the handler to four-point symmetry, rather than three-point symmetry in the original handler, and incorporates a second detector position for future application.
- Reduced maintenance on particle singularizer by addition of a self-cleaning mechanism to the assembly. The current singularizer, without this mechanism, frequently becomes plugged and requires complete singularizer disassembly and removal from the IMGA cubical to unplug and make operational again.
- Readily accessible and modular components decrease downtime for maintenance.

Two views of the new handler are shown in Fig. 2.15, Fig. 2.15(*a*) being a front view showing the two detector port positions 90° apart and Fig. 2.15(*b*), a back view showing component positions. The detector port at the far left of Fig. 2.15(*a*) is for the high-energy Ge(Li) detector currently in use with the IMGA system. The detector port to the right is the additional detector position made possible by the four-point symmetry of the Geneva drive mechanism. This position will not be used in the immediate future but remains available for further application. Noticeable along the top of the lead shielding and sample changer mechanism are numerous hooks, which provide for attachment to a small in-cell crane that greatly facilitates handler disassembly. The sample changer, particle singularizer, and sample collector shown in Fig. 2.15(*b*) are all modular in design, and each is easily removed without disturbing the other components. Figure 2.16 shows the new particle handler with each of the components removed and disassembled: from left to right, the particle collector and particle-dropping mechanism, the sample changer and Geneva drive assembly, and the particle singularizer.

R76068

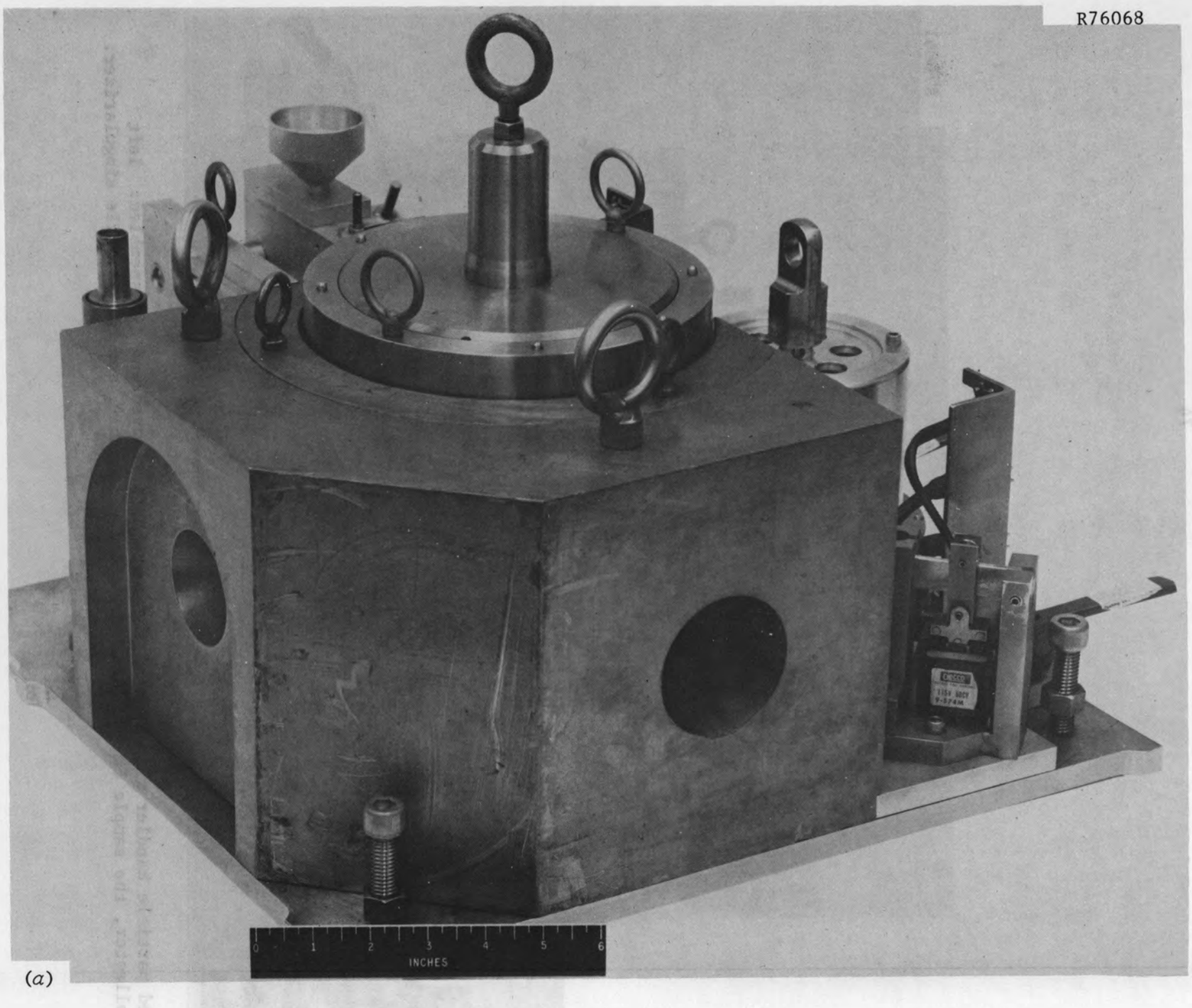

(*a*)

R76059

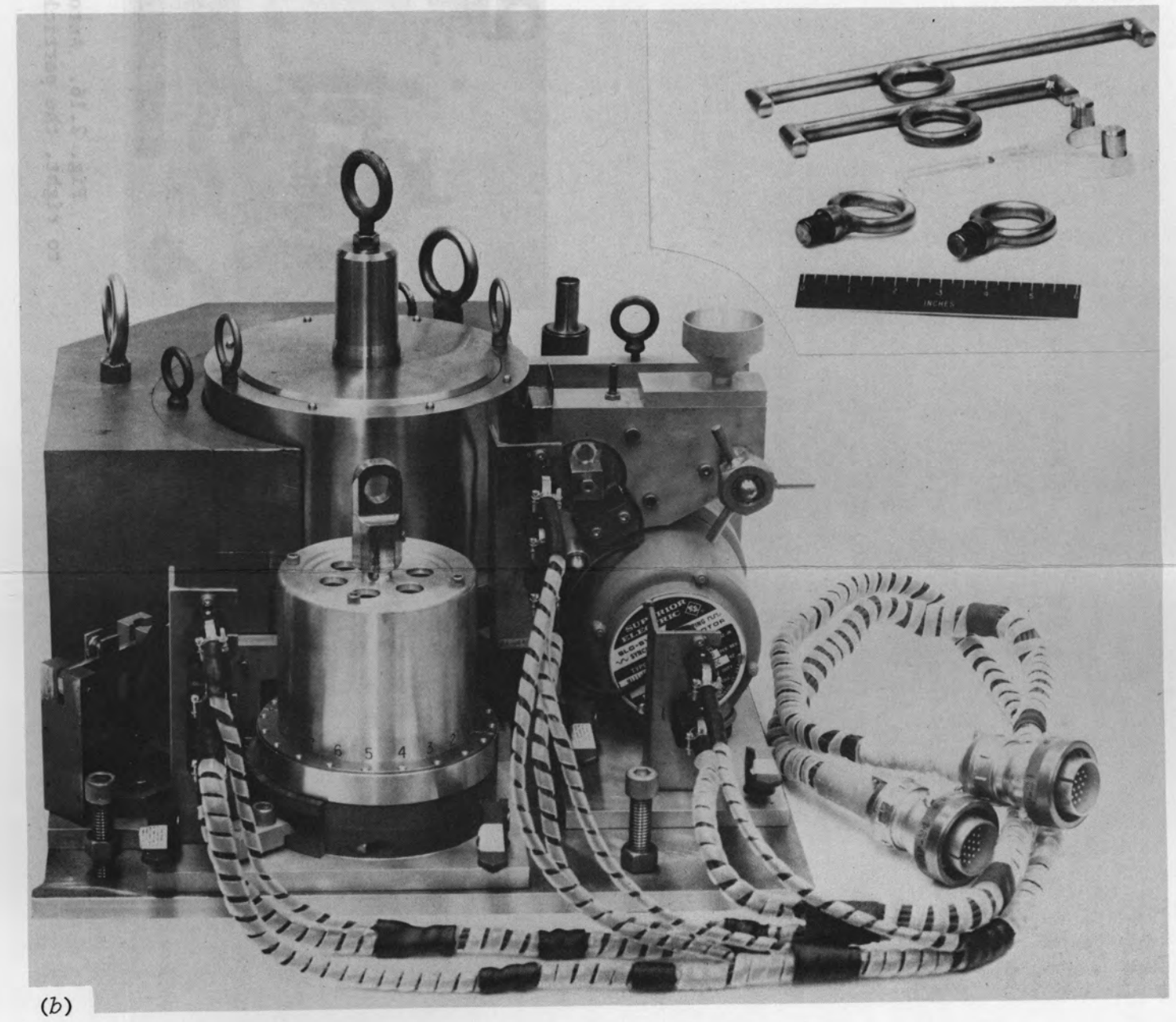

(*b*)

Fig. 2.15. Two different views of the new automated particle handler: (*a*) front view showing the two detector ports 90° apart and (*b*) back view showing the easily accessible and modular components.

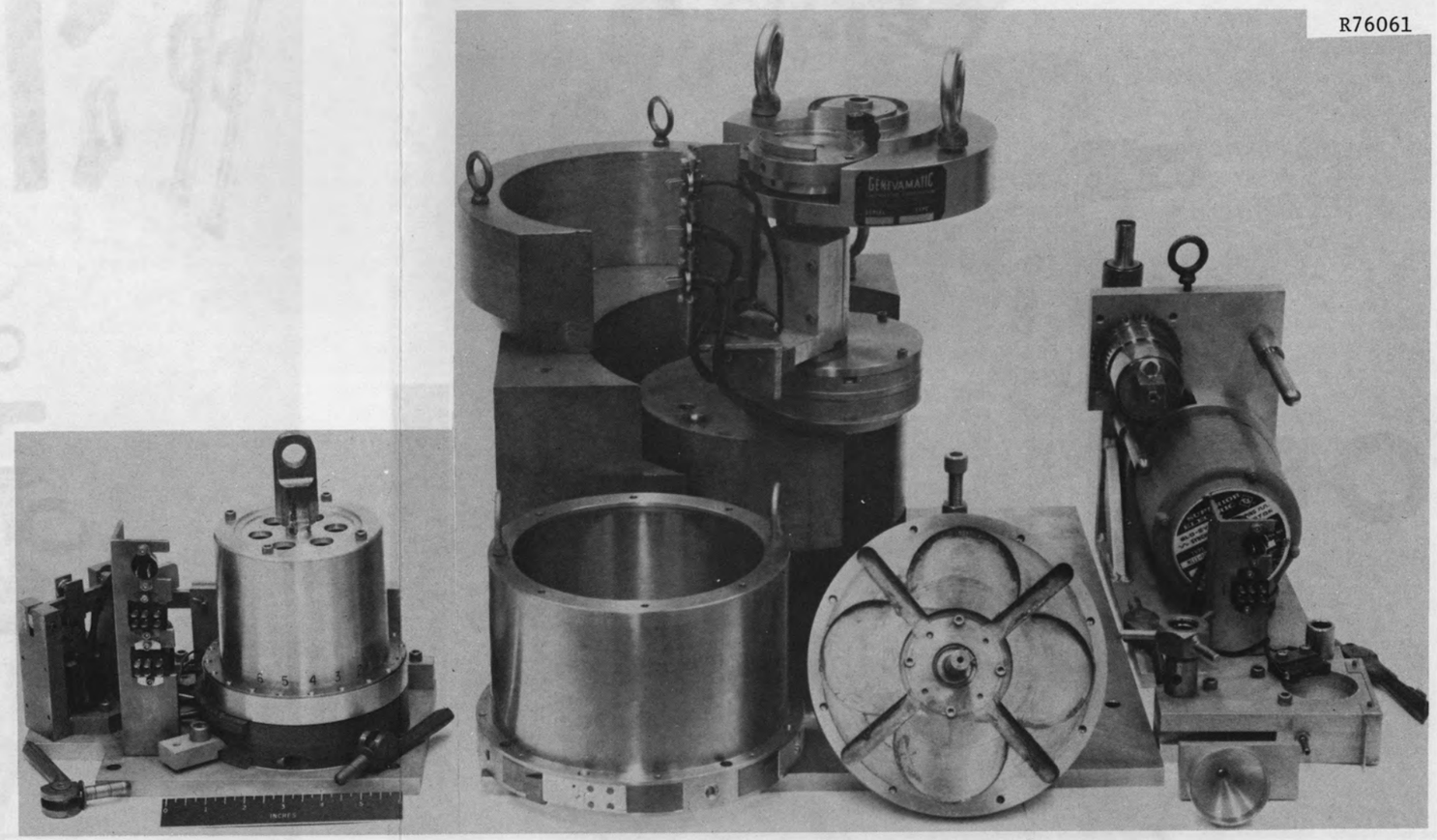

Fig. 2.16. Automated particle handler with each of the components removed and disassembled: left to right, the particle collector, the sample changer and Geneva drive assembly, and the particle singularizer.

The current particle handler is in good operating condition, and its use will be continued until the sample-changer drive mechanism fails. At that time the new handler will be installed into the IMGA cubicle.

2.5.2 Postirradiation Gas Analyzer — M. J. Kania, E. L. Long, J M Robbins, and E. L. Ryan

The PGA system is used to determine the quantitative measure of fission- and reactive-gas inventories in irradiated coated-particle fuels.[35] During the past report period the PGA system has been used for fission-gas content measurements on selected irradiated fuel particles from experiments HT-13, HT-14, HT-15, HT-34, HRB-14, and HRB-15b. The data for experiments HT-34 and HRB-14 are reported in Sect. 2.4.2, and the data for experiment HRB-15b are presented in Sect. 2.7.1.

The fission-gas content measurements for irradiated particles from experiments HT-13, HT-14, and HT-15 are presented in Tables 2.17, 2.18, and 2.19, respectively. Specific particle batches selected for these measurements include

- OR-1849 and OR-1850 — reference 500-μm ThO_2 kernels with buffer and LTI thickness variations;
- OR-1749 or 1830 and OR-1838 — 400-μm ThO_2 kernels with variation in buffer thickness; and
- OR-1749 and OR-1826 — 400-μm ThO_2 kernels with nearly the same buffer thicknesses but with variations in LTI thickness.

All particles selected for this analysis were determined to be "intact" by visual inspection. Detailed descriptions of the coating designs, fabrication conditions, irradiation history, and general irradiation performance have been reported.[29]

The data in Table 2.17 for HT-13 show that only particles 17/1 and 17/2 retained a significant part of the fission gas generated during irradiation. Particles from holders 24 and 32 showed some minimal retention, but significant leakage obviously occurred. The higher gas retention by these particles in the high-temperature magazines is thought to be simply the result of the greater release of the fission gases from the kernel at these high temperatures compared with their counterparts in

Table 2.17. Results of fission gas content measurements on particles from experiment HT-13

Holder/ particle	Batch	Quantity of gas, nmol								
		^{83}Kr	^{84}Kr	^{86}Kr	Σ Kr	^{131}Xe	^{132}Xe	^{134}Xe	^{136}Xe	Σ Xe
				Low-temperature magazines						
4/1, 3	OR-1850	*a*	*a*	*a*	0.08[b]	*a*	*a*	*a*	*a*	0.25[b]
11/1	OR-1749	*a*	*a*	*a*	0.13	*a*	*a*	*a*	*a*	0.35
13/1	OR-1849	0.01	0.05	0.15	0.21	0.13	0.22	0.25	0.49	1.10
13/2	OR-1849	0.03	0.16	0.15	0.34	0.09	0.15	0.17	0.37	0.78
13/3	OR-1849	0.03	0.09	0.08	0.21	0.09	0.12	0.20	0.31	0.77
13/4	OR-1849	0.01	0.13	0.24	0.38	0.21	0.29	0.28	0.51	1.30
42/1,2,3,4	OR-1838	*a*	*a*	*a*	0.12[c]	*a*	*a*	*a*	*a*	0.36[c]
45/1,2,4	OR-1826	*a*	*a*	*a*	0.08[d]	*a*	*a*	*a*	*a*	0.20[d]
48/1,2,3,4	OR-1830	*a*	*a*	*a*	0.08[c]	*a*	*a*	*a*	*a*	0.19[c]
				High-temperature magazines						
17/1	OR-1850	0.25	1.28	1.26	2.72	1.73	3.45	3.71	6.92	15.81
17/2	OR-1850	0.39	2.39	2.91	5.69	2.00	6.06	6.41	12.29	26.76
17/3	OR-1850	0.09	0.46	0.69	1.25	0.40	1.17	1.29	2.69	5.56
24/1	OR-1749	0.06	0.34	0.57	0.97	0.34	0.96	0.97	2.00	4.26
24/2	OR-1749	0.06	0.28	0.43	0.78	0.27	0.74	0.80	1.64	3.46
24/4	OR-1749	0.14	0.65	0.92	1.72	0.58	1.80	1.84	3.78	8.01
32/2	OR-1826	0.11	0.59	0.83	1.52	0.49	1.43	1.61	3.32	6.84
32/3	OR-1826	0.12	0.68	1.01	1.81	0.56	1.87	1.92	4.04	8.40
32/4	OR-1826	0.20	0.95	1.40	2.55	0.80	2.51	2.76	5.47	11.55

[a]Individual values are so low that they are considered insignificant.

[b]Average of two particles.

[c]Average of four particles.

[d]Average of three particles.

Table 2.18. Results of fission gas content measurements on particles from experiment HT-14 (low-temperature magazines)

Holder/ particle	Batch	Quantity of gas, nmol								
		^{83}Kr	^{84}Kr	^{86}Kr	Σ Kr	^{131}Xe	^{132}Xe	^{134}Xe	^{136}Xe	Σ Xe
11/1	OR-1749	0.02	0.13	0.21	0.37	0.14	0.42	0.47	0.99	2.02
11/2	OR-1749	0.07	0.34	0.57	0.98	0.33	1.07	1.14	2.40	4.94
11/3	OR-1749	0.02	0.12	0.18	0.31	0.13	0.34	0.41	0.81	1.70
11/4	OR-1749	0.03	0.15	0.26	0.44	0.16	0.48	0.44	1.00	2.09
13/1	OR-1849	0.02	0.22	0.29	0.54	0.18	0.57	0.61	1.19	2.55
13/2	OR-1849	0.06	0.29	0.49	0.84	0.27	0.91	0.91	1.96	4.06
13/3	OR-1849	0.44	3.45	4.27	8.16	2.27	9.14	9.16	17.80	38.38
13/4	OR-1849	0.05	0.75	1.00	1.80	0.60	2.11	2.23	4.40	9.35
42/1	OR-1838	0.07	0.41	0.63	1.11	0.50	1.79	1.79	3.75	7.84
42/2	OR-1838	0.13	0.80	1.04	1.97	0.68	2.33	2.40	4.90	10.31
42/3	OR-1838	0.05	0.34	0.53	0.91	0.46	1.59	1.60	3.35	7.01
42/4	OR-1838	0.05	0.29	0.49	0.83	0.22	0.80	0.79	1.74	3.56
45/1	OR-1826	0.25	1.60	2.04	3.89	1.25	4.15	4.40	8.65	18.45
45/2	OR-1826	0.05	0.26	0.38	0.69	0.48	1.76	1.89	3.81	7.94
45/3	OR-1826	0.09	0.53	0.79	1.40	0.41	1.43	1.46	2.96	6.26
45/4	OR-1826	0.11	0.44	0.70	1.25	0.40	1.39	1.45	3.00	6.25
48/3	OR-1830	0.14	0.76	1.07	1.97	0.65	2.26	2.40	4.93	10.24

Table 2.19. Results of fission gas content measurements on particles from experiment HT-15

Holder/ particle	Batch	Quantity of gas, nmol								
		^{83}Kr	^{84}Kr	^{86}Kr	Σ Kr	^{131}Xe	^{132}Xe	^{134}Xe	^{136}Xe	Σ Xe
					Low-temperature magazines					
4/1	OR-1850	0.07	0.45	0.68	1.20	0.37	1.31	1.33	2.78	5.80
4/2	OR-1850	0.06	0.44	0.63	1.13	0.31	1.14	1.10	2.41	4.96
4/3	OR-1850	0.09	0.44	0.63	1.16	0.46	1.64	1.63	3.44	7.18
4/4	OR-1850	0.05	0.34	0.52	0.91	0.22	0.90	0.90	1.91	3.93
11/1	OR-1749	0.23	1.09	1.42	2.74	1.09	3.18	3.45	6.78	14.51
11/2	OR-1749	0.20	1.13	1.51	2.85	1.15	3.23	3.59	6.94	14.91
11/3	OR-1749	0.28	1.47	1.84	3.60	1.20	4.03	4.35	8.55	18.13
11/4	OR-1749	0.20	1.06	1.40	2.67	1.12	3.11	3.38	6.62	14.24
13/1	OR-1849	0.07	0.24	0.43	0.74	0.27	0.86	0.91	1.94	3.98
13/2	OR-1849	0.47	3.74	4.50	8.71	2.89	12.17	12.18	23.75	51.00
13/3	OR-1849	0.05	0.12	0.25	0.42	0.25	0.47	0.51	1.08	2.31
13/4	OR-1849	0.06	0.23	0.44	0.73	0.30	0.78	0.92	1.84	3.85
45/1,2,3,4	OR-1826	*a*	*a*	*a*	0.08[b]	*a*	*a*	*a*	*a*	0.64[b]
48/1,2,3,4	OR-1830	*a*	*a*	*a*	0.04[b]	*a*	*a*	*a*	*a*	0.09[b]
					High-temperature magazines					
24/1	OR-1749	0	0.01	0.04	0.05	0.02	0.04	0.02	0.03	0.10
24/2	OR-1749	0.10	0.29	0.56	0.95	0.36	0.89	1.29	2.55	5.10
24/3	OR-1749	0.01	0.06	0.11	0.18	0.12	0.20	0.33	0.56	1.23
24/4	OR-1749	0.04	0	0.02	0.06	0.03	0.01	0.03	0.03	0.11
32/1	OR-1826	0	0.01	0.01	0.02	0.01	0.01	0.04	0.03	0.09
32/2	OR-1826	0.03	0.19	0.28	0.51	0.20	0.52	0.62	1.27	2.62
32/3	OR-1826	0.07	0.37	0.59	1.03	0.43	1.15	1.43	2.83	5.85
32/4	OR-1826	0.03	0.10	0.16	0.29	0.15	0.33	0.41	0.90	1.80

[a]Individual values are so low that they are considered insignificant.

[b]Average of four particles.

the low-temperature magazines. The remaining particles in capsule HT-13 showed essentially complete loss of their fission gases. The data in Tables 2.18 and 2.19 show essentially the same for HT-14 and HT-15. Very few particles exhibited significant fission gas retention because most of them lost nearly all their fission gases.

During this past report period the high-temperature breaking chamber has been checked out, and the graphite heating element has been taken up to temperatures of 1700 to 1800°C and held for extended periods. The purpose of these tests was to examine the outgassing of CO from the graphite heating element that will contain the particle to be heated and then broken. The temperatures that will be required are those similar to the original irradiation environment (1000–1500°C).

The heating was accomplished in increments of 200°C until a final temperature in the 1700 to 1800°C range was achieved. During the heatup, the mass spectrometer was set to monitor the CO mass peak (28 amu), and the pressure in the flight tube was also monitored. The diffusion pump for the spectrometer was used to pump on the whole system. In the initial heating test, large amounts of CO were outgassed, and in some cases pressure surges occurred, which kicked off the spectrometer electronics. In the second heating of the same graphite holder, CO outgassing was at a much reduced rate, and the system pressure was maintained on the 1.3×10^{-5} Pa (10^{-7} torr) range through the test. A final temperature of 1750°C was reached and held for approximately 1 h. After this period the current to the graphite holder was shut off, and the CO mass peak was monitored closely. The CO output dropped rapidly to a linear decrease after 1 min, and the output was nearly stable after 2 min.

From these heating tests, it is clear that, to avoid CO outgassing problems during heatup, it is necessary to anneal the graphite holders for a short time at temperatures near 2000°C. The holders will then be stored in an inert argon environment until their use is required. This requirement is relatively simple. These tests also showed that it is possible to establish a stable CO background before and shortly after breaking a particle. This fact is significant because a good background is important to the final measurement of the CO content of single particles.

The calibration gas containing CO, CO_2 plus Kr, and Xe was installed in permanent position, so the high-temperature chamber can soon begin operation. The current computer program that analyzes the krypton and xenon contents of particles will be modified to include CO and CO_2 analyses. At the present time the system, including the glove box, is being cleaned to reduce the background radiation to operating personnel. On completion of this task we will begin further work on the high-temperature capabilities of the PGA system.

2.5.3 X-Ray Micrographic Facility — M. J. Kania and E. L. Long

The x-ray micrographic facility[36] provides the capability of preparing x-ray micrographs of irradiated coated particles for detecting heavy-metal and fission product redistribution. This system is installed in the High Radiation Level Examination Laboratory (HRLEL) and is fully operational. The system has been evaluated and optimized, using small-diameter compacts made up of irradiated particles and loose irradiated particles. In each case the x-ray microradiographs were of sufficient quality to detect heavy-metal and fission product redistributions. Irradiated particles from experiment HRB-13 were evaluated with this system, and fission product redistribution within the particles was detected.[11] Figure 2.17 is a photograph of an x-ray microradiograph of loose irradiated particles from experiment HRB-14. These particles had been subjected to hot gaseous chlorine leaching for 16 h [Fig. 2.17(*a*)] and 32 h [Fig. 2.17(*b*)] before the x-ray radiographs were made. Clearly visible in both figures is the dispersion of the heavy metal into the buffer coating. This type of chemical interaction is caused by the chlorine's penetrating through permeable LTI PyC coatings and reacting with the ThO_2 kernel material. These photographs demonstrate that hot gaseous chlorine leaching at 1000°C on irradiated particles followed by x-ray microradiography can detect permeable PyC coatings. This facility in conjunction with the chlorine leaching procedure will be used in the PIE of selected particle batches for HRB-14.

2.6 FOREIGN ASSIGNMENT — M. J. Kania

The work outlined in this section was carried out while the author was on assignment to the Institut für Reaktorwerkstoffe (IRW) at KFA,

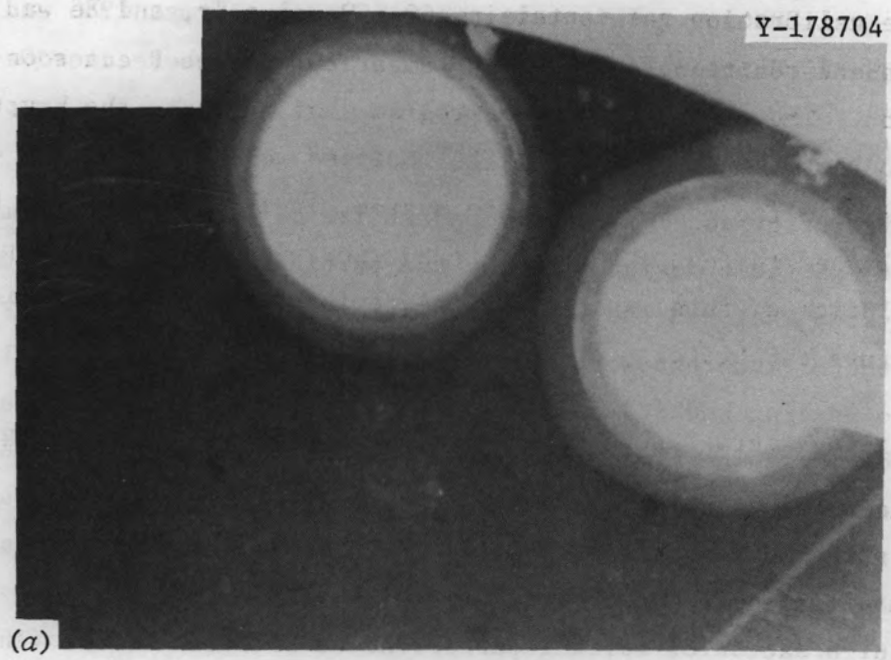

200 μm

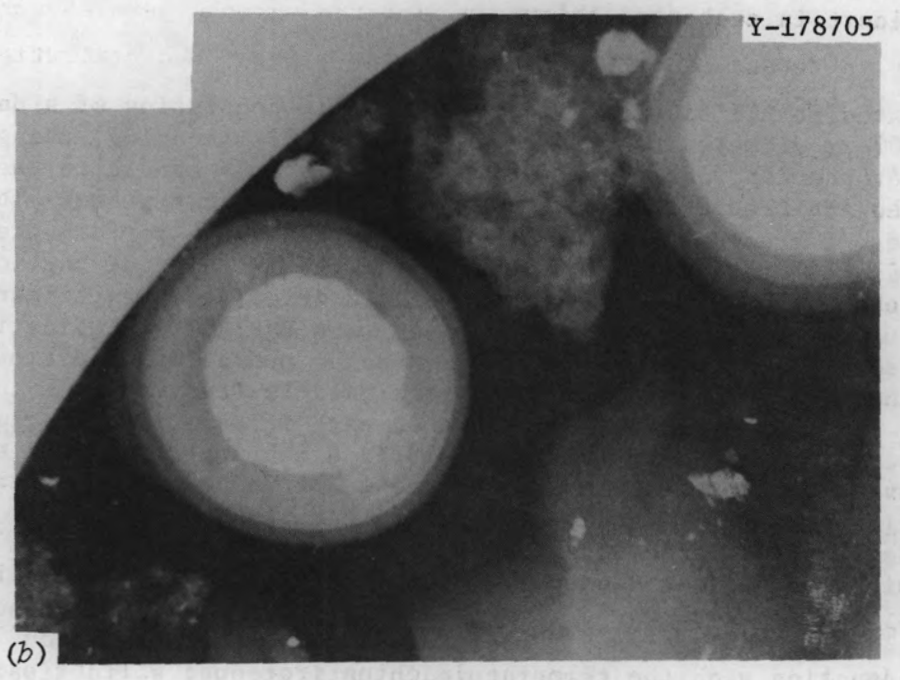

Fig. 2.17. Photographs of x-ray microradiographs of low-temperature isotropic Biso-coated particles from experiment HRB-14 that were subjected to (*a*) 16 h and (*b*) 32 h chlorine leaching at 1000°C. Noticeable in both photographs is the dispersion of heavy metal into the buffer region of coatings.

Jülich, West Germany. This assignment ended in August 1980 and was part of the US-FRG Umbrella Agreement on High Temperature Reactor Development.

2.6.1 $(Th,U)O_2$ Performance Assessment

This performance assessment had as its objective to determine the candidate particle design from the one-particle, thorium-uranium mixed-oxide system that had the best irradiation behavior. Initially, the two candidates of interest were (1) the 400-μm-diam $(Th,U)O_2$ kernel with an HTI Biso coating and (2) the 500-μm-diam $(Th,U)O_2$ kernel with an LTI Triso coating. The LTI Triso particle was dropped in this assessment due to a lack of available performance data. Two irradiation tests containing this particle design are currently in PIE; however, detailed data were not available for inclusion here.

The formation of a final performance evaluation of the $(Th,U)O_2$ kernel with a methane-derived HTI Biso coating was achieved. A final report describing this evaluation was completed,[37] and the abstract of that report is presented below.

> The HTI Biso Particle, Variant-I: consisting of a dense 400-μm diameter $(Th,U)O_2$ kernel with a Biso coating, using a methane-derived pyrocarbon layer (HTI), is a candidate fuel for the advanced PNP/HHT High Temperature Reactor systems. This report presents the results of a comprehensive performance assessment of Variant-I represented by six relevant particle batches irradiated in 12 accelerated irradiation experiments. Fuel performance was judged based upon PNP/HHT qualification requirements with regard to in-reactor operating conditions and end-of-life (EOL) coated particle failure fraction.
>
> Fuel operating conditions in each irradiation experiment were obtained from two sources: (1) a thorough review of all available irradiation data on each experiment and (2) a two-dimensional (R,Θ) thermal modeling computer code, R2KTMP, developed to calculate fuel operating temperature distributions within spherical elements. End-of-life particle failure fractions were determined from gaseous fission product release, based on in-reactor R/B measurements and postirradiation annealing and room temperature investigations; solid fission product release, from single particle ^{137}Cs release into fuel element matrix and hot gaseous chlorine leaching; and visual and ceramographic examinations. Failure fractions determined by solid fission product release yielded values 2 to 35 times higher than those determined by gaseous fission product release.

In-service HTI particle performance in loose particle tests exhibited massive failure at low fluences, 2 to 3 × 10^{25} neutrons/m^2 (E > 0.1 MeV), due to the severe irradiation environment. In contrast, similar particles irradiated in fuel element tests had much higher survival rates. At average EOL fluence for PNP/HHT of 4.5 × 10^{25} neutrons/m^2 (E > 0.1 MeV), the results were

- cycled experiments, 650 to 950°C average fuel temperature, failure fraction range of 0.1 to 0.4% and
- isothermal experiments, 950 to 1250°C average fuel temperature, failure fraction range of 2 to 8%.

With EOL fluence >6 × 10^{25} neutrons/m^2 (E > 0.1 MeV) and fuel temperatures of 950 to 1250°C, failure fractions beyond 10% up to near 100% were observed. Neutron-induced pyrocarbon cracking was the dominant failure mechanism for the HTI Biso particle.

A correlation between EOL failure fraction and accumulated neutron fluence at temperatures ≳950°C yielded a value of 4%. This compares with a PNP/HHT qualification requirement for the HTI Biso particle of 0.04%. Therefore, a final recommendation was made that Variant-I no longer be considered for application in the advanced PNP/HHT systems.

2.7 SERVICE WORK FOR GENERAL ATOMIC COMPANY — F. J. Homan

All irradiation capsules up to and including HRB-15b have contained fuel fabricated at both ORNL and GA. After irradiation, the GA fuel has been shipped to San Diego for PIE. ORNL's PIE capabilities include many facilities unavailable at GA (shielded electron microprobe, IMGA, PGA, and remote x-radiography). Because these examinations have been shown to be useful, ORNL has conducted examinations on GA fuel as a service, paying for the work out of the ORNL budget. This practice will continue with fuel from capsules HRB-15a and beyond. The service work for GA during this reporting period is described below.

2.7.1 Electron Microprobe Studies for General Atomic Company — T. N. Tiegs

Selected GA samples from experiments HT-31, HT-34, HRB-14, and HRB-15b underwent electron microprobe examination at ORNL. General Atomic's primary interest in examining the particles was to identify the fission products associated with the SiC attack in the Triso-coated ThO_2 and MEU fissile particles.

The results from HT-31 and HT-34 on Triso-coated ThO_2 showed that there had been a redistribution of the SiC and that iron and chromium were identified in the SiC corrosion zone. General Atomic is looking into possible sources of contamination in these particles.

The particles from HRB-14, Triso-coated ThO_2 and UO_2, both showed corrosion of the SiC coating by fission product palladium. This was the first time fission product Pd-SiC interactions have been observed in ThO_2 particles.

The particles from HRB-15b, Triso-coated UC_2 and UO_2 (the latter with a zirconium-carbide buffer), both showed very little fission product release (Cs, for example) from the kernels. This can be related to the relatively low irradiation temperatures of HRB-15b. In addition, unusual phases in the UO_2 particles were identified as areas of high carbon content, with cesium as the only fission product present in appreciable quantity.

These results of the microprobe work were given to GA in May 1980 and were subsequently included in two GA publications.[38,39]

2.7.2 PGA Studies for General Atomic Company — J M Robbins

Selected particles from GA's portion of irradiation capsule HRB-15b were broken, and their fission gas contents were measured with the PGA system. The results of the measurements are shown in Table 2.20. The kernel and coating types of the GA particles are listed in Table 2.21.

All the particles measured had Triso coatings and were expected to be gastight. The data in Table 2.20 show that the gas content measured in particles from the same batch is quite consistent. The amount of fission gases present varied considerably from one batch of particles to another; however, this is the result of the different kernel types and burnups represented in the coated particles described in Table 2.21. The results of these measurements were forwarded to GA for their review and assessment.

2.7.3 IMGA Studies for General Atomic Company — T. N. Tiegs

Select GA fissile particle batches irradiated in experiment HRB-15b were analyzed with the IMGA system, with particular attention focused on

Table 2.20. Results of fission gas content measurements on General Atomic Company particles from experiment HRB-15b

Tray/ particle	Quantity of gas, nmol									
	Batch	^{83}Kr	^{84}Kr	^{86}Kr	Σ Kr	^{131}Xe	^{132}Xe	^{134}Xe	^{136}Xe	Σ Xe
12/1	6157-08-0311-1	0.34	1.52	2.24	4.11	2.42	6.75	9.34	15.61	34.13
12/2	6157-08-0311-1	0.23	1.08	1.69	3.01	1.67	5.02	5.86	11.40	24.95
12/3	6157-08-0311-1	0.37	1.48	2.30	4.16	2.34	7.01	9.56	15.99	34.90
12/4	6157-08-0311-1	0.35	1.57	2.38	4.31	2.40	7.30	9.93	16.44	36.07
12/5	6157-08-0311-1	0.33	1.35	2.15	3.84	2.13	6.36	8.65	14.40	31.54
18/1	6157-08-0210-1	0.29	1.58	2.36	4.24	2.27	7.34	9.77	16.43	35.81
18/2	6157-08-0210-1	0.29	1.40	2.17	3.86	2.10	6.79	9.04	14.94	32.88
18/3	6157-08-0210-1	0.32	1.56	2.31	4.20	2.20	7.29	9.67	16.31	35.46
18/4	6157-08-0210-1	0.31	1.51	2.24	4.06	2.20	7.08	9.49	15.84	34.61
18/5	6157-08-0210-1	0.35	1.64	2.36	4.35	2.42	7.69	10.27	17.17	37.55
84/1	6157-09-0120-3	0.30	2.83	3.69	6.81	3.28	15.37	18.02	30.92	67.59
84/2	6157-09-0120-3	0.26	2.66	3.37	6.29	2.97	14.52	17.17	29.44	64.10
84/3	6157-09-0120-3	0.25	2.49	3.42	6.17	2.92	14.52	16.95	29.99	64.39
84/4	6157-09-0120-3	0.21	2.07	2.82	5.10	2.47	11.14	13.61	23.60	50.81
84/5	6157-09-0120-3	0.31	2.85	3.81	6.98	3.42	15.76	18.27	31.73	69.19
90/1	6151-21-0111-3	0.20	2.29	3.06	5.55	2.27	11.55	13.89	24.21	51.92
90/2	6151-21-0111-3	0.24	2.42	3.21	5.88	2.40	12.73	14.70	25.15	54.99
90/3	6151-21-0111-3	0.23	2.43	3.22	5.88	2.35	13.18	15.19	25.99	56.71
90/4	6151-21-0111-3	0.25	2.37	3.18	5.80	2.44	12.74	14.95	25.52	55.66
90/5	6151-21-0111-3	0.22	2.49	3.34	6.06	2.45	13.51	15.67	27.04	58.68
92/1	6155-05-0111-3	0.23	1.70	2.11	4.05	1.87	8.45	9.63	17.37	37.31
92/2	6155-05-0111-3	0.24	1.86	2.34	4.43	2.05	8.98	10.33	18.13	39.49
92/3	6155-05-0111-3	0.24	1.67	2.08	4.00	1.92	7.98	9.38	16.43	35.72
92/4	6155-05-0111-3	0.26	1.95	2.45	4.67	2.22	9.36	10.91	19.20	41.69
92/5	6155-05-0111-3	0.27	1.66	2.25	4.18	1.82	8.46	9.33	16.95	36.57
98/1	6152-03-0111-4	0.18	1.52	2.10	3.80	1.86	9.27	10.90	18.91	40.96
98/2	6152-03-0111-4	0.14	1.59	2.18	3.92	1.96	9.44	11.21	19.33	41.94
98/3	6152-03-0111-4	0.15	1.50	2.00	3.65	1.86	9.08	10.43	18.17	39.54
98/4	6152-03-0111-4	0.16	1.61	2.16	3.93	1.93	9.22	10.88	18.96	40.99
98/5	6152-03-0111-4	0.17	1.57	2.12	3.86	1.95	9.44	11.07	19.37	41.83

Table 2.20. (continued)

Tray/ particle	Quantity of gas, nmol									
	Batch	^{83}Kr	^{84}Kr	^{86}Kr	Σ Kr	^{131}Xe	^{132}Xe	^{134}Xe	^{136}Xe	Σ Xe
71/1	6252-15-0140-3	0.35	1.53	1.99	3.87	1.24	3.82	3.97	8.17	17.21
71/2	6252-15-0140-3	0.36	1.32	1.84	3.52	1.10	3.62	3.72	7.54	15.98
71/3	6252-15-0140-3	0.28	1.31	1.75	3.35	1.06	3.26	3.41	7.02	14.75
71/4	6252-15-0140-3	0.29	1.33	1.79	3.42	1.05	3.47	3.50	7.19	15.22
71/5	6252-15-0140-3	0.34	1.35	1.83	3.52	1.07	3.61	3.72	7.59	15.99
168/1	6157-09-0120-5	0.37	2.19	3.14	5.71	3.29	11.11	14.85	24.90	54.16
168/2	6157-09-0120-5	0.40	2.32	3.25	5.96	3.37	11.63	15.04	25.64	55.69
168/3	6157-09-0120-5	0.44	2.10	3.00	5.45	3.08	10.59	13.94	23.65	51.27
168/4	6157-09-0120-5	0.32	2.17	3.07	5.55	2.72	11.08	13.73	23.47	50.99
168/5	6157-09-0120-5	0.39	2.22	3.21	5.81	3.18	11.11	14.50	24.84	53.63
150/1	6157-08-0210-3	0.32	2.21	3.09	5.62	2.77	11.27	13.99	23.95	51.97
150/2	6157-08-0210-3	0.28	2.09	2.88	5.25	2.52	10.47	13.05	22.39	48.43
150/3	6157-08-0210-3	0.24	2.00	2.73	4.98	2.39	9.76	12.01	20.98	45.14
150/4	6157-08-0210-3	0.34	2.07	3.06	5.48	3.03	10.47	13.90	23.62	51.02
150/5	6157-08-0210-3	0.37	2.44	3.39	6.20	3.03	13.32	16.41	28.01	60.78
104/1	6157-08-0320-6	0.26	2.57	3.37	6.20	3.02	16.16	18.54	31.95	69.67
104/2	6157-08-0320-6	0.23	2.26	3.11	5.60	2.72	13.49	15.46	26.83	58.50
104/3	6157-08-0320-6	0.26	2.55	3.43	6.24	2.97	15.39	17.92	31.46	67.74
104/4	6157-08-0320-6	0.23	2.31	2.92	5.47	2.61	13.40	15.68	27.32	59.01
104/5	6157-08-0320-6	0.22	2.28	2.97	5.47	2.81	13.80	16.45	28.36	61.42
124/1	6152-02-0110-3	0.19	1.43	1.96	3.58	1.72	8.11	9.78	16.83	36.44
124/2	6152-02-0110-3	0.18	1.31	1.84	3.33	1.78	8.47	9.91	17.52	37.68
124/3	6152-02-0110-3	0.14	1.38	1.86	3.38	1.80	8.47	10.11	17.55	37.95
124/4	6152-02-0110-3	0.14	1.26	1.69	3.09	1.64	7.44	8.87	15.17	33.12
124/5	6152-02-0110-3	0.13	1.42	1.91	3.46	1.72	8.04	9.58	16.41	35.75

Table 2.21. Kernel and coating types for General Atomic Company particles in experiment HRB-15b

Tray	Batch	Kernel type	Coating type
12	6157-08-0311-1	UCO, O/U ~1.0	Triso
18	6157-08-0210-1	UCO, O/U ~0.5	Triso
84	6157-09-0120-3	UCO, O/U ~1.5	Triso
90	6151-21-0111-3	UC_2	Triso
92	6155-05-0111-3	1:1$(Th,U)O_2$	Triso
98	6152-03-0111-3	UO_2	Triso[a]
71	6252-15-0140-3	ThO_2	Triso
168	6157-09-0120-5	UCO, O/U ~1.5	Triso
150	6157-08-0210-3	UCO, O/U ~0.5	Triso
104	6157-08-0320-6	UCO, O/U ~1.0	Triso
124	6152-02-0110-3	UO_2	Triso[b]

[a]Five-micrometers ZrC deposited on the UO_2 kernel.

[b]ZrC buffer.

the gamma emissions of ^{110m}Ag. These particles represent some of the first MEU fuel available that had been irradiated at moderate temperatures (~1000°C) and to high fast neutron fluences (4.2 to 6.95 × 10^{25} neutrons/m^2, $E > 29$ fJ). Descriptions of the particles examined are given in Table 2.22.

In the past, IMGA results were based on ratios using ^{95}Zr as the stable isotope. However, based on some recent calculations, we believe that the activity ratios that use ^{106}Ru as the stable isotope may be more representative of the quantitative release values. We are now in the process of examining our (and GA's) calculational methods for determining fission product inventories in the particles. It is hoped that we will arrive at a standard procedure that will accurately predict fission product inventories.

Although the measured $^{137}Cs/^{106}Ru$ activity ratios (Table 2.23) showed that ^{137}Cs was being retained by the particles, the $^{110m}Ag/^{106}Ru$ activity ratio (Table 2.24) indicated that ^{110m}Ag was being released. The calculated activity ratios represent the best estimates at the present time; however, we do not consider them final. As mentioned previously, the calculational methods are now being analyzed so that the

Table 2.22. Description of GA HRB-15b fissile particles examined with the IMGA system

Tray	Kernel type	Coating type	Fast neutron fluence (neutrons/m^2), $E > 29$ fJ
12	$UC_{0.49}O_{1.12}$	Triso	4.35
18	$UC_{0.69}O_{1.64}$	Triso	4.55
50	$(Th,U)O_2$	Triso	6.25
80	$UC_{0.49}O_{1.12}$	Triso	6.90
84	$UC_{0.20}O_{1.64}$	Triso	6.93
90	UC_2	Triso	6.95
92	$(Th,U)O_2$	Triso	6.95
98	UO_2 w/ZrC coat	Triso	6.90
104	$UC_{0.49}O_{1.12}$	Triso	6.85
114	$(Th,U)O_2$	SiBiso	6.60
116	$UC_{0.49}O_{1.12}$	SiBiso	6.55
118	UO_2	SiBiso	6.55
124	UO_2 w/ZrC buffer	Triso	6.25
138	UO_2 w/ZrC buffer	Triso	5.75
148	UO_2	Triso	5.10
150	$UC_{0.69}O_{0.51}$	Triso	5.00
156	UO_2 w/ZrC buffer	SiBiso	4.65
168	$UC_{0.20}O_{1.64}$	Triso	4.05

Table 2.23 Results on $^{137}Cs/^{106}Ru$ ratio for HRB-15b

Position	Observed ratio	Calculated ratio[a]	Observed ratio as percent of calculated ratio
12	1.676E-1	1.819E-1	92.2
18	1.627E-1	1.529E-1	106.4
50	1.418E-1	1.443E-1	98.3
80	1.142E-1	1.140E-1	100.2
84	1.170E-1	1.136E-1	103.0
90	1.170E-1	1.132E-1	103.3
92	1.337E-1	1.321E-1	101.2
98	1.144E-1	1.121E-1	102.1
104	1.074E-1	1.124E-1	95.6
114	1.305E-1	1.325E-1	98.5
116	1.187E-1	1.138E-1	104.3
118	1.183E-1	1.173E-1	100.8
124	1.186E-1	1.179E-1	100.6
138	1.194E-1	1.257E-1	95.0
148	1.322E-1	1.329E-1	99.5
150	1.331E-1	1.331E-1	100.0
156	1.330E-1	1.381E-1	96.3
168	1.501E-1	1.542E-1	97.3

[a]Using ORNL No. 2 cross sections from W. E. Thomas et al., *HTGR Experiment HRB-15b: Particle Loadings and Irradiation in the High-Flux Isotope Reactor*, ORNL/TM-6892 (December 1979).

Table 2.24 Results on $^{110m}Ag/^{106}Ru$ ratio for HRB-15b

Position	Observed ratio	Calculated ratio[a]	Observed ratio as percent of calculated ratio
12	4.088E-3	5.703E-3	71.7
18	4.821E-3	6.335E-3	76.1
50	7.360E-3	9.443E-3	77.9
80	7.991E-3	1.070E-2	73.9
84	7.589E-3	1.074E-2	70.7
90	7.787E-3	1.078E-2	72.2
92	7.573E-3	1.065E-2	71.1
98	7.709E-3	1.087E-2	70.9
104	7.369E-3	1.086E-2	67.9
114	8.137E-3	1.062E-2	76.6
116	7.845E-3	1.073E-2	73.1
118	7.533E-3	1.050E-2	71.7
124	7.264E-3	1.033E-2	70.3
138	7.317E-3	9.600E-3	76.2
148	6.450E-3	9.111E-3	70.8
150	6.523E-3	8.958E-3	72.8
156	5.845E-3	8.551E-3	68.4
168	5.714E-3	7.358E-3	77.7

[a]Using ORNL No. 2 cross sections from W. E. Thomas et al., *HTGR Experiment HRB-15b: Particle Loadings and Irradiation in the High-Flux Isotope Reactor*, ORNL/TM-6892 (December 1979).

calculated ratios may be changed, resulting in different release values. Changes in the calculated ratios will be reported as they become available. All the results on the IMGA examinations were sent to GA for inclusion as an appendix to their final topical report on capsule HRB-15b.

2.8 REFERENCES

1. M. J. Kania, "Capsule HT-34," *HTGR Base-Technology Program Annu. Prog. Rep., Dec. 31, 1977*, ORNL-5412, pp. 71–85.
2. E. L. Long, Jr., "Capsule HT-34," *HTGR Base-Technology Program Annu. Prog. Rep., Dec. 31, 1978*, ORNL-5536, pp. 31–38.
3. T. N. Tiegs et al., "Irradiated Microsphere Gamma Analyzer System," *HTGR Base-Technology Program Annu. Prog. Rep., Dec. 31, 1978*, ORNL-5536, pp. 89–95.
4. T. N. Tiegs, "Capsule HT-34," *HTGR Base-Technology Program Annu. Prog. Rep., Dec. 31, 1979*, ORNL-5643, pp. 70–76.
5. E. L. Long, Jr., et al., *Performance of HTGR Biso and Triso Fertile Particles Irradiated in Capsule HT-34*, ORNL/TM-7674, to be published.
6. E. L. Long, Jr., "Capsule HT-35," *HTGR Base-Technology Program Annu. Prog. Rep., Dec. 31, 1979*, ORNL-5643, pp. 75–81.
7. M. J. Kania et al., "Capsule HRB-13," *HTGR Base-Technology Program Prog. Rep., July 1, 1975–Dec. 31, 1976*, ORNL-5274, pp. 289–99.
8. E. L. Long, Jr., and K. R. Thoms, "Capsule HRB–13," *HTGR Base-Technology Program Annu. Prog. Rep., Dec. 31, 1977*, ORNL-5412, pp. 98–102.
9. T. N. Tiegs, "Capsule HRB-13," *HTGR Base-Technology Program Annu. Prog. Rep., Dec. 31, 1978*, ORNL-5536, pp. 40–42.
10. T. N. Tiegs, "Capsule HRB-13," *HTGR Base–Technology Program Annu. Prog. Rep., Dec. 31, 1979*, ORNL-5643, pp. 84–86.
11. T. N. Tiegs et al., "Irradiation Performance of HTGR Fuel in HFIR Capsule HRB-13," ORNL/TM to be prepared.
12. M. J. Kania and E. L. Long, Jr., "Capsule HRB-14," *HTGR Base-Technology Program Annu. Prog. Rep., Dec. 31, 1977*, ORNL-5412, pp. 98–105.
13. K. R. Thoms, "Capsule HRB-14," *HTGR Base-Technology Program Annu. Prog. Rep., Dec. 31, 1978*, ORNL-5536, pp. 41–46.

14. T. N. Tiegs, E. L. Long, Jr., and K. R. Thoms, "Capsule HRB-14," *HTGR Base-Technology Program Annu. Prog. Rep., Dec. 31, 1979*, ORNL-5643, pp. 84–95.

15. E. L. Long, Jr., and D. P. Stinton, "Capsule HRB-15b," *HTGR Base-Technology Program Annu. Prog. Rep., Dec. 31, 1977*, ORNL-5412, pp. 105–09.

16. T. N. Tiegs et al., "Capsule HRB-15b," *HTGR Base-Technology Program Annu. Prog Rep., Dec. 31, 1979*, ORNL-5643, pp. 95–97.

17. W. E. Thomas et al., *HTGR Experiment HRB-15b: Particle Loadings and Irradiation in the High Flux Isotope Reactor*, ORNL/TM-6892 (December 1979).

18. F. J. Homan, "Nuclear Evaluation and Thermal Analysis," *HTGR Base-Technology Program Annu. Prog. Rep., Dec. 31, 1979*, ORNL-5643, pp. 113–17.

19. D. P. Stinton, *Deposition and Characterization of Pyrocarbon Coatings Produced Using CO_2 Dilution*, ORNL/TM report to be prepared.

20. R. J. Lauf and D. N. Braski, *Characterization of SiC Coatings on HTGR Fuel Particles: Final Report*, ORNL/TM-7571 (January 1981).

21. R. J. Lauf and D. N. Braski, *Dependence of Silicon Carbide Coating Properties on Deposition Parameters, Preliminary Report*, ORNL/TM-7209 (May 1980).

22. P. Krautwasser et al., "Material Properties and Fission Product Retention of SiC coatings," translated from German, unidentified publication, 4 pp.

23. R. J. Lauf, *The Interaction of Silver and Palladium with Silicon Carbide in HTGR Fuel Particles — Preliminary Report*, ORNL/TM-7393 (July 1980).

24. R. L. Pearson, T. B. Lindemer, and C. E. Beahm, *Simulated Fission Product–SiC Interaction in Triso-Coated LEU or MEU HTGR Fuel Particles*, ORNL/TM-6991 (November 1980).

25. D. P. Stinton, W. J. Lackey, and R. D. Spence, *Production of Spherical UO_2-UC_2 for Nuclear Fuel Applications Using Thermochemical Principles*, ORNL/TM-7651 (March 1981).

26. E. L. Long, Jr., "PWS FD-12," *HTGR Base-Technology Annu Prog. Rep., Dec. 31, 1979*, ORNL-5643, pp. 119–20.

27. E. J. Allen, *CACA-2: Revised Version of CACA — A Heavy Isotope and Fission-Product Concentration Calculational Code for Experimental Irradiation Capsules*, ORNL/TM-5266 (February 1976).

28. Private communication, B. F. Myers, General Atomic Company, to E. L. Long, Jr., July 1978.

29. M. J. Kania, T. B. Lindemer, M. T. Morgan, and J M Robbins, *Irradiation Performance of HTGR Fertile Fuel in HFIR Target Capsules HT-12 Through HT-15: Part I — Experimental Description and Fission Product Behavior*, ORNL/TM-5305 (February 1977).

30. E. L. Long, Jr. et al., *Irradiation Performance of HTGR Biso Fertile Particles in HFIR Experiments HT-17, -18, and -19*, ORNL/TM-6414 (November 1978).

31. M. J. Kania and K. H. Valentine, *The Irradiated Microsphere Gamma Analyzer (IMGA) — An Integrated System for HTGR Fuel Performance Assessment*, ORNL-5606 (February 1980).

32. B. A. Thiele and M. Herren, *Determination of End-of-Life Failure Fractions of HTGR-Fuel Particles by Postirradiation Annealing and Beta Autoradiography*, ORNL/TM-6619 (November 1978).

33. K. H. Valentine, "Irradiated Microsphere Gamma Analyzer System," *HTGR Base-Technology Program Prog. Rep., Jan. 1, 1974–June 30, 1975*, ORNL-5108, pp 446–56.

34. T. B. Lindemer, T. M. Besmann, and C. E. Johnson, "Thermodynamic Review and Calculations — Alkali Metal Oxide Systems with Nuclear Fuels, Fission Products and Structural Materials," *J. Nucl. Mater.* 100: (in press).

35. J M Robbins, M. J. Kania, and E. L. Ryan, "Postirradiation Gas Analyzer System," *HTGR Base-Technology Program Annu. Prog. Rep., Dec. 31, 1978*, ORNL-5536, pp. 95–99.

36. E. L. Long, Jr., "X-Ray Microradiographic Facility," *HTGR Base-Technology Program Annu. Prog. Rep., Dec. 31, 1979*, ORNL-5643, pp. 125–27.

37. M. J. Kania and H. Nickel, *Performance Assessment of the $(Th,U)O_2$ HTI-Biso-Coated Particle Under PNP/HHT Irradiation Conditions*, JUL-1685-Dissertation Kernforschungsanlage, Jülich (February 1981).

38. C. A. Young, *Pre- and Postirradiation Evaluation of Fuel in Capsule HRB-14*, GA-A15969, General Atomic Company, San Diego, Calif. (September 1980).

39. C. A. Young and C. S. Jones, *Pre- and Postirradiation Evaluation of Triso ThO_2 Particles Irradiated in Capsule HT-34*, GA-A15612, General Atomic Company, San Diego, Calif. (October 1980).

3. PRESTRESSED CONCRETE PRESSURE VESSEL DEVELOPMENT

D. J. Naus

3.1 INTRODUCTION

The Prestressed Concrete Reactor Vessel (PCRV) research and development program consists of generic studies designed to provide technical support for ongoing PCRV activities, to contribute to the technological data base, and to provide independent review and evaluation of the relevant technology. These studies are identified through direct communication with PCRV designers, participation in American Concrete Institute-American Society of Mechanical Engineers (ACI-ASME) committee activities, literature reviews, and communications with researchers in other countries. The program involves four basic interrelated activities: (1) assessments, (2) analysis development, (3) materials studies, and (4) model testing. During this reporting period studies have been conducted in five task areas: (1) analysis methods development, (2) concrete properties in nuclear environment, (3) instrumentation evaluation and development, (4) structural model tests, and (5) liner and penetration studies.

3.2 ANALYSIS METHODS — J. R. Dougan, Z. P. Bazant,* and E. C. Rossow*

The objective of the PCRV analytical effort is to develop techniques that can be incorporated into existing modern finite-element computer programs to improve the accuracy and efficiency of these codes. We are currently investigating revisions to the endochronic concrete constitutive relations and finite-element computation of creep effects in concrete structures.

3.2.1 Revisions to the Endochronic Concrete Constitutive Relations

A major activity of the PCRV program is the development and demonstration of accurate structural analysis of PCRVs and their related structural components. The accuracy of such analyses depends heavily on the ability of the concrete constitutive relations to represent both the

---

*Northwestern University, Evanston, Ill.

elastic and inelastic behavior of the concrete under complex loading conditions. One effort to provide suitable concrete constitutive relations was performed for ORNL by Z. P. Bazant of Northwestern University. This effort culminated in a report[1] that documents the use of an endochronic theory to describe the behavior of concrete. Basically, the endochronic theory characterizes the accumulation of inelastic strain through the use of a parameter called intrinsic time, whose increment is a function of the strain increments. Periodically revisions have been made to the endochronic constitutive relations for concrete as incorporated into the ADINA[2,3] finite-element code at ORNL.

Bazant proposed two sets of constitutive relations for concrete. Both sets were incorporated into ADINA and are referred to as the base model relations and the refined model relations. One primary difference between the two sets of relations is the inclusion in the refined model relations of inelastic volume changes caused by hydrostatic stress. The stress-strain relationships for both the base and the refined model relations are separated into their respective volumetric and deviatoric components, which are defined as functions of several parameters, of which one is intrinsic time. These parameters are defined as functions of a variety of other parameters, whose values were determined by curve-fitting a large amount of test data. Of particular importance is that, for those parameters not found to be constant, all were related to only one other parameter, the concrete compressive strength f'_c.

3.2.1.1 Base Model Constitutive Relations

The incremental stress-strain relations proposed by Bazant for the base model are separated into increments of the deviatoric and volumetric components, which in turn are expressed as the sum of their respective elastic and inelastic portions. For the deviatoric component, the equations are written as

$$de_{ij} = ds_{ij}/2G + de''_{ij} \ ,$$
$$de''_{ij} = (s_{ij}/2G)dz \ , \tag{3.1}$$

where de_{ij} = increment of the deviator of the strain tensor,

ds_{ij} = increment of the deviator of the stress tensor,

G = shear modulus,

de''_{ij} = inelastic increment of de_{ij},

s_{ij} = deviator of the stress tensor,

dz = increment of intrinsic time.

For the volumetric component, the equations are written as

$$d\varepsilon = d\sigma/3K + d\varepsilon''$$

and (3.2)

$$d\varepsilon'' = d\lambda + (\sigma/3K)(dt/\tau_1) + d\varepsilon^0 ,$$

where $d\varepsilon$ = increment of volumetric strain,

$d\sigma$ = increment of volumetric stress,

K = bulk modulus,

$d\varepsilon''$ = inelastic increment of $d\varepsilon$,

$d\lambda$ = increment of inelastic dilatancy,

σ = volumetric stress,

dt = increment of time,

τ_1 = relaxation time,

$d\varepsilon^0$ = increment of stress-independent inelastic strain (thermal dilatation plus shrinkage).

The notation employed in these and the remaining constitutive equations presented in this report is identical to that used by Bazant in ref. 1, which includes considerably more detail about the terms defined above.

For incorporation of these equations into ADINA, consideration was given to only short-term deformations, which thereby allowed creep to be neglected. Also, no stress-independent inelastic strains, such as thermal dilantancy and shrinkage, were considered. Therefore, Eq. (3.2), in order to represent the time-independent form of the base model constitutive relations, may be rewritten as

$$d\varepsilon = (d\sigma/3K) + d\varepsilon'',$$

$$d\varepsilon'' = d\lambda$$

or, more directly,

$$d\varepsilon = (d\sigma/3K) + d\lambda \ . \tag{3.3}$$

Equations (3.1) and (3.3) represent the stress-strain relations used in implementing the base model.

The base model constitutive relations and the corresponding solution routine are contained in a subroutine called ENDO. The solution routine follows the one recommended in ref. 1 and utilitizes the step-by-step numerical integration technique. A listing of the two-dimensional (2-D) version of ENDO as it is used in conjunction with ADINA is provided in ref. 4.

In addition to ENDO, a number of other subroutines are utilized in an analysis employing the endochronic constitutive relations. Four of the subroutines are (1) EL2D14, which sets the pointers for vector storage; (2) IENDO, which initializes the storage parameters; (3) EIGEN, which calculates eigenvalues; and (4) MAXMIN, which determines the maximum and minimum stress and strain for each integration point. MAXMIN is not used in 3-D problems because the current ADINA output format does not have space for printing the maximum stresses and strains for such problems. The 2-D versions of the remaining subroutines are also listed in ref. 4 and are concerned with the cracking routines. WCRACK is used to check the status of existing cracks, that is, whether they are open or closed. ECRACK calculates the true stresses and strains on the basis of nodal displacements and the existing crack status. POSINV is used by ECRACK to invert portions of the material matrix.

3.2.1.2 Refined Model Constitutive Relations

The refined model relations resulted from the analysis of further test data. The equations developed to model the behavior of concrete became more complicated than were the ones developed for the base model relations and included volumetric inelastic strains caused by hydrostatic stress. The revised relations involved the use of two intrinsic times,

one for distortion and the other for compaction. The resulting time-independent form of the stress-strain relations may be written as follows. For the deviatoric component

$$de_{ij} = ds_{ij}/2G + de''_{ij} \ ,$$
$$de''_{ij} = (s_{ij}/2G)dz \ , \tag{3.4}$$

in which the variables are defined as before, except dz, which is now defined as the increment of intrinsic time for distortion. As before, the strain increment is the sum of its elastic and inelastic parts. For the volumetric component

$$d\varepsilon = d\sigma/3K + d\varepsilon'' \ ,$$
$$d\varepsilon'' = d\lambda + (\sigma/3K)dz' + d\lambda' \ , \tag{3.5}$$

in which the variables are defined as before, dz' represents the increment of intrinsic time for compaction, and $d\lambda'$ represents the increment of shear compaction. These equations represent the stress-strain relations used in implementing the refined model.

Subroutine ENDOR contains the refined-model relations and the solution routine. Reference 4 contains a listing of the 2-D version of ENDOR. The additional subroutines utilized when employing the refined model relations are identical in function to the ones listed for the base model relations. In fact, subroutines WCRACK, ECRACK, POSINV, and MAXMIN are the same for both sets of relations, but subroutines EL2D14 and IENDO contain minor changes to reflect the increase in the parameters used in the refined relations.

3.2.1.3 Cracking

The endochronic theory, as presented in ref. 1, does not include realistic provisions for handling the tensile cracking of concrete. Therefore, a separate routine for concrete cracking was developed. In this routine, the cracks are modeled by setting the stresses normal and

parallel to the crack plane equal to zero. The criteria for cracking are defined by user input values for a tensile stress limit and a tensile strain limit. Current stress and strain values at the integration points used in the numerical evaluation of the particular element's material matrix are checked against these limits. A crack is assumed to occur if either of these limits is exceeded.

A crack is assumed to close if the strain normal to the crack plane and calculated from the displacements is less negative than the actual strain in the material, assuming that a crack is present. The status of a crack is checked after the change in the parameters Δz and $\Delta\lambda$ (plus $\Delta z'$ and $\Delta\lambda'$ for the refined model) is less than 5% from one iteration to the next.

We originally attempted to model the effect of aggregate interlock by the cracking routine through the use of a "shear transfer" factor. However, use of the factor generated conflicting results, and it has been removed for the time being because of our impression that ignoring the phenomenon of aggregate interlock will produce conservative results.

3.2.1.4 Strain Subdivisions

The complex equations of the endochronic constitutive relations are numerically integrated by using the method specified in ref. 1 as it pertains to the solution routine used in ADINA. In ADINA, the approximate stiffness of the structure is calculated, and approximate displacements are determined that correspond to the known loads on the structure. Strains are then determined by using the element strain displacement relations. The internal stresses that arise from these strains are computed and compared with the stresses that were assumed to exist when the stiffness was determined.

When the material model equations are used, all the strain components are known, and the stress components must be calculated. The most practical method of solving for the stresses requires an iterative procedure. Initially, the stress increment and the material parameters Δz and $\Delta\lambda$ (plus $\Delta z'$ and $\Delta\lambda'$ for the refined model) are assumed to be zero. Mean values are calculated for the strain components, and an approximate stress-strain matrix is developed. Approximate stress increments are then

calculated by using the approximate stress-strain matrix and the known strains. Mean stresses are calculated, and new values of the material parameters Δz and $\Delta\lambda$ (plus $\Delta z'$ and $\Delta\lambda'$ for the refined model) are determined. These new values are used to determine a better approximation of the stress-strain matrix, with which new values of the stress increments may be calculated. Again updated values of the material parameters are determined, and the process is repeated until the values of the material parameters do not vary from their previous values by more than 0.1%.

Early experience with the endochronic constitutive relations as originally incorporated into ADINA indicated that the constitutive equations were ill-conditioned; that is, convergence to the 0.1% criterion was often very slow, requiring numerous iterations. In some instances, the equations diverged. To help alleviate this situation, a method of subdividing the increments of strain was devised.

As currently implemented, the strain increment that is applied to the constitutive model equations is divided into n equal subincrements. After each subincrement is applied, the iterations proceed as usual, with the next subincrement being applied after the 0.1% convergence criterion has been satisfied for the current subincrement. The equation for the number of subincrements is

$$n = 200|I_1| + 500J_2^{1/2} + 11{,}000|I_3|^{1/3} + 1 \ , \qquad (3.6)$$

where n = number of equal subincrements,

I_1 = the first invariant of the incremental strain,

J_2 = the second invariant of the deviator of incremental strain,

I_3 = the third invariant of the incremental strain.

This equation was developed by trial and error on the basis of representative cases that tended to diverge before the application of the strain subdivisions.

3.2.1.5 Modulus of Elasticity

The endochronic constitutive relations, as currently implemented in ADINA, require only the knowledge of the concrete compressive strength f'_c to define the shape of the compression portion of the stress-strain curve.

Other required information, such as the initial tangent modulus, is generated from functions of f'_c and specified values of material parameters determined from the fitting of test data. Therefore, for a specified f'_c, only one shape of the compression portion of the stress-strain curve may be generated. Although this one shape may represent something of an average of all the possible shapes of stress-strain curves for concrete of a specific f'_c, it clearly does not allow the flexibility required for analysis of PCRVs and their related components.

In one analysis performed at ORNL by using the refined endochronic constitutive relations, the dependence of the initial tangent modulus, E_0 on f'_c led to nonconservative results, in part, if not completely. The analysis was conducted on a small-scale flat end-slab of a cylindrical prestressed concrete nuclear reactor vessel that had been tested to failure by the University of Illinois.[5] The slab was designated PV26-2, and the concrete properties were recorded as 46.3 MPa for f'_c and as 26.9 GPa for E_0. Using the equation for E_0 contained in the refined model relations, a value of 41.8 GPa was generated and used in the analysis. The resulting analytical displacements were significantly less than the recorded displacements, a fact that contributed to the ability of the analytical structure to withstand a much higher loading before failure than did the test slab. The most probable reason for this result was the considerable difference in the recorded and the calculated E_0. The calculated value, being the higher of the two, defined a concrete that was considerably more stiff than it should have been.

The most direct method for correcting this discrepancy is to specify E_0 rather than to calculate it on the basis of f'_c. Originally we hoped that merely inputting the desired value of E_0 would solve the problem. However, this procedure, while correcting E_0, significantly reduced the maximum compressive stress even though f'_c was left unchanged as an input value. Apparently, the interrelationships between the various material parameters used in the refined model relations are such that any change in the value of E_0 has not only the desired effect on E_0 but also an undesirable effect on the magnitude of the maximum stress. Some effort has been devoted to examining certain material parameters known to affect the value of the maximum stress by assuming that these parameters could be

manipulated in such a way as to force the stress-strain curve through the desired maximum stress. Thus far, however, nothing conclusive has been determined.

It should be noted that this problem is not confined to the refined model relations but also exists in the base model relations, where E_0 is likewise calculated from f'_c by using a slightly different equation.

3.2.1.6 Investigation Conclusions

The endochronic constitutive relations, as currently implemented in ADINA, represent a potentially powerful tool for use in the analysis of PCRVs and their related structural components. Unfortunately, some discrepancies still exist, which reduce the reliability of the relations. A method for determining the effect of creep must be developed. A procedure for incorporating some consistent measure of the effect of aggregate interlock is also desirable. But, most important, until a way is found for better control over the shape of the stress-strain curve, the relations are of limited use.

3.2.2 Finite-Element Computation of Creep Effects in Concrete Structures

During this reporting period a subcontract was initiated with Northwestern University to develop a set of computer subroutines for creep analysis of concrete structures.

3.2.2.1 Background

To evaluate the full benefit of the safety and reliability of concrete containment structures, it is necessary to include not only the strength effects for the concrete and reinforcing materials but also the actual inelastic behavior of these materials. In concrete vessels acting as primary containments (PCRVs) or secondary containments, creep of the concrete causes the major source of inelastic behavior during their service life. During the 1970s the knowledge of this phenomenon advanced tremendously, and methods that allow an accurate and realistic analysis were developed.[6-16] From these researches, the method for a large-scale computer finite-element analysis of creep effects was deemed to be feasible.

3.2.2.2 Approach

A set of FORTRAN IV subroutines that extend the capability of the finite-element code NONSAP (University of California at Berkeley) will be developed for analysis of concrete creep. For analysis, creep will be characterized as:

- The creep law will be assumed to be linear; that is, to follow the principle of superposition, which is applicable within the service stress range, especially for mass concrete.
- Aging (the gradual change of creep properties as a function of age) will be considered.
- The dependence of creep properties on given temperature variations will be considered. This will include both (1) the increase of the creep rate from heating and (2) the acceleration of aging, as modified by the equivalent hydration period (maturity).

The principal characteristics of the numerical method will be

- The integration will be carried out in discrete time steps. A rate-type (rather than an integral-type) form of the creep law, with age-dependent properties, will be used. (This will eliminate the need for storing the history of stresses for each finite element and evaluating in each time step long sums over this history.)[6]
- Among the various possible rate-type forms, the one based on a Maxwell chain will be adopted because of its advantages documented in the literature.[6-10,15]
- The age-dependent elastic moduli characterizing the Maxwell chain model will be automatically generated by one subroutine from the relaxation function, which itself will be automatically determined from the creep function. A check by reproducing the creep curves from the Maxwell chain model will also be included.[9,10,14]
- The exponential algorithm, which is unconditionally stable and allows increasing the time step so that it appears constant in the log-time scale, will be used.[9,10,14]

The characterization of creep for computations may follow either of the following two methods.

- The creep function is defined empirically on the basis of creep tests for one particular concrete that the user has in mind, the input being an array of values for various discrete creep durations and ages at loading.
- The creep function is characterized in terms of the double power law, whose parameters will be automatically generated in the program from the given standard cylindrical strength of concrete, its mix ratio, and cement type.[11,13] Two options will be possible: (1) either the user will also specify the elastic modulus or some short-time creep value or (2) the elastic modulus will be calculated from the strength. Only normal weight and normal strength concretes made of portland cement will be considered.

Effects of time-variable humidity will not be considered in this development. These effects would bring about a major complication of the program and would require that many additional variables be used to characterize partial stresses in solid and water components.[6] Omission of moisture effects is admissible for massive structures such as PCRVs because of their thickness and the use of a steel liner on the interior surface, which does not permit significant drying except possibly at the outer surface. However, an approximate consideration of the humidity effect, which does not cause major complication of the analysis, will be possible. The user will be allowed to specify the mean humidity of each element during its lifetime, and the coefficients of the creep law will be determined on this basis.[13] Moreover, the user will be able either to supply his own shrinkage function for each element or to generate the shrinkage function on the basis of the supplied mean relative humidity.[13]

The coding will be in FORTRAN IV for the CDC-6600 computer operated at Northwestern University. Care will be exercised to make the coding machine-independent for maximum portability of the routines. Incorporation of the subroutines into the NONSAP program will not cause a change in input to the program for current uses. Input into the creep routines will be of a form that is compatible with NONSAP and that is familiar to current NONSAP users. Every effort will be made to minimize running time and storage requirements. All I/O with high-speed auxiliary storage will be executed with standard FORTRAN statements but will be

blocked by using large buffers. This will permit, at the user's option, an easy implementation of highly efficient machine-dependent I/O routines at particular installations.

3.2.2.3 Results to be Provided

On completion of the investigation, a report will be provided, to contain the following parts: (1) general description of results, (2) detailed description of the subroutines with user instructions, and (3) complete FORTRAN IV listing of all subroutines developed for the CDC-6600. The general description of results (part 1) will contain (1) an introduction, (2) a description of the mathematical model used for creep analysis of concrete structures and of creep characterization methods, (3) a description of the numerical time-integration method, (4) a description of main features of subroutines developed, (5) documentation of an illustrative example, (6) a summary and conclusions, and (7) a list of references. The detailed description of the subroutines (part 2), which is intended as user's instructions, will consist of (1) a description of changes made in the NONSAP program to accommodate subroutines developed, (2) a listing of various subroutines and their flowcharts, (3) a description of communication between subroutines and the main program, (4) a detailed description of input and output, and (5) an example problem complete with sample input and output. The program listing (part 3) will be supplemented with sufficient comments to explain the coding.

The investigation will be completed, and a final report will be developed during the next reporting period.

3.3 CONCRETE PROPERTIES IN A NUCLEAR ENVIRONMENT — G. C. Robinson and D. J. Naus

The objectives of the concrete properties in a nuclear environment are to provide basic information required to support development of improved analysis methods and to develop a bank of highly reliable data. Activities during this reporting period were directed at assembling information on available concrete property data and developing a performance specification for a concrete multiaxial testing system.

3.3.1 Review of Concrete Property Data

Prestressed concrete reactor vessels are designed to serve as primary pressure containment structures. The safety of these vessels depends on (1) a correct assessment of the loadings (including overloads) likely to be applied to the vessel, together with the probability of their occurring, and (2) the proper design of the vessel to accept these loadings. Proper design of the vessel thus requires a knowledge of the component (material) properties. Since the last survey of concrete properties[17] was completed about five years ago, an updated review of concrete properties was conducted to identify areas requiring additional concrete property development. The results of the review of concrete properties have been used to develop a report,[18] to be published during the next reporting period. A summary of the report follows.

> Concrete material systems were reviewed with respect to constitutents, mix design, placing, curing, and strength evaluations. Although somewhat limited for the extreme environmental conditions, typical concrete property data are presented for both normal and extreme environments (elevated temperature, multiaxial, and irradiation). Data shortcomings were identified with respect to interpretation of concrete properties under (1) elevated temperatures (samples tested hot or cold, moisture migration state either free or restricted, specimens loaded or unloaded during heating, constituents and mix proportions varied, specimen size inconsistent, degree of specimen hydration varied, heatup rate and heat-soak duration varied, and limited basalt and serpentine aggregate concrete data available); (2) multiaxial loadings (different materials utilized, specimen preparation techniques varied, platen-specimen interface influenced results, instrumentation techniques varied and perhaps not of sufficient accuracy, and elevated-temperature data extremely limited); and (3) irradiation (technical and experimental difficulties encountered in conducting tests, different materials utilized, mix proportions varied, specimen size varied, temperatures differed, and cooling and dry conditions). Specialty concrete material systems (high-strength concrete, fibrous concrete, polymer concrete, elevated-temperature concrete, lightweight concrete, and refractory concrete) were overviewed and property data presented.

Based on an overview of concrete material systems for application to prestressed concrete pressure vessels (PCPVs) the following conclusions can be derived.

- Portland cement concrete property data for normal operating conditions is adequate (some additional multiaxial property data is desirable).
- Portland cement concrete property data for elevated-temperature conditions requires development, especially for basalt and serpentine aggregate concretes.
- Multiaxial concrete property data, especially at elevated temperatures, is required for development of improved constitutive relations for concrete.
- Additional data on the effects of irradiation on concrete properties are required.
- High-strength concretes (>41.4 MPa) have application to PCRVs, but they need to be investigated to define their mechanical behavior more clearly, to develop fracture criteria, and to assess current American Concrete Institute Code applicability.
- Fibrous concrete exhibits significant potential to effect improved PCRV performance at reduced costs as a result of property enhancements provided by the fiber reinforcement.
- Polymer concrete and lightweight concrete material systems have limited application to PCRVs because of high costs and poor hot strengths of the former and low strengths of the latter.
- Refractory concretes offer potential as thermal barrier (hot liner) materials for PCRVs.

3.3.2 Concrete Multiaxial Material Testing System

Results of the reviews that have been conducted on concrete properties in a nuclear environment[17,18] show that the availability of data representative of concrete behavior under multiaxial and thermal loadings likely to be encountered in a PCRV, particularly under postulated accident conditions, is somewhat limited. Conducting studies to develop supplemental data, however, requires the development of a relatively unique testing system; that is, the system must be capable of loading concrete specimens multiaxially in tension, in compression, or in a combination of tension and compression at either room or elevated temperatures. Activities during this period were directed toward developing a performance specification for such a system and fabrication of an enclosure for the test system.

3.3.2.1 Concrete Multiaxial Material Test System Performance Specification

The specification developed for a concrete multiaxial material testing system[19] consists basically of six major sections: (1) general requirements, (2) load frame assembly, (3) environmental system, (4) specimen development and actuator stroke instrumentation, (5) interactive computer control and data acquisition system, and (6) functional requirements of computer programs for system control data acquisition and analysis.

Requirements for the testing system are such that it shall be designed for imposition of static or cyclic loading profiles to 102-mm concrete cube specimens having their edges modified by a 3.2-mm 45° bevel. The closed-loop servohydraulic dynamic materials testing system shall be computer controlled, complete with a computer-controlled, variable-temperature environmental system, with instrumentation for feedback control and data acquisition, with a complete load frame assembly, and with computer system hardware and software. The test system design may be developed by using either a "fixed" or a "floating" specimen centroid. Control of loading shall be independent for each axis. The system shall also have the capability of cyclic loading.

The load frame assembly shall consist of components or assemblies as follows: (1) base frame and x, y, and z actuator assemblies, including hydraulic actuators, servovalves, load sensor, thermal barrier platens and self-alignment features, fixtures, and guide, and (2) hydraulic supply system, including hydraulic power supply, hydraulic service manifold, hydraulic servovalves, and required interconnected piping and/or hoses. The load frame assembly, except for the thermal barrier platens and brush platens, shall be designed to permit simultaneous loading in each of the x, y, and z orthogonal directions.

An electric-resistance heated environmental system that is computer controlled and temperature and power controlled shall be provided to enable a programmable, variable-temperature history within the system. The environmental system shall be partitioned to enable ready access for insertion and removal of specimens and for assembly and disassembly of actuator subassembly components and instrumentation. The

environmental system shall be designed to achieve a maximum temperature rise of 33°C/h with a controllable temperature range from 20 to 316°C.

Instruments for sensing displacement and/or deformation of the specimen shall be located such that movement of the center of each face of the cubic specimen can be sensed with respect to the center of the opposite face as a differential measurement or with respect to a fixed frame of reference. Components of the system penetrating the environmental system or external to it shall be designed to have either self-correction or demonstrable correction for any temperature gradient to which they are exposed. Specimen-computed strains and loading strokes for the x, y, and z axes shall be traceable to National Bureau of Standards references. Procedures shall be provided to ensure that the test specimen is properly positioned within the test system.

The computer system shall provide for closed-loop, real-time control and for simultaneous data acquisition of user-selected control profiles. It shall also provide for the processing of data and graphic display of computed parameters by either seller-supplied or by in-house-developed programs. The system shall consist of the following hardware: computer, random-access storage system, programmable function generator or equivalent software, environmental system power controllers or equivalent software, video terminal, and accessory facilities (interfaces, electronic modules, cables, cabinets, and other equipment necessary for the system to perform its functions as defined in the performance specification and to be a complete stand-alone system). To function as a closed-loop controller of the load frame assembly and the environmental chamber, the system shall generate electrical control signals, shall accept feedback from activated transducers, shall compare feedback from the controlled parameter with the controlled signal to form an error signal, and shall amplify the error signal for application to the control device, servovalve, and power controller in order to achieve the user-selected control profiles designated for the test specimen. Software requirements include an interactive operating system capable of closed-loop control and simultaneous data acquisition for the control profiles specified, data processing as specified, and a FORTRAN or BASIC incremental compiler to permit concurrent program deveolpment by two users. Diagnostic and debug routines shall be provided.

Compliance with provisions of the performance specification shall be demonstrated for transitional and static loading of test specimens according to prescribed procedures, which shall be provided. The prescribed loadings shall be designed so that the ability of the control program for various modes and sequences of loading (including strain, stroke, or load control, etc.) and for various sequences of heating and loading can be demonstrated. Software capabilities for plotting on the video terminal provided and a data plotter shall be demonstrated. The software shall include features such as logarithmic or linear scaling, labeling of axes with alphanumeric characters in user-selected engineering units, numbering of axis grids, sizing and locating of area covered by the plot, and tilting and noting of graph at user-selected positions. Provisions shall be made for representation of an arbitrary, noncyclic ascending temperature profile for heating control of the environmental chamber by user-designated assemblage of segmented vectors (ramp function) or by supervisory control (hardware module). Software capability shall also be provided for determining stress and strain invariants, octahedral normal stress and strain, octahedral shear stress and strain, effective stress and strain, deviatoric stress tensors, bulk modulus, shear modulus, Young's modulus, and Poisson's ratio. In addition, complete documentation, including drawings, wiring diagrams, operating and maintenance manuals, and source and object programs for software, shall be provided.

3.3.2.2 Test System Enclosure

Fabrication of the enclosure to house the concrete multiaxial testing machine has been completed (Fig. 3.1). The enclosure is required both to provide standard laboratory conditions so that data obtained will be meaningful and to protect the complex servohydraulic loading system and peripheral equipment from thermal fluctuations and contaminants that would impair their operation.

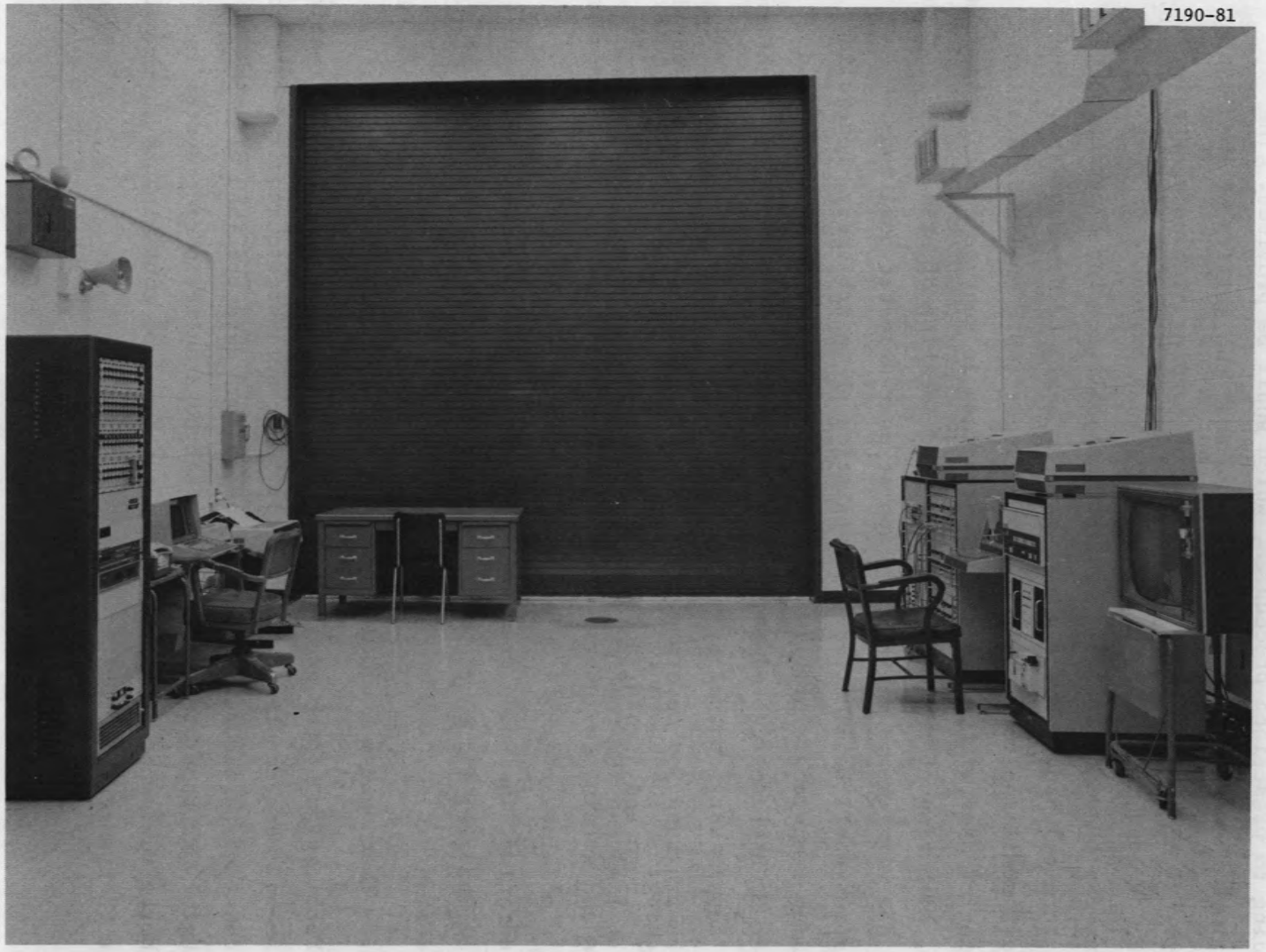

Fig. 3.1. Enclosure for concrete multiaxial material testing system.

3.4 INSTRUMENTATION EVALUATION AND DEVELOPMENT — D. J. Naus

An evaluation of the ability of acoustic emission (AE) to monitor structural elements has continued through laboratory studies. To develop a reservoir of data on AE, both steel and concrete structures are monitored. During this reporting period, the multichannel AE source location system (Fig. 3.2) was used to monitor a flawed, thick-wall thermal shock specimen (TSE-5A).

The thermal shock test series is being conducted under the Heavy-Section Steel Technology Program to reveal the behavior of inner-surface flaws in thick-wall steel cylinders subjected to severe thermal-shock loading conditions. Thermal-shock specimen TSE-5A was fabricated from ASTM A 508 class 2 steel plate. It was 1200 mm long with an outside diameter of 991 mm and a 152-mm wall thickness (Fig. 3.3). Contained on the inner surface was a flaw approximately 11 mm deep, which ran the complete length of the vessel. The flaw was placed in the test specimen by using a technique involving electron-beam welding and hydrogen-charge cracking.[20] The thermal shock was administered to the inner surface by first lowering the test cylinder, which was at an initial wall temperature of 92°C, into a container of LN_2 and suddenly releasing a nitrogen gas bubble from the interior cavity, allowing LN_2 (−196°C) to flood the cavity. Natural convection provided circulation of liquid upward through the central cavity and downward over the insulation on the outside of the specimen. Nitrogen vapor exited through the top of the tank containing the LN_2, and most of the entrained liquid fell back into the tank; LN_2 was added as required. A schematic of the test facility is shown in Fig. 3.4. Data obtained during the test included indications of crack initiation and arrest [crack-opening displacement (COD), AE, and ultrasonic transmission (UT) instrumentation], crack depth (COD and UT) and radial temperature distributions in the wall as a function of time.

Acoustic emission was used to monitor flaw propagation during thermal-shock testing of specimen TSE-5A. Four active sensors, positioned relative to the flaw as shown in Fig. 3.5, were used to monitor the entire vessel circumference. Sensors were located on the outer surface of the test specimen, where they were protected from the thermal shock by

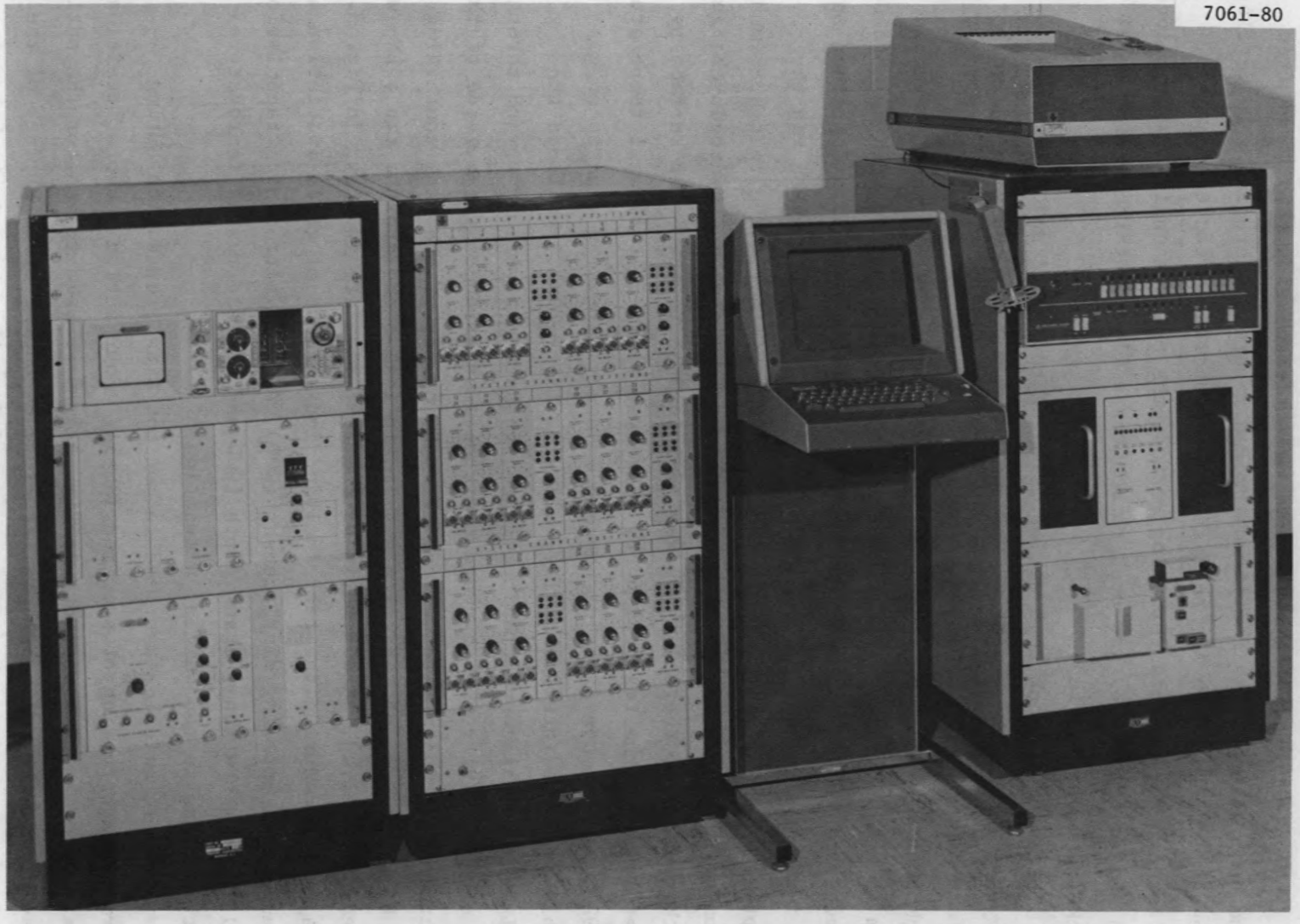

Fig. 3.2. Acoustic emission multichannel source location system.

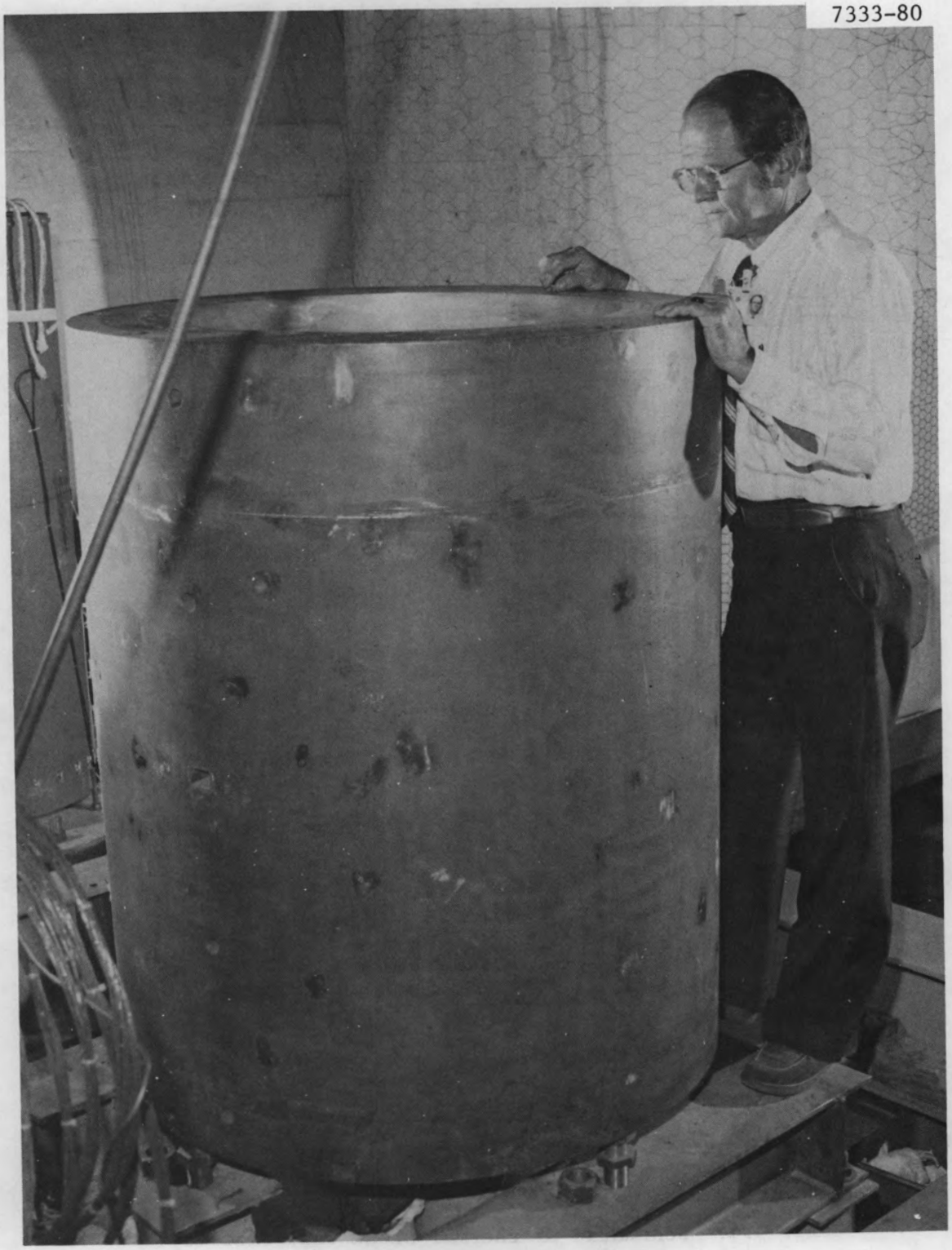

Fig. 3.3. TSE-5A thermal shock test specimen.

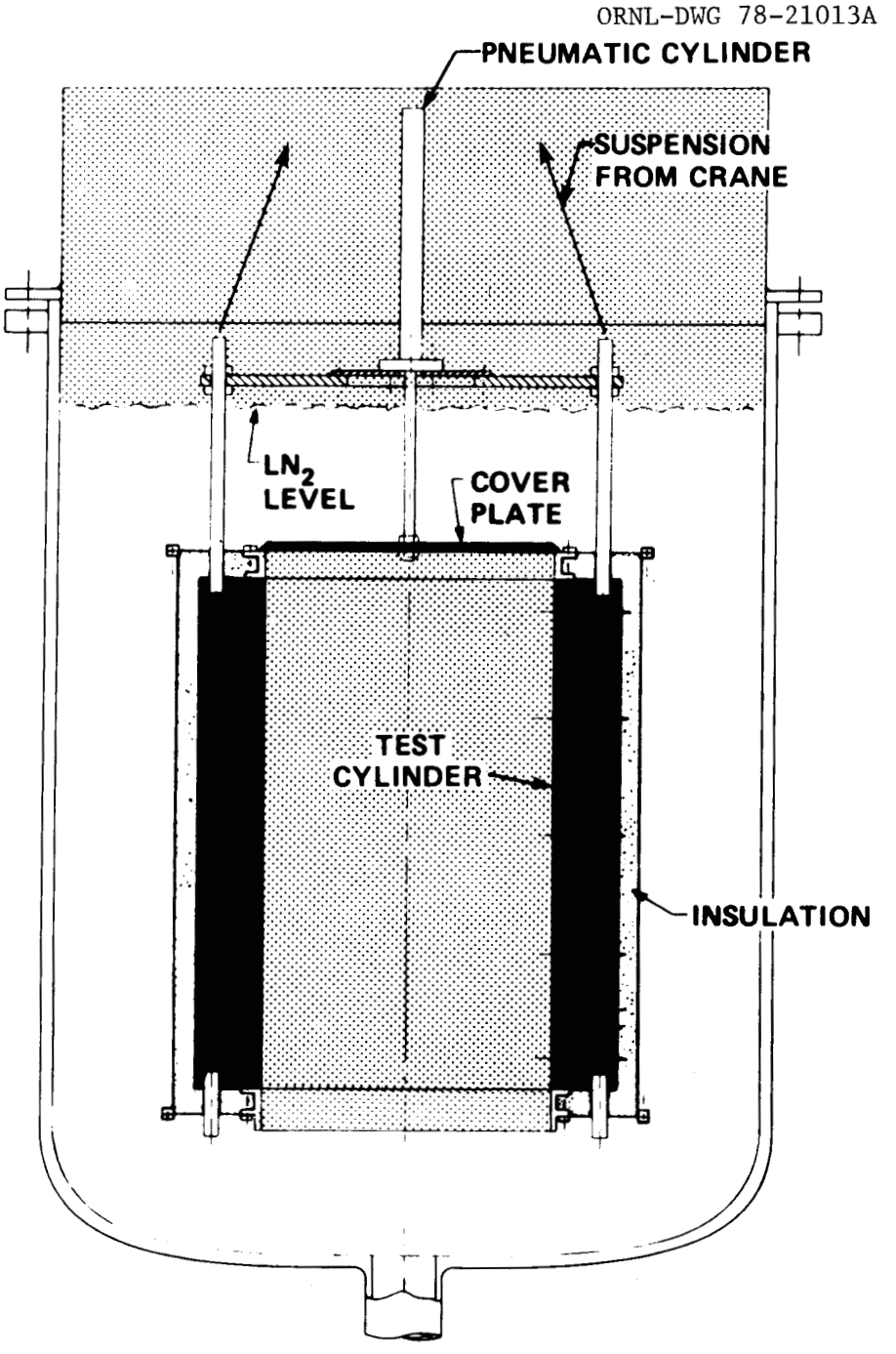

Fig. 3.4. Schematic of thermal shock test facility.

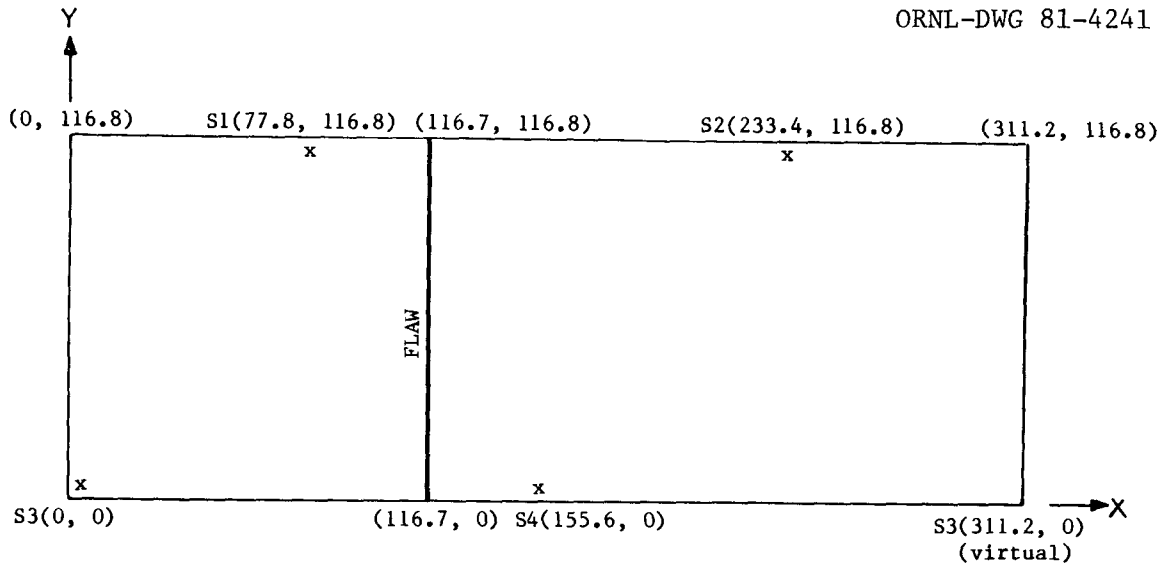

Fig. 3.5. Developed view of TSE-5A showing four sensor positions relative to the flaw. Coordinates are in centimeters.

insulation (Fig. 3.4). The sensors were attached to the specimen by use of a structural acrylic adhesive that had been shown to retain its bonding characteristics over the temperature range of interest (−196 to 92°C). Acoustic emission specifications during the test were

transducers — 300-kHz resonant frequency, differential;

filters — 200 to 800 kHz;

preamplifier gain — channel 1, 25 dB (65 dB total); channel 2, 27 dB (67 dB total); channel 3, 24 dB (64 dB total); and channel 4, 25 dB (65 dB total);

arrival time resolution — 0.5 μs;

threshold — 1.2 V; and

ΔT range selector — 500 μs.

Output of a COD gage was used as a parametric input to the AE system. Data as a function of elapsed time were also obtained during the test.

During AE monitoring of TSE-5A, a total of 780 valid events were recorded over the entire surface of the specimen. Figure 3.6 presents a 2-D grid display of event activity (upper number in each grid square corresponds to the total number of accepted events, and lower number is the summation of the magnitudes of the voltages of the events; A and B are scaling factors, with A = 1 and B = 10). Areas where significant AE

ORNL-DWG 81-4240

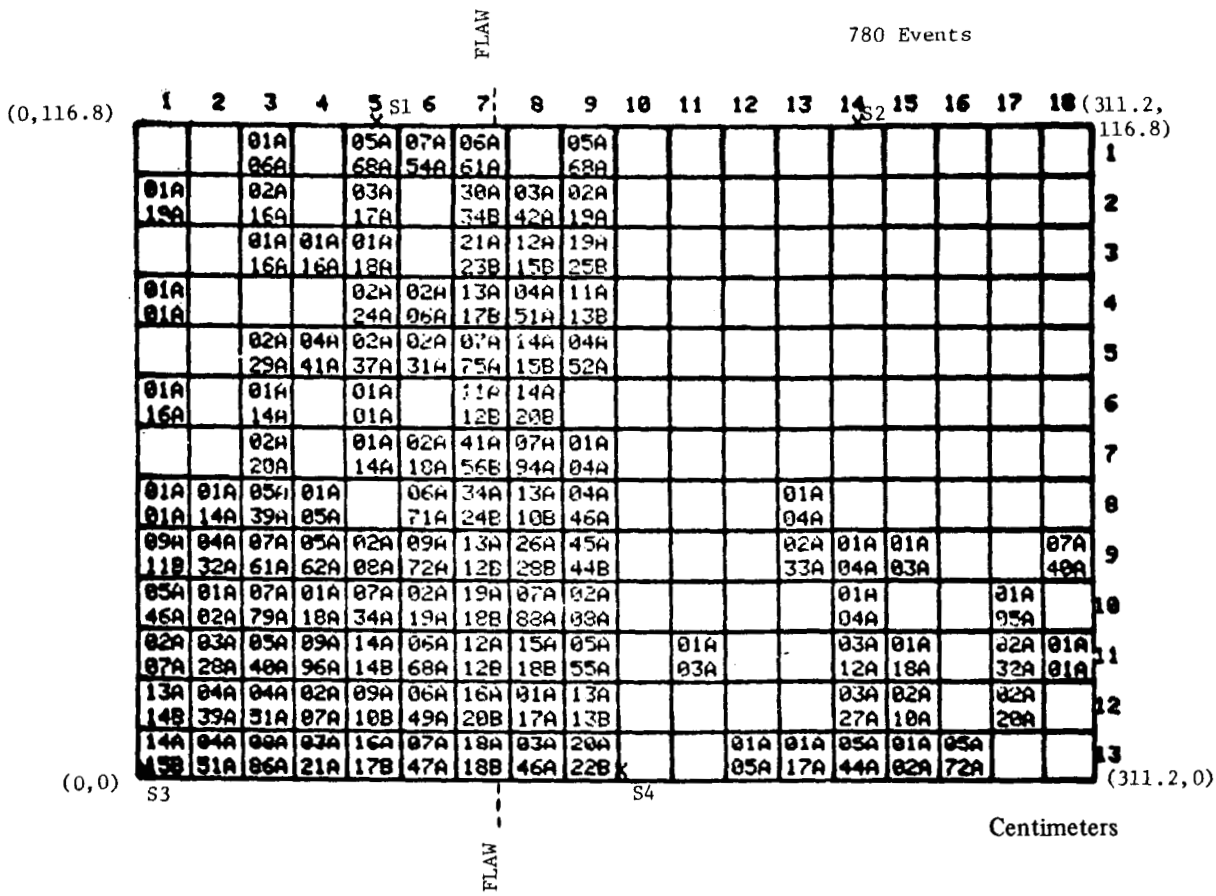

Fig. 3.6 Two-dimensional grid display of event activity. Upper number in each square of grid corresponds to total number of accepted events, and lower number, the summation of the magnitudes of the voltages of the events. *A* and *B* are scaling factors with *A* = 1 and *B* = 10.

activity occurred (high event count) were generally in the vicinity of the flaw, with 286 events occurring within ±100 mm (16.6% of the area monitored) of the flaw. Activity along the length of the flaw was relatively uniform except for the length of the flaw from y = 36 cm to y = 63 cm, where the event count was approximately twice that of the rest of the flaw length. The only area showing significant activity that was not immediately adjacent to the flaw was at a position corresponding to approximately x = 147 cm and y = 50 cm.

During the test, COD gage output indicated that four major initiation-arrest events (flaw growth) took place. The first two flaw jumps occurred simultaneously, with AE events having extremely large

oscillation counts; that is, the number of times the transducer output voltage flip-flopped (back and forth across the threshold of 1.2 V) was in excess of 10,700 times. During jumps three and four, the events occurred so rapidly and over such a short time that the system saturated (locked itself out to further event activity such as that which occurs when a leak develops in a pressurized system) and had to be manually reset. As shown in Fig. 3.7, the majority of recorded events occurred at a relatively uniform rate after the flaw jump-ins, when the activity was of lower intensity and frequency of occurrence. Events recorded thus reflected that inelasticity occurred in the region of the flaw, possibly the result of ligament tearing or flaw relaxing as the temperature stabilized. Peak voltages of events recorded during the test were extremely large, averaging 10.5 V per event. (For AE monitoring of a vessel of similar geometry that was slowly pressurized to failure, the maximum peak voltage obtained was approximately 5.8 V, with the majority of values being less than 2 V. This was for amplifier gains of 83 to 96 dB as compared with gains of 64 to 67, which were used for monitoring TSE-5A.)

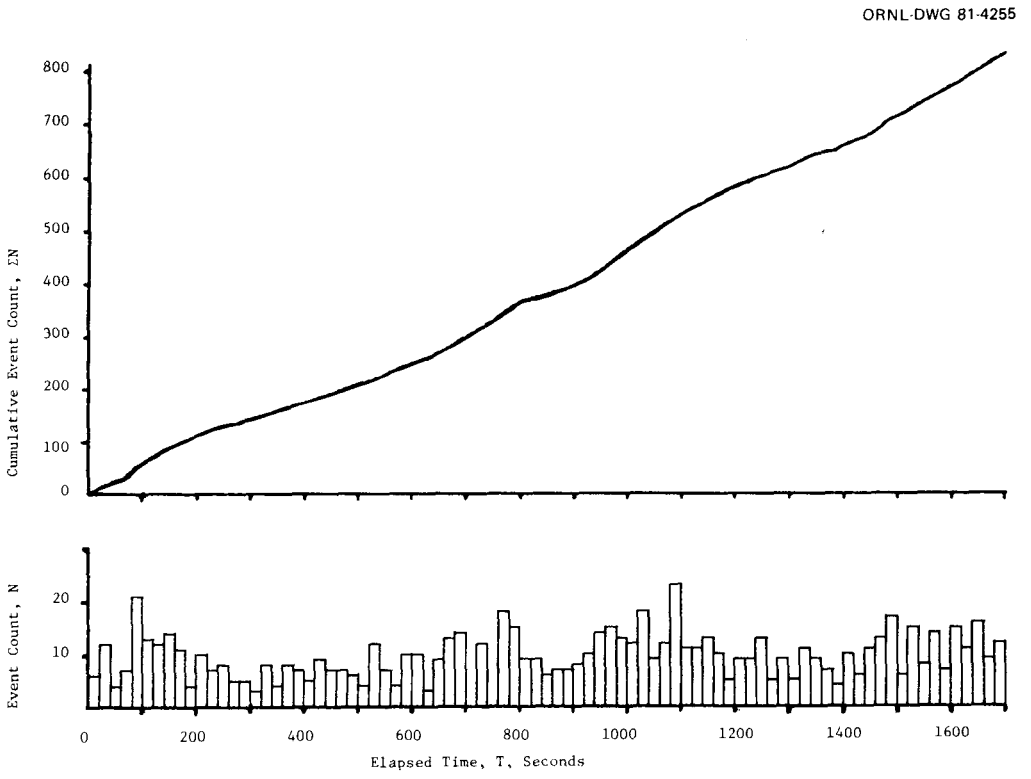

Fig. 3.7 Event count and summation versus elapased time.

3.5 STRUCTURAL MODEL TESTS — C. B. Oland and D. J. Naus

The objective of this task is to conduct PCRV—related model tests in support of the development of reference and advanced HTGR plant designs. Model tests are required for PCRV development to (1) verify elastic response as predicted by design analysis, (2) determine structural response to overpressurization, (3) permit design optimization, (4) justify taking exceptions to design code conservatism, and (5) support licensing. In line with this objective, two activities have been undertaken during this reporting period: (1) a review of PCRV-related structural model tests and (2) development of model testing techniques.

3.5.1 Review of PCRV—Related Model Tests

A review of the literature was conducted to establish the state of the art of PCRV-related structural model tests. The report developed[21] consists of eight sections:

- requirements for PCRV structural model testing (U.S., British, and French PCRV codes);
- model testing methods (direct and indirect);
- structural model types (true-to-scale, slightly simplified, distorted, and small prototype);
- materials for structural models (selection criteria);
- size effects (material effects, scale selection, and overview of investigations conducted to evaluate size effects);
- instrumentation for model testing (selection criteria and typical devices);
- hydraulic versus pneumatic pressure loading of models (pressurized flaw effects and summary of results of investigations conducted to determine effects of the pressurizing medium);
- review of model tests (overview of results for single-cavity PCRV models, multicavity PCRV models, end-slab models, closure models, and thermal and moisture migration models).

More detailed information is in the report.[21]

3.5.2 Development of Model Testing Techniques

Based on results of previous model tests and the review of PCRV-related model tests, we established that two areas require additional

development: wire-winding of models and nonleak liner systems. A test program was therefore initiated to establish satisfactory methods for circumferentially prestressing PCRV models ranging in scale from about 1/30 to 1/10 and for lining the models so that they do not prematurely leak to terminate a test. Associated with this activity is an evaluation of the ability of fibrous concrete to produce cost- and performance-effective PCRVs. Verification of the techniques developed will be made through two models, which will be fabricated and tested to failure. Because one of the two models tested is to be fabricated from fibrous concrete, the results obtained will also provide an indication of the effectiveness of fibrous concrete for application to PCRV construction.

Activities during this reporting period have been focused primarily on development of a fibrous concrete mix that meets strength and workability requirements and on definition of the model tests to be conducted.

3.5.2.1 Fibrous Concrete Evaluations

Background. An evaluation of the merits of fibrous concrete for application to PCRVs was initiated on the basis of results of an overview of candidate construction materials for application to PCRVs[22] and the suggestion in ref. 23 that chopped-wire fiber concrete be used to reduce concrete volume requirements.

Fiber-reinforced concrete consists of plain concrete to which small cross-section steel fibers (0.5 to 2.0 vol %) are added during the mix process. Addition of the fiber reinforcement enhances concrete's material properties by increasing the "first crack flexural strength," direct tensile strength, impact and spalling resistance, fatigue strength, thermal conductivity, and ductility.[24] Although addition of fibers to the mix increases the material cost, enhanced properties of the concrete will potentially produce a PCRV that is cost-effective as a result of reduced material and labor requirements.

Testing Program for Fiber-Reinforced Concrete. A testing program[25] was prepared to demonstrate the advantages of fiber-reinforced concrete over the conventional plain concrete used for PCRV applications. Included in the test program were 11 tasks designed to provide the basis for developing fibrous concrete to the point of verifying its cost and

performance effectiveness for application to PCRVs: (1) mix design, (2) placement demonstration, (3) mechanical property tests, (4) analytical development, (5) PCRV model tests, (6) analytical comparisons with plain concrete models, (7) failure comparisons with plain concrete models, (8) elevated-temperature property tests, (9) combined load tests, (10) design recommendations, and (11) an economic assessment. Based on discussions with the General Atomic Company (GA), we decided to reduce the scope of the investigation so that it could be combined with the development of model testing techniques, at least initially. This reduced scope has the advantages: (1) the study can be pursued at a minimal incremental cost because a model test is required to demonstrate the model-testing techniques developed and (2) results obtained from a fibrous concrete model test will provide data to determine if fibrous concrete is sufficiently cost- and performance-effective that the next phase of the test program should be pursued. Thus, phase 1 of the fibrous concrete testing program is the development of a mix that satisfies current PCRV concrete property requirments for strength (≥55 MPa), modulus of elasticity (≥38 GPa), and workability (slump ≥ 102 mm).

Trial Mix Results. Fourteen trial batches of plain and fibrous concrete were prepared to determine cement factors, water-to-cement ratios, maximum aggregate size and quantities, fine aggregate quantities, water-reducing agent type and quantities, fiber content (fibrous mix), and mix procedures required to produce mixes meeting the property requirements cited above (ref. 26 was used as a guide for preparing the trial batches). Materials used for the mixes were typical of those used for production of high-strength concretes (>41.4 MPa) for construction applications. Briefly, the materials consist of

cement — type II portland, conforms to ANSI/ASTM C 150-78a;

flyash — class F, conforms to ANSI/ASTM C 618-78;

aggregates — limestone, crushed and oven dried, 19-mm maximum size coarse aggregate, conforming to ANSI/ASTM C 33-78;

admixture — water reducing, conforming to ANSI/ASTM C 494 type A;

water — laboratory, potable; and

fibers — collated steel with 50-mm-long, 0.50-mm-diam, 1170- to 1380-MPa yield strength hooked ends (Fig. 3.8).

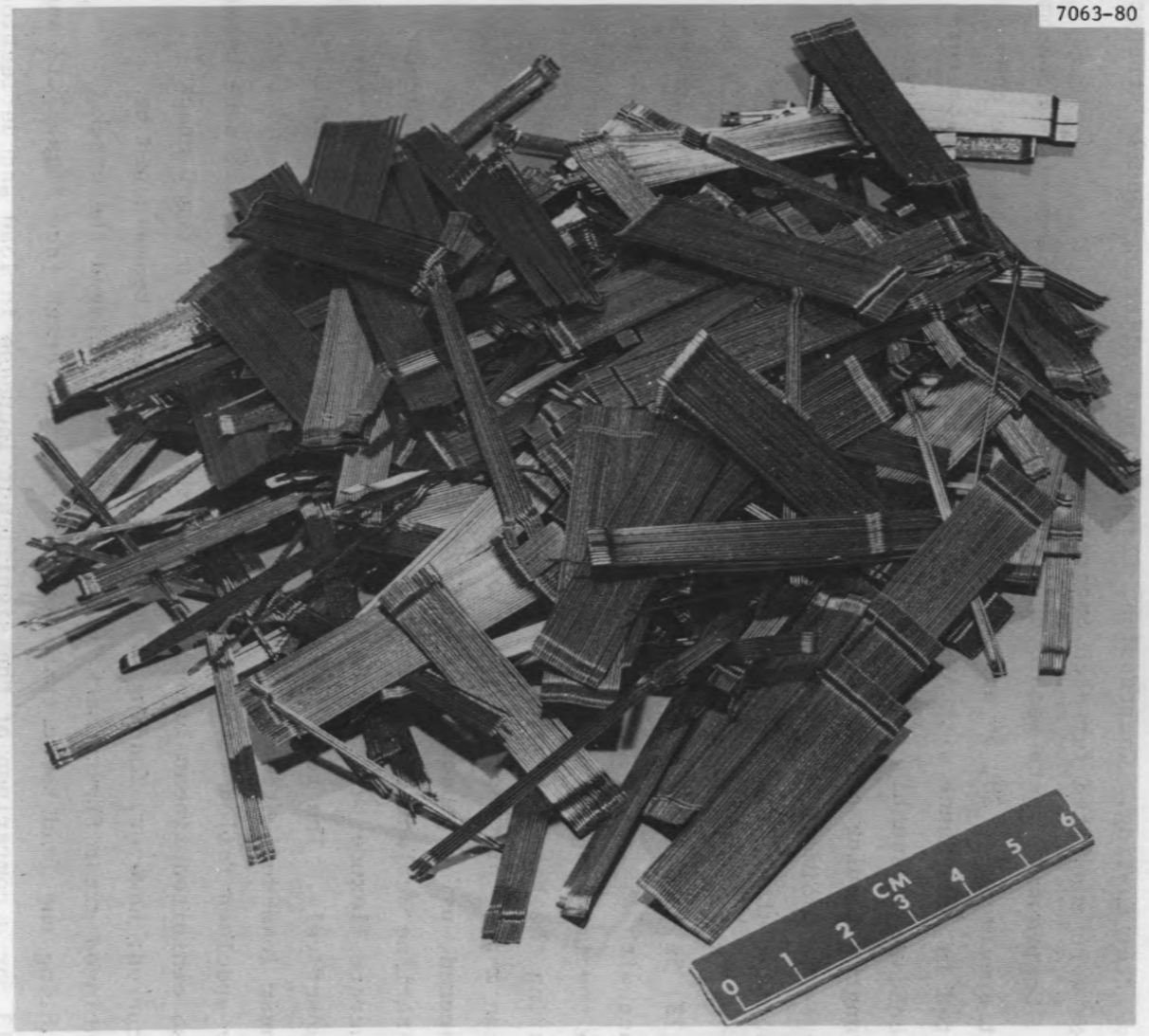

Fig. 3.8. Steel fiber reinforcement.

Plastic concrete properties determined for each trial batch included slump, unit weight, air content, and Vebe time (fibrous concrete mixes only). Eighteen specimens (nine compression, six flexure, three splitting tensile) were cast from each concrete batch. Specimens were cured in a saturated limewater solution until they were tested at either 28, 56, or 90 d after casting. Compression, flexure, and splitting-tensile strength tests were conducted for each concrete batch.

Compressive tests were conducted on cylindrical 152-mm-diam, 304-mm test specimens at 28, 56 and 90 d after casting. The tests were conducted in accordance with ANSI/ASTM C 469-65, using the compressometer-extensometer assembly shown in Fig. 3.9. Stress-strain, compressive strength, modulus of elasticity, and Poisson's ratio data were obtained for each specimen. A comparison of plain and fibrous concrete test specimens after failure in compression is presented in Fig. 3.10.

Flexure tests were conducted on beam specimens 152 × 152 × 559 mm at 28, 56, and 90 d after casting. The tests were conducted in accordance with ANSI/ASTM C 469-65, using the apparatus shown in Fig. 3.11. The specimens were loaded to failure in third-point loading. During testing the beam centerline deflection was obtained and recorded on an x-y-y' plotter as a function of load. Flexure strength was computed, using procedures in ANSI/ASTM C 78-75. Typical load-centerline deflection curves obtained from a plain and from a fibrous concrete flexure test specimen are presented in Figs. 3.12 and 3.13, respectively. The results show that the plain concrete beams exhibited linear load-deflection response until a first crack occurred and that the specimen failed (broke into two pieces). The fibrous concrete beams also exhibited linear load-deflection response until a first crack occurred; however, loading of the fibrous concrete beams could be continued after first crack because the fibers bridged the crack, enabling the load to be transferred across the crack [see Figs. 3.12 and 3.13 for a comparison of the significant increase in load and deflection (ductility, toughness) that the fibers impart]. The effect of fiber content in a particular mix was to change the shape of the

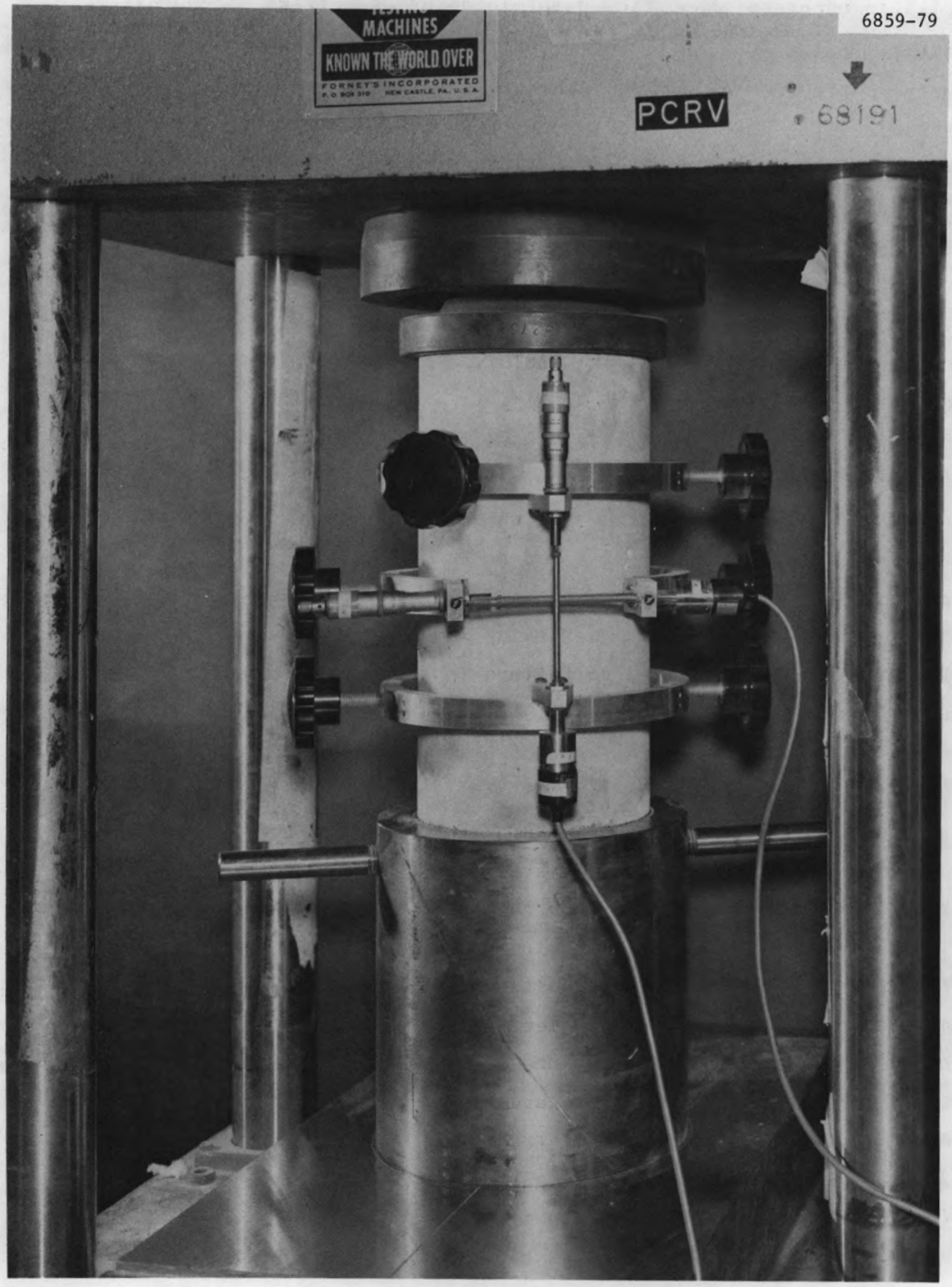

Fig. 3.9. Compressometer-extensometer compression test setup.

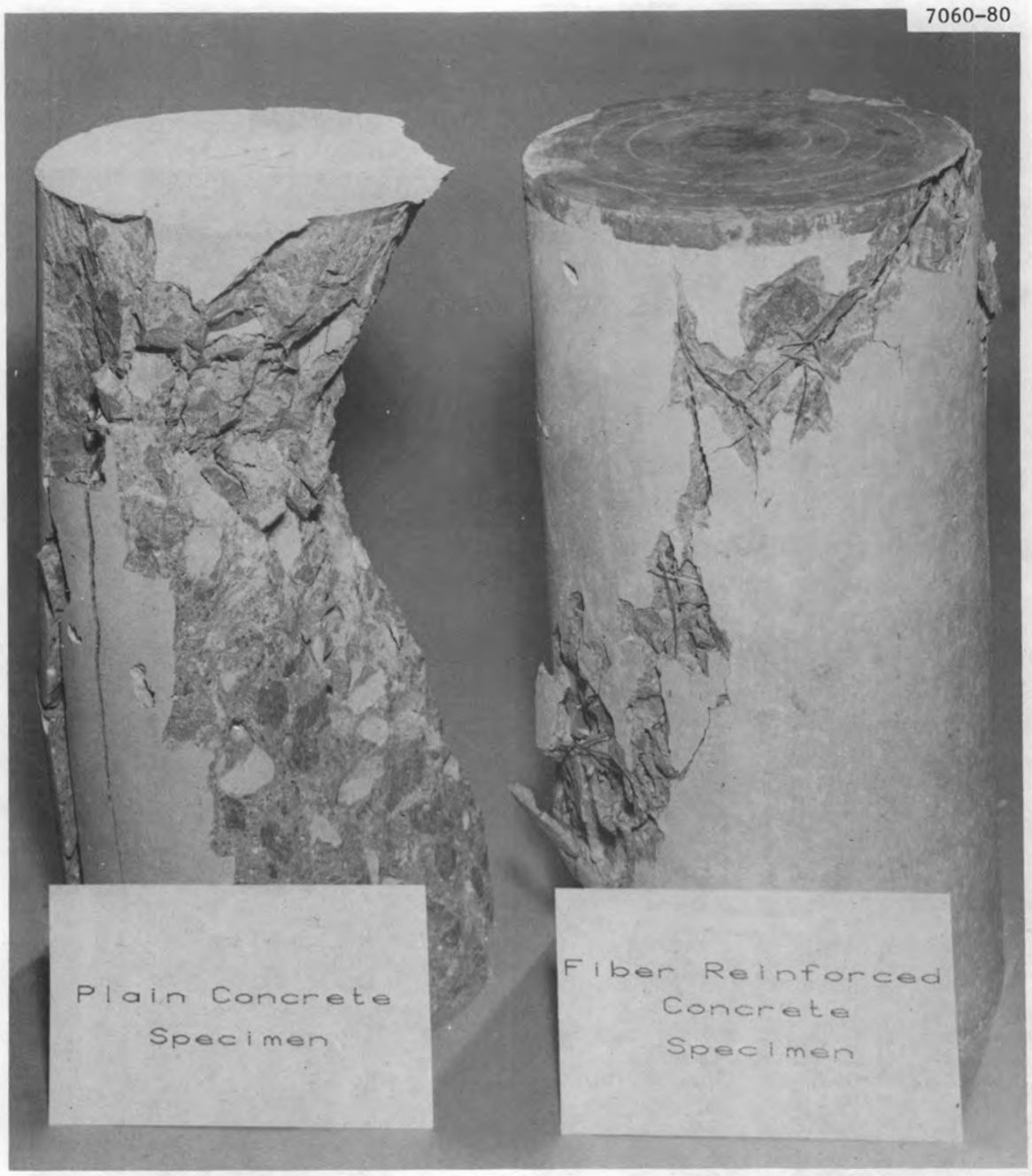

Fig. 3.10. Plain and fiber-reinforced concrete compression test specimens after testing.

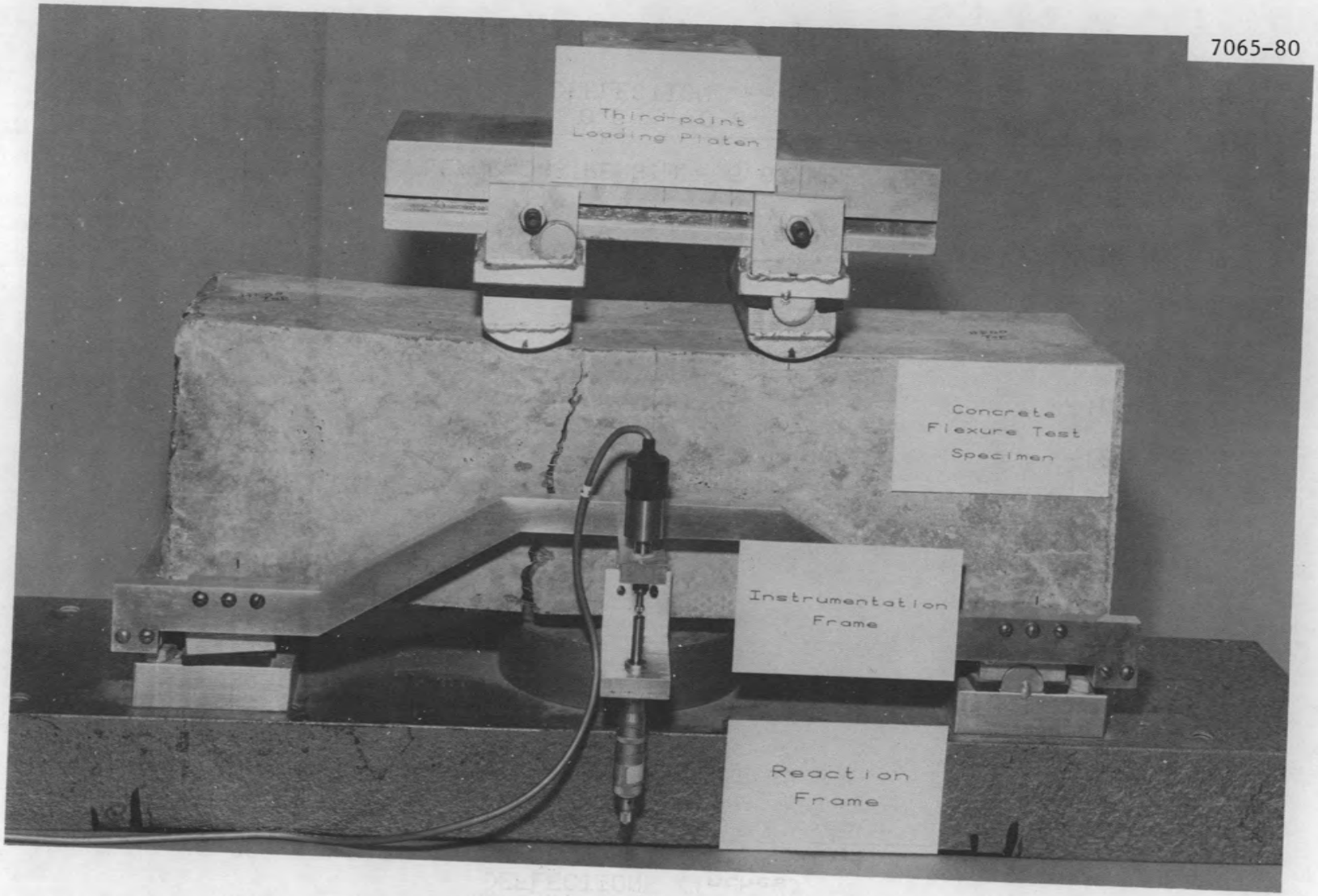

Fig. 3.11. Test apparatus for flexure beams.

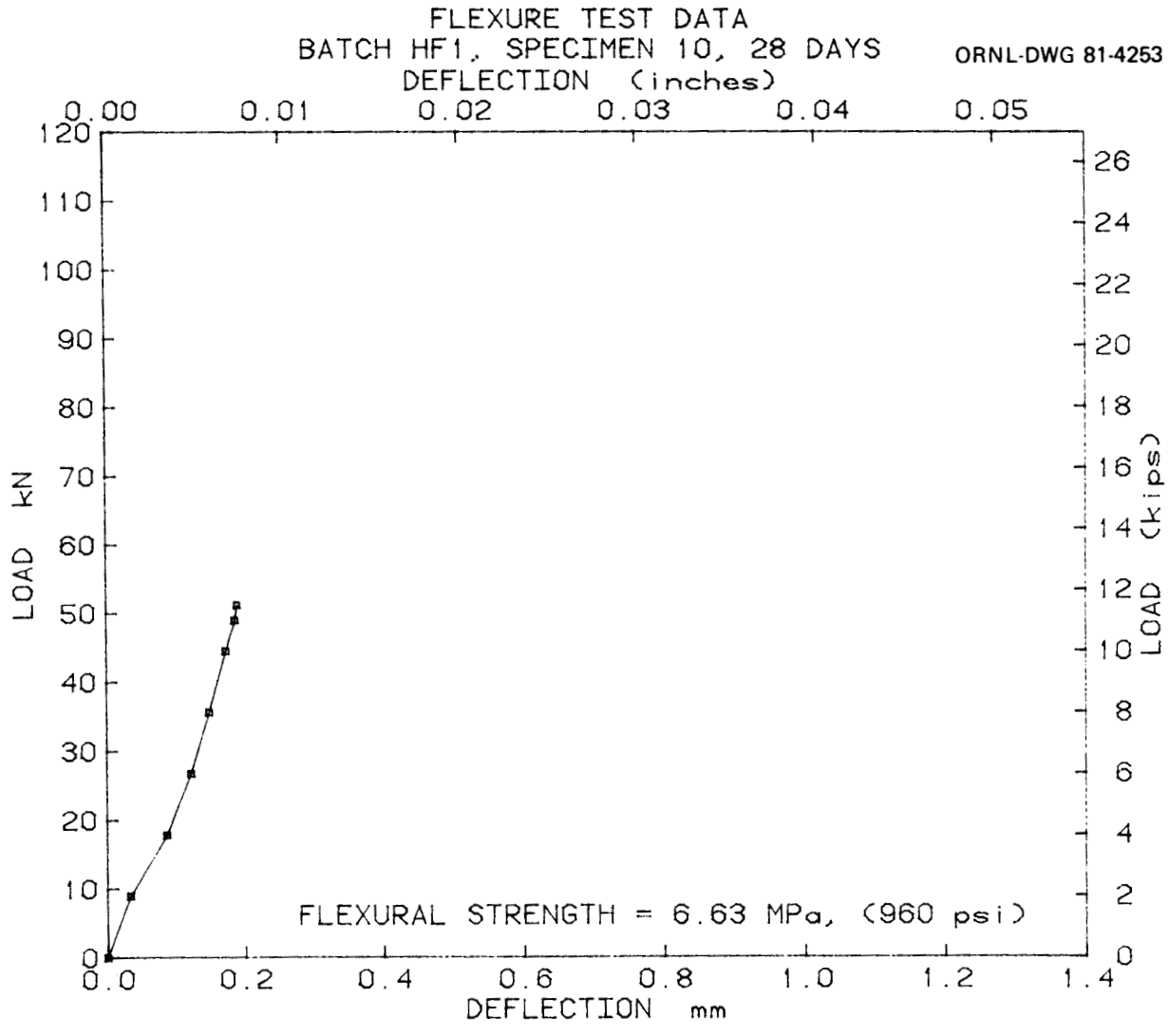

Fig. 3.12. Load-deflection response of plain concrete beam.

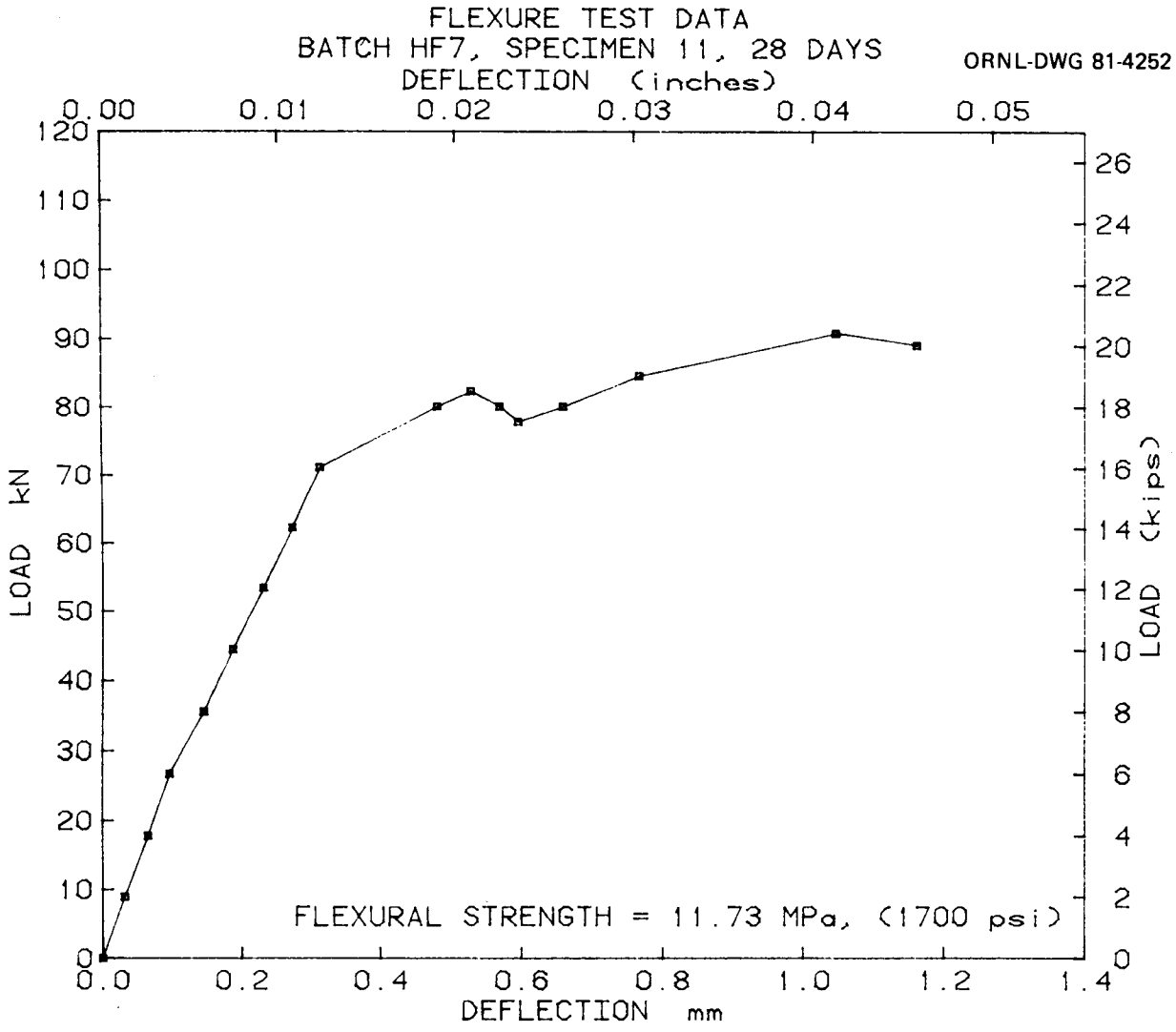

Fig. 3.13. Load-deflection response of fiber-reinforced concrete beam.

load-deflection curve and the flexure strength. Figure 3.14 presents failed sections* of beams, which had fiber contents ranging from 0 to 89 kg/m^3.

A second indication of the tensile strength of the mixes was determined by conducting splitting-tensile tests on cylindrical 152-mm-diam by 152-mm test specimens in accordance with ANSI/ASTM C 496-71. Splitting-tensile strength tests were conducted only at a concrete age of 90 d. Although the test is used as an indication of concrete's tensile strength, it is an indirect method because the specimen is actually loaded in compression as shown in Fig. 3.15. The plain concrete specimens failed abruptly at first crack and separated into two pieces at maximum load; however, the fibrous concrete specimens remained intact at first crack and continued to accept load until a maximum load was reached. [Even though this test method does not actually reveal the ultimate tensile strength of the fibrous concrete because it is valid only to first cracking (elastic), it does provide an indication of the ductility imparted to a concrete mix as a result of the addition of fibers.] Figure 3.16 presents a comparison of plain and fibrous concrete specimens at the conclusion of a splitting-tensile strength test.

Mechanical property and workability results obtained from the plain and fibrous concrete mixes were used to determine recommended mixes for fabrication of PCRV models to demonstrate the validity of model-testing techniques being developed. Table 3.1 presents mix designs and property data for these mixes.

3.5.2.2 PCRV Model Technique Validation Studies

A PCRV model test is being designed to demonstrate the (1) validity of procedures developed for wire-winding PCRV models and (2) that the PCRV liner system developed will not leak prematurely during pressure testing of a model to failure. Two models such as shown in Fig. 3.17 will be fabricated and tested: a plain concrete model and a fibrous concrete model fabricated by using the mix designs in Table 3.1

---

*The plain concrete beam (0 fiber content) failed as shown at first crack. The fiber-reinforced beams had to be subjected to several flexure load reversals to separate the beam halves completely.

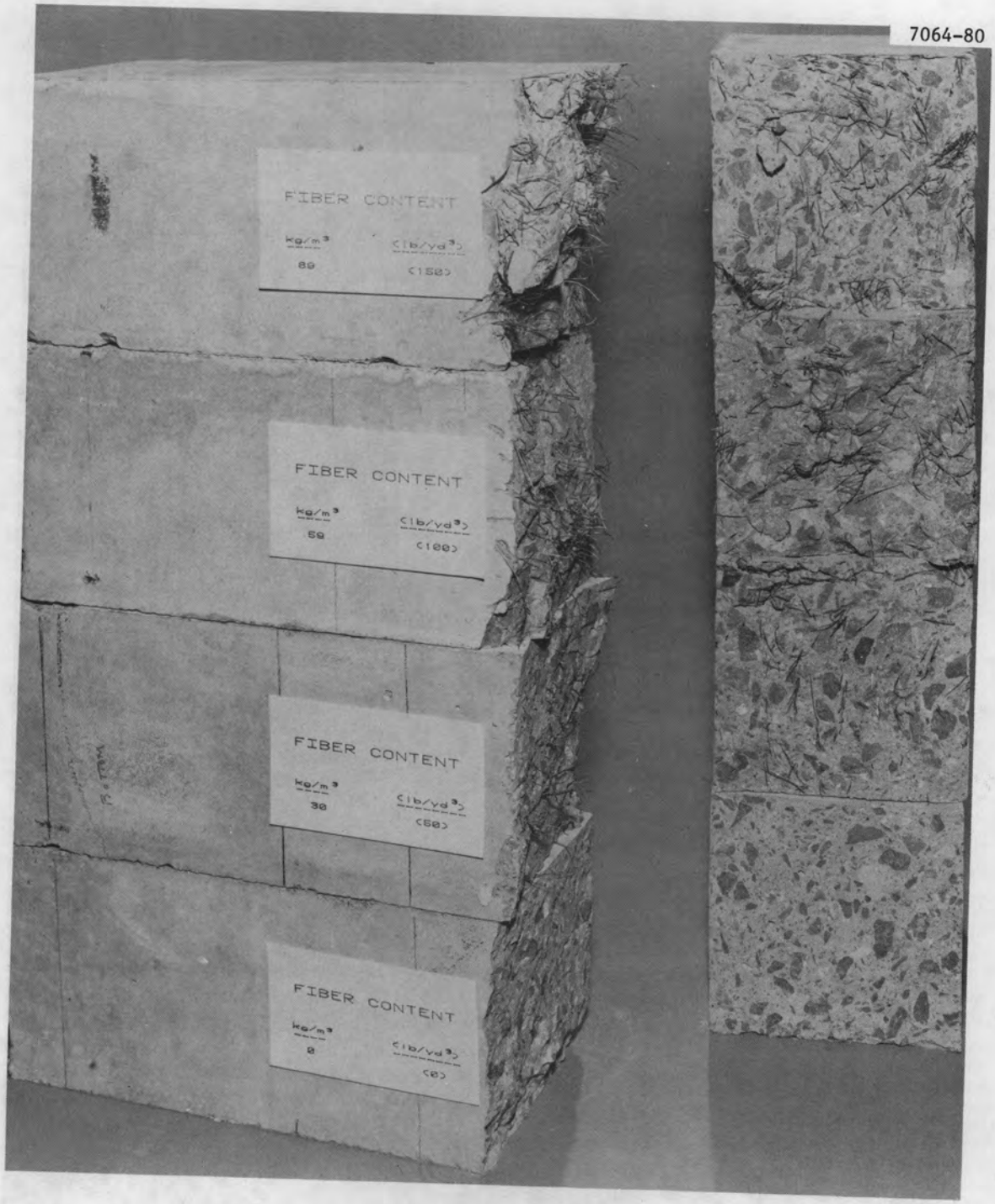

Fig. 3.14. Flexure test specimens with various amounts of steel fiber reinforcement.

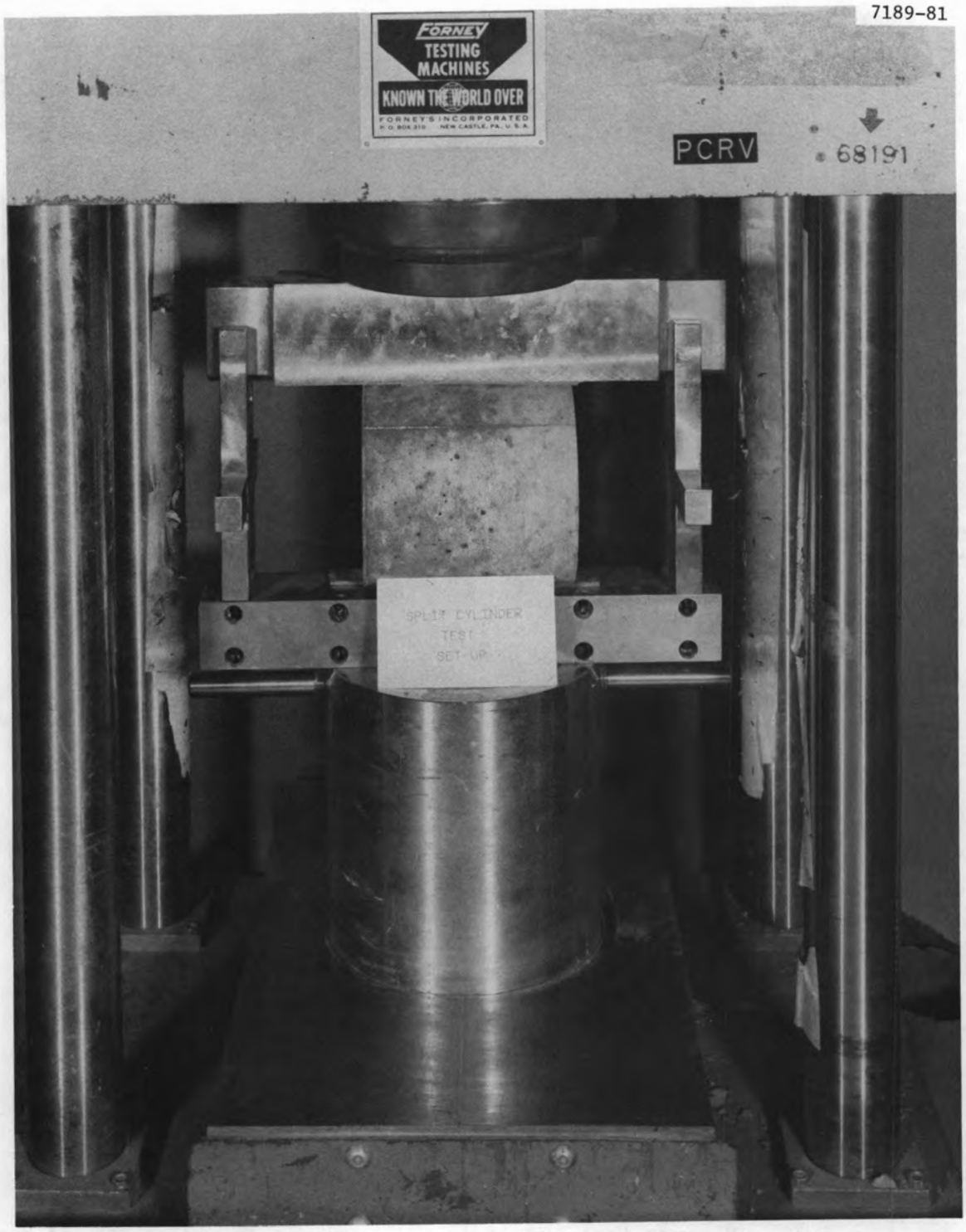

Fig. 3.15. Splitting-tensile strength test setup.

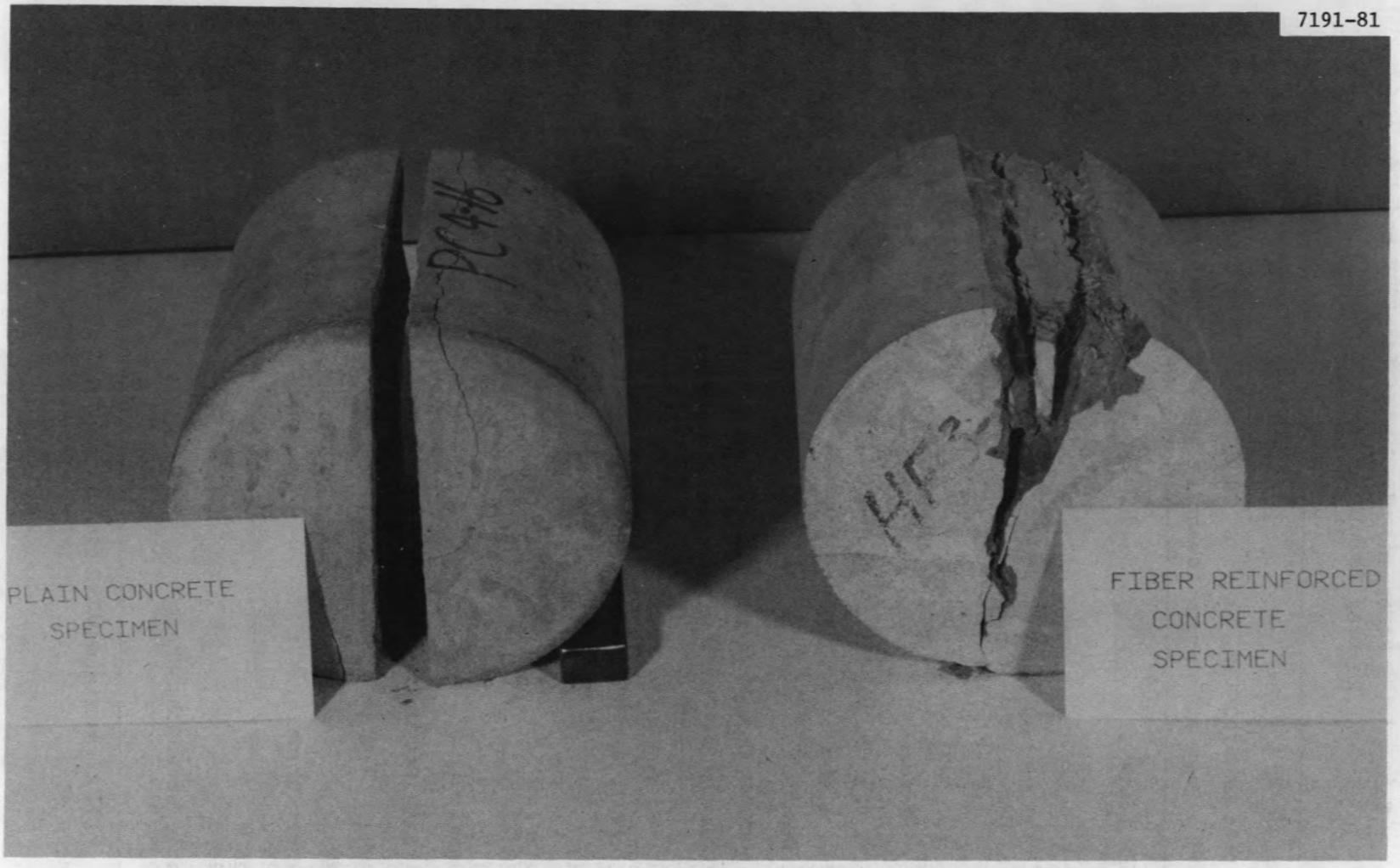

Fig. 3.16. Plain and fiber-reinforced concrete splitting-tensile strength specimens after testing.

Table 3.1. Recommend mix design for PCRV model testing technique verification

Material or property	Type concrete	
	Plain (quantity per m^3)	Fibrous (quantity per m^3)
Cement (type II)	529 kg	530 kg
Fly ash	67 kg	67 kg
Sand	621 kg	622 kg
Gravel[a]	931 kg	932 kg
Fibers	0 kg	88 kg
Water	238 kg	239 kg
Admixture	794 ml	796 ml
Slump	146 mm	127 mm
Unit weight	2387 kg/m^3	2476 kg/m^3
Air content	1.1%	2.0%
Vebe time		4 s
Compressive strength, MPa		
28 d	55.5	56.1
56 d	62.5	66.7
90 d	62.7	69.6
Modulus of elasticity, GPa		
28 d	34.1	37.2
56 d	36.9	41.0
90 d	40.3	42.4
Poisson's ratio		
28 d	0.21	0.24
56 d	0.23	0.27
90 d	0.26	0.26
Flexure strength, MPa		
28 d	6.34	12.03
56 d	6.69	10.65
90 d	7.38	10.51
Tensile strength, MPa		
90 d	4.72	7.79

[a]191 mm maximum size for plain mix; 95 mm maximum size for fibrous mix.

Fig. 3.17. Prestressed concrete reactor vessel model.

The liner system for each test will consist of a flanged head to which a skirt section is joined. Use of the flanged head will eliminate the corner joint, which has been a weak point in previous liner designs. Material used for the liner will be a 12-gage AISI 1008 drawing-quality steel.

Axial prestressing will utilize 19-mm-diam A 722 type I bars. Techniques for stressing the bars and for circumferentially prestressing the model are being developed.

Design of the mold for casting the models has been completed and will incorporate provisions for the two prestressing systems and for the liner system. A minicomputer-controlled data acquisition system (Fig. 3.18) has been modified so that it can accept 80 channels of instrumentation. Design of the instrumentation layout for the model test has been completed. A pressurization system capable of hydraulically loading the model to 62 MPa is being developed. The models will be tested in the PCRV model test facility (Fig. 3.19) located in Building K-702 at the Oak Ridge Gaseous Diffusion Plant.

3.6 LINER AND PENETRATION STUDIES — D. O. Hobson, R. K. Nanstad, and D. A. Canonico

Testing continued during the past year on weldments for steel penetrations and closures of the liner system for the PCRV for the HTGR. In the previous annual report,[27] data for the W-3 weldment were reported and discussed in detail. The W-3 weldment is the first, followed by W-5 and W-1, in the list of identified priorities in the testing sequence for the liner materials. Additional tests have been performed on the W-3 weldment material including drop-weight, dynamic precracked Charpy, and compact tests of the weld material and the heat-affected zones (HAZs). Testing of the W-5 weldment is also under way.

Drop-weight testing was effected with six specimens in accordance with ASTM E 208-69, *Standard Method for Conducting Drop-Weight Test to Determine Nil-Ductility Transition Temperature of Ferritic Steels*. The nil-ductility temperature (NDT) was found to be -80°C for impact perpendicular to the welding direction (in which case the cracks on the tension surface propagate parallel to the welding direction). In order for this

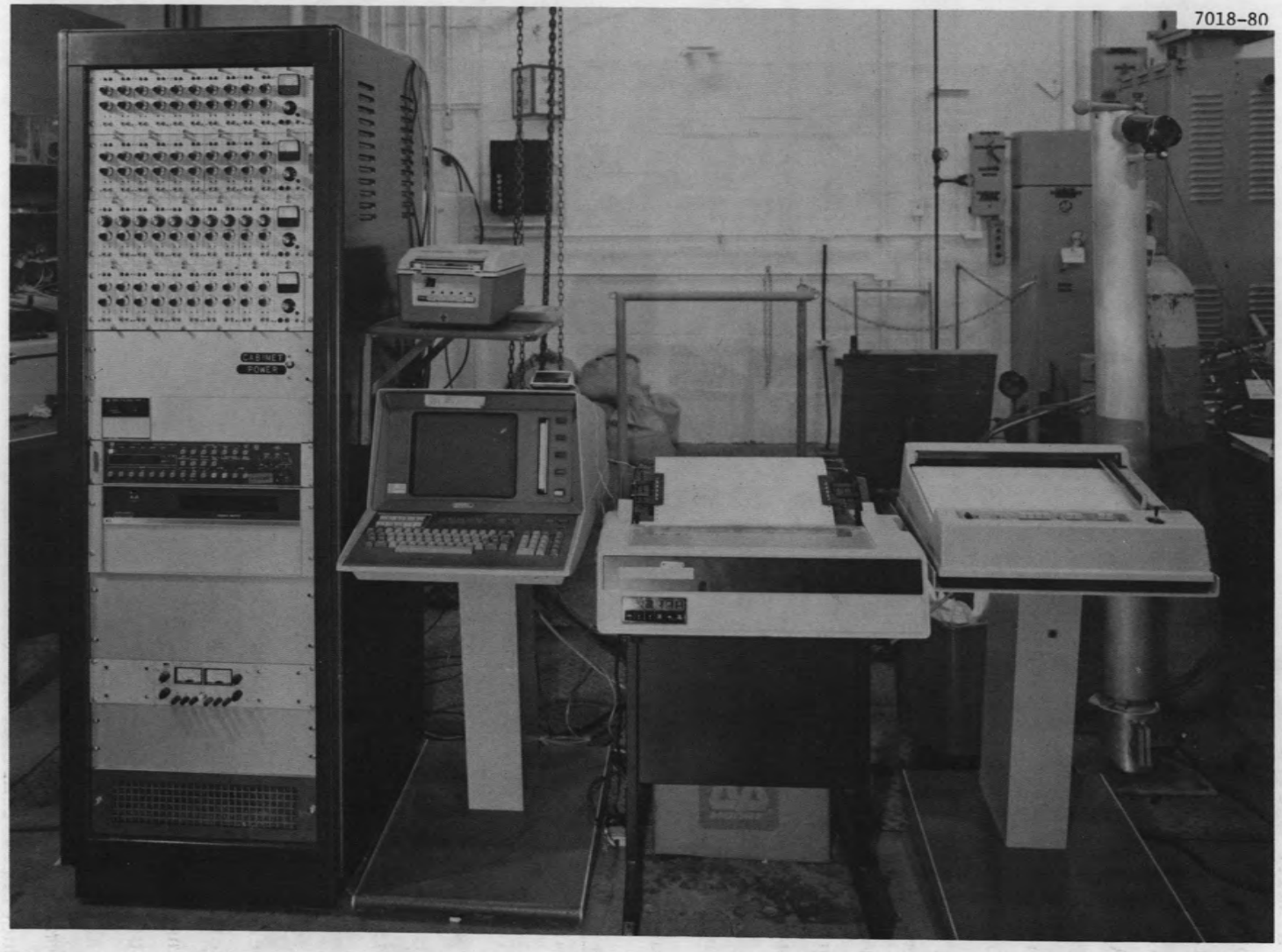

Fig. 3.18. Microcomputer-controlled data acquisition system.

Fig. 3.19. Interior of prestressed concrete reactor vessel model test cell as viewed from the top opening.

NDT to be equal to RT_{NDT},[28] two specific criteria must be met. Three Charpy V-notch impact (C_V) tests conducted at NDT + 33°C (60°F) must each exceed 68-J (50-ft-lb) absorbed energy and 0.89-mm (0.035-in.) lateral expansion. Two C_V tests were conducted at NDT + 33°C = −47°C. Both failed the criteria, one with 73.4 J (54 ft-lb) and 0.81 mm (0.032 in.) and the other with 39.4 J (29 ft-lb) and 0.37 mm (0.014 in.). Therefore, the NDT of −80°C established by the drop-weight test is not a valid RT_{NDT}, and retesting at that temperature is precluded by the ND-2300 criteria.[20] Additional C_V tests of the W-3 weld metal will be conducted at temperatures higher than NDT + 33°C (60°F) to define RT_{NDT}.

Additional dynamic precracked Charpy fracture toughness tests were preformed in both the plate HAZ (PHAZ) and the forging HAZ (FHAZ) and in the root weld metal of the W-3 weldment. These tests augment the results reported in the previous annual report. Figure 3.20 shows the fracture toughness data and an estimated transition curve for the PHAZ. Figure 3.21 shows the fracture data for the FHAZ. A large amount of scatter is apparent in the data so that a lower bound curve is believed to be

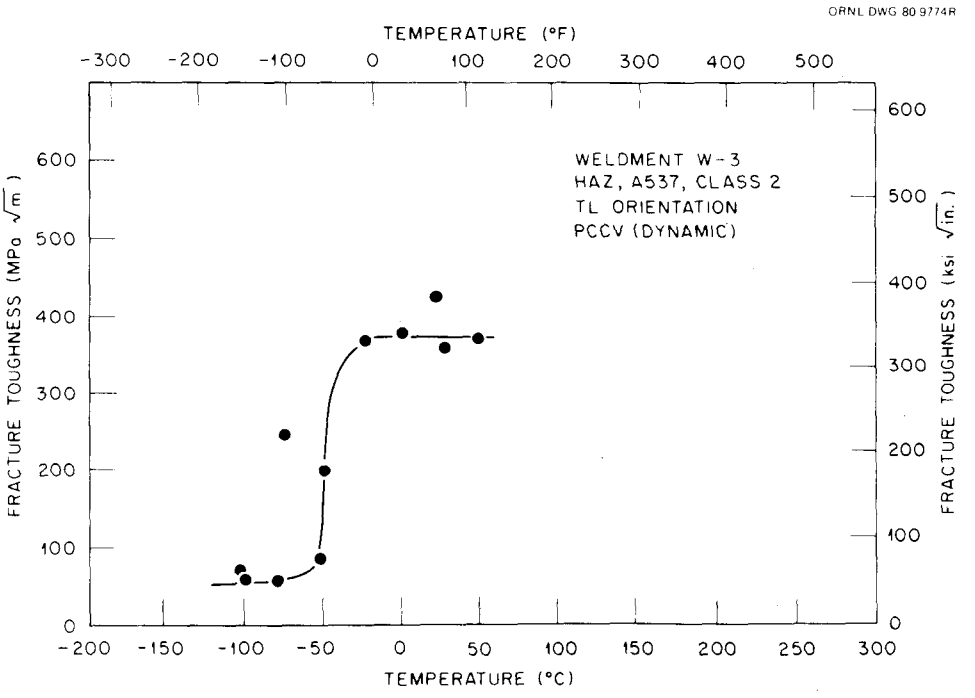

Fig. 3.20 Dynamic precracked Charpy fracture toughness of plate heat-affected zone, weldment W-3.

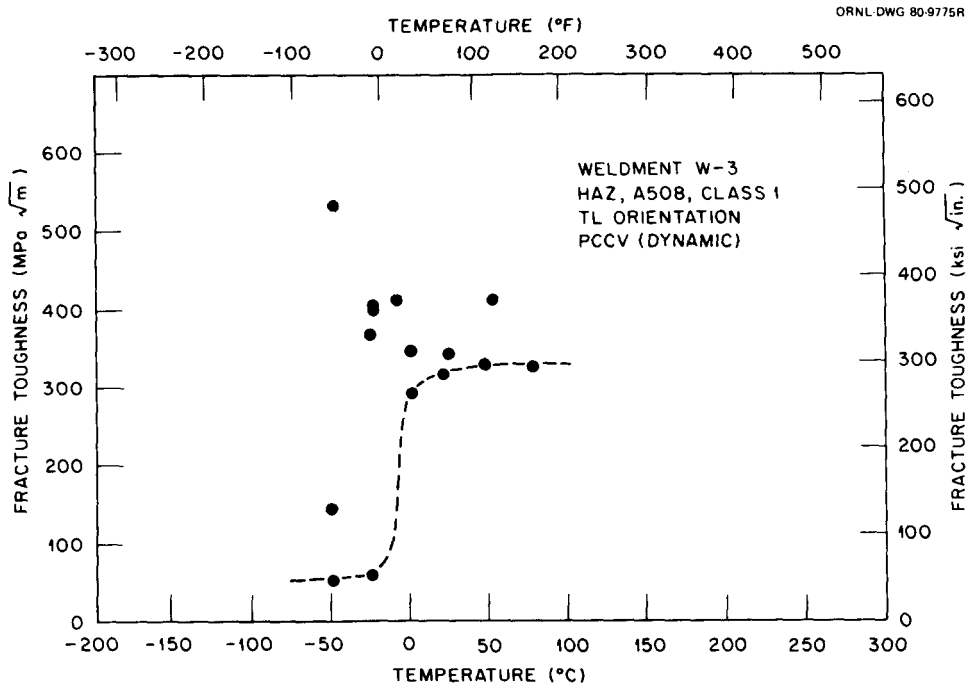

Fig. 3.21. Dynamic precracked Charpy fracture toughness of forging heat-affected zone, weldment W-3.

appropriate. The wavy nature of the HAZs often results in portions of the crack front residing in, or propagating into, regions of weld metal. This results in asymmetry of loading and crack propagating, with artifically high tough values being measured. Figure 3.22 illustrates the fracture toughness data for the root weld metal.

The upper-shelf fracture toughness is slightly higher for the PHAZ than for the FHAZ or the root weld metal (approximately 360 MPa $\sqrt{m}$ versus approximately 320 or 300 MPa $\sqrt{m}$, respectively. The lower-shelf fracture toughness values for the PHAZ and FHAZ are slightly lower than the root weld metal, with the transition region for the FHAZ starting approximately 25 to 30°C higher than either the PHAZ or the root-weld metal.

The W-5 weldment consists of SA-537 class 1 normalized plate material welded to SA-508 class 1 quenched and tempered forged material, using E8018-C2 shielded metal arc welding (SMAW) metal for the root weld (10%) and 210172-S W/0091 flux submerged arc welding (SAW) metal for the bulk (90%) of the weld. The assembly was preheated to 121°C (250°F) minimum

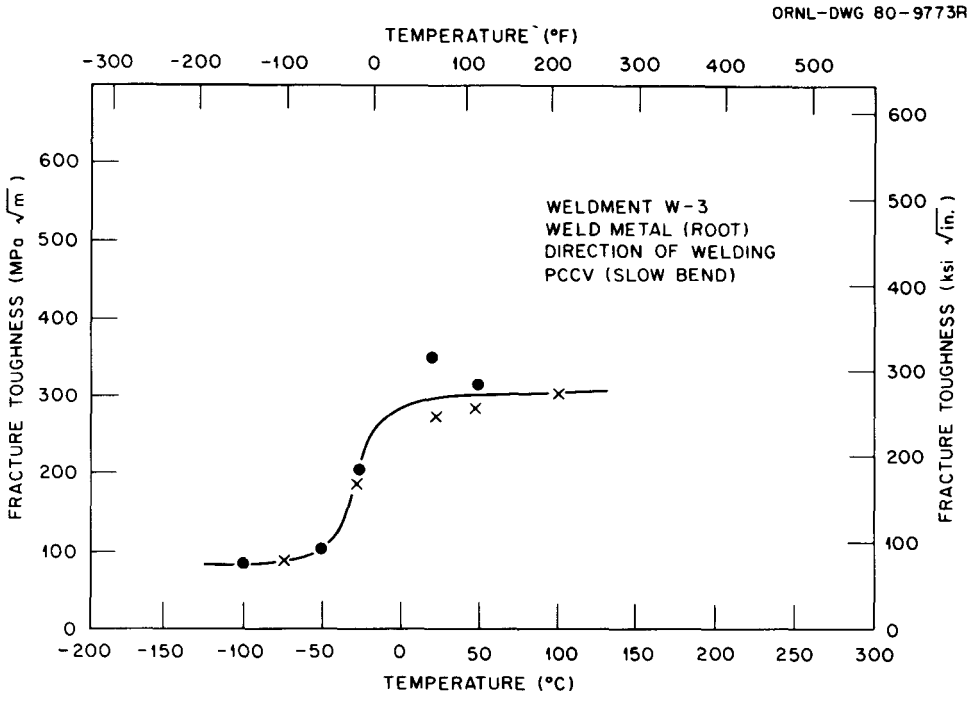

Fig. 3.22. Dynamic precracked Charpy fracture toughness of root weld metal, weldment W-3.

with interpass reheats to 204°C (400°F) maximum. Postweld heat treatment was at 566 to 621°C (1050 to 1150°F) for 7 h. Figure 3.23 shows an etched cross section of the W-5 weldment. The weldment can be characterized macroscopically as having a relatively narrow root and a generally uneven weld pass distribution in the smaller weld deposit (in fact, two passes cut deeply into the base metal near the root region). Evidence of weld repair occurs along one side of the larger weld deposit. No evidence of microcracking was found, even in the base metal near the root region.

Microhardness traverses (0.2-kg load) were made over several areas of the weld deposit. Each weld pass created an HAZ, which appears as a circular arc around each deposited bead. Microhardness values were characterized by determining whether they were in the weld bead (W), the HAZ (H), the plate (P), or the forging (F). Figure 3.24 shows a plot of hardness versus distance for the outer surface of the weldment. The hardness impressions were made at fairly uniform intervals and therefore randomly tested the various areas of the weld. An obvious hardness pattern emerged in which the central portion of each weld pass in the more shallow half

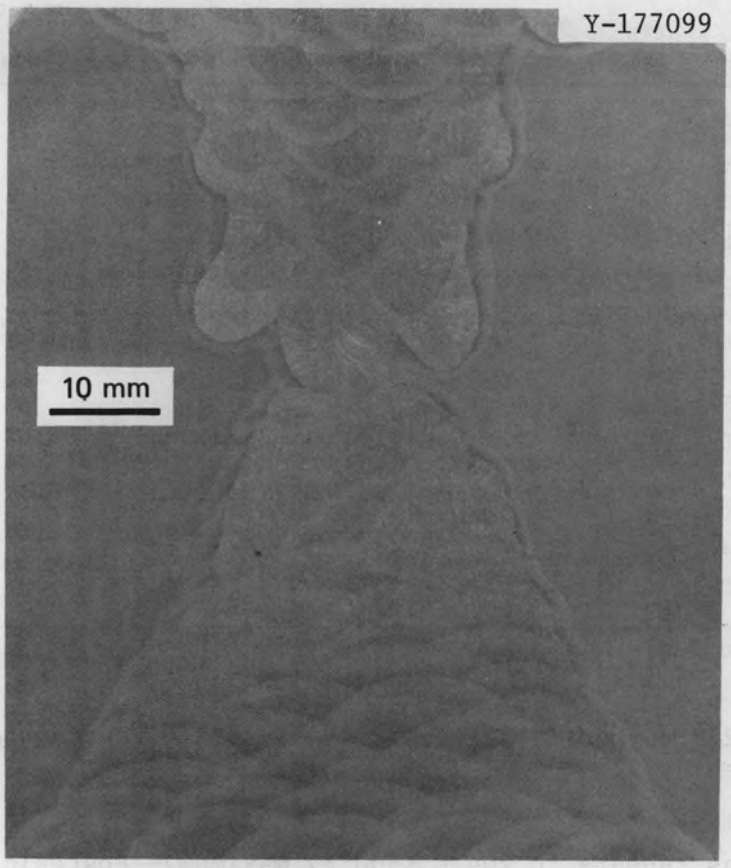

Fig. 3.23. Macroscopic view of weldment W-5 cross section.

of the weldment had higher hardnesses than the HAZs of those passes. This pattern was not as obvious in the other half of the weldment (from the approximate midpoint of the weldment to the inner surface). In general, the average hardness of the inner half was approximately 30 diamond-pyramid hardness (DPH) less than the average hardness of the remainder of the weld.

Two additional traverses were made, one along the length of the forging HAZ and the other within the central portion of a single weld pass. The forging HAZ had an average hardness of 198 DPH, and the central pass weld metal, a hardness of 220 DPH.

A block from the W-5 weldment was sectioned into slabs, from which 48 Charpy V-notch specimens were machined (six from each slab). This produced eight specimens each from six positions in the weld body. Numbered from 1 to 6, the specimens represented positions (1) about 15 mm from the

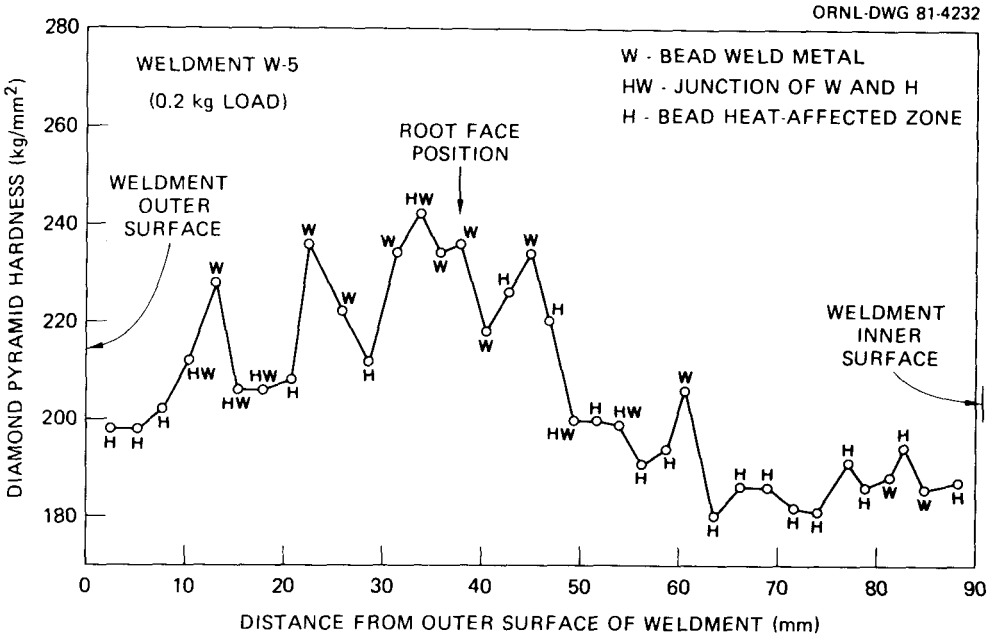

Fig. 3.24. Hardness (diamond-pyramid) traverse results as a function of distance for the outer surface of the W-5 weldment.

weldment outer surface, (2) the outer 1/4 thickness (1/4 t) position, (3) the root weld region, (4) about 40 mm from the weldment inner surface, (5) the inner 1/4 t position, and (6) about 15 mm from the weldment inner surface, respectively. This arrangement allowed testing for the variation in toughness, both across the weld thickness and from slab to slab.

All specimens were precracked and tested in the dynamic fracture toughness mode. The tests were divided into four groups: (1) five type 1 (see above) specimens tested at 50°C on the upper shelf to determine whether slab-to-slab variations existed; (2) types 2 and 5 (1/4 t) specimens, tested from −100 to 100°C to characterize the fracture toughness as a function of temperature; (3) types 1 through 6, machined from a single slab and tested at −10°C (the estimated midpoint of the transition region based on the curve generated by the previous test group); and (4) type 3 root weld specimens tested from −75 to 50°C. Figure 3.25 presents the results and a lower bound curve. A small number of future tests will be performed in the −50 to 0°C range to define better the transition curve.

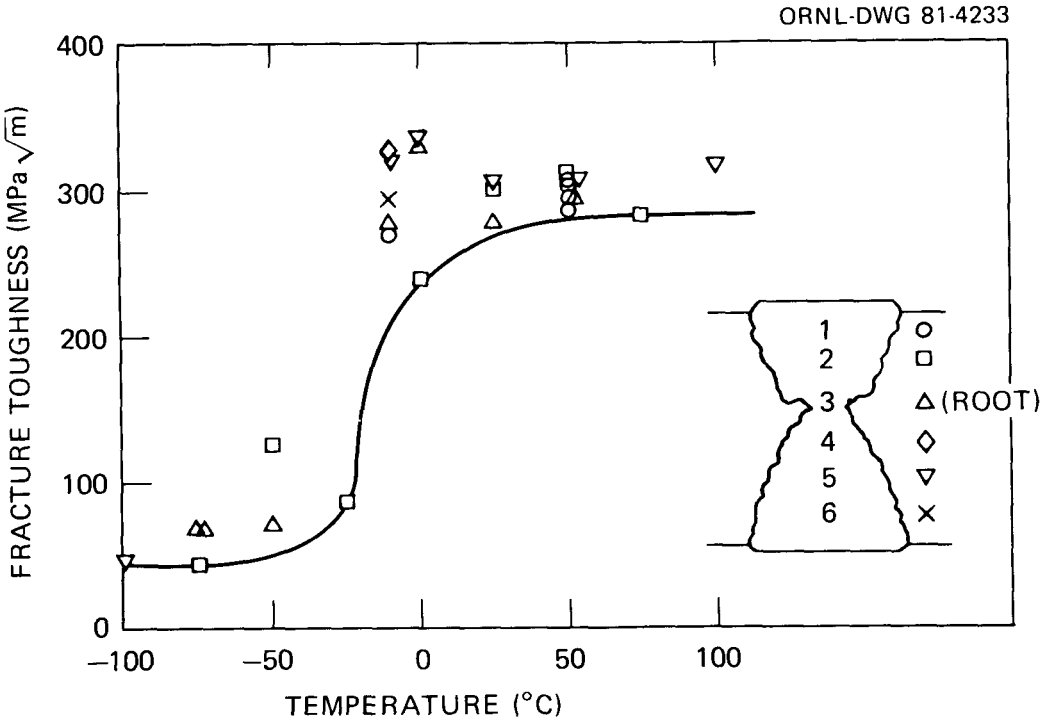

Fig. 3.25. Dynamic precracked Charpy fracture toughness of the W-5 weld metal.

Tests of the first group of specimens showed little, if any, fracture toughness variation from slab to slab. The third group of tests at −10°C, which resulted in upper-shelf behavior, showed similar behavior through the weld thickness. The upper-shelf fracture toughness was found to be greater than 280 MPa $\sqrt{m}$, and the lower was greater than 40 MPa $\sqrt{m}$ for all parts of the weld region. This compares with approximately 400 MPa $\sqrt{m}$ upper-shelf and approximately 60 MPa $\sqrt{m}$ lower-shelf fracture toughness for the W-3 weldment bulk weld metal and approximately 300 MPa $\sqrt{m}$ upper- and 80 MPa $\sqrt{m}$ lower-shelf fracture toughness for the W-3 root weld region.

The computerized J-integral unloading compliance system is operational and was used to test a 1 T compact specimen from plate P2. The unloading compliance methodology involves a series of loadings and partial unloadings with a single specimen to generate a J-integral versus crack growth (Δa) curve. The J-Δa curve may be used to determine a fracture toughness result J_{Ic} or to obtain a measure of the material resistance to tearing, the tearing modulus T. The methods of analysis for both J_{Ic} and

T are still evolving technologies, and the results reported here are, in that sense, preliminary. It is noteworthy that the American Society for Testing and Materials is publishing a new standard procedure for elastic-plastic fracture toughness testing, which utilizes the resistance curve (*R*-curve) concept to determine J_{Ic}.

Figure 3.26 shows a plot of *J* versus Δa data obtained from a single specimen unloading compliance test. The *J*-integral and crack extension are computed at each unloading. The analysis used here provides a crack growth correction as well as a correction for displacement measuring point rotation off the load-line. The blunting line appears to be quite representative of the results in the early portion of the test until in-place crack extension dominates. Maximum load during the test occurred at the fifth unloading and is annotated on the figure. The line drawn through the subsequent data points represents a hand-drawn linear resistance curve (*R*-curve).

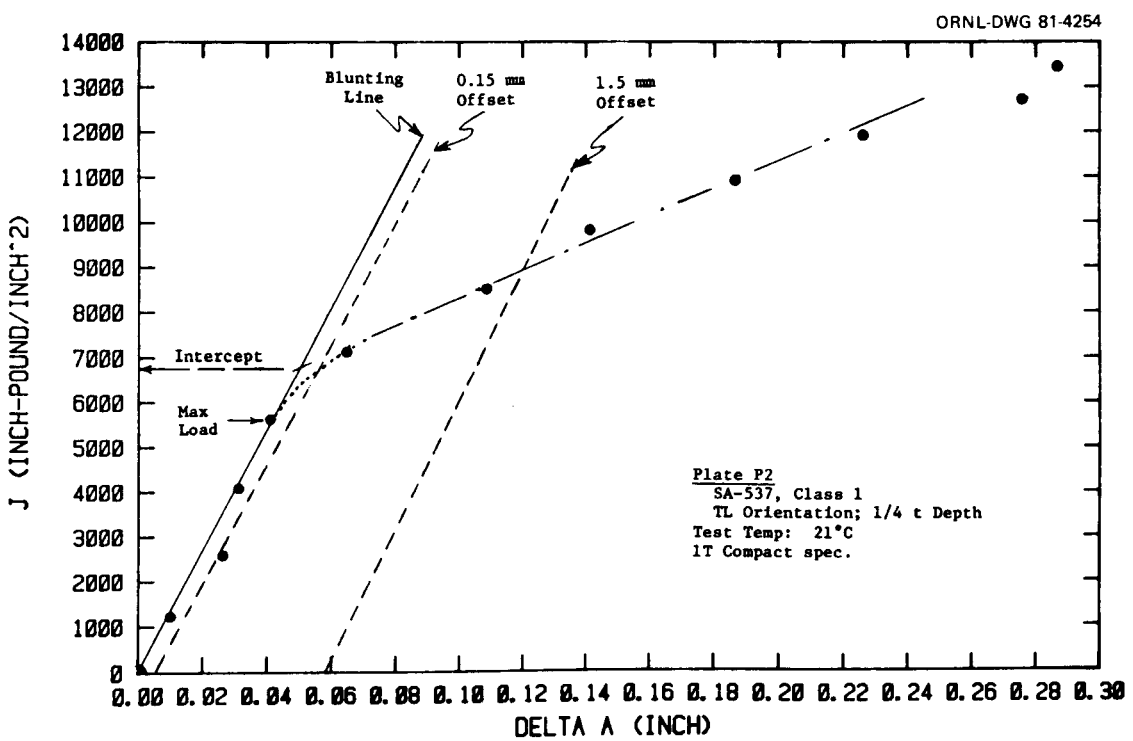

Fig. 3.26. Plot of *J*-integral versus crack extension (Δa) obtained from a single specimen unloading compliance test with PCRV liner plate P2. 1 in.-lb/in.^{2} = 175 N/m. 1 in. = 25.4 mm.

Values of $K_{(J)}$ can be calculated from the J_{Ic}, determined by using the intercept of the R-curve with the blunting line, and this results in a $K_{(J)}$ of about 500 MPa $\sqrt{m}$. If the J_{Ic} is determined at the maximum load point, a $K_{(J)}$ of about 450 MPa $\sqrt{m}$ is calculated. These values are comparable to previously reported fracture toughness results of about 450 MPa $\sqrt{m}$ for plate P2 at room temperature. It is important that the point at which maximum load occurs in the test falls on the blunting line and not out on the R-curve. This indicates that previously reported fracture toughness results for PCRV liner steels, using the energy to maximum load in a load-to-fracture test, are similar to those obtained with the most recent state-of-the-art testing techniques.

Beyond the determination of J_{Ic}, the R-curve can be used to determine T. For the R-curve shown in the figure, T (dimensionless) is about 200.

This testing and analysis technique will be used to evaluate future test specimens of PCRV liner program materials such as weldments W-3, W-5, and W-1.

3.7 REFERENCES

1. Z. P. Bazant, P. D. Bhat, and C. L. Shieh, *Endochronic Theory for Inelastic and Failure Analysis of Concrete Structures*, Northwestern University Structural Engineering Rep. 1976-12/259 (ORNL/Sub-4403-1) (December 1976).
2. K. J. Bathe, *ADINA, Finite-Element Program for Automatic Dynamic Incremental Nonlinear Analysis*, Massachusetts Institute of Technology Rep. 82448-1, Cambridge (September 1975, rev. May 1977).
3. K. J. Bathe, *Static and Dynamic Geometric and Material Nonlinear Analysis Using ADINA*, Massachusetts Institute of Technology Rep. 82448-2, Cambridge (May 1976, rev. May 1977).
4. J. R. Dougan and D. N. Fanning, unpublished results, June 1980.
5. J. D. Reins et al., *Shear Strength of End Slabs of Prestressed Concrete Nuclear Reactor Vessels*, University of Illinois Rep. UILC-ENG-76-2022 (ORNL/Sub-4164-1) (July 1976).
6. Z. P. Bazant, "Theory of Creep and Shrinkage in Concrete Structure: A Précis of Recent Development," *Mech. Today*, 2: 1–93 (1975).

7. W. G. Dodge, Z. P. Bazant, and R. H. Gallagher, *A Review of Analysis Methods for Prestressed Concrete Reactor Vessels*, ORNL-5173 (February 1977).

8. Z. P. Bazant and S. T. Wu, "Thermoviscoelasticity of Aging Concrete," *J. Eng. Mech. Div., Proc. Am. Soc. Civ. Eng.*, 100: 575–97 (1974).

9. Z. P. Bazant and S. T. Wu, "Rate-Type Creep Law of Aging Concrete Based on Maxwell Chain," *Mater. Const. (Paris)* 7: 45–60 (1974).

10. Z. P. Bazant and A. Asghari, "Computation of Age-Dependent Relaxation Spectra," *Cem. Concr. Res.* 4: 567–79 (1974).

11. Z. P. Bazant and E. Osman, "Double Power Law for Basic Creep of Concrete," *Mater. Const. (Paris)* 9: 3–11 (1976).

12. Z. P. Bazant, E. Osman, and W. Thonguthai, "Practical Formulation of Shrinkage and Creep in Concrete," *Mater. Const. (Paris)* 9: 395–406 (1976).

13. Z. P. Bazant and L. Panula, "Practical Prediction of Time-Dependent Deformations of Concrete, Part I, Shrinkage," *Mater. Const. (Paris)* 11: 307–16 (1978); "Part II, Basic Creep," 11: 317–28 (1978); "Part III, Drying Creep," 11: 415–25 (1978); "Part IV, Temperature Effect on Basic Creep," 11: 424–34 (1978); "Part V, Temperature Effect on Drying Creep," 12: 169–74 (1979); "Part VI, Cyclic Creep, Nonlinearity and Statistical Scatter," 12: 175–83 (1979).

14. Z. P. Bazant, "Numerical Determination of Long-Range Stress History from Strain History in Concrete," *Mater. Const. (Paris)* 5: 135–41 (1972).

15. Z. P. Bazant, "Thermodynamics of Solidifying or Melting Viscoelastic Material," *J. Eng. Mech. Div., Proc. Am. Soc. Civ. Eng.* 105: 933–52 (December 1979).

16. Z. P. Bazant and S. S. Kim, "Approximate Relaxation Function for Concrete," *J. Struct. Div., Proc. Am. Soc. Civ. Eng.* 105: 2695–705 (December 1979).

17. R. K. Nanstad, *A Review of Concrete Properties for Prestressed Concrete Pressure Vessels*, ORNL/TM-5497 (October 1976).

18. D. J. Naus, *A Review of Concrete Material Systems for Application to Prestressed Concrete Pressure Vessels*, ORNL/TM-7632 (1981)

19. G. C. Robinson, *Purchase Specification for Elevated-Temperature Multiaxial Concrete Testing System,* Specification No. M-11926-RS-001-0, Oak Ridge National Laboratory (November 1980).

20. P. P. Holz, *Flaw Preparations for HSST Program Vessel Fracture-Mechanics Testing: Mechanical-Cyclic Pumping and Electron-Beam Weld-Hydrogen-Charge Cracking Systems*, NUREG/CR-1274 (ORNL/NUREG/TM-369) (May 1980).

21. D. J. Naus, unpublished data, June 1980.

22. D. J. Naus and C. B. Oland, *HTGR Base-Technology Program Annu. Prog. Rep., Dec. 31, 1979*, ORNL-5643 pp. 178–83.

23. H. L. Gotschall et al., *Plan for Development of an Optimized PCRV for an HTGR Power Plant*, ORNL/TM-6606 (December 1978) pp. 38–39.

24. American Concrete Institute, "A State-of-the-Art Report on Fiber Reinforced Concrete," ACI Committee 544 Report, *Proc. Am. Concr. Inst.* 70(11): 729–44 (November 1973).

25. C. B. Oland, unpublished data, May 1980.

26. Chicago Committee on High-Rise Buidlings, *High Strength Concrete in Chicago High-Rise Building*, Report 5, Task Force, Chicago, Ill. (1977).

27. R. K. Nanstad and D. A. Canonico, "Liner and Penetration Studies," *HTGR Base-Technology Program Annu. Prog. Rep., Dec. 31, 1979*, ORNL-5643, pp. 164–75.

28. "Fracture Toughness Requirements for Materials," ND-2300, Sect. III, Division I, *ASME Boiler and Pressure Vessel Code*, 1974 ed., 1976 Addendum.

4. STRUCTURAL MATERIALS

P. L. Rittenhouse

4.1 INTRODUCTION — P. L. Rittenhouse

Work at ORNL on HTGR structural materials is directed toward development of the materials technology necessary to design and license HTGR systems. The program is closely coordinated with similar efforts at the General Atomic Company (GA) and the General Electric Company (GE) and, together with these, constitutes the national structural materials program in support of HTGR technology.

The ORNL structural materials program during 1980 was divided into five major task areas:

- mechanical properties of alloys, weldments, and ceramics;
- corrosion of alloys;
- joining technology;
- structural ceramics; and
- fission product — materials interactions.

The first area involves the determination of tensile, creep, fatigue, creep-fatigue, and crack growth properties of alloys and their weldments as well as various tests on structural ceramics. Many of the tests are conducted in a simulated HTGR-helium environment to determine the effects of reactions between the materials and reactive components of the environment. Additionally, the thermal stabilities of materials are evaluated by aging and postexposure testing.

At the beginning of the year the work on corrosion was divided into two distinct subtasks: steam corrosion and oxidation-carburization behavior in HTGR helium. However, early in the year the mode of operation of the oil-fired steam plant at which the steam corrosion exposures were performed was changed from base load to peaking operation. This change resulted in the termination of our exposures. The availability of other facilities for future steam corrosion work is being investigated. Corrosion studies in HTGR helium have emphasized the effect of carburization on dimensional stability and the influence of H_2O level and supply rate on oxidation and carburization behavior.

Three separate efforts have been in progress in the area of joining. The first, now completed, involved the fusion welding of three experimental wrought alloys based on the Inconel 617 composition. In the second, the weldability of several cast nickel-base alloys of potential application for thermal barriers and hot ducts is being evaluated. Finally, laser and electron beam welding are being investigated as possible suitable joining techniques for the iron-base oxide-dispersion-strengthened alloy MA956.

Work on ceramics during the year involved both fibrous materials for thermal barrier insulation and dense materials for core support applications. All planned work on fibrous ceramics, with the exception of some long-term aging-resilience tests, was completed. Characterization of dense ceramics continued, and studies to determine the effects of rapid depressurization on material integrity were completed successfully.

A study of the possible effects of fission product—materials interactions was initiated late in the year to evaluate the potential degradation of properties of structural materials as a result of exposure to tellurium- and cesium-containing environments. A significant background of information on this subject is available from past studies at ORNL on other reactor systems.

Responsibility for fracture toughness studies on prestressed concrete reactor vessel (PCRV) liner and penetration steels was transferred to the Structural Materials Program on October 1. Reporting of the year's activities is covered in the PCRV chapter.

4.2 MECHANICAL PROPERTIES OF HTGR ALLOYS, WELDMENTS, AND CERAMICS — C. R. Brinkman

4.2.1 Creep and Tensile Testing of Metallic Materials — H. E. McCoy

The materials being evaluated in this program are described in Tables 4.1 and 4.2. Tensile tests have been run on most of these materials, and the results have been reported.[1-5] These tests showed that the yield and tensile strengths of Inconel 617, Hastelloy X, and Incoloy 802 were quite similar but that HD556 was significantly stronger over the entire temperature range.

Table 4.1. Alloy characterizations

Material	Heat	Source	Product form	Grain size (μm)	Heat treatment
Alloy 617	XX01A3US	INCO	12.7-mm (1/2-in.) plate		Solution annealed by vendor
Hastelloy X	2600-3-4936	Cabot	12.7-mm (1/2-in.) plate	80	Solution annealed by vendor
	2600-3-2792	Cabot	31.8-mm (1 1/4-in.) bar	55	Solution annealed by vendor
Alloy 800H	HH6993	INCO	19-mm (3/4-in.) bar		Solution annealed by vendor
2 1/4 Cr-1 Mo	X-6216	B&W	51-mm-OD (2.0-in.) tube	27	Isothermally annealed[a]
	36202	B&W	51-mm-OD (2.0-in.) tube	20–27	Isothermally annealed[a]
	72768	B&W	51-mm-OD (2.0-in.) tube	27	Isothermally annealed[a]
9 Cr-1 Mo	316381				Annealed
Hastelloy S	8635-3-8365T	Cabot	12.7-mm (1/2-in.) plate		Unknown — by vendor
HD556	8556-5-7305	Cabot	6.4-mm (1/4-in.) plate		Unknown — by vendor
Inconel 618	Y09B9	INCO	12.7-mm (1/2-in.) plate		Unknown — by vendor
Incoloy 802	HH6863B	INCO	7.9-mm (0.312-in.) plate		Solution annealed by vendor

[a]927 ± 14°C for 30 min, cooled to 704 ± 14°C at a maximum rate of 83°C/h, held at 704 ± 14°C for 2 h, cooled to room temperature at a maximum rate of 6°C/min.

Table 4.2. Alloy compositions

Material	Content (%)													
	Ni	Cr	Co	Mo	Fe	Al	Si	C	Mn	S	W	Ti	Cu	Others
Alloy 617	57.35	20.30	11.72	8.58	1.01	0.76	0.16	0.07	0.05	0.004				
Hastelloy X 4936	Bal.	21.82	1.68	9.42	19.09		0.44	0.07	0.58	<0.005	0.63			
2792	Bal.	21.25	1.94	8.99	18.96		0.41	0.10	0.57	<0.005	0.56			
Alloy 800H 6993[a]	33.43	20.36			43.60	0.43	0.39	0.07	0.77	0.004		0.46	0.49	
2 1/4 Cr-1 Mo X-6216		2.19		1.00	Bal.		0.26	0.12	0.44	0.016				
36202		2.24		0.96	Bal.		0.34	0.12	0.43	0.023				
72768		2.16		0.94	Bal.		0.38	0.10	0.41	0.012				
9 Cr-1 Mo	0.4	8.83		1.0	Bal.		0.6	0.0803	0.5	0.0208				0.02 V
Hastelloy S 8365T	Bal.	15.3	0.15	15.3	0.5	0.40	0.40	0.0129	0.5			0.01	0.04	0.02 La
HD 556	19.44	21.39	19.08	2.72	Bal.	0.26	0.49	0.11	1.20	<0.005	2.08			0.01 La, 0.76 Cb + Ta
Inconel 618	56.49	22.5			14.79	0.01	0.021	0.05	0.09	0.005	5.85		0.04	
Incoloy 802	33.45	19.74			44.57		0.37	0.30	1.11	0.001			0.46	

[a]Chemical composition not available for this heat; analysis shown is for HH13-6979.

Creep tests are being performed on these same materials, and those in progress are summarized in Table 4.3. Significant differences in creep strength occur between the alloys, with the weakest being 2 1/4 Cr-1 Mo steel and the strongest being Inconel 617. However, the only clearly demonstrated effect of HTGR helium on the creep strength was with 2 1/4 Cr-1 Mo steel. The alloy was decarburized by HTGR helium at elevated temperatures, and the creep strength was less than that measured in air. All other alloys tested thus far have carburized in HTGR helium, but no detectable changes have occurred in the creep rate. However, the fracture strain of the carburized material has generally been less than that of uncarburized material.

Several modified alloys in which the concentrations of chromium, titanium, and aluminum have been varied are being studied. These elements are known to have significant effects on the resistance of nickel-base alloys to carburization.

All alloys studied thus far have been welded satisfactorily. Hastelloy X was welded by both the gas tungsten arc (GTA) and the shielded metal arc welding (SMAW) processes, using Hastelloy X and Hastelloy S filler metals. With Hastelloy X filler metal, creep failures consistently occur in the Hastelloy X weld metal, but the creep strength is not outside the range of expected values for Hastelloy X base metal. With Hastelloy S filler metal, creep failures consistently occurred in the Hastelloy X base metal. Satisfactory welds were obtained in Inconel 617 and Incoloy 802 base metals by using Inconel 617 weld metal. In the Inconel 617 weldment, the creep strength is equivalent to the base metal, and failures occur randomly in the base and weld metals. In the Incoloy 802 weldment, the strength of the Inconel 617 weld metal was greater than that of the Incoloy 802, and failure occurred in the Incoloy 802 base metal. Alloy HD556 was welded with filler metal of the same material, and satisfactory welds were obtained by the GTA process. Creep failures consistently occurred in the weld metal, but the creep strength fell within the expected range for the base metal.

The yield and tensile strengths of the all-weld-metal samples of Hastelloy X and Inconel 617 were higher than those of the base metal. The yield and tensile strengths of the Hastelloy X weld metal were 50 and 10%,

Table 4.3. Status of creep tests currently in progress

Test	Material	Environment	Temperature (°C)	Stress (MPa)	Stress (ksi)	Time (h)	Approximate creep strain (%)
18434	Hastelloy X, heat 4936, flat	He	649	138	20	32,467	8.7
17376	Hastelloy X, heat 4936	Air	704	103	15	39,671	12.2
18150	Hastelloy X, heat 4936	He	649	138	20	33,788	5.3
18448	Hastelloy X, heat 2792	Air	760	69	10	31,176	6.8
21565	Hastelloy X, heat 4936, aged 20,000 h at 538°C in inert gas	He	538	345	50	6,859	8.9
22195	Hastelloy X, heat 4936, aged 10,000 h at 593°C in HTGR He	He	593	276	40	189	2.9
22193	Hastelloy X, heat 4936, aged 20,000 h at 871°C in HTGR He	He	871	35	5	189	0.6
20559	Hastelloy X weld, X/X/X, GTA, aged 2000 h at 593°C in inert gas	He	593	241	35	8,513	3.3
21567	Hastelloy X weld, X/X/X, SMAW, aged 2000 h at 593°C in inert gas	He	593	241	35	6,584	2.3
18430	Hastelloy X weld, X/S/X, GTA	He	593	241	35	32,703	4.4
21561	Hastelloy X weld, X/S/X, GTA, aged 2000 h at 593°C in inert gas	He	593	241	35	7,075	2.0
22201	Hastelloy X weld, X/X/X, GTA, aged 10,000 h at 593°C in HTGR He	He	593	276	40	12	0.2
22186	Hastelloy X weld, X/X/X, GTA, aged 20,000 h at 871°C in HTGR He	He	871	35	5	45	0.3
21602	Inconel 617	He	871	21	3	2,724	0.1
21603	Inconel 617	Air	871	21	3	2,663	0.1
19393	Inconel 617	He	871	34	5	25,811	9.9
19761	Inconel 617	Air	871	34	5	22,732	16.7
18869	Inconel 617	Air	760	69	10	24,213	2.4
19182	Inconel 617	He	649	207	30	28,048	0.9
22188	Inconel 617	He	593	414	60	837	19.8

Table 4.3. (continued)

Test	Material	Environment	Temperature (°C)	Stress (MPa)	Stress (ksi)	Time (h)	Approximate creep strain (%)
22180	Inconel 617, aged 20,000 h at 704°C in HTGR He	He	704	207	30	1,127	1.4
22200	Inconel 617, aged 10,000 h at 593°C in HTGR He	He	593	345	50	45	6.9
22185	Inconel 617, aged 20,000 h at 871°C in HTGR He	He	871	48	7	1,005	10.4
20534	Inconel 617, aged 20,000 h at 538°C in inert gas	He	538	414	60	11,277	14.8
21589	Inconel 617, aged 28,300 h at 482°C in steam	Air	649	345	50	957	10.2
21612	Inconel 617 weld, GTA, aged 2000 h in HTGR He	He	704	207	30	1,797	1.2
20553	Inconel 617, all weld metal	He	649	241	34	8,589	0.9
21594	Modified Inconel 617, alloy J492	He	649	345	50	3,238	7.9
22182	Modified Inconel 617, J492 weld, 1 h at 1177°C	He	760	138	20	1,148	8.9
22187	Modified Inconel 617, J493 weld, 1 h at 1177°C	He	649	345	50	827	8.9
22192	Modified Inconel 617, J494 weld, 1 h at 1177°C	He	649	345	50	143	16.1
22196	Inconel 618, 1 h at 1177°C	He	871	34	5	189	0.2
22199	Inconel 618, 1 h at 1177°C	He	760	69	10	189	0.5
22189	Inconel 618, 1 h at 1177°C	He	871	34	5	791	4.5
22190	Incoweld A	Air	760	69	10	793	0.8
22198	Incoloy 802	He	760	103	15	45	0.2
22181	Incoloy 802	Air	760	69	10	1,151	0.4

Table 4.3. (continued)

Test	Material	Environment	Temperature (°C)	Stress (MPa)	Stress (ksi)	Time (h)	Approximate creep strain (%)
20532	HD556	He	649	207	30	11,277	14.2
20548	HD556	He	871	34	5	8,645	0.2
21563	HD556	Air	760	103	15	7,032	3.8
20536	HD556, weld	Air	871	34	5	10,968	1.5
18860	2 1/4 Cr-1 Mo steel, heat 72768	He	538	69	10	28,925	12.3
18446	2 1/4 Cr-1 Mo steel, heat 72768	He	649	21	3	31,568	1.4
19796	2 1/4 Cr-1 Mo steel, heat 72768	Air	649	21	3	19,960	4.9
18252	2 1/4 Cr-1 Mo steel, heat 72768	He	538	41	6	33,610	0.3
18508	2 1/4 Cr-1 Mo steel, heat 72768, flat specimen	He	538	41	6	32,227	1.7
19945	2 1/4 Cr-1 Mo steel, heat 72768	He	538	41	6	22,080	0.7
20508	9 Cr-1 Mo steel	Air	538	103	15	16,118	11.3
20560	SiO_2, Corning 7941 — compressive	He	871	14	2	8,343	2.7
20555	SiO_2, Corning 7941 — compressive	He	816	14	2	8,420	2.1
21597	SiO_2, Corning 7941 — compressive	He	816	41	6	3,070	0.7
22197	Si_3N_4, NC-132, compressive	He	1,010	448	65	189	1.5
22194	Si_3N_4, NC-132, four-point bending	He	1,010	448	65	44	5.6
21606	Si_3N_4, NCX-132 four-point bending	He	1,010	448	65	2,804	2.4

respectively, higher than those of the base metal, and the yield and tensile strengths of Inconel 617 weld metal were 75 and 10%, respectively, higher than those of the base metal. The fracture strains of all-weld-metal specimens ranged from 20 to 40%.

Tensile tests were run on all-weld-metal samples of Incoweld A, a filler metal for making welds in nickel- or iron-base alloys by the SMAW process. Incoweld A weld deposits were stronger than those for Incoloy 800H at all test temperatures and compared favorably with Hastelloy X in short-term tensile properties.

4.2.2 Aging Studies — H. E. McCoy

Many of the alloys being considered for HTGR use change properties as a function of time at temperature, and the problem is likely worsened by carburization in HTGR helium. The agings in progress to study these effects are summarized in Table 4.4. The aged specimens are being evaluated by tensile, creep, and fatigue tests, which are still in progress. Many of the samples are still in the furnaces undergoing aging.

The property change of primary interest is the loss in fracture toughness as a result of aging. Several Charpy impact samples have been included in the program, and typical results for an aging temperature of 871°C and a test temperature of 25°C are shown in Fig. 4.1. The impact energies of HD556 and Hastelloy X are reduced rapidly at 871°C. Although Inconel 617 is affected more slowly than Hastelloy X, the impact value of Inconel 617 after 20,000 h of aging is within a factor of 2 of that of Hastelloy X. Inconel 618 base metal and welds appear after 1000 h of aging to be much tougher than either Hastelloy X or Inconel 617.

4.2.3 Fatigue and Fatigue Crack Growth — J. P. Strizak

An invesitgation of the effects of thermal aging and environment on the low-cycle fatigue behavior of Hastelloy X and Inconel 617 was undertaken during the current reporting period. Continuous-cycle fatigue tests were conducted in air to compare the fatigue behavior of material aged in argon for periods of 10,000 and 20,000 h at 538, 704, and 871°C, with cyclic lifetime for solution-annealed material. Interim data to date are shown in Figs. 4.2 through 4.6.

Table 4.4. Summary of ORNL aging programs

Material	Aging conditions			Status
	Temperature (°C)	Time (h)	Environment	
Base metals				
Hastelloy X	538	2.5, 10, 20	Inert	Complete
Hastelloy X	704	2.5, 10, 20	Inert	Complete
Hastelloy X	871	2.5, 10, 20	Inert	Complete
Incoloy 802	593, 704, 871	10	HTGR He	Complete
Inconel 617	538	2.5, 10, 20	Inert	Complete
Inconel 617	704	2.5, 10, 20	Inert	Complete
Inconel 617	871	2.5, 10, 20	Inert	Complete
Hastelloy X	593, 704, 871	10, 20	HTGR He	Complete
Hastelloy X	593, 704, 871	50	HTGR He	23,000 h
Inconel 617	593, 704, 871	10, 20	HTGR He	Complete
Inconel 617	593, 704, 871	50	HTGR He	23,000 h
Inconel 618	593, 704, 871	10	HTGR He	3,000 h
HD556	593, 704, 871	10	HTGR He	3,000 h
Modified Inconel 617	593, 704, 871	10	HTGR He	3,000 h
Welds[a]				
X/X/X, GTA	538, 704, 871	2	Inert	Complete
X/82/Incoloy 800H, GTA	427, 538, 649	2	Inert	Complete
X/X/X, GTA	593, 649, 760, 871	2, 10	Inert	Complete
X/X/X, SMAW	593, 649, 760, 871	2, 10	Inert	Complete
X/S/X, GTA	593, 649, 760, 871	2, 10	Inert	Complete
X/182/800H, GTA	482, 538, 649	2, 10	Inert	Complete
X/A/800H, SMAW	482, 538, 649	2, 10	Inert	Complete
X/X/X, GTA	593, 704, 871	10, 20	HTGR He	Complete
X/X/X, GTA	593, 704, 871	50	HTGR He	23,000 h
617/617/617, GTA	593, 704, 871	10, 20	HTGR He	Complete
617/617/617, GTA	593, 704, 871	50	HTGR He	23,000 h
802/617/802, GTA	593, 704, 871	10	HTGR He	Complete
618/618/618, GTA	593, 704, 871	10	HTGR He	3,000 h
556/556/556, GTA	593, 704, 871	10	HTGR He	3,000 h
M617/M617/M617, GTA	593, 704, 871	10	HTGR He	3,000 h

[a]The following designation is used for welds: Base metal 1/filler metal/base metal 2; GTA = gas tungsten-arc process; and SMAW = shielded metal arc weld.

ORNL-DWG 80-19106R

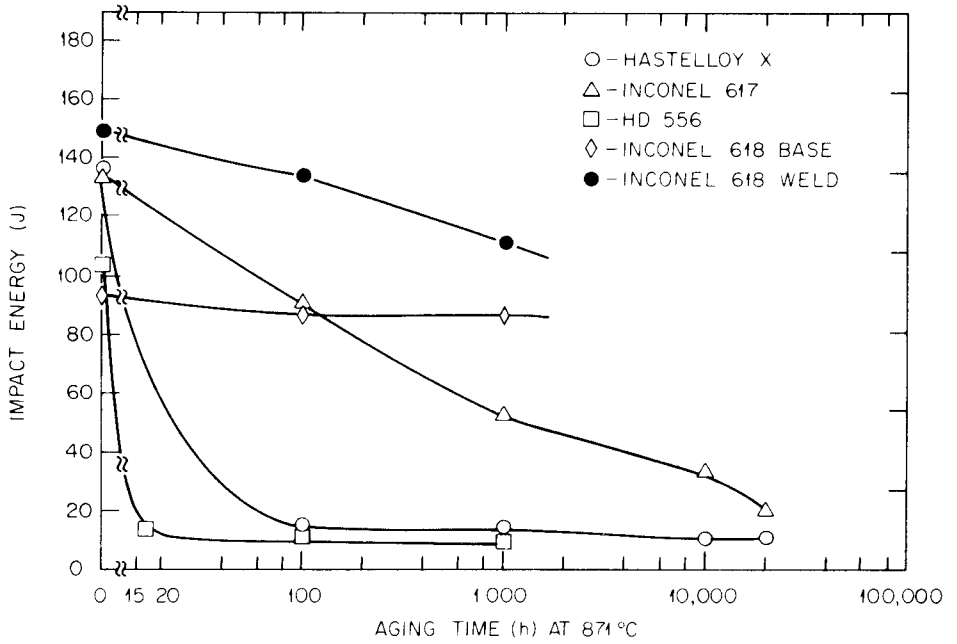

Fig. 4.1. Impact energy of all alloys is reduced by aging at 871°C.

ORNL-DWG 80-15888

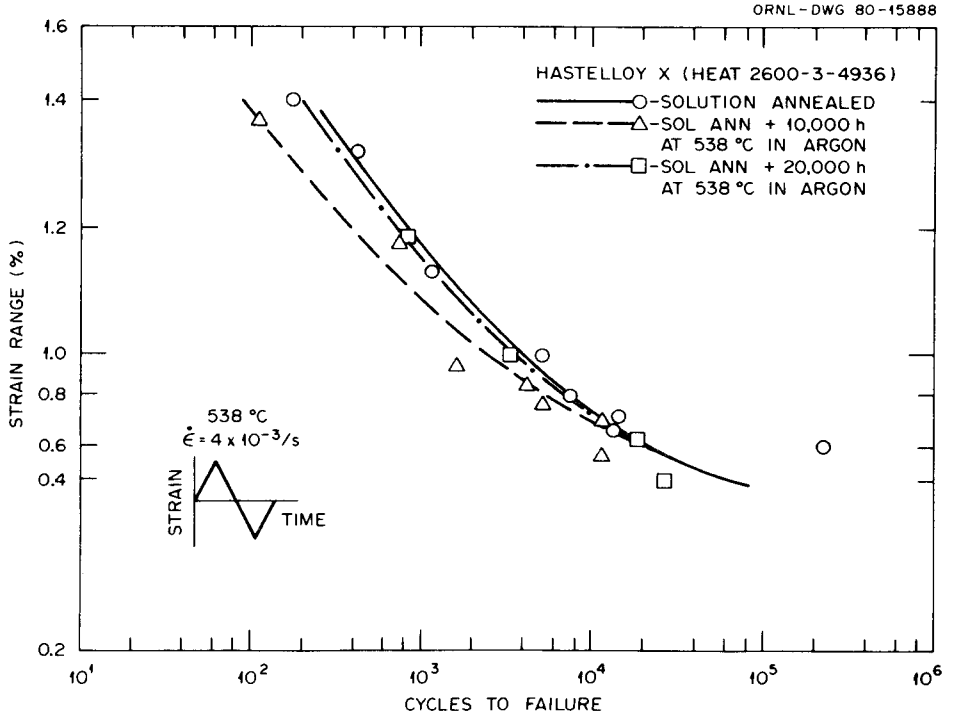

Fig. 4.2. Low-cycle fatigue behavior of Hastelloy X at 538°C.

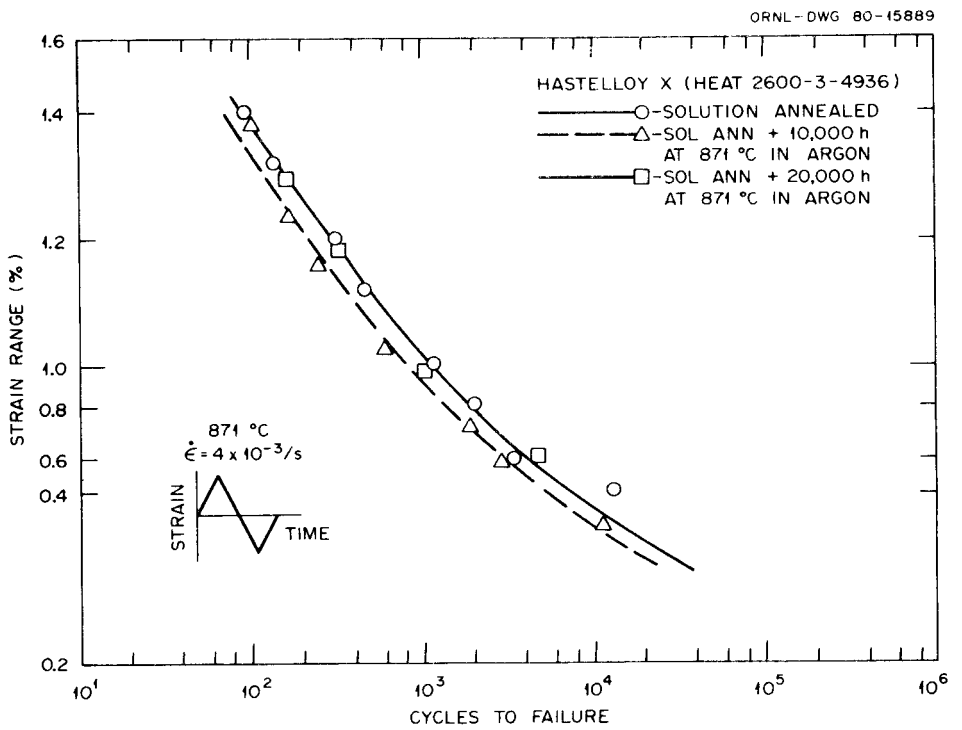

Fig. 4.3. Low-cycle fatigue behavior of Hastelloy X at 871°C.

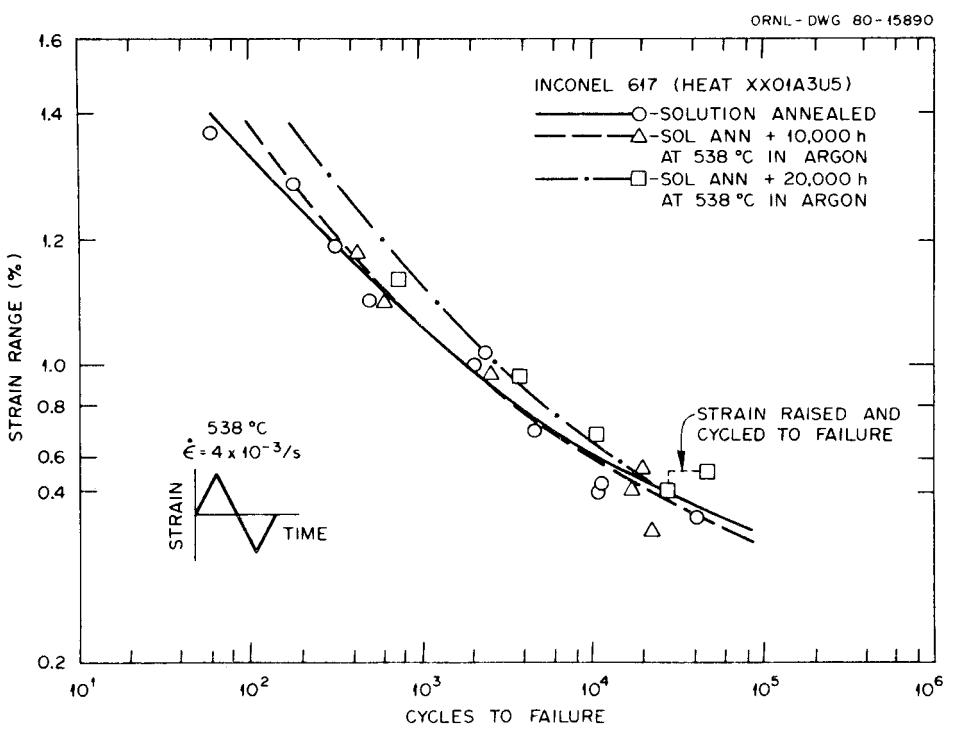

Fig. 4.4. Low-cycle fatigue behavior of Inconel 617 at 538°C.

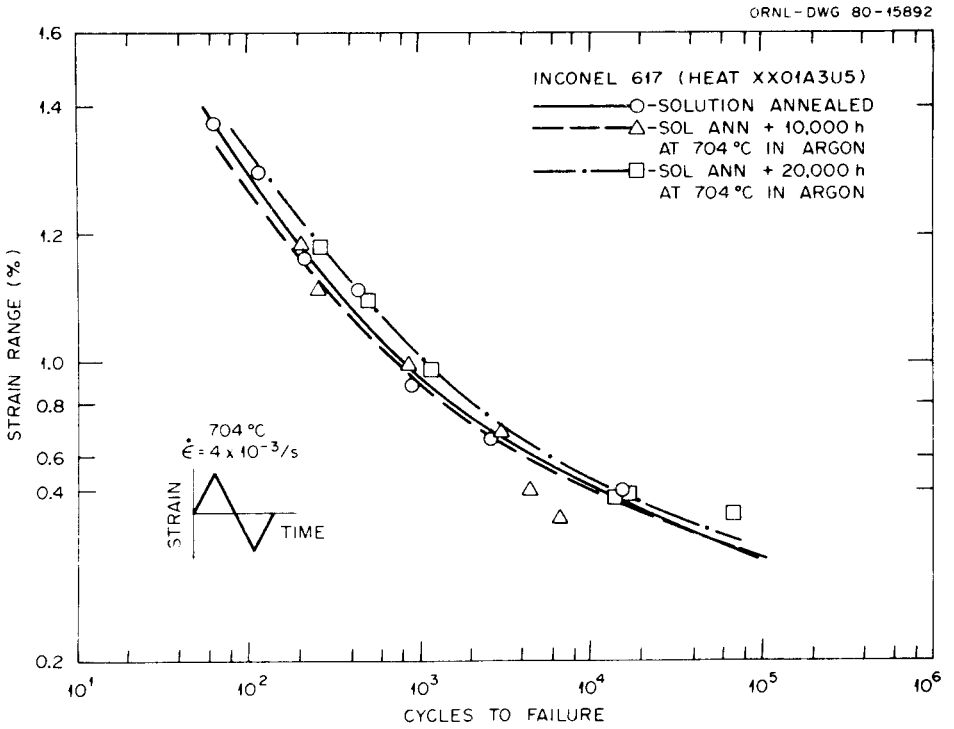

Fig. 4.5. Low-cycle fatigue behavior of Inconel 617 at 704°C.

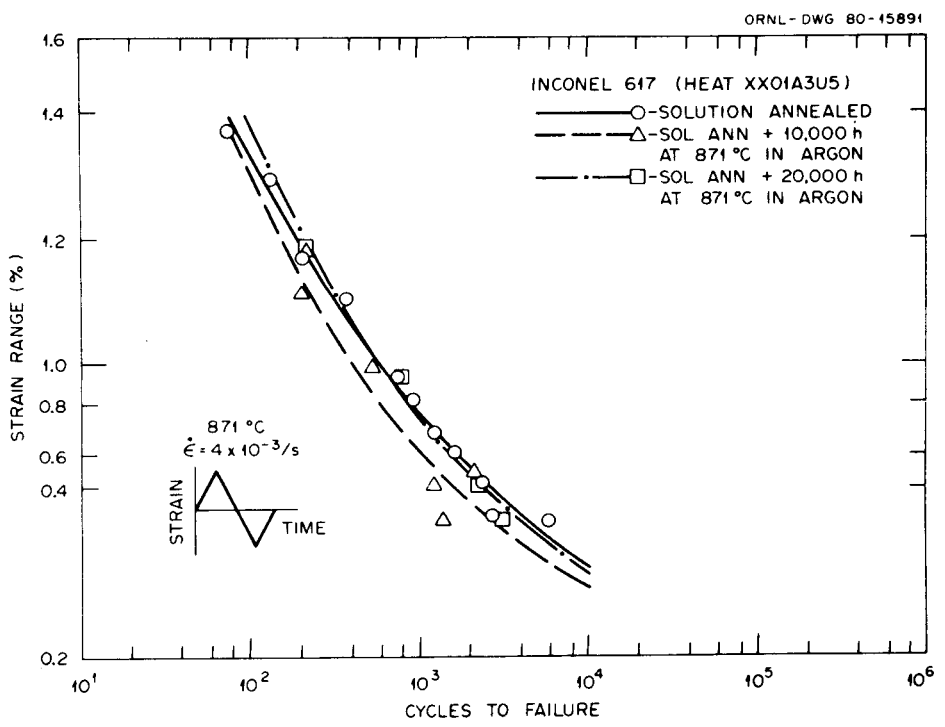

Fig. 4.6. Low-cycle fatigue behavior of Inconel 617 at 871°C.

Aging Hastelloy X for 10,000 h at 538°C before testing at high strain ranges (>1%) reduced fatigue life by a factor of 2 to 3 compared with solution-annealed material (see Fig. 4.2). However, the effect of this aging was very slight when the tests were run at low strain ranges. Aging for 20,000 h at 538°C had little effect on fatigue life at any strain range. Finally, aging at 871°C for 10,000 h reduced cyclic lifetimes by a factor of approximately 1.5 throughout the strain range investigated, whereas 20,000 h of aging had essentially no effect (see Fig. 4.3).

For Inconel 617, aging for 10,000 h at 538°C before testing had essentially no effect on fatigue life. Aging for 20,000 h doubled fatigue life at high strain ranges but essentially made no change at low strain levels (see Fig. 4.4). At 704°C, 10,000 h of aging slightly lowered fatigue lifetimes, whereas 20,000 h of aging increased fatigue life by a factor of about 1.5 throughout the range of cyclic life investigated (Fig. 4.5). Similar to the behavior of Hastelloy X, aging of Inconel 617 for 10,000 h at 871°C decreased cyclic lifetimes by a factor of 1.5 compared with solution-annealed material, but 20,000 h of aging resulted in slightly increased fatigue lifetimes (Fig. 4.6).

These low-cycle fatigue tests on Hastelloy X and Inconel 617 have shown that, although both aging time and temperature affect cyclic life, the effect of aging is relatively minor. Similar series of low-cycle fatigue tests are being run in a simulated HTGR-helium environment.

Interim results to date of low-cycle fatigue tests of Hastelloy X and Inconel 617 conducted in HTGR helium are given in Table 4.5. Cyclic lifetimes are seen to be greater (up to a factor of 20) in all cases for Inconel 617 tested in HTGR helium compared with air. The ratio of lifetime in helium to lifetime in air increases as the total strain range is decreased. For Hastelloy X this ratio is very close to unity except at the lowest strain range where a ratio of 2 has been observed.

Further testing will be conducted on solution-annealed Hastelloy X and Inconel 617 in HTGR helium at 871°C.

Additional specimens to be tested during this investigation of the effects of thermal aging and environment on low-cycle fatigue behavior include Inconel 617 and Hastelloy X aged in HTGR helium for 10,000 and 20,000 h at 593 and 871°C.

Table 4.5. Low cycle fatigue tests conducted in HTR-helium

Specimen	Total strain range (%)	Cycles to failure (N_f)	Estimated N_f in air
	Hastelloy X at 538°C		
HXL93	2.74	378	450
HXL86	1.85	861	940
HXL85	0.96	4,277	4,500
HXL73	0.63	65,797	20,000
HXL94	0.50	1,978,430	1,000,000
	Inconel 617 at 538°C		
IN57	1.86	990	300
IN49	0.96	6,680	2,000
IN60	0.55	383,580	16,000
	Inconel 617 at 704°C		
IN52	1.81	400	220
IN54	0.87	2,531	1,200
IN55	0.55	30,789	6,000
IN54	0.54	89,404	6,800

The effect of thermal aging on the fatigue crack propagation rates in Hastelloy X and Inconel 617 is also under investigation. The status of planned crack growth tests in air is given in Table 4.6.

Table 4.6. Status of crack growth tests[a]

Material[b]	Aging[c]		Test temperature (°C)	Frequency (Hz)	R-ratio[d]	Stress intensity (MPa$\sqrt{m}$)
	Temperature (°C)	Time (h)				
Hastelloy X	704	20,000	650	1	0.05	20–50
Inconel 617	704		650	1	0.05	20–50
Inconel 617	704	20,000	650	1	0.05	20–50

[a]Tests conducted in air.

[b]Material solution annealed and aged as indicated.

[c]Aged in argon.

[d]Ratio of minimum load to maximum load.

4.2.4 Creep Crack Growth — R. W. Swindeman and B. C. Williams

The objective of this work is to develop methods for understanding how the HTGR environment will affect creep crack growth. Earlier, Weerasooriya and Strizak[6] examined creep crack growth in Hastelloy X by using single-edge notch tension (SENT) specimens fabricated as shown in Fig. 4.7. Constant load tests were run in air and HTGR helium at 650°C, and correlations were made between the crack growth rate da/dt and the stress intensity factor K and between the crack growth rate and the net stress σ_{net}. Crack growth rates correlated equally well with both parameters. The creep crack growth rates were found to be greater in air than in HTGR helium. Interpretation of the experimental data was complicated by the severe geometric distortion and the associated eccentric loading produced by crack opening displacement on only one side of the sample. Weerasooriya and Strizak suggested that a center-cracked panel (CCP) specimen might be more suitable for creep crack growth studies. The specimen selected for continuation of the

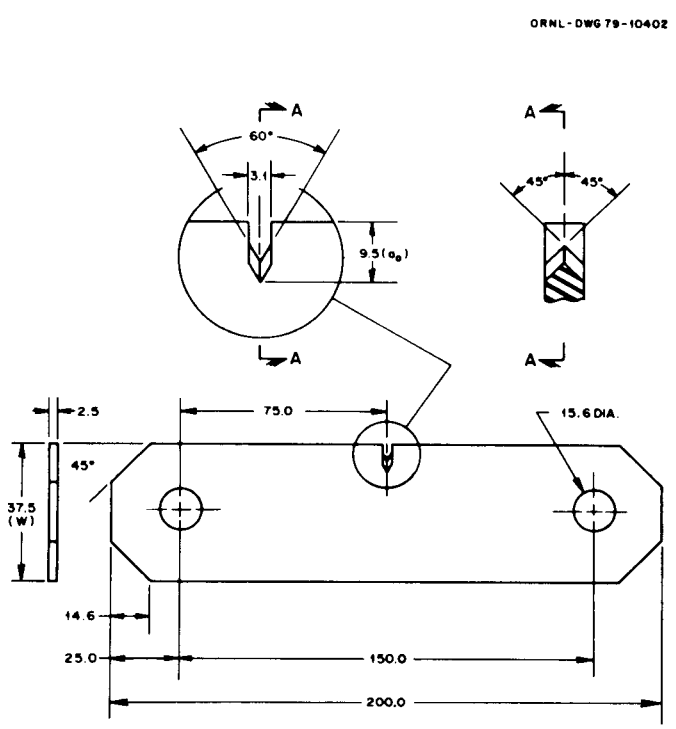

Fig. 4.7. Dimension of single-edge notch tension specimen used for creep crack growth studies.

creep crack growth work is shown in Fig. 4.8. Dimensions are similar to the SENT specimen shown in Fig. 4.7 except that the center crack was used.

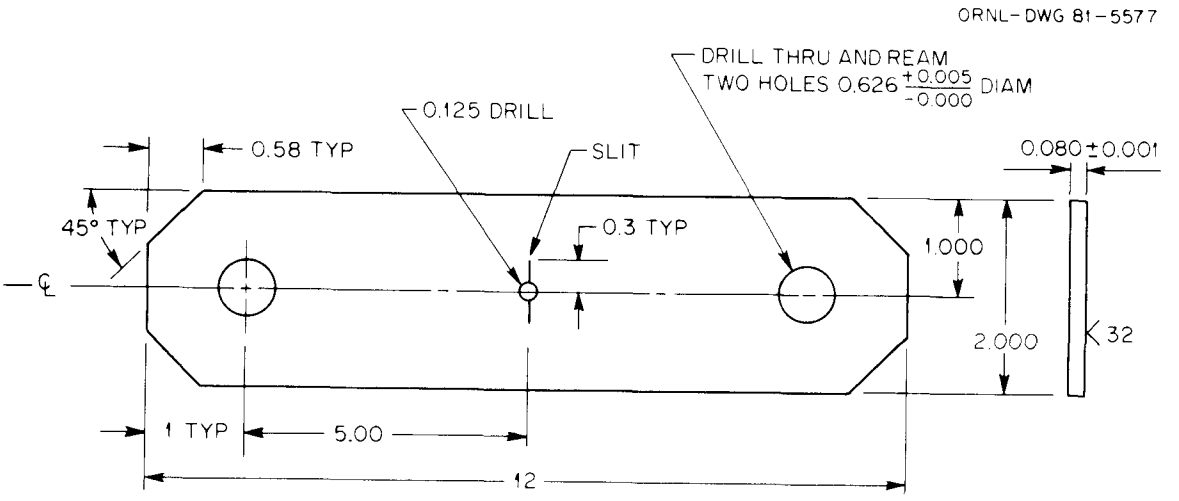

Fig. 4.8. Dimension of a center-cracked panel specimen used for creep crack growth studies.

The specimen was prefatigued to produce cracks about 2 mm deep from either saw-cut. An extensometer was attached to two points centered 25 mm above and below the center hole. The specimen was loaded by pins at an initial net stress near 172 MPa. Periodically, the specimen was cooled to room temperature, and the crack width ($2a$)* and opening displacement (COD) at the center hole were measured with a cathetometer.

A plot of creep elongations versus time is provided in Fig. 4.9, and a plot of COD versus creep strain is provided in Fig. 4.10. From these plots the extensometer appears to provide a good indication of the COD. Examination of the crack tips, however, suggested that the crack was severely blunted and growing in a rather erratic way. Similar observations were made for the SENT specimens.[6] Much of the elongation and increase in COD could be attributed to creep in the ligament ahead of the cracks. For this reason we would expect σ_{net} to be as good as K for correlating the data. We plan to perform one more test on the CCP specimen

*a = half the crack width.

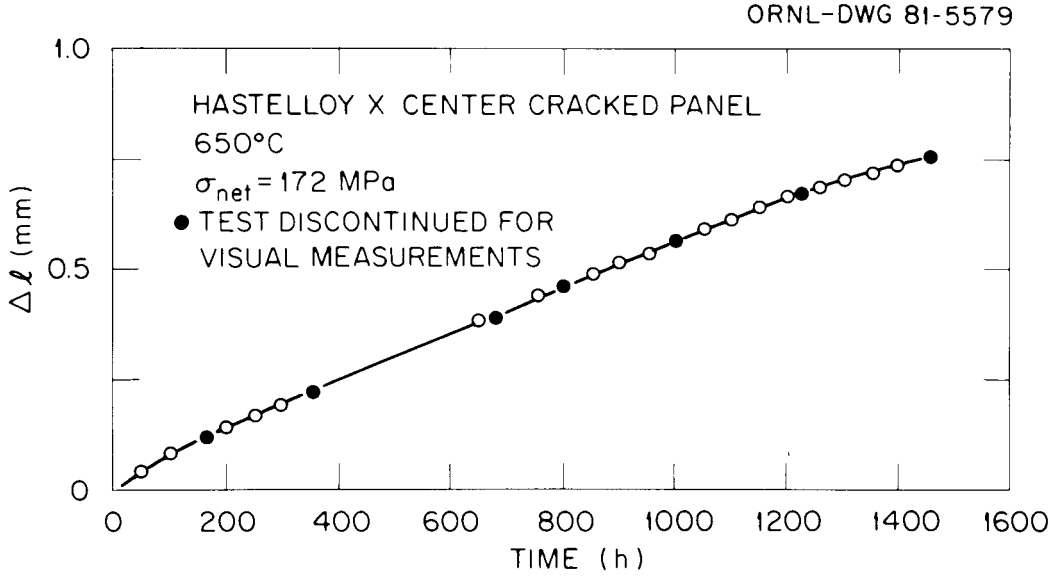

Fig. 4.9. Creep elongation versus time for Hastelloy X center-cracked panel specimen tested at 650°C and 172 MPa net stress.

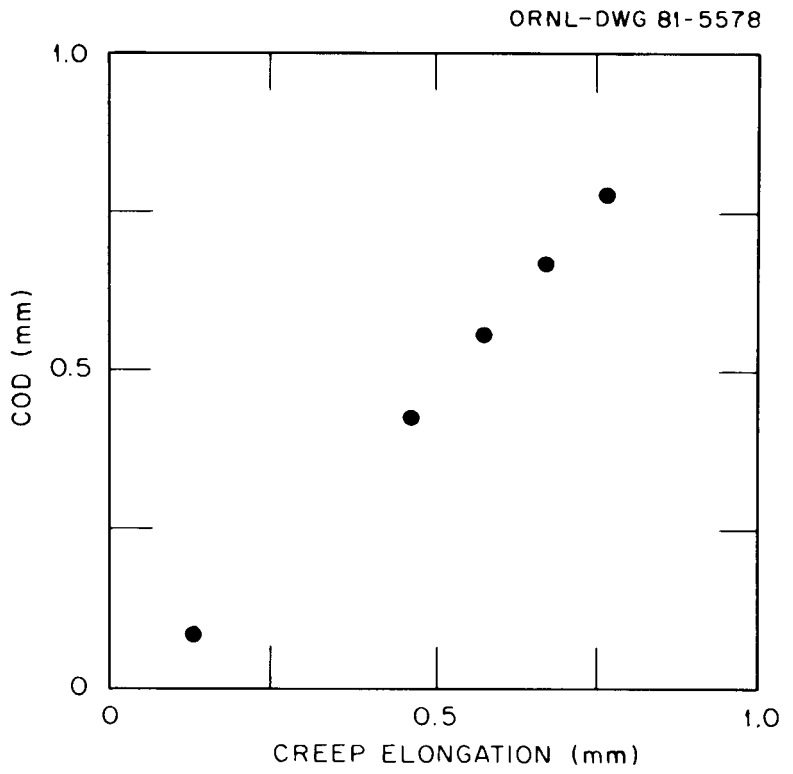

Fig. 4.10. Crack opening displacement (COD) versus creep elongation for Hastelloy X center-cracked panel specimen tested at 650°C and 172 MPa σ_{net}.

(in helium) and to begin tests on side groove compact tension type specimens, to be followed by tests with low-frequency cyclic stresses.

4.2.5 Testing of Ceramics — H. E. McCoy

Testing of ceramics has involved developing equipment for running (1) uniaxial compressive creep tests, (2) four-point bending creep tests, and (3) relaxation tests under four-point loading. All tests are to be carried out in HTGR helium.

Four creep chambers were constructed for running compressive creep tests on 1.01-cm-diam by 3.18-cm-long right circular cylinders of fused SiO_2. Each chamber was constructed of alumina; the internal fixtures were made of Mo-TZM.* Typical test results for Corning 7941 fused SiO_2 are shown in Fig. 4.11. The two tests at 816°C demonstrate the problem of sample-to-sample variation. The results would appear more consistent if the stresses were reversed.

*Arc-cast or powder metallurgy Mo—0.5 wt % Ti—0.1 wt % Zr (TZM type) alloy.

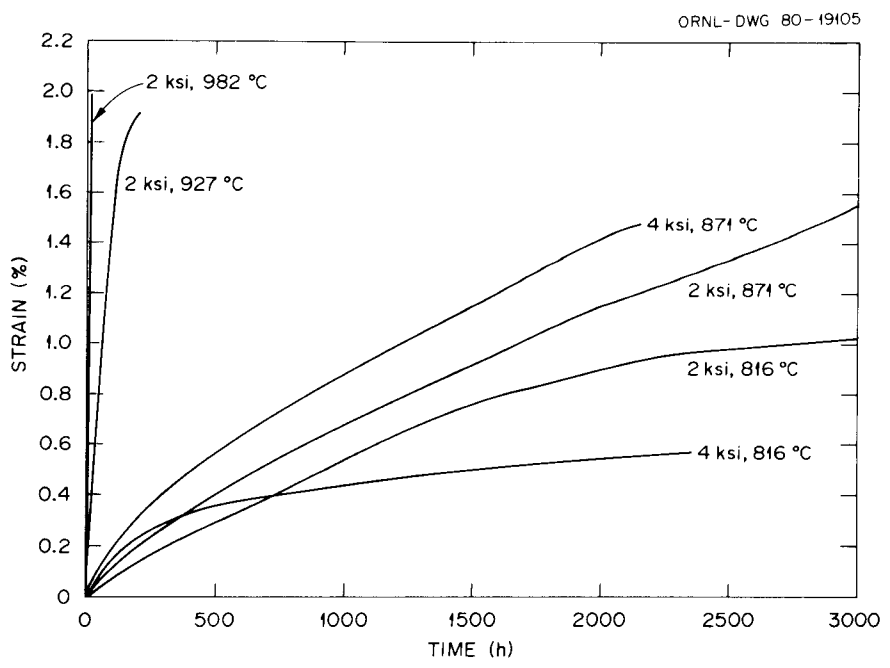

Fig. 4.11. High-precision compressive creep results are available on fused silica; 2 ksi = 13.8 MPa, 4 ksi = 27.6 MPa.

Two test chambers were constructed for performing four-point bend tests. The test fixture is shown in Fig. 4.12 with a sample in place, and the assembled test apparatus is shown in Fig. 4.13. The chamber walls are made of Al_2O_3, and the bend fixture, of Mo-TZM. The only serious experimental problem has been that the dimensional tolerances of the Mo-TZM parts were so close that self-welding occurred if creep movement slowed. This problem has been reduced, if not corrected, by abrading some of the closest fitting surfaces and oxidizing the contacting surfaces. Tests are being run on Si_3N_4.

A system was designed for performing stress relaxation tests on four-point bend specimens. One test system has been fabricated, assembled, and run through initial tests. The system makes use of a high-frequency stepping motor to position the loading train as needed. Initial tests look very promising.

4.3 CORROSION OF HTGR ALLOYS — J. H. DeVan

4.3.1 Steam Corrosion of Engineering Alloys — J. C. Griess

Our steam corrosion program at the Bartow Plant of the Florida Power Corporation was terminated in March 1980 because the operating mode of the plant was changed from base load to peaking, resulting in only sporadic periods of steam generation. All equipment and test specimens were returned to Oak Ridge at that time. We are currently looking for a power plant in which to relocate our facilities and continue the isothermal corrosion studies, which had logged 28,339 h when the program was stopped.

A report summarizing all the isothermal corrosion data obtained in recent years from the Florida operation has been prepared;[7] an abstract of that report follows.

> The oxidation of several chromium-molybdenum steels and austenitic materials in superheated steam at 482 and 538°C (900 and 1000°F) was studied. The investigation was conducted in a once-through loop that received steam from the superheater circuit of the Bartow Power Plant of the Florida Power Corporation. This report presents the results from our investigation, which was terminated after 28,339 h, when the mode of the power plant operation was changed from base load to peaking.
>
> At both temperatures all materials examined exhibited parabolic oxidation kinetics during the first year and

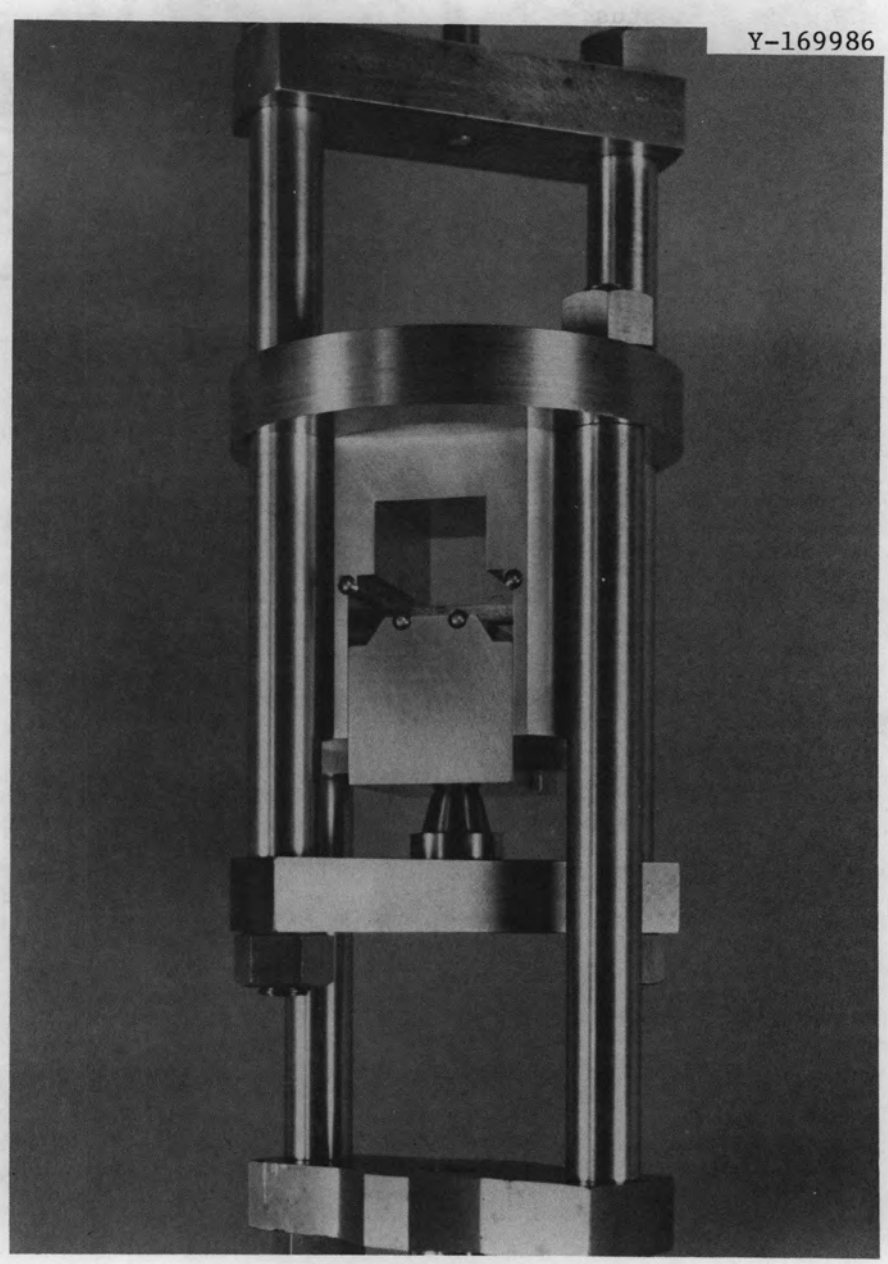

Fig. 4.12. Test fixture for four-point bend tests; fixture is made of Mo-TZM; test sample in place.

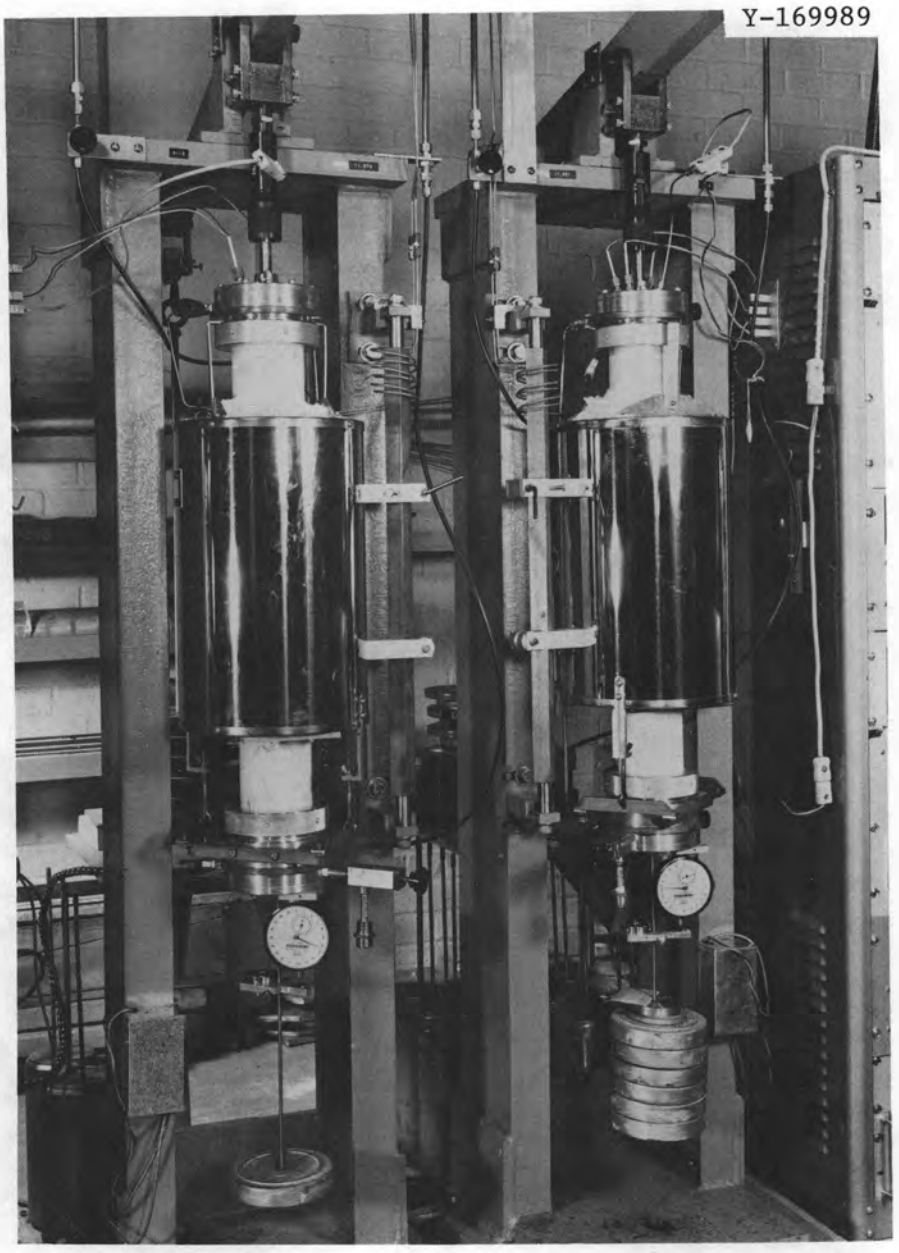

Fig. 4.13. Assembled test stands with four-point bend tests in progress.

subsequently oxidized at constant rates, which were lower than expected from extrapolation of the initial parabolic curves. The chromium-molybdenum steels containing 2 1/4 and 9% Cr oxidized at about the same rate, averaging 3.6 and 8.5 μm/year (0.14 and 0.33 mils/year) at 482 and 538°C, respectively, after the first year. Sandvik HT-9 (11.4% Cr) corroded at only slightly lower rates. Oxidation rates were nearly independent of surface condition, but in two cases the presence of mill scale on the surface before steam exposure seemed to retard oxidation. All chromium-molybdenum steels developed two layered scales in which the ratio of the thickness of the outer to the inner layer was 1.3, independent of alloy composition, exposure time, and temperature. At 482°C only one of many specimens showed evidence of exfoliation, but at 538°C exfoliation occurred on some specimens of most chromium-molybdenum steels; the exceptions were the alloy with the highest chromium content (Sandvik HT-9), one heat of 9 Cr-1 Mo steel with the highest silicon content, and Sumitomo 9 Cr-2 Mo, which was in test for only 19,345 h.

Cold-worked surfaces of alloy 800 corroded at lower rates than did annealed and pickled ones, but in both cases the rates were very low. Alloy 800 specimens that had intergranular penetrations before exposure to steam corroded at much higher rates. Type 304 stainless steel oxidized nonuniformly, but the total extent of damage was low at both temperatures. Alloy 617 oxidized at the lowest rate of any material; even after 28,339 h surface films were thin enough to show interference colors.

4.3.2 Oxidation-Carburization-Vaporization in HTGR Helium — H. Inouye

This task is that of characterizing the corrosion behavior of selected alloys in an attempt to understand the processes that occur and to identify the variables that control the extent of these processes. Specifically, the corrosion runs described below determine the reason(s) for wide variability of the carburization rates under exposure conditions considered to be equivalent. For example, we reported in our 1979 annual report[8] that Hastelloy X and Incoloy 800H carburize at a rate that increases with the exposure time after a slower incubation period of 1000 to 2000 h, in contrast to a parabolic or a linear-parabolic time dependence deduced by Lupton.[9] As a consequence of this "breakaway" carburization rate, the carbon uptake by these alloys in our experiments was up to an order of magnitude greater than that observed by Lupton. Dean[10] also observed similar differences in the carburization of several alloys in experiments he conducted at different times.

4.3.2.1 Variability of Carbon Potential of Flowing HTGR Helium in Retorts

The carburization of Hastelloy X, Incoloy 800H, and pure iron is not only dependent on the exposure time and temperature but is strongly influenced by the position of the corrosion specimens in the retort relative to the direction of the HTGR-helium flow and the location of corrosion specimens relative to each other. At the same flow rate and entering test gas composition, the carburization of Hastelloy X is up to a factor of 2 lower when the flow direction is up a temperature gradient rather than vice versa, as indicated by the data in Table 4.7. Further insight of the variability of the test gas is provided by the results in Table 4.8. These tables show that the carburization of Incoloy 800H can vary by a factor as high as 9, depending on whether or not there are upstream specimens present to react with the impurities in the helium. Iron foils exposed simultaneously with both Hastelloy X and Incoloy 800H specimens show that the upstream positions are more carburizing than the downstream positions and that the difference in the carburization rates between these positions increases with the P_{H_2O} (Table 4.9).

Table 4.7. Effect of HTGR helium flow direction on the carburization of Hastelloy[a]

Exposure temperature (°C)	Average carburization rate, μg/(cm^2·h)	
	He flows from 850 to 1000°C[b]	He flows from 1000 to 850°C[c]
850	0.172	0.275
900	0.219	0.223
1000	2.174	4.470

[a]Partial pressures: H_2, 50.7; CH_4, 5.1; CO, 3.9; and H_2O, 0.02 Pa (H_2, 500, CH_4, 50; CO, 38; and H_2O, 0.2 μatm); flow of 1 L/min (23 mm/s velocity). System pressure: 136 kPa (1.34 atm).

[b]2000-h exposure.

[c]2500-h exposure.

Table 4.8. Effect of upstream corrosion specimens on the corrosion of Incoloy 800H[a]

Exposure temperature (°C)	Carburization rate [μg/(cm^2·h)]	Weight gain [μg/(cm^2·h)]
	No specimens upstream[b]	
850	0.174	0.316
900	0.282	0.298
950		0.688
1000	0.292	0.365
	Specimens upstream[c]	
850	0.051	0.353
900	0.182	0.133
950		0.431
1000	2.548	2.572

[a]Partial pressures: H_2, 50.7; CH_4, 5.1; CO, 3.9; and H_2O, 0.02 Pa (H_2, 500; CH_4, 50; CO, 38; and H_2O, 0.2 μatm); flow of 1 L/min (23 mm/s velocity) flowing at 1000 to 850°C. System pressure: 136 kPa (1.34 atm).

[b]2500-h exposure.

[c]2000-h exposure.

Table 4.9. Dependence of the carburization rate of iron foils on their position in a retort[a]

Exposure condition			ΔC, carbon increase, 10^{-4}%/h	
Temperature (°C)	P_{H_2O}[b] [mPa(μatm)]	Time (h)	Upstream	Downstream
950	30 (0.3)	700	1.8	2.9
950	20 (0.2)	2000	4.2	5.6
950	10 (0.1)	4000	5.7	6.8

[a]Partial pressures: H_2, 50.7; CH_4, 5.1; and CO, 3.9 Pa (H_2, 500; CH_4, 50; and CO 38 μatm); flow of 1 L/min (23 mm/s velocity). System pressure: 136 kPa (1.34 atm).

[b]Entering gas.

4.3.2.2 Effect of P_{H_2O} on Carburization

Table 4.10 summarizes the effects of varying the P_{H_2O} from 20 to 140 mPa (0.2 to 1.4 μatm) on the carburization of Hastelloy X and Incoloy 800H. These data show that the critical level of P_{H_2O} (which determines whether carburization or decarburization occurs) lies between these limits at 1000°C. Because the downstream specimens (i.e., at 950°C and lower) do not show dependency on the P_{H_2O}, we concluded that the 1000°C specimens (two specimens totaling 10 cm^2) had depleted all the entering H_2O in the helium at supply rates as high as 200 $cm^3/(cm^2 \cdot min)$.

4.3.2.3 Oxidation and Vaporization

Table 4.11 summarizes the mass balance of the corrosion processes based on weight gain, carbon, and oxygen analyses. These data show that the weight gain is consistently less than that accounted for by carburization and oxidation and suggest that vaporization is also part of the corrosion process. Furthermore, a metallic deposit has been observed near the entrance of the corrosion retort after several months of corrosion testing in the closed loop system. It is currently thought that the deposit originated from the decomposition of a metal carbonyl.

4.3.3 Mechanical Property—Corrosion Interactions — H. Inouye

Stress generation in alloy surfaces induced by carburization was proposed as the reason that the creep rates of alloys tend to be higher in HTGR helium than in air and that carburized corrosion specimens dilate.[8] Experimental data in support of the proposed phenomenon have been presented in greater detail elsewhere.[11] Dilation data for Hastelloy X and Incoloy 800H with their corresponding weight changes and carburization levels are presented in Table 4.12. These data also illustrate the reproducibility problems described in Sect. 4.3.2; however, within a given run, the dilation ΔL appears to follow the carbon uptake ΔC. The relationship between ΔL and ΔC, while not that apparent in Table 4.12, is clarified by Fig. 4.14. The plot shows that most of the dilation data (irrespective of exposure time, temperature, or alloy) fall within a scatter band showing the approximate relationship $\Delta L \propto C^n$, where $n < 1$.

Table 4.10. Effect of H_2O on the carburization of Hastelloy X and Incoloy 800H in HTGR helium[a]

Exposure temperature (°C)	ΔC, carbon change, μg/cm^2	
	20 mPa (0.20 μatm) H_2O[b]	140 mPa (1.4 μatm) H_2O[c]
	Hastelloy X[d]	
750	122	122
800	314	306
850	687	542
900	558	875
950	1210	2,090
1000	11,170	-623
	Incoloy 800H[e]	
750	173	363
800	472	451
850	434	442
900	704	442
950	1,219	1,453
1000	731	-767

[a]0.635 mm-diam by 22.2 mm-long rod specimens exposed for 2500 h. HTGR helium flowing from 1000 to 750°C.

[b]Partial pressures: H_2, 50.8; CH_4, 5.0; CO, 3.9; CO_2, 0.00; and H_2O, 0.02 Pa (H_2, 501; CH_4, 49; CO, 38; CO_2, 0.00; and H_2O, 0.2 μatm at a helium flow velocity of 23 mm/s (1000 cm^3/min). System pressure: 136 kPa (1.34 atm).

[c]Partial pressures: H_2, 50.6; CH_4, 5.1; CO, 3.9; CO_2, 0.00; and H_2O, 0.14 Pa (H_2, 499; CH_4, 50; CO, 38; CO_2, 0.00; and H_2O, 1.4 μatm) at a helium flow velocity of 46 mm/s (2000 cm^3/min). System pressure: 136 kPa (1.34 atm).

[d]Initial carbon content of 805 ppm.

[e]Initial carbon content of 795 ppm.

Table 4.11. Mass balance of Hastelloy X and Incoloy 800H exposed 2500 h to HTGR helium containing 140 mPa (1.4 μatm) H_2O[a]

Exposure temperature (°C)	ΔW, weight change (μg/cm^2)	Δ carbon (μg/cm^2)	Δ oxygen (μg/cm^2)	$\Delta W-(\Delta C + \Delta O)$ (μg/cm^2)
	Hastelloy X			
750	129	122	66	−59
800	381	306	143	−68
850	520	542	238	−260
900	987	875	390	−278
950	1392	2090	130	−828
1000	−267	−623	360	−4
	Incoloy 800H			
750	405	363	223	−181
800	576	451	271	−146
850	548	442	203	−97
900	526	442	226	−142
950	888	1453	346	−911
1000	−641	−767	1273	−1147

[a]Partial pressures: H_2, 50.6; CH_4, 5.06; CO, 3.82; CO_2, 0.00 and H_2O, 0.14 Pa (H_2, 499; CH_4, 49.9; CO, 37.7; CO_2, 0.00; and H_2O, 1.4 μatm); flow from 1000 to 750°C at 2L/min. System pressure: 136 kPa (1.34 atm).

Table 4.12. Summary of dilation experiments on Hastelloy X and Incoloy 800H[a]

Gas Composition,[b] Pa (μatm)					Temperature (°C)	Hastelloy X[b]			Incoloy 800H[c]		
H_2	CH_4	CO	CO_2	H_2O		W (μg/cm²)	C (μg/cm²)	L (%)	W (μg/cm²)	C (μg/cm²)	L (%)
					1200 h (run 1)						
51.0	5.0	3.9	0.0036	0.03	734	177	42	0.11	459	177	0.061
(504)	(49)	(38)	(0.036)	(0.3)	828	366	199	−0.05	752	329	0.097
					854	516	330	−0.14	643	390	0.012
					902	609	389	−0.036	592	314	0.109
					946	364	483	0.084	862	383	−0.024
					2041 h (run 2)						
51.2	5.03	3.64	0.0034	0.02	847	710	344	0.347	811	102	0.240
(505)	(49.6)	(35.9)	(0.034)	(0.2)	897	752	438	0.538	646	364	0.286
					996	8,423	4,347	0.934	4,963	5,095	0.741
					3997 h (run 2)						
50.9	5.07	3.70	0.0043	0.01	748	626	432	−0.07	545	400	0.02
(502)	(50.0)	(36.5)	(0.042)	(0.1)	798	671	536	0	931	190	0.28
					847	869	699	0.16	910	164	0.04
					896	894	1,996	0.23	497	626	−0.06
					952	9,296	9,923	0.47	3,768	4,396	0.12
					997	17,280	15,255	0.60	12,850	13,830	0.48
					1500 h (run 3)						
51.3	5.14	3.93	0.003	0.01	850	429		−0.089	756		−0.068
(506)	(50.7)	(38.8)	(0.03)	(0.1)	900	490		−0.140	490		0.027
					950	672		−0.069	744		0.053
					1,000	5,467		0.070	3,690		0.205
					2434 h (run 3)						
50.8	5.03	3.69	0.001	0.01	850	565		−0.089	882		−0.068
(501)	(49.6)	(36.4)	(0.01)	(0.1)	900	706		−0.068	333		−0.048
					950	1,039		−0.070	1,078		0.013
					1,000	12,470		0.364	6,430		0.526
					3494 h (run 3)						
50.9	5.15	3.71	0.001	0.01	850	698	459[a]	0.007	967	900	−0.034
(502)	(50.8)	(36.6)	(0.01)	(0.1)	900	764	715	−0.056	−75	608	0.095
					950	1,382	1,593	−0.063	1,084	1,526	0.067
					1,000	19,286	17,504	0.644	8,337	8,282	0.396
					2500 h (run 5)						
50.8	4.96	3.86	0.00	0.02	750	237	122	−0.036	395	173	−0.061
(501)	(49.0)	(38.1)	(0.00)	(0.2)	800	591	314	0.024	867	472	0
					850	1,126	687	−0.024	789	432	0.012
					900	947	558	0.061	746	704	0.109
					950	1,756	1,210	0.120	1,671	1,219	0.073
					1,000	12,524	11,167	0.636	965	731	0.061
					2496 hd (run 4, ph 4 + 1.4 μatm H_2O)						
50.6	5.06	3.82	0.00	0.1	750	129	122	0.027	405	363	−0.054
(499)	(49.9)	(37.7)	(0.00)	(1.4)	800	381	306	−0.049	576	451	−0.040
					850	592	542	−0.067	548	442	0.013
					900	987	875	−0.100	526	442	0.094
					950	1,392	2,090	−0.040	888	1,453	0.040
					1,000	−267	−623	−0.067	−641	−767	0.053

[a]Flow rate of 1 L/min. System pressure: 136 kPa (1.34 atm).

[b]Time-compensation average.

[c]ΔW, ΔC, ΔL = weight, carbon, length changes, respectively.

[d]Flow rate of 2 L/min.

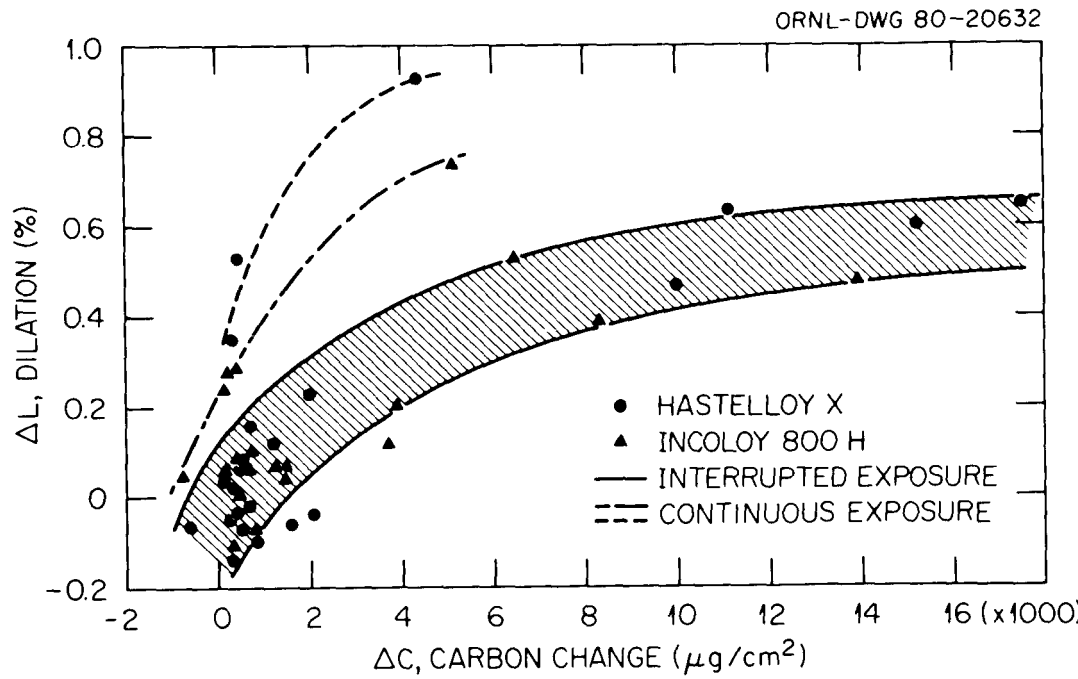

Fig. 4.14. Dilation versus carbon change in HTGR helium.

The data in the scatter band are from specimens that were interrupted in the test to measure dilation or to remove other specimens. The two curves above the scatter band represent data for specimens that were continuously exposed to the HTGR helium. Interpretation of these differences in terms of the dilation model suggests that the magnitude of stress in the alloy surfaces is not constant but goes through a maximum before saturation. Stress relaxation on cooling and reheating the corrosion specimens may account for the lower dilation levels in the specimens from interrupted tests.

Additional characteristics of carburization-induced stress are provided by Figs. 4.15 and 4.16. A plot of ΔL versus exposure time (Fig. 4.15) at 1000°C in dry HTGR helium [20 mPa (0.2 μatm) H_2O] shows that both alloys exhibit an incubation period of about 1000 h, achieve maximum dilation rates between 1500 and 2500 h, and level off to a constant value beyond 2500 h. Corresponding carbon concentration gradients in Hastelloy X calculated by a method previously described[12] are shown in Fig. 4.16. This plot shows that about 2000 h is required for the diffusing carbon to

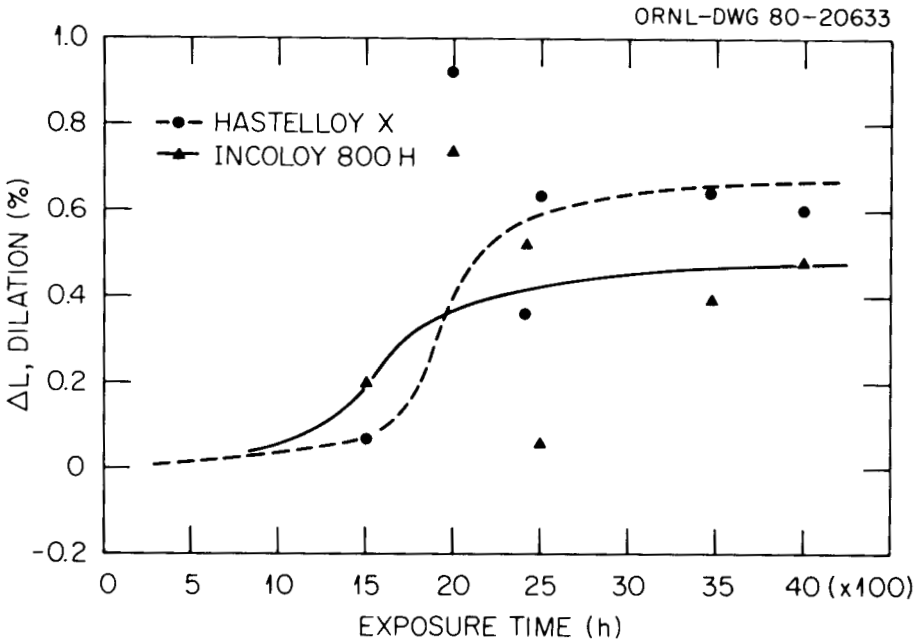

Fig. 4.15. Dilation versus exposure time in HTGR helium with 0.2 μatm (0.02 Pa) H_2O.

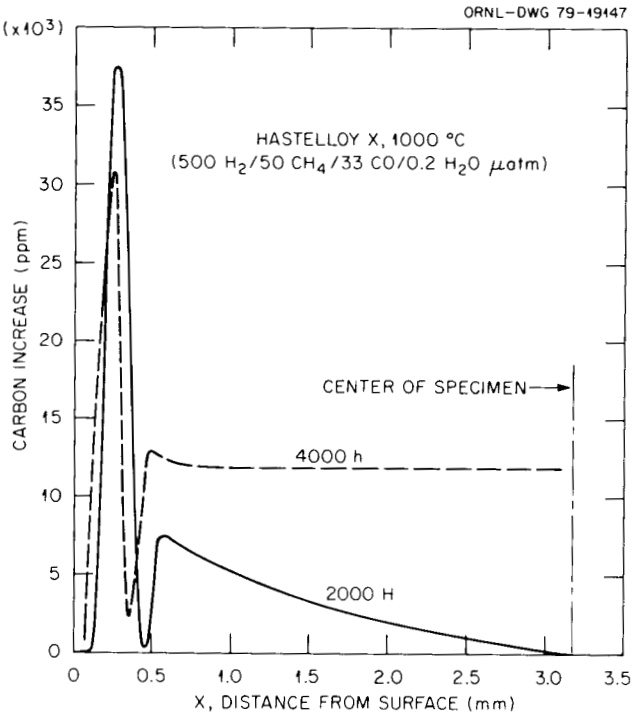

Fig. 4.16. Carbon gradient resulting from the exposure of Hastelloy X to HTGR helium; 1 μatm = 0.101 Pa.

reach the center of the cylindrical specimen (i.e., a penetration depth of 3.175 mm) and that no carbon gradient exists after a 4000-h exposure (except for the anomalous carbon peak near the surface). The disappearance of the carbon gradient in Fig. 4.16 between 2000 and 4000 h coincides with the leveling out of the ΔL versus time curves in Fig. 4.15. The proposed carburization-induced stress model in alloys is supported by experimental data: (1) the creep rates of several alloys are higher in HTGR helium than in air[13] and are increased by increasing the surface-to-volume ratio of the specimen[14] and (2) dilation occurs without an applied mechanical stress.

4.3.4 Gas Composition Studies — H. Inouye

Depletion and generation of impurities in HTGR helium are observed whenever alloys are corrosion tested in retorts. However, the significance of these test gas perturbations is not well documented (i.e., the relationship between carburization rates and the impurity supply rates has been mentioned as another important test variable,[15] but no experiments have been run to confirm this). Sections 4.3.2 and 4.3.3 provide ample evidence that ignoring this factor can lead to quite different appraisals of the corrosion behavior of Hastelloy X and Incoloy 800H.

The data presented in Sect. 4.3.2 clearly show that the H_2O level in the HTGR helium is probably the most important factor controlling the carburization of alloys, particularly in the range under 150 mPa (1.5 μatm) where its measurement and control become difficult. Extensive calibration runs and measurements of P_{H_2O} with a Panametrics 2000 hygrometer indicate that measurement capabilities to a minimum value of about 5 mPa (0.05 μatm) are achievable; however, controlling H_2O depletion during corrosion testing in retorts may prove to be quite difficult. For example, the depletion of CH_4 and the generation of H_2 and CO in an empty ceramic retort provide evidence that H_2O reacts with CH_4. The probable reaction, $CH_4 + H_2O \rightarrow 3H_2 + CO$, begins at about 800°C and becomes increasingly significant as the temperature is increased to 1000°C (Table 4.13). In addition to being temperature dependent, this reaction is also influenced by the residence time in the retort (i.e., the flow rate) which, according to Table 4.14, becomes insignificant at flow rates exceeding 2 L/min.

Table 4.13. Gas phase reactions in HTGR helium[a]

Retort temperature[b] (°C)	Concentration change: outlet—inlet, Pa (μatm)		
	H_2	CH_4	CO
22	0.02 (0.2)	0.1 (0.7)	0.0 (0.0)
500	1.14 (11.3)	0.1 (0.5)	0.1 (0.9)
800	−0.59 (−5.8)	−0.20 (−2.0)	0.17 (1.7)
900	1.9 (19.0)	−0.88 (−8.7)	0.31 (3.1)
950	1.07 (10.6)	−1.33 (−13.1)	1.13 (11.2)
1000	3.95 (39.0)	−1.61 (−15.7)	1.32 (13.1)

[a]Approximate partial pressures: H_2, 50.66; CH_4, 5.1; CO, 3.6; and H_2O, 0.15 Pa (H_2, 500; CH_4, 50; CO, 36; and H_2O, 1.5 μatm); flow rate of 100 cm^3/min in empty mullite tube (no metal components). System pressure: 136 kPa (1.34 atm).

[b]127-cm flow distance at uniform temperature; residence time = 552 s.

Table 4.14. Effect of flow conditions on gas phase reactions at 1000°C[a]

HTGR helium flow conditions			Concentration change: outlet—inlet, Pa (μatm)		
Rate (L/min)	Velocity (mm/s)	Residence time (s)	H_2	CH_4	CO
0.1	2.3	552	4.0 (39)	−1.59 (−15.7)	1.32 (13.1)
1.0	23	55.2	0.2 (2)	−0.60 (−5.9)	−0.19 (−1.9)
2.0	46	27.6	−0.2 (−2)	−0.27 (−1.7)	0.13 (1.3)
5.0	115	11.0	−0.1 (−1)	−0.17 (−1.5)	−0.03 (−0.3)
10.0	230	5.5	0.7 (7)	0.1 (0.8)	0.1 (0.6)

[a]Partial pressures: H_2, 50.66; CH_4, 5.1; CO, 3.7; and H_2O, 0.15 Pa (H_2, 500; CH_4, 50; CO, 36; and H_2O, 1.5 μatm) in helium flowing in empty mullite tube. System pressure: 136 kPa (1.34 atm).

In the presence of corrosion specimens, however, depletion of CH_4 and generation of H_2 and CO are still measurable even after no trace of H_2O can be detected in the exit gas. This is true at flow rates as high as 10 L/min (Table 4.15).

Table 4.15. Effect of supply rate on generation/depletion of HTGR helium impurities at 1000°C[a]

GCR helium flow conditions		Concentration change: outlet–inlet, Pa (μatm)			
Flow rate (L/min)	Supply rate [$cm^3/(cm^2/min)$]	H_2	CH_4	CO	H_2O
0.5	5.4	7.6 (75)	−3.52 (−34.7)	1.46 (14.4)	[b]
1.0	10.9	6.3 (62)	−1.88 (−18.6)	1.29 (12.7)	[b]
2.0	21.7	3.7 (36)	−1.55 (−15.3)	0.78 (7.7)	[b]
5.0	54.3	2.6 (26)	−0.52 (−5.1)	0.42 (4.1)	−0.1 (−1.0)
10.0	108.6	1.5 (15)	−0.32 (−3.2)	0.29 (2.9)	−0.1 (−1.0)

[a]92 cm^2 of corrosion specimens exposed to inlet HTGR helium containing H_2, 51.37; CH_4, 5.3; CO, 5.6; and H_2O, 0.10 Pa (H_2, 507; CH_4, 52; CO, 55; and H_2O, 1.0 μatm). System pressure: 136 kPa (1.34 atm).

[b]Not measured.

4.4 JOINING TECHNOLOGY — G. M. Goodwin and J. F. King

Advanced gas-cooled reactor system designs call for reactor outlet temperatures of 850°C or higher. Materials screening test programs have suggested some alloys that possess elevated-temperature mechanical properties, oxidation resistance, and carburization resistance sufficient for their application in the impure helium environments of these advanced systems. These materials include cast nickel-base superalloys, mechanically alloyed oxide-dispersion-strengthened (ODS) alloys, and some nickel-base wrought alloys possibly modified to improved carburization resistance. Fabrication of the various reactor components will depend to a large extent on welding, and many of these materials are difficult to join. We have examined the fusion weldability of materials from each of the three types being considered. These are modified Inconel 617 wrought alloys, IN-100 and alloy 713LC cast alloys, and MA956 ODS alloys.

4.4.1 Weldability of Modified Inconel 617 Alloys — J. F. King

Three experimental alloys were obtained for evaluation of their carburization resistance in HTGR helium. These alloys were basically the Inconel 617 composition with titanium additions and variations in the

chromium content. The chemical composition of these three alloys are listed in Table 4.16. Determination of the weldability of these materials was desired to prevent long-term aging and characterization of an alloy that had poor fabrication characteristics. Weldments were also included in the aging study, and a brief evaluation was performed.

Table 4.16. Chemical composition of experimental alloys

Element	Content, wt %		
	Composition 1	Composition 2	Composition 3
C	0.059	0.051	0.066
S	0.002	0.001	0.001
Mn	0.03	<0.01	<0.01
Si	0.07	0.07	0.06
Cr	22.74	16.19	12.44
Mo	9.43	9.26	9.03
Co	12.10	12.21	12.22
Ti	1.98	1.75	1.79
Al	0.04	0.05	0.03
B	0.001	<0.001	0.001
Fe	0.07	0.03	0.03
Cu	0.01	0.02	0.04
Ni	Balance	Balance	Balance
P	0.001	0.001	0.001

Tests welds were made in 12.5-mm-thick plates from each of the three compositions. Filler wire was fabricated directly from plates of each composition. All three alloys were then successfully joined by using the gas tungsten arc welding (GTAW) process. We concluded that the welding characteristics of these materials were very similar to Inconel 617. Side-bend test coupons from each weldment revealed no indications of cracking and showed that all possess good room temperature ductility.

These preliminary results indicated that all three alloys had good fabrication characteristics. Plate weldment specimens were prepared for the aging studies. More detailed weldment characterization will be necessary in the future if any of these alloys are found to possess mechanical property and corrosion resistance characteristics that make them promising for HTGR applications.

4.4.2 Welding of Cast Nickel—Base Superalloys — J. F. King

We initiated a program to develop fusion welding techniques applicable to cast nickel—base superalloys. Solid state joining processes, diffusion welding, and brazing may have merit for joining these alloys, but larger components will probably require fusion welding processes for successful fabrication.

Two cast, precipitation hardenable nickel-base alloys were obtained for the welding evaluation: alloy 713LC and IN-100 with the nominal compositions in Table 4.17. Slices were cut from ingots to provide specimens for the welding tests, and welds were made on the two alloys in the as-cast condition.

Table 4.17. Chemical composition of alloys used in welding investigation

Element	Nominal composition, wt %	
	Alloy 713LC	IN-100
Nickel	74	60
Chromium	12	10
Cobalt		15
Molybdenum	4.5	3.0
Niobium	2.0	
Aluminum	5.9	5.5
Titanium	0.6	4.7
Carbon	0.12	0.18
Boron	0.01	0.014
Zirconium	0.1	0.06
Vanadium		1.0

The initial welding trials for these two cast materials were made by using the electron beam welding (EBW) process. These partial penetration welds showed IN-100 to be extremely crack sensitive (Fig. 4.17) and alloy 713LC to be better suited to welding (Fig. 4.18). A similar test was made with the GTAW process. Low heat input bead-on-plate weld deposits were made on each alloy with Inconel 617 filler metal. Inconel 617 does not possess high-temperature properties similar to those of the two cast alloys and would therefore not be suitable for most applications requiring these properties. Inconel 617 was used for experimental purposes to produce sound weld deposits and to provide heat affected zones (HAZs) for examination of hot cracking. We found that the IN-100 weldment contained considerable HAZ hot cracking but observed none in alloy 713LC, as shown in Fig. 4.19. From these two welding experiments, we concluded that alloy 713LC offered the best potential for being successfully joined and therefore selected it for continued study.

Welding thicker sections of crack-sensitive materials generally increases the cracking problems because of the higher restraints placed on the weldment. Plate specimens of 10-mm-thick alloy 713LC were prepared and welded by using the EBW process. Extensive weld hot cracking was observed in the initial welds made in this thickness. Further work with this process showed welding parameters that produce high depth-to-width ratio fusion zones to be beneficial in reducing weld cracking. Figure 4.20 shows this weld configuration. Weld cracking was confined mainly to the upper portion of the weld bead. The lower parallel side fusion zone contained very few cracks, but some small fissures were present similar to those in Fig. 4.21. These were predominantly in the fusion zone but extended into the HAZ.

Gas tungsten arc welding was also used to join 10-mm-thick alloy 713LC. Again, Inconel 617 filler metal was used to join this alloy. The weld was completed with little difficulty and had the cross sectional appearance shown in Fig. 4.22. No restraint was placed on the base-metal sections being joined in this weldment. Examination of the weld HAZ (Fig. 4.23) showed that considerable hot cracking had occurred. This weldment and the previous electron beam weld in the thicker sections indicate the difficulties encountered as base-metal thickness increases.

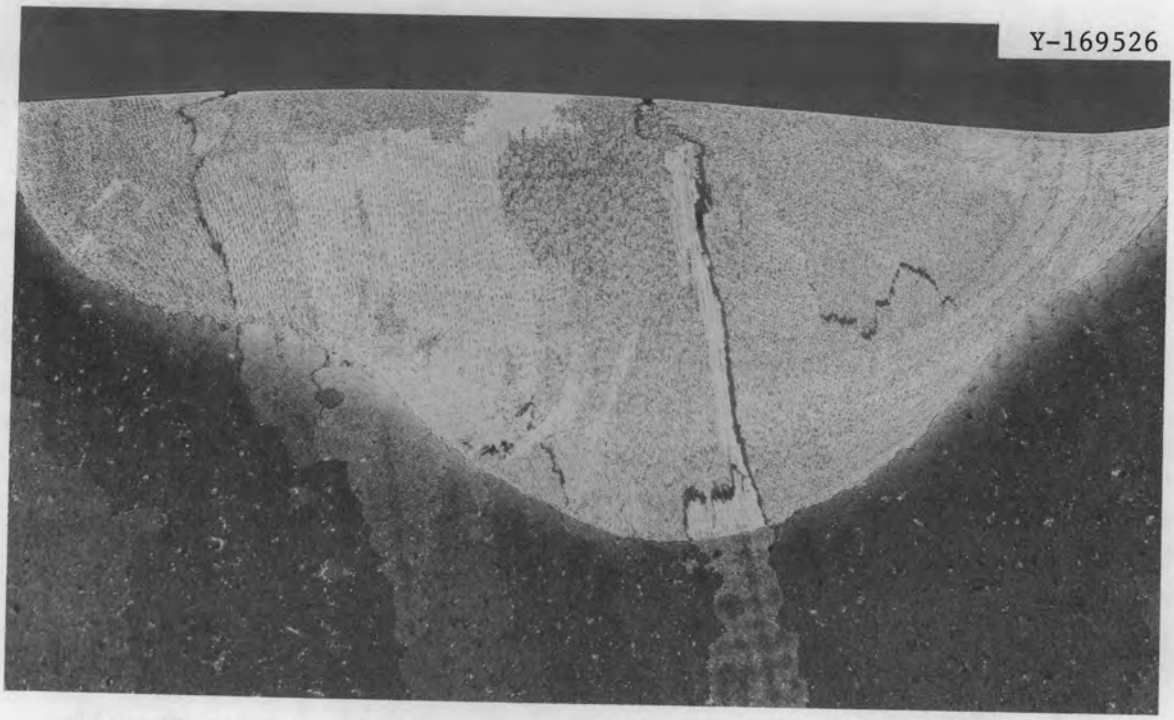

Fig. 4.17. A partial penetration electron beam weld on IN-100 alloy revealed it to be highly crack sensitive.

0.5 mm

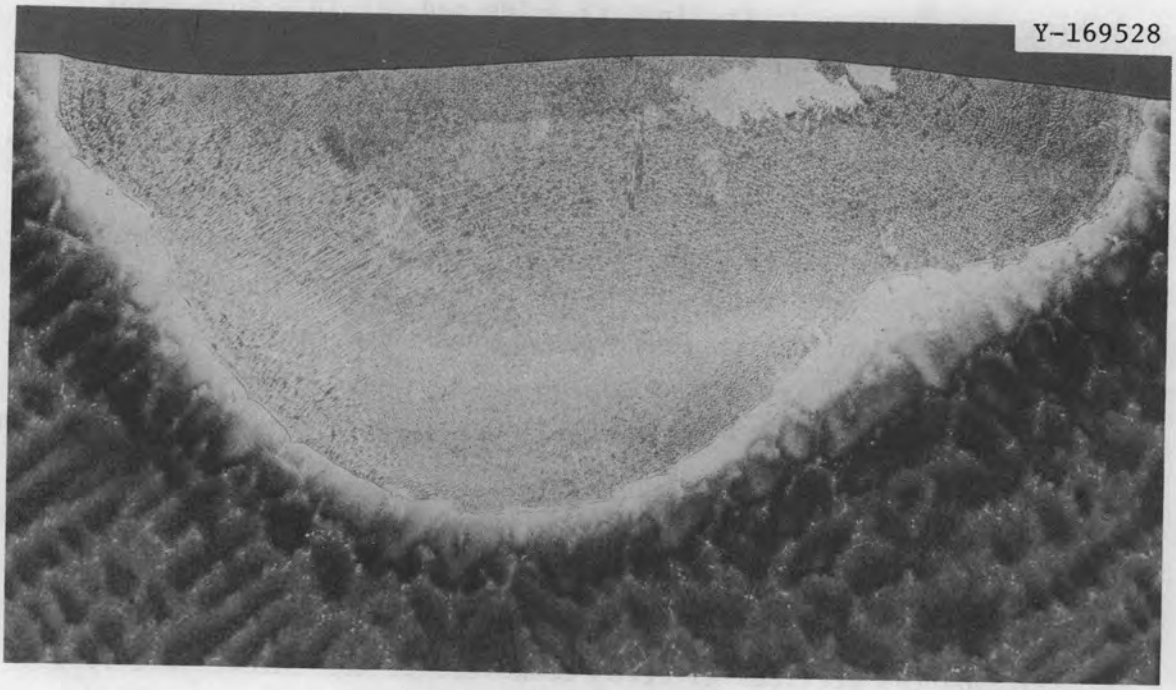

Fig. 4.18. The electron beam welding process was successfully used on alloy 713LC with no evidence of cracking in a partial penetration weld.

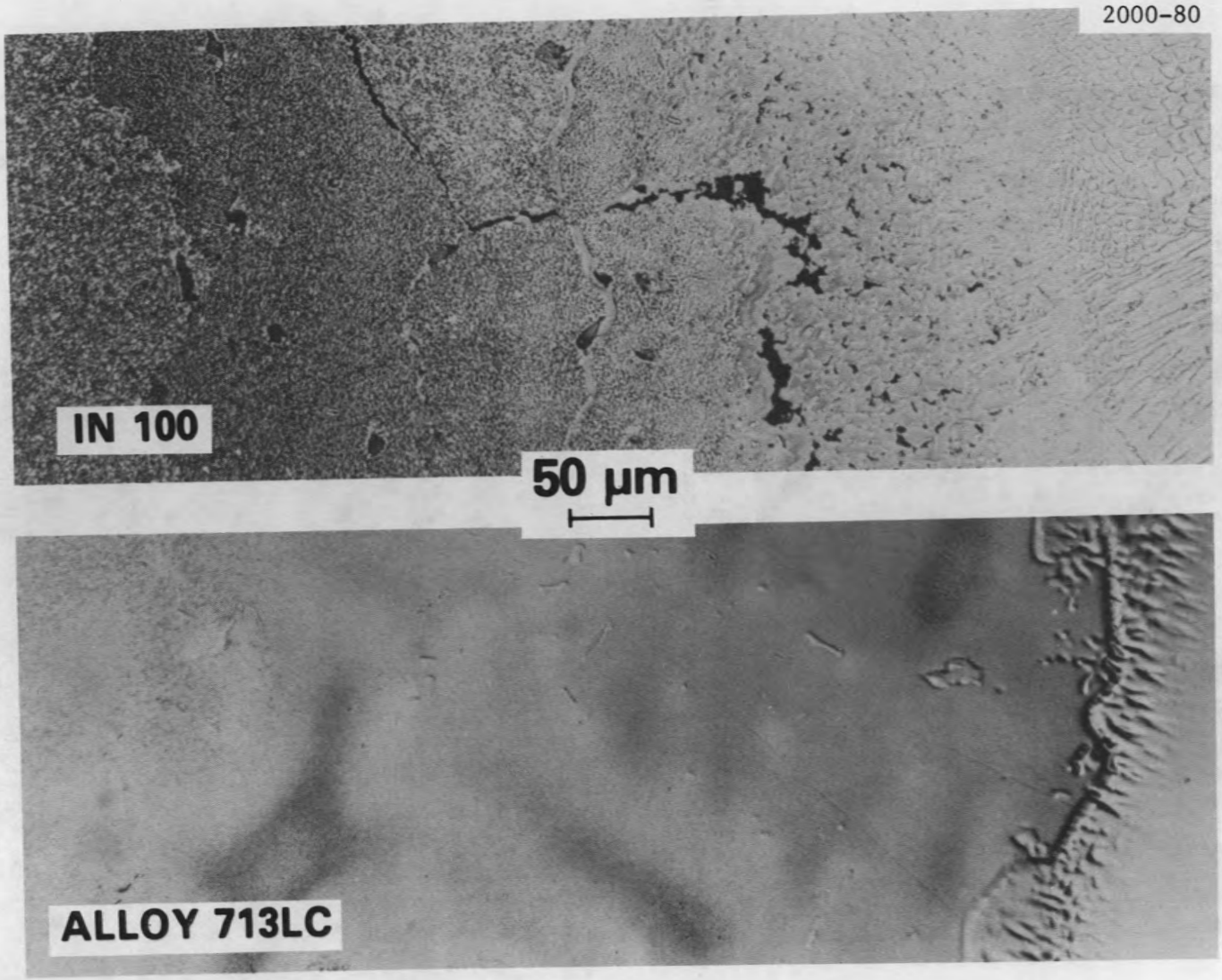

Fig. 4.19. Gas tungsten arc deposits of Inconel 617 on IN-100 and alloy 713LC. Hot cracking was prevalent in the heat-affected zone of the IN-100.

Fig. 4.20. Electron beam welding parameters that produce high depth-to-width ratio fusion zones reduced cracking in alloy 713LC.

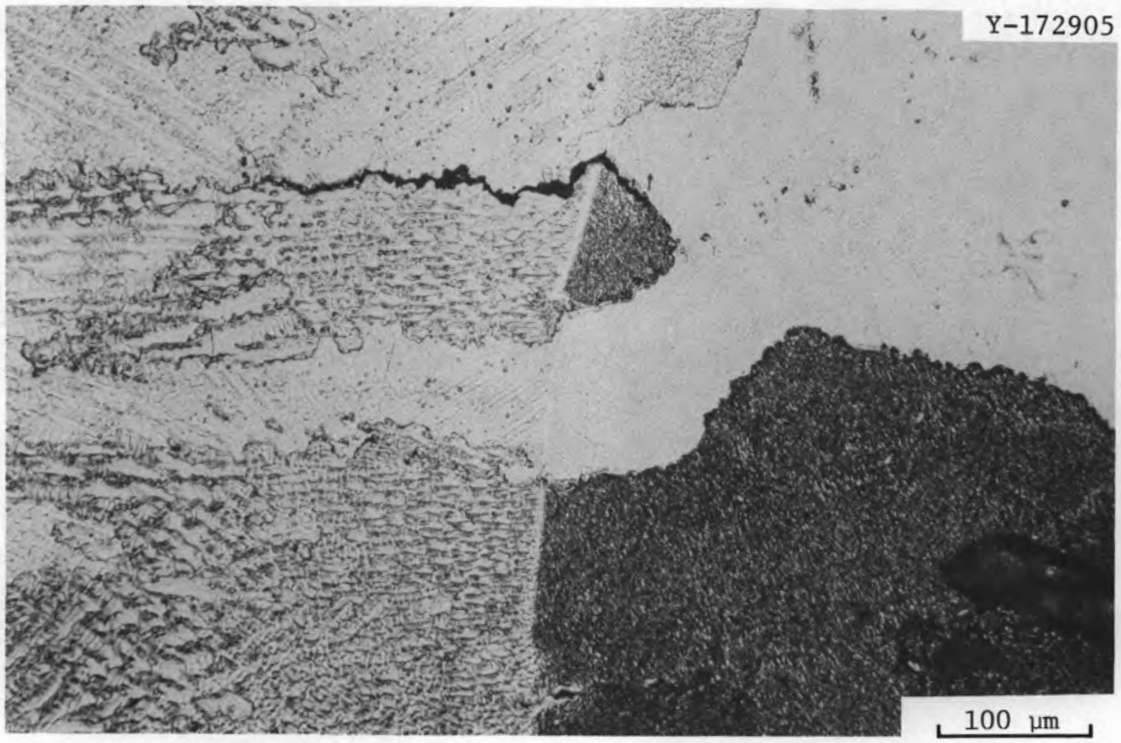

Fig. 4.21. Small fissures were found in the heat-affected and fusion zones of alloy 713LC electron beam weldments.

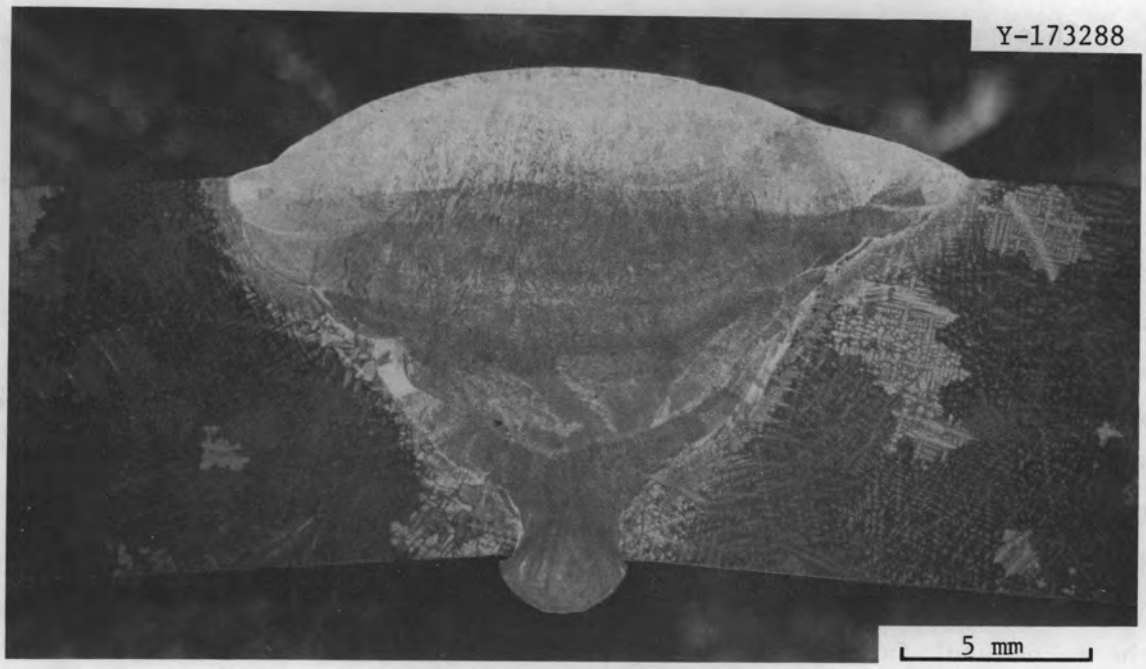

Fig. 4.22. Gas tungsten arc weldment made in 10-mm-thick alloy 713LC by using Inconel 617 filler metal.

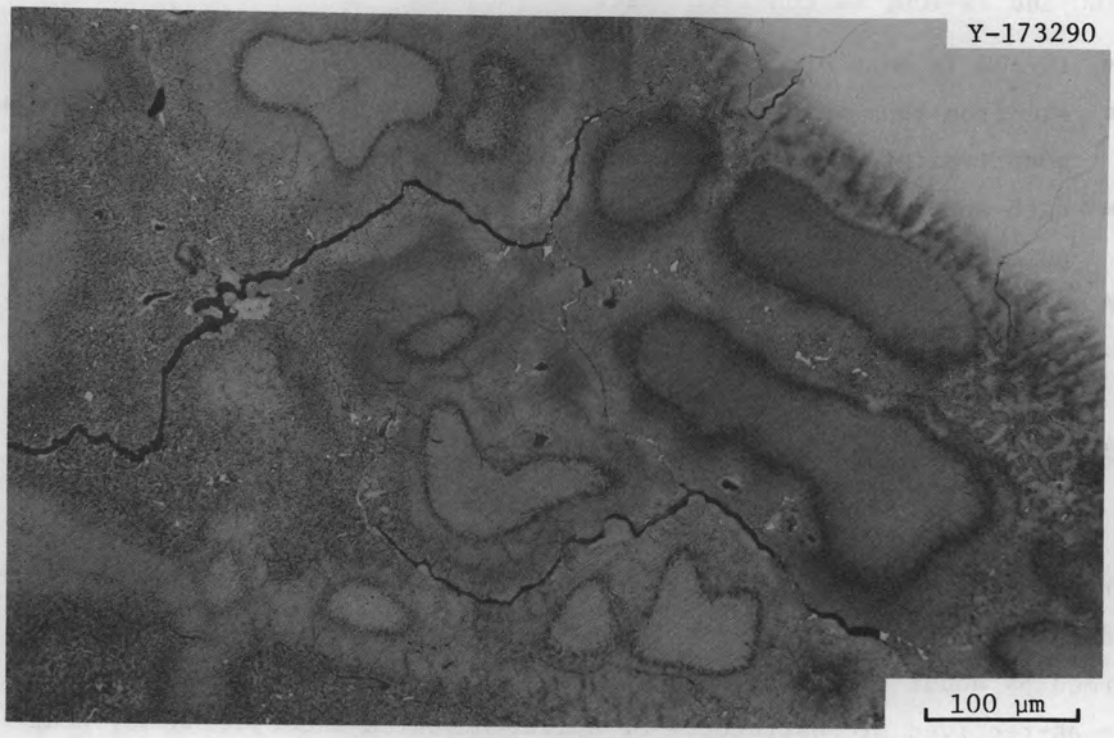

Fig. 4.23. Heat-affected-zone cracking found in 10-mm-thick 713LC weldments made with the gas tungsten arc process.

This preliminary welding evaluation has shown that fabrication by welding of the cast nickel-base superalloys will be very difficult. It is also likely that welding problems will increase with increasing section thickness because of weld metal and HAZ cracking. Previous work toward welding and postweld heat treatment of these alloys has indicated the complexity of the problem, but some success has been achieved for specific applications.[16] Filler metal development efforts have been conducted to improve the weldment mechanical properties and weldability of these crack-sensitive materials.[17] From the available information, we judge that extensive work will be required on the alloy or alloys, including the specific component requiring welding for an advanced gas-cooled reactor. Consideration of component design, alloy composition, welding process, and heat treatments will be necessary for the successful fabrication of superalloys by welding. Experience with similar alloys has shown that satisfactory welding has been accomplished when proper precautions were taken.

From this preliminary welding evaluation of cast nickel-base alloys 713LC and IN-100, we conclude that:

- IN-100 is more crack sensitive than alloy 713LC,
- electron beam welding parameters (high depth-to-width ratio) have a positive influence on reducing cracking,
- high-energy density welding processes show promise for making autogenous fusion welds in alloy 713LC, and
- alloy 713LC may be weldable by using the gas tungsten arc process, but a suitable filler metal must be found.

4.4.3 Laser and Electron Beam Welding of Oxide-Dispersion-Strengthened Alloy MA956 — J. F. King

Investigations into the joining of ODS alloy MA956 were initiated during this reporting period. This material is a ferritic iron-chromium-aluminum alloy that is dispersion strengthened with yttrium aluminates formed by about 1 vol % Y_2O_3. Figure 4.24 is a photomicrograph showing the as-received microstrucutre of a 1.22-mm-thick sheet of MA956, heat ZCDW. We have conducted our preliminary joining studies on this material.

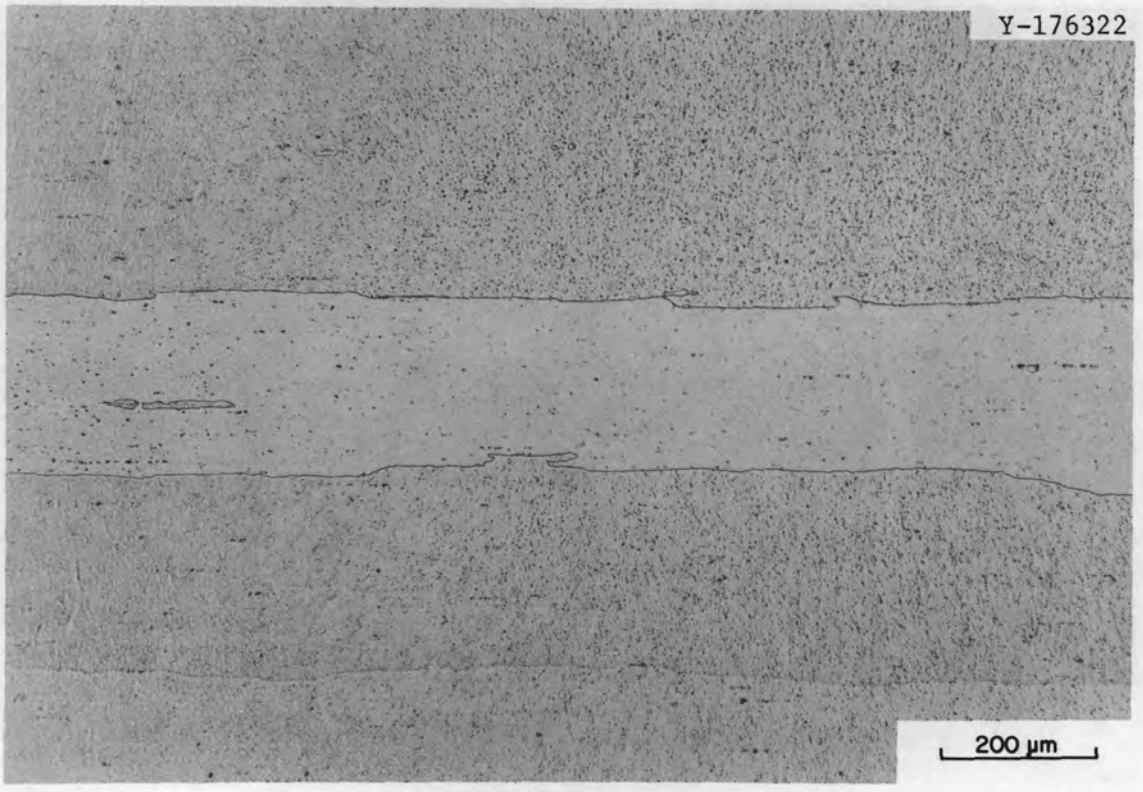

Fig. 4.24. Microstructure of as-received sheet of oxide-dispersion-strengthened MA956 alloy.

The EBW process was used initially to join the MA956 sheet material. Our initial welds involved using two sets of welding parameters, with travel speed being the main variable. The photomicrograph in Fig. 4.25 shows the cross section of the weld made with 125 kV, 6 MA, and 8.5 mm/s. The weld contained a relatively fine-grain structure at its center, which is desirable from stress rupture considerations, but it also contained a large amount of porosity.

For comparison, a second weld was made by using the same welding parameters except that the travel speed was increased to 10.6 mm/s. Figure 4.26 shows that the porosity has been reduced but that the weld centerline contains only a few elongated grains perpendicular to the plane of the sheet.

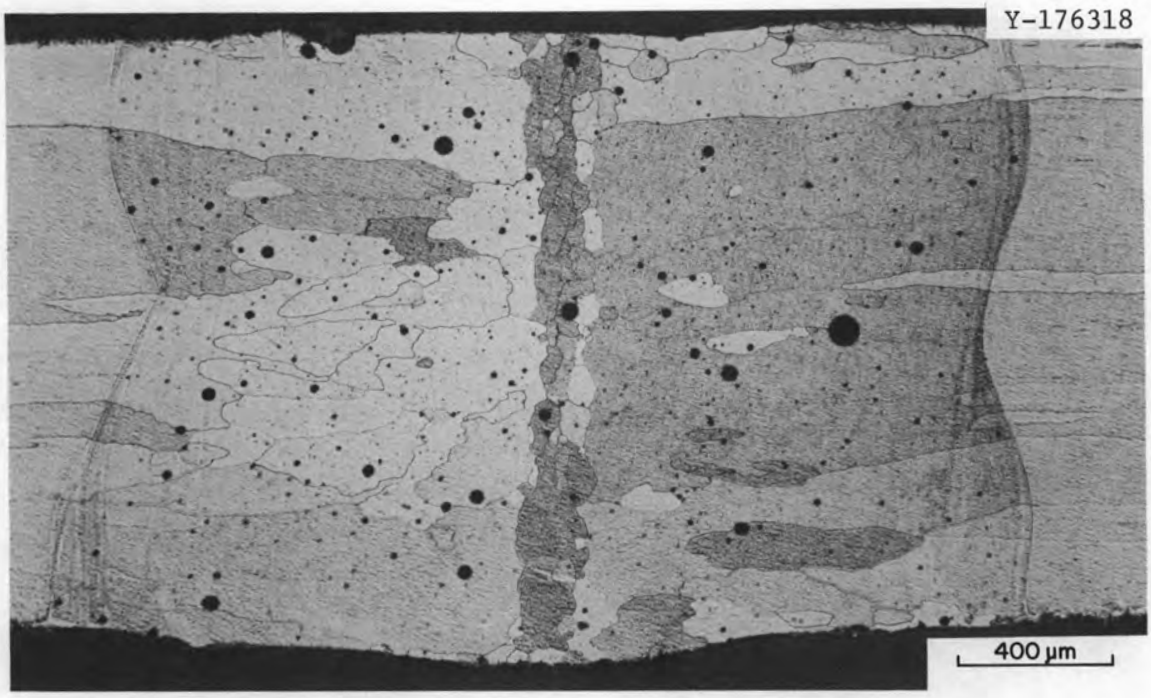

Fig. 4.25. Electron beam weld in MA956 sheet made at 8.5-mm/s travel speed.

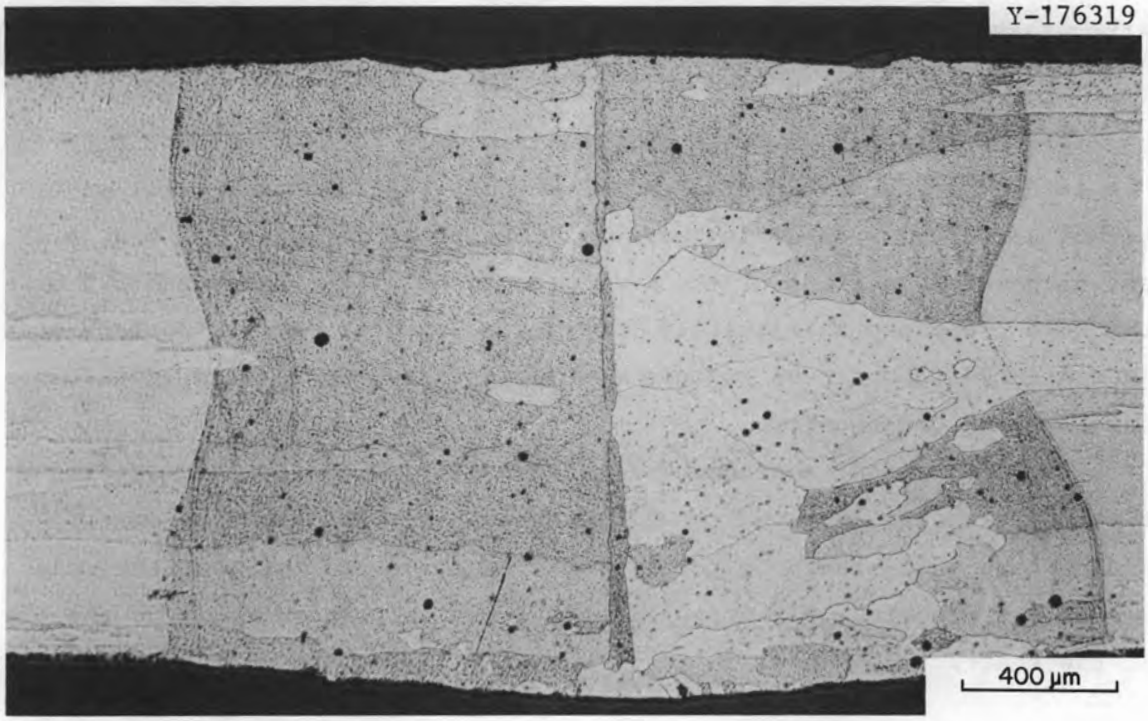

Fig. 4.26. Electron beam weld in MA956 sheet made with a travel speed of 10.6 mm/s.

These two preliminary EBWs show that MA956 may be sensitive to welding parameters. Conditions must be found that will eliminate weld porosity and produce a suitable grain structure for optimum mechanical properties.

The pulsed-laser welding process was also used on the 1.2-mm-thick sheet of MA956. A beam power of 350 W at 75 pulses per second with a travel speed of 4.2 mm/s was used to produce the weld shown in Fig. 4.27. Very little porosity was evident in this weld, and its size was smaller than that of the EBWs. This laser-produced weld also had less centerline grain boundary alignment than the EBWs, which can be seen from a top surface (Fig. 4.28) photomicrograph.

Both the laser beam welding (LBW) and the EBW processes show promise for joining MA956. The laser process may have some advantages, but insufficient welding parameter variations have been examined to make a conclusion. The main problem will be to obtain a weld microstructure that will result in elevated-temperature mechanical properties approaching

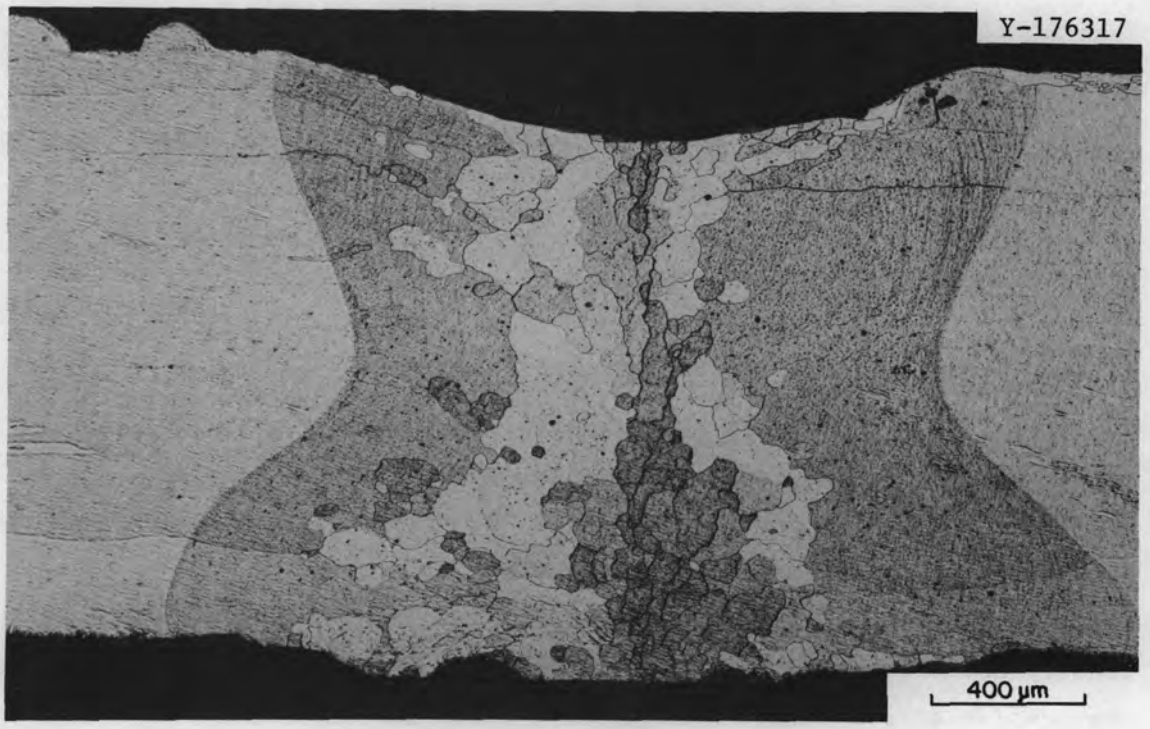

Fig. 4.27. Pulsed-laser weld in MA956 sheet.

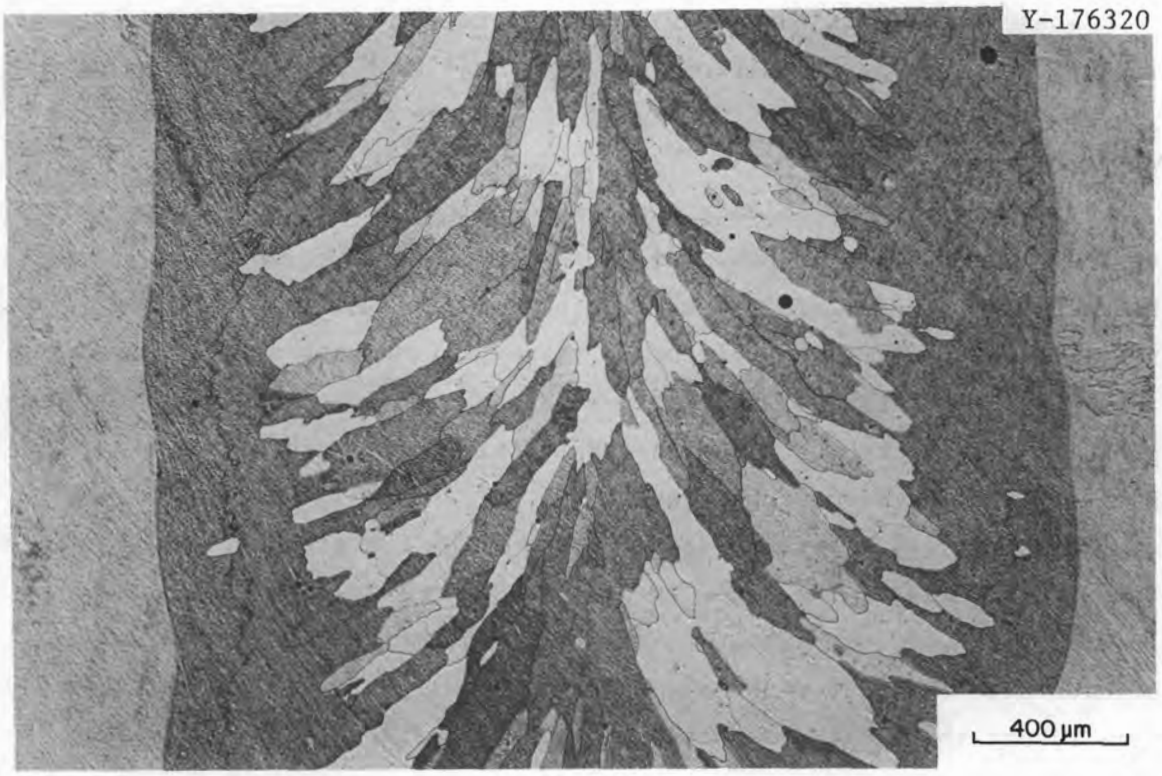

Fig. 4.28. Top surface view of pulse-laser-welded MA956.

those of the base material. Weldment specimens have been produced, and testing is under way. These data will provide a base for comparing future weldments.

4.5 STRUCTURAL CERAMICS — R. L. Beatty

4.5.1 Characterization of Fibrous Insulations — R. L. Beatty

Three fibrous insulation materials manufactured by Babcock and Wilcox were characterized for possible use as HTGR core thermal insulations. These materials (Unifelt 3000 board, Unifelt 2600 board, and Kaowool blanket) were characterized by spectrographic analysis, x-ray diffractometry, scanning electron microscopy, ignition studies and bulk density measurements, resilience tests, helium permeation tests, and compressive stress-strain tests. Details of the experimental work and results have been published.[18]

Of the properties measured, resilience is probably the most important for determining the acceptability of a fibrous insulation for HTGR use. Resilience, both initially and after aging, will affect the ability to retain the material clamped between metal cover plates. Resilience of 90% or greater after 20 h at 816°C (1500°F) in a simulated HTGR environment has been chosen as an arbitrary acceptability criterion. Test data for resilience measurements on the three materials after treatment for 20 h at two temperatures are given in Table 4.18. These data show that, based on the acceptance criterion of 90%, Unifelt 3000 is acceptable, Unifelt 2600 is marginal, and Kaowool is definitely unacceptable.

Table 4.18. Resilience test data for fibrous insulations

Material	Resilience, %			Number of specimens
	Mean	Range	Standard deviation	
Unifelt 3000[a]	97.3	95.5–100.4	1.92	8
Unifelt 2600[a]	88.3	85.7–88.8	1.19	8
Kawool[a]	76.2	75.6–77.2	0.45	8
Unifelt 3000[b]	87.1	85.4–88.8	2.40	2
Unifelt 2600[b]	76.5	75.6–77.4	1.27	2

[a]After 20 h at 816°C (1500°F).

[b]After 20 h at 982°C (1800°F).

To determine long-term aging effects on resilience, we have placed specimens of Unifelt 3000 and Unifelt 2600 in aging furnaces in a simulated HTGR environment at 816°C (1500°F). Specimen pairs will be exposed for periods of three months, six months, one year, and two years, and measurements will be made of resilience and compressive stress-strain.

4.5.2 Depressurization Testing — R. L. Beatty

We conducted a study to determine the effects of rapid depressurization on the integrity of structural ceramics and fibrous insulations. Tests were conducted at room temperature, considered to represent the worst case.

Depressurization was accomplished in the system shown schematically in Fig. 4.29. Test materials were placed in the upper chamber of the pressure vessel (autoclave). After several cycles of evacuating and back-filling with helium to assure essentially complete removal of air and moisture, the system was pressurized with helium to 7.9 MPa (1100 psi) and held for 20 h. Rapid depressurization was then effected through a series pair of rupture disks. The blowdown rate was controlled by a

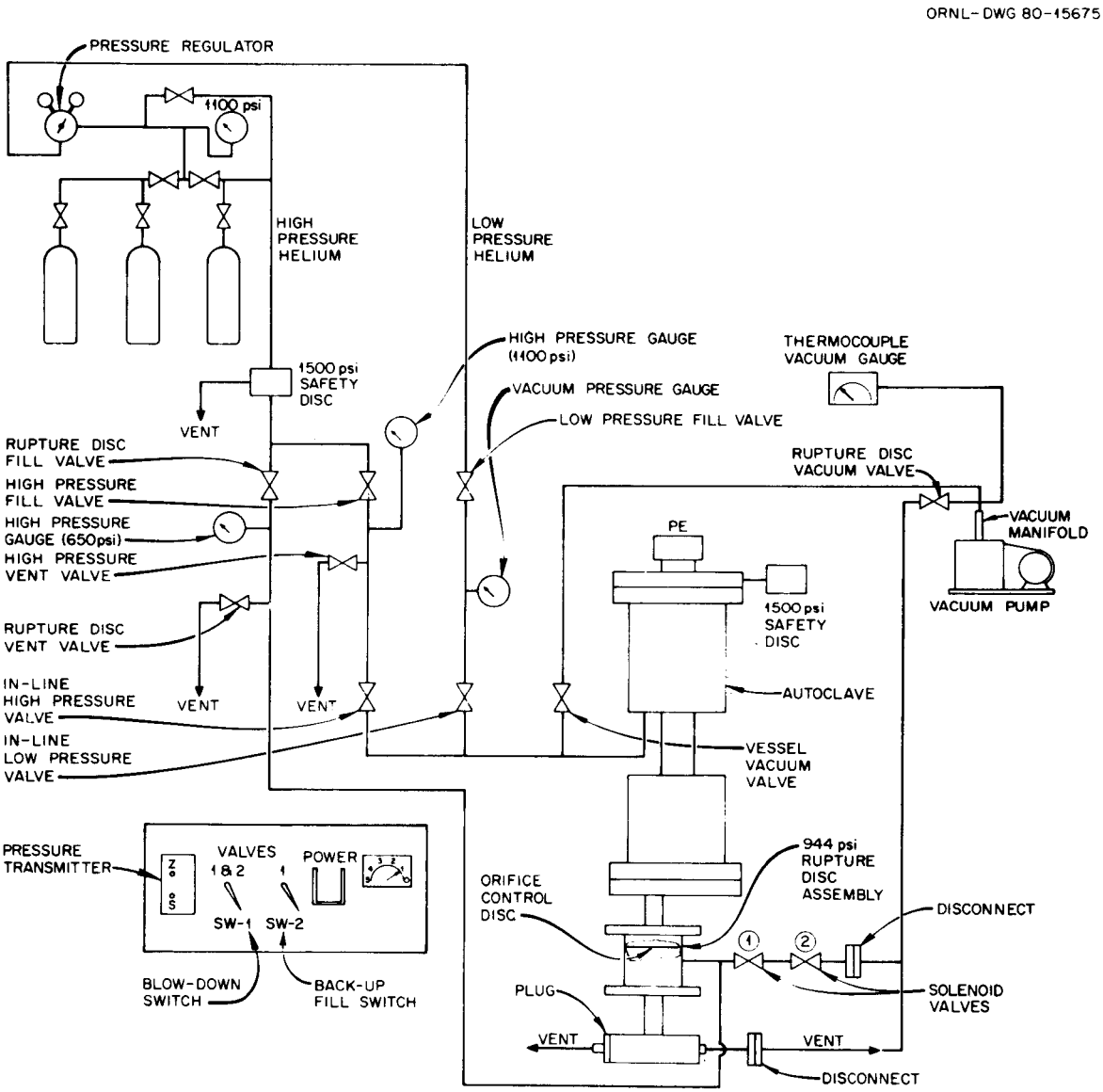

Fig. 4.29. Depressurization test system; 1 psi = 6.9 kPa.

fixed-orifice control disk, which gave very reproducible depressurization rates from run to run. The maximum rate was approximately 53 MPa/s (7700 psi/s) over a 1.4-MPa (200-psi) pressure drop. The average rate over a 4.8-MPa (700-psi) pressure drop was about 39 MPa/s (5600 psi/s). This compares with a postulated HTGR-gas turbine (GT) rate of 43 MPa/s (6300 psi/s) following a turbine-deblading accident.

Materials tested included five ceramics being considered for core support use and two fibrous insulations. Specimen geometry for the structural ceramics was a machined cylinder 50.8 mm (2 in.) in diameter and either 25.4 or 50.8 mm long (1 or 2 in.). Fibrous insulation specimens were cut from slabs nominally 57 mm (2.25 in.) thick (with binder). They were cut to a 6.35- by 96.2-mm (2.5- by 3-in.) size, and the organic binder was burned out. Each test block was compressed between two thin stainless steel plates to a dimension corresponding to a load of 10.4 kPa (1.5 psi).

Materials tested and results obtained are given in Table 4.19. Of all the materials tested, only the Harbison-Walker Masrock showed readily discernable effects. Three of the four specimens of this material disintegrated into piles of rubble. This is a low-strength material and is no longer being considered for HTGR core support use. All the other materials appeared to be acceptable from the standpoint of rapid depressurization effects. Possible subtle structural damage to the dense ceramics is being evaluated by diametral crushing tests at GA.

This work concludes the depressurization testing of ceramic materials unless additional data are required in the future.

4.5.3 Characterization of Dense Ceramics — R. J. Lauf and P. S. Sklad

Two silicon nitrides, NC-132 and NCX-34, were characterized in detail by transmission electron microscopy (TEM) in the as-received condition. When creep specimens having approximately 1 to 2% plastic strain become available, they will be characterized in the same way. This will allow us to identify the dominant modes of creep deformation.

The results of TEM characterization of NC-132 and NCX-34 were reported by P. S. Sklad and coworkers.[19] The following conclusions were reached in that study.

Table 4.19. Materials tested and results obtained from depressurization testing of potential HTGR core support ceramics and insulations

Material (vendor)	Number of specimens	Results
Silicon nitride-bonded SiC, Refrax 20 (Carborundum)	4	No visible change
99.5% alumina, Alundum HS (Norton)	4	No visible change
Fused silica, Masrock (Harbison-Walker)	4	No visible change in one; three disintegrated
Fused silica, fine-grained (Thermo Materials)	3	No visible change
Fused silica, coarse-grained (Thermo Materials)	3	No visible change
Fibrous insulation, Unifelt 3000 (Babcock & Wilcox)	2	No visible change or significant weight loss
Fibrous insulation, Unifelt 2600 (Babcock & Wilcox)	2	No visible change or significant weight loss

- Both structural ceramics examined, NC-132 and NCX-34, contained regions of porosity. These regions were inhomogeneously distributed.
- The phases identified in NC-132 (Si_3N_4 + MgO) are Si_3N_4, Si_2N_2O, a metal carbide, and a glassy phase containing magnesium and aluminum.
- Four phases were observed in NCX-34 (Si_3N_4 + Y_2O_3): Si_3N_4, a yttrium-rich phase, which is probably $Si_3N_4 \cdot Y_2O_3$; a glassy silica phase; and metal carbide particles.
- The glassy silica region in NCX-34 showed no evidence of yttrium, magnesium, or aluminum.
- The yttrium-rich phase in NCX-34 is present as small grains and contains small amounts of magnesium and aluminum.
- High-magnification phase contrast examination of the yttrium-rich regions of NCX-34 reveals that these regions contain small areas of differently oriented fringes.

Other silicon nitride types have been obtained for characterization and creep testing. These include a reaction-bonded type (RBN-104) and one produced by plastic forming (SSN-522).

Compressive creep specimens of Corning 7941 fused silica were examined before and after creep testing to understand better the microstructural changes that took place during creep. X-ray diffraction showed no trace of devitrification as a result of creep testing for about 2000 h at 982°C. Optical microscopy did not detect any crystalline second phases, particularly optically anisotropic phases. The only visible change was a coalescense of porosity.

As a result of discussions with personnel at GA, several candidate materials have been added to the characterization effort, including AD-85 alumina, AD-995 alumina, KBI-AME reaction-sintered silicon nitride, Corning 9606 cordierite, and fine-grained fused silica (Thermo Materials). These additions will bring the characterization program into line with current core support design options. Milestones for the structural ceramics activity have been modified to incorporate these new data needs.

4.5.4 Environmental Testing of Ceramics — R. J. Lauf and P. L. Rittenhouse

The structural ceramics atmospheric testing system (SCATS) was brought into operation in March 1980. It was designed to provide for the thermal aging and environmental exposure of a large number of samples of a variety of candidate core support and fibrous insulation ceramics. However, recently improved definitions of designs and design requirements have led to a reduction in the number of ceramics under active consideration. This, in turn, has resulted in a very large decrease in the load factor for SCATS and, as almost one-third of the HTGR Structural Ceramics budget is involved with SCATS, it is now impossible to justify continuation of its operation. Shutdown of the facility will not be detrimental to the program because other arrangements have been made for those exposures that will be needed. All the components of SCATS will be used in other HTGR subtasks.

4.6 FISSION PRODUCT—MATERIALS INTERACTIONS — H. E. McCoy

4.6.1 Evaluation of Existing Data and Specimens

Considerable work was done previously on the effects of tellurium on nickel-base alloys, which was summarized in various progress and topical reports.[20-22] These studies involved molten fluoride salts, and the tellurium was introduced by putting various chromium and nickel tellurides in the salt melts to release continuously small quantities of tellurium. Because the metal samples were not corroded appreciably by the salts, most observations made in these studies are felt to be relevant to materials exposed to small concentrations of tellurium in helium systems.

The general picture of the tellurium embrittlement developed in the previous studies is that tellurium diffuses selectively along the grain boundaries of nickel-base alloys and results in severe intergranular embrittlement. We found that this process was affected significantly by the chemical composition of the alloy and that niobium additions of 1 to 2% were optimum for retarding the embrittlement of modified Hastelloy N (Ni—12% Mo—7% Cr). This alloying effect was noted in samples exposed to tellurium-containing salt for 250, 1000, and 2500 h at 700°C.[22]

Another identical group of specimens was exposed for 6000 h but was not evaluated until recently. These samples were strained to failure in a tensile test at 25°C. Metallographic sections were prepared, and the frequency and depth of cracking were evaluated visually. The results for the alloys containing niobium are shown in Fig. 4.30. The severity of cracking is minimum at a niobium content of about 1%. Results for other alloys containing both titanium and niobium showed clearly that the presence of titanium negated the beneficial effects of niobium.

4.6.2. High-Temperature Exposure of Hastelloy X and Inconel 617 in Tellurium-Cesium Environments

Test systems are being assembled in which Hastelloy X, Inconel 617, and several alloys will be exposed to helium that contains small partial pressures of tellurium and cesium. The oxygen concentration of the

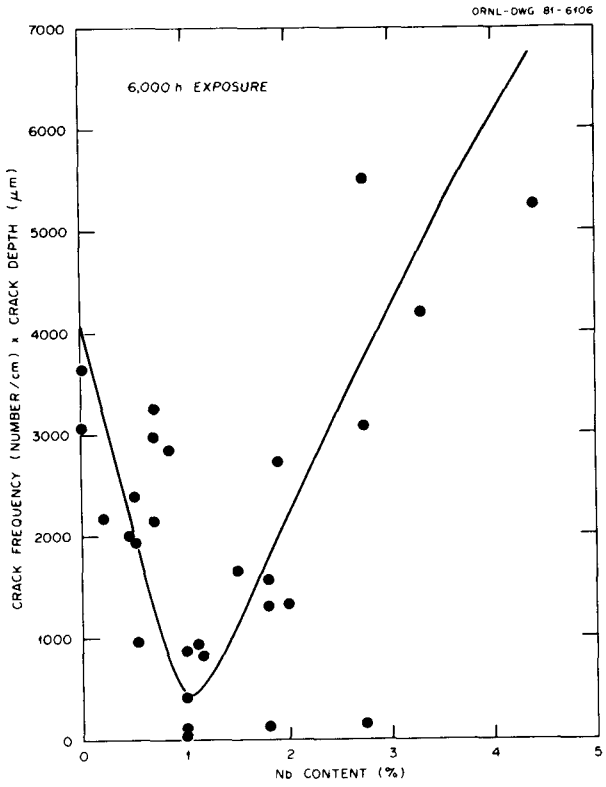

Fig. 4.30. Intergranular cracking of several nickel-base alloys as a function of niobium content.

environment will be controlled by the Cr-Cr_2O_3 couple, and the concentrations of cesium and tellurium will be controlled by fixing the temperature of each of these materials in the gas stream.

Small tensile samples of each material will be exposed to the environment, strained in a tensile test at 25°C, and sectioned metallographically to determine the extent of cracking. Exposures will be at 750, 850, and 950°C.

4.6.3 Strain-Cycle Tests in Tellurium-Cesium Environments — H. E. McCoy

The techniques described in the previous section can be used to generate a test environment for numerous types of tests. One of the most sensitive tests to intergranular embrittlement is the strain-cycle test in which test samples are alternately strained in tension and compression. This type of straining should dislodge grains with embrittled boundaries and help the line of embrittlement move into the sample more quickly.

Test equipment for running strain-cycle tests in controlled environments was constructed previously,[23] and this equipment will be modified to run tests in helium containing cesium and tellurium.

4.7 REFERENCES

1. P. L. Rittenhouse, "Tensile Testing," *HTGR Base-Technology Program Prog. Rep., Jan. 1, 1974–June 30, 1975*, ORNL-5108, pp. 67–73.
2. A. Lystrup, "Tensile Testing," *HTGR Base-Technology Program Prog. Rep., July 1, 1975–Dec. 31, 1976*, ORNL-5274, pp. 69–73.
3. H. E. McCoy, "Tensile Testing," *HTGR Base-Technology Program Annu. Prog. Rep., Dec. 31, 1977*, ORNL-5412, pp. 255–70.
4. H. E. McCoy, Jr., *Creep Behavior of Hastelloy X, 2 1/4 Cr-1 Mo Steel, and Other Alloys in Simulated HTGR Helium*, ORNL/TM-6822 (June 1979).
5. H. E. McCoy, "Creep and Tensile Testing," *HTGR Base-Technology Program Annu. Prog. Rep., Dec. 31, 1979*, ORNL-5643, pp. 186–95.
6. T. Weerasooriya and J. P. Strizak, *Crack Propagation in Hastelloy X*, ORNL/TM-7255 (May 1980).
7. J. C. Griess and W. A. Maxwell, *The Long-Term Corrosion of Selected Alloys in Superheated Steam at 482 and 538°C*, ORNL report to be published.
8. F. J. Homan and P. R. Kasten, *HTGR Base-Technology Program Annu. Prog. Rep., Dec. 31, 1979*, ORNL-5643, pp. 203–12.
9. D. F. Lupton, *The Carburization Kinetics of Hastelloy X in Simulated HTR Environments at 871 and 900°C (A Preliminary Study)*, KFA-IRW-1B-21/78, Kernforschungsanlage, Jülich (January 1979).
10. A. V. Dean, *The Corrosion Resistance of Modified Commercial Alloys*, KFA-IRW-1B-24/78, Kernforschungsanlage, Jülich (October 1978).
11. H. Inouye, *Status and Interpretation of Dilation Experiments on Hastelloy X and Incoloy 800H*, unpublished data.
12. F. J. Homan and P. R. Kasten, *HTGR Base-Technology Program Annu. Prog. Rep., Dec. 31, 1978*, ORNL-5536 pp. 197–201.
13. S. N. Rosenwasser and W. R. Johnson, *Gas Turbine and Advanced HTGR Materials Screening Test Program*, GA-A14407, General Atomic Company, San Diego, Calif. (Mar. 31. 1977).

14. General Atomic Company, "Environmental Creep Tests," *Mechanical Properties Test Data for Structural Materials Quart. Prog. Rep., Oct. 31, 1977*, ORNL-5349, pp. 286–88.

15. D. F. Lupton, *Mechanisms of Surface Scale Formation in HTR Helium*, Jül-1639, ISSN 0366-0885, Kernforschungsanlage, Jülich (January 1980).

16. M. Prager and C. S. Shira, "Welding of Precipitation Hardening Nickel-Base Alloys," *Weld. Res. Coun. Bull.* 128 (1968).

17. W. H. King and D. W. Anderson, *Superalloy Weld Filler Alloy Development*, Technical Report AFML-TR-76-154, Air Force Materials Laboratory, Dayton, Ohio (December 1976).

18. J. E. Selle, *Characterization of Three Fibrous Insulations for Potential HTGR Application*, ORNL/TM-7507 (November 1980).

19. P. S. Sklad, R. W. Carpenter, N. J. Zaluzek, and J. E. Selle, "Phase Identification in Si_3N_4/MgO and Si_3N_4/Y_2O_3 Compacts by Convergent Beam Diffraction and Energy Loss Spectroscopy," paper presented at the Annual Meeting of the American Ceramic Society, April 27–30, 1980. Chicago, Ill., to be published in the proceedings.

20. L. E. McNeese, *MSR Program Semiannu. Prog. Rep., Aug. 31, 1975*, ORNL-5078, pp. 100–31.

21. L. E. McNeese, *MSR Program Semiannu. Prog. Rep., Feb. 29, 1976*, ORNL-5132, pp. 85–128.

22. H. E. McCoy, Jr., *Status of Materials Development for Molten Salt Reactors*, ORNL/TM-5920 (January 1978).

23. L. E. McNeese, *MSR Program Semiannu. Prog. Rep., Aug. 31, 1975*, ORNL-5078, pp. 52–65.

5. HTGR GRAPHITE STUDIES

W. P. Eatherly

5.1 GRAPHITE IRRADIATIONS — J. A. Conlin

5.1.1 Creep Capsule OC-4 — R. L. Senn

The fourth in a series of graphite creep irradiation experiments (capsule OC-4) was inserted in the Oak Ridge Reactor (ORR) on November 25, 1980. Capsule OC-4 contains graphite specimens previously irradiated in capsule OC-2 to a fast fluence of 2×10^{21} neutrons/cm^2 ($E > 0.18$ MeV). The experiment was designed to operate at 600 ± 10°C specimen temperature, with compressive stresses of 13.8 and 20.7 MPa being applied to the stressed specimens. The objective of capsule OC-4 is to extend the exposure of the test graphites to $>4 \times 10^{21}$ neutrons/cm^2 ($E > 0.18$ MeV) under the operating conditions established for the first 600°C experiment (capsule OC-2). Detailed design descriptions of the graphite creep irradiation experiments have been published.[1–4]

We experienced considerable delays in construction of this experiment. Failure of a vendor to manufacture the graphite specimen holders to the required dimensional specifications was the principal cause of this delay. Our supply of AXF-5Q graphite previously used for these parts was therefore depleted. Stackpole grade 2020 graphite, with additional heat treating, was substituted for the specimen holders. We also were forced to make the outer sleeve of grade 2020 graphite in order to match the graphite materials. Further difficulties were encountered in attempting to install the closely fitting graphite sleeve over the specimen holder. Two such parts cracked during assembly, and we were ultimately forced to increase the inside diameter of the graphite sleeve slightly. This should have a minimal effect on capsule operation but would cause some increased thermal resistance from the experimental samples to the coolant water. Assembly of the capsule proceeded without further difficulty after installation of the modified sleeve.

Soon after bringing the reactor to full power operation (30 MW), it became obvious that the upper regions of the capsule would operate at temperatures above the desired 610°C maximum specimen temperature.

Capsule OC-4 was designed to operate with 100% helium in the gas gap between the outer sleeve and the outer capsule containment vessel by using electrical heaters to bring the specimen temperatures to the design point. The heaters are arranged in ten 50.8-mm-long (2-in.) zones along the length of the specimen columns. We found that, as the reactor cycle proceeded and the control rods were retracted in the normal course of reactor operation, the upper three zones required less and less heater power. When the required zero heater power was reached, the only way to control the experiment temperature was by a reduction in reactor power. With the concurrence of other experimenters, we therefore requested a reactor power level of 27 MW. The experiment could be controlled satisfactorily at this power level for most of a refueling cycle (~10 d). Even at 27 MW, near the end of the fuel cycle the upper zones exceed the design temperature, reaching about 630°C average specimen temperature in zone 2 during the last day of the fuel cycle.

The unexpected high temperatures in the upper zones of capsule OC-4 are probably caused by a combination of factors: (1) The reactor core loading is significantly different from the core loadings used when capsule OC-2 was operated. The current core-loading patterns are designed to accommodate the needs of the Magnetic Fusion Energy Program experiments in operation. (2) New control rods have been installed near CP-E5. As described above, the OC-4 experiment seems to be especially sensitive to the control rod positions, as evidenced by the increasing temperatures near the end of a fuel cycle. (3) Although the design of capsule OC-4 is essentially the same as that of capsule OC-2, the above-noted slight differences in thermal resistance may have exacerbated the tendency for the experiment to operate at excessive temperatures in the upper zones.

After analyzing the temperature conditions under which capsule OC-4 could operate without jeopardizing the data, we concluded that the experiment should continue with the reactor operating at 27 MW, recognizing that some additional error in determining the secondary creep coefficient would be unavoidable for those specimens in the upper zones. The extent of the resulting error is not clear-cut because we do not have information on thermal annealing rates. However, a 20°C error on the upward side will

lead to a 2.8% error in the secondary creep. A 30°C error will lead to a 5.4% error in the creep coefficient, which would be unacceptable except for a very short (few days) time.

In all other respects, capsule OC-4 operated satisfactorily. Temperature profiles were measured each working day with the movable thermocouples, and temperatures were adjusted accordingly to maintain the design 600 ± 10°C specimen temperatures for all zones except the upper three. Pressures were maintained within design limits on the bellows system used to apply the compressive stress to the stressed specimens. Three tests were conducted with the pneumatic electromechanical[5] cells located at the bottom of each stressed column. These tests showed that each column was being compressed by the upper bellows system and that there were no cocked or jammed specimens in the columns that might compromise the application of the intended stress to all the specimens.

As of December 31, 1980, capsule OC-4 had been irradiated for 33 d of a planned 110-d exposure.

5.1.2 Design of 1200°C Creep Capsule OC-X — H. C. Roland and Amir Mobasherani*

Design studies were continued during this reporting period for graphite creep irradiation experiment, OC-X, to be operated at 1200°C specimen temperature with compressive stresses of 13.8 and 20.7 MPa being applied to the specimens. Results from a 1200°C bench test (previously reported)[6] were applied to this new design.

Preliminary studies indicated that the modeling used on the earlier 600 and 900°C graphite creep test capsules would not be sufficient for the 1200°C capsule. Radiation heat transfer is a significant factor around the sample column for this capsule, so it requires a better geometric description in this region to apply accurately the radiation shape factor capability of the HEATING 5 program.

The modeling chosen was cylindrical geometry with the cylindrical axis at the center of the test column. Although this greatly simplifies

---

*Work performed at University of Tennessee, Knoxville, under subcontract.

the modeling immediately around the specimens, it requires approximation of the outer boundary in cylindrical steps. A program was written to calculate rapidly an outer boundary perimeter for heat transfer and cross-sectional areas of the various components for comparison with the true values. This allowed variation of the stepping of the outer boundary so that these values could be kept very close to the true values. Small gaps were placed in the outer stainless steel at the cylindrical steps to prevent erroneous coupling of the stainless steel to the graphite block. Examination of the calculated results for the two-dimensional (2-D) calculations shows that this decouples the two regions satisfactorily.

Preliminary 2-D calculations were completed to specify broadly the required gaps at various gamma heating rates. To hold the main support graphite block temperature down to 950°C or less with gamma heating of 5 W/g, these calculations show that it is necessary to increase the gap around the tungsten radiation shield above that used at the maximum gamma heating rate of 8 W/g. This, of course, complicates the design and assembly and the 3-D heat transfer calculations.

A test run was made by using the 3-D code. The input data were generated for this run by using a special new subprogram written for input data processing to the HEATING 5 code and this geometry. This subprogram will allow rapid data input for further parametric-type calculations for minor changes in the configuration.

Preliminary calculations were completed, and final 3-D calculations are under way.

5.1.3 Graphite Irradiations in HFIR — R. L. Senn

Graphite irradiation in outer target positions of the High Flux Isotope Reactor (HFIR) continued during this reporting period with the completion of the HTU-1 experiment and the insertion and continuing irradiation of target capsule HTK-4, the fourth in a series of graphite irradiations[7] for the Federal Republic of Germany (FRG).

The HFIR target capsule HTU-1, containing 64 graphite specimens (principally TSX), was designed to operate at 575 ± 25°C specimen

temperature. The capsule was inserted August 9, 1979, and was removed March 5, 1980, after an exposure of nine HFIR cycles to a maximum fast fluence of 2.2×10^{22} neutrons/cm^2 ($E > 50$ keV).

As discussed in our previous annual report,[8] target capsule HTC was irradiated for one cycle in the HFIR to serve as a flux calibration measurement for correcting discrepancies detected in the apparent temperatures of earlier target capsules. Results from the HTC capsule were used to redesign the HTU experiment for 575 ± 25°C specimen temperatures. Measurements resulting from two silicon carbide (SiC) temperature monitors corroborated that capsule HTU-1 did indeed operate at 580 and 570°C, in good agreement with the design temperature.

The HFIR target capsule HTK-4 contains 48 specimens of various German graphites and two graphite holders loaded with SiC specimens as supplied by the General Atomic Company (GA). The experiment was designed to operate at 715 ± 25°C. It was inserted into HFIR outer target position B-1 on August 17, 1980. The experiment is scheduled for a ten-cycle irradiation, which should be completed about April 1981.

5.2 IRRADIATION RESULTS — W. P. Eatherly

5.2.1 Behavior of Graphite Grade TSX — C. R. Kennedy

Graphite grade TSX is used in the core of the N-Reactor at Hanford. It is an AGOT-type material manufactured from anisotropic needle-coke and purified after a high-temperature graphitization. Manufactured by Carbon Products Division of Union Carbide Corporation, the material is considered to be quite similar to the H327 graphite used in the Fort St. Vrain Reactor.

The proposal to continue operation of the N-Reactor* for some years requires irradiation data to "end-of-life" for prognosticating the future behavior of the core. Only the HFIR at Oak Ridge offered a rapid and simple way to do this, representing a 50-fold increase in flux over the

---

*The N-Reactor is operated by United Nuclear Corporation, Nuclear Industries Division; the program was funded by the U.S. Department of Energy (DOE).

N-Reactor. While the work on TSX graphite was not supported by the HTGR program, the results of these studies are of sufficient importance to gas-cooled reactor concepts to warrant inclusion in this report. Our pertinent conclusions are (1) TSX is similar to H327 graphite, and the TSX data are relevant to those of Fort St. Vrain; (2) the definition of end-of-life to be the zero-volume change fluence is overly conservative because structural integrity and usable mechanical strength persist well beyond this fluence; and (3) the correlation of data between the N-Reactor and HFIR validates the use of test reactor experiments to predict graphite behavior in power reactors; that is, there is no so-called "flux effect," at least at 600°C.

Samples of grade TSX were largely exposed in the United Nuclear capsule HTU-1; however, some exchange of space was made between this capsule and the Kernforschungsanlage (KFA)-related capsules HTC-1 (temperature calibration experiment) and HTK-3. The final data base included exposure of the TSX material to a fluence of 2.3×10^{25} neutrons/m^2 ($E > 50$ KeV) at 575°C, with some additional data at 620°C.

Dimensional changes, electrical resistivity, elastic constants, and coefficient of thermal expansion (CTE) measurements have been completed on all the specimens from the HTU-1 experiment. The specimens were then destructively tested as brittle rings to evaluate the strength alteration by irradiation. The physical property changes at 575°C (the HTU-1 irradiation temperature) are similar to previous 620°C HTK experiments.

The dimensional changes given in Figs. 5.1 and 5.2 permit comparison of the 575°C with the 620°C results. Little difference was found in the with-grain ($\Delta l/l$) direction; however, the against-grain ($\Delta D/D$) dimensional changes at 620°C reach a minimum at a shorter fluence and thereafter begin to expand. This enhanced against-grain expansion at 620°C produces an achievement of maximum density at a shorter fluence, and the resulting expansion yields a reduced lifetime. These results are in general agreement with past behavior demonstrated for the highly anisotropic graphites made from needle-coke, such as grades CSF and AGOT, and are also in accord with design curves for the various HTGRs. The physical property degradation is not expected to become serious until the volume expansion

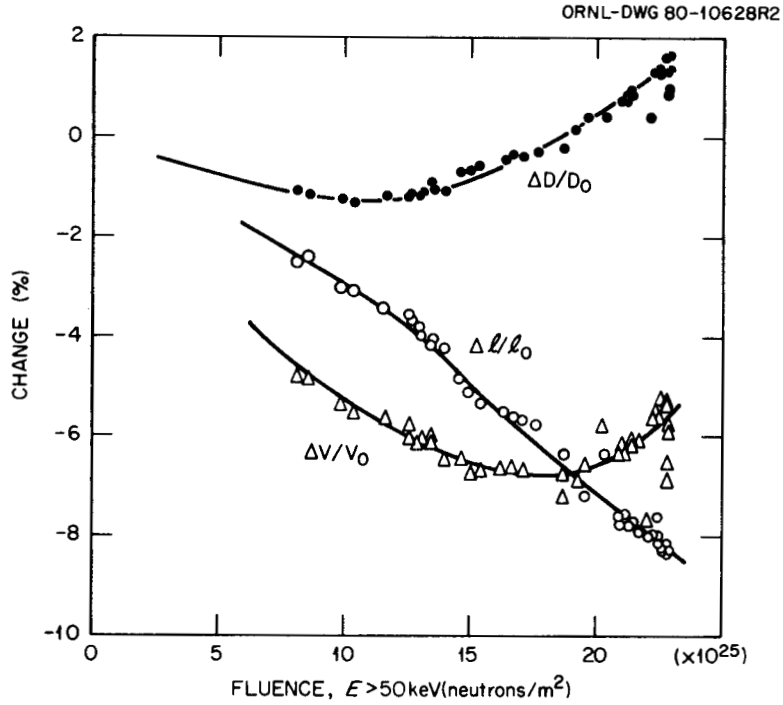

Fig. 5.1. Dimensional changes of grade TSX caused by irradiation at 570°C.

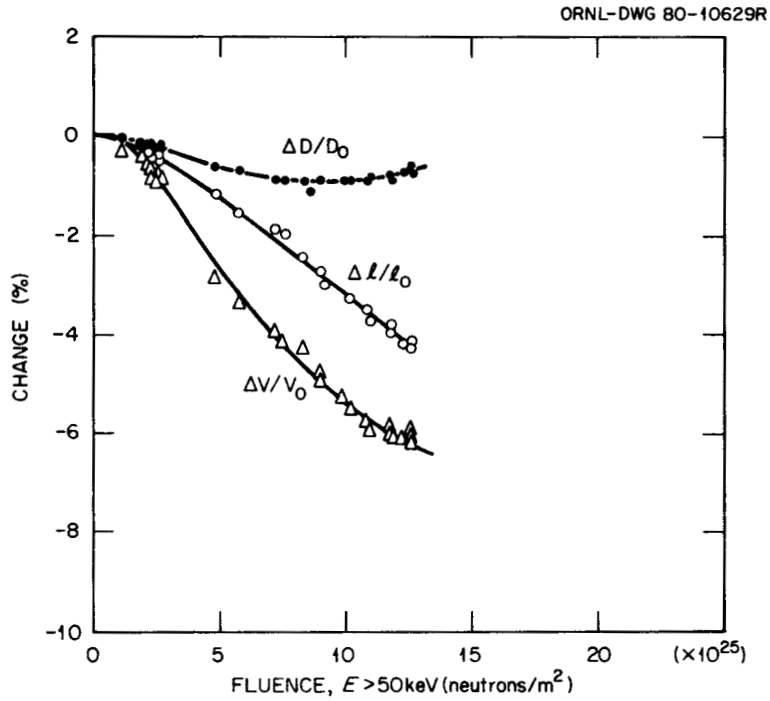

Fig. 5.2. Dimensional changes of grade TSX caused by irradiation at 620°C.

reduces the density to values of less than the original density. Comparing the physical properties at the extended fluences of HTU-1 confirms this initial assumption.

The electrical resistivity measurements given in Fig. 5.3 again compare the 575°C results with the 620°C results. In both cases a rapid initial increase in resistance is followed by a decrease and eventual saturation. These curves must start initially at a value of unity. The initial increase, caused by defect generation, saturates rapidly; however, the subsequent densification and reduction of void volume with reduced pore size apparently improves the conductivity. The major difference in the 575 and 620°C results is the slightly higher defect density at 575°C. The general behavior of graphite is eventually to exhibit a significant increase in resistivity as the volume expansion becomes large. These data indicate that grade TSX has not entered the region of final increased resistance caused by structural degradation.

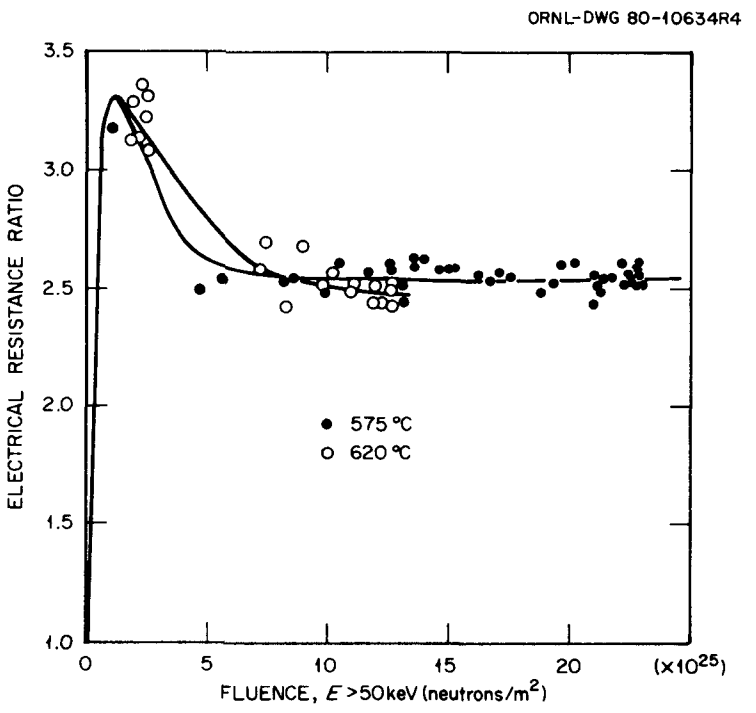

Fig. 5.3. Effect of irradiation on against-grain electrical resistivity of TSX graphite.

The CTE results are given in Fig. 5.4 for both with-grain and against-grain directions. The relative rapid increase in CTE in the against-grain and minor initial changes in the with-grain direction are consistent with past data. This type of behavior reflects the closure of existing defects normal to the *c*-axis by irradiation; thus, the CTE in the preferred *c*-axis direction (against-grain) will be strongly affected and increased. The effects of the large degree of anisotropy in the TXS grade is reflected by the large difference in the with-grain and against-grain values and by the lack of a significant irradiation effect initially in the with-grain direction. The eventual increase of the CTE in the with-grain direction is a result of structural alteration in the creation of a new porosity, which allows the *c*-axis material to influence fully the bulk properties. The restraint of the *a*-axis is gradually reduced with increased fluence. The implication that there is some structural degradation occurring is slight.

The real evaluation of structural integrity is reflected by the mechanical properties, the elastic constants, and strength. Shown in

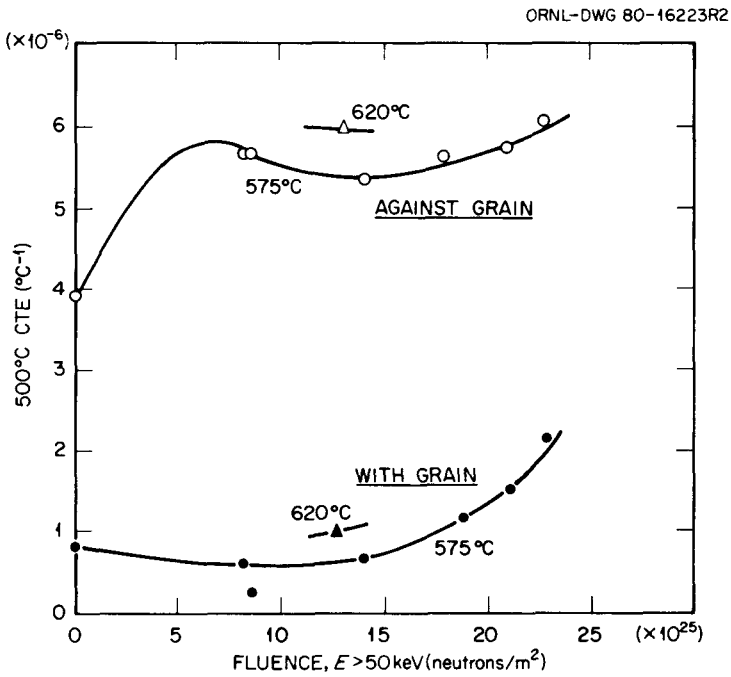

Fig. 5.4. The 500°C coefficient of thermal expansion of grade TSX as affected by irradiation.

Fig. 5.5 are the elastic constants derived from velocity measurements, and given in Fig. 5.6 are the 2 1/4-MHz sonic attenuation measurements, which yield a direct indication of the size of the critical defect in the material. Finally, Fig. 5.7 shows the brittle-ring-strength results of testing both 575 and 620°C specimens.

The elastic constants (Fig. 5.5) yield the typical increase from defect density generation. Again, the slightly higher modulus for the 575°C data is in agreement with electrical resistance results, indicating a slightly higher defect density at 575°C. Both the Young's modulus and the shear modulus are affected proportionally, which is an indication that Poisson's ratio is unchanged by irradiation. A second increase in the modulus values generally results from densification; however in grade TSX, either it does not exist or only the slight increase shown is all that results. Significantly, the onset of structural degradation suggested by the CTE results is not reflected by a loss in the elastic constant. This must, however, eventually occur with continuing loss in bulk density.

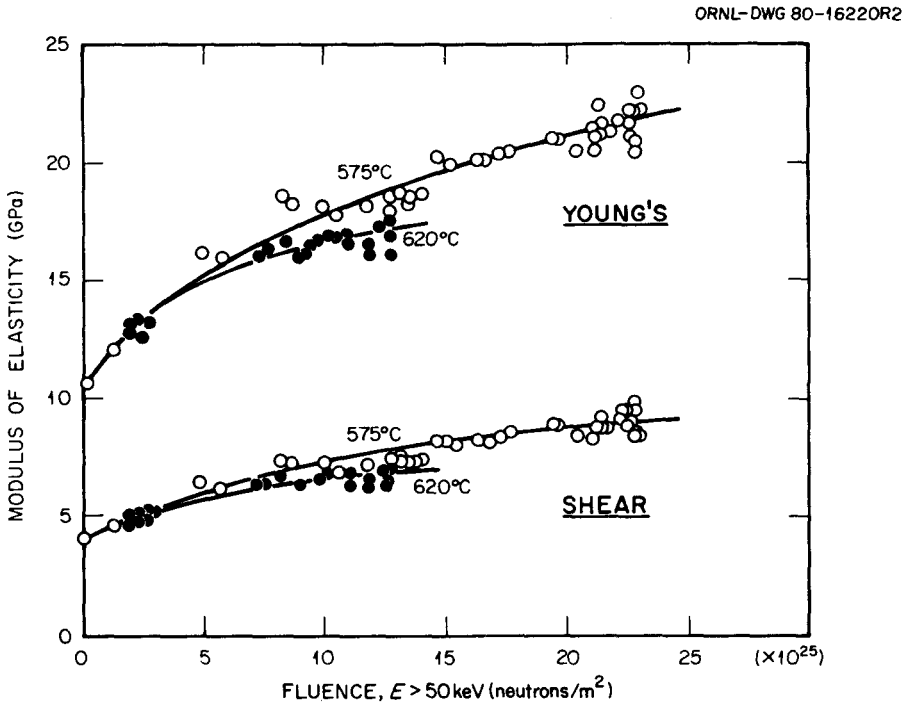

Fig. 5.5. Modulus of elasticity of grade TSX as affected by irradiation.

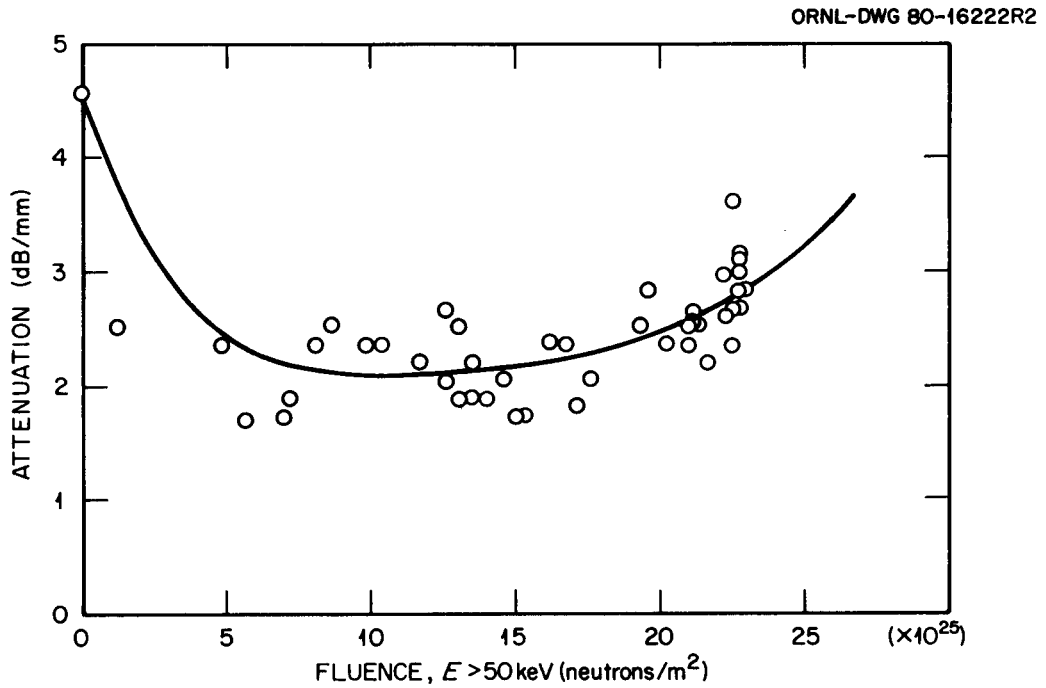

Fig. 5.6. Sonic attenuation of TSX graphite irradiated at 575°C in HFIR.

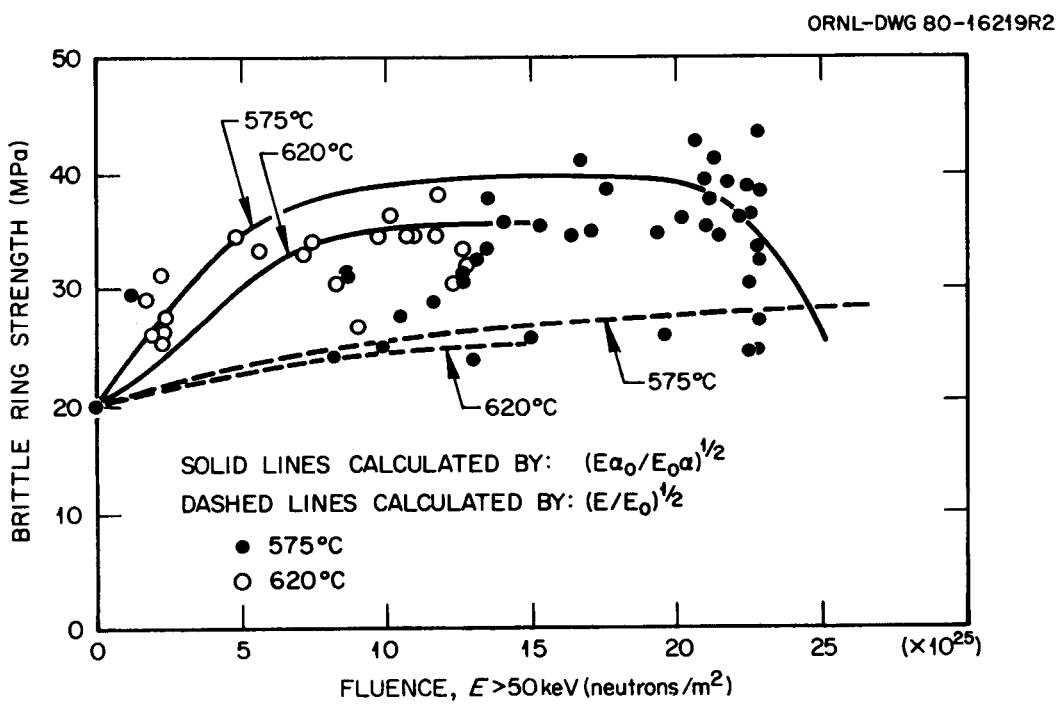

Fig. 5.7. Fracture strength of TSX as affected by irradiation.

The attenuation results (Fig. 5.6) reflect to some extent the variability in the material. The expected initial reduction in attenuation reflects a reduced defect size caused by initial densification. The densification at 575°C does reduce the defect size slightly faster than that obtained at 620°C. These data further reflect an increase in defect size as the graphite begins to expand.

Significantly the increase in defect size resulting from the volume expansion is larger than would be expected from the initial densification. This tends to confirm that the CTE results indicate the beginning of structural degradation from irradiation damage.

The brittle-ring strength (Fig. 5.7) is a measure of the flexural strength in the against-grain (tangential) direction. The scatter again reflects the variability in grade TSX, shown previously by the attenuation results. The implication is that the variability in strength is the result of the variation in defect size, rather than that in the elastic constants, for which the variability was much less (Fig. 5.5). The results suggest that the increase in strength at 575°C is possibly faster than that at 620°C, in agreement with the attenuation results, and again reflect the role of defect size in affecting the fracture strength.

The two curves in Fig. 5.7 are predicted strengths, based on hypothetical models of the material behavior. The dashed curves represent the relative strength calculated from the Young's modulus, assuming that the work to fracture is constant. The solid curves represent the strength calculated from the modulus and sonic attenuation, assuming that fracture mechanics concepts apply and that the energy to create new surface is unaffected by irradiation damage. The scatter in the data is too extreme to be conclusive, but clearly the fracture model utilizing both defect size and Young's modulus is a better representation of the data.

It is clear that the strength of the graphite has not been reduced below its unirradiated value, even to the extreme fluence of 2.3×10^{25} neutrons/m^2. But clearly the attenuation data indicate an increasing defect size, which promises an impending loss of strength below the initial value.

The overall conclusion from the HTU-1 irradiation experiment on grade TSX graphite is that no detrimental results exist that would prevent the

graphite from being used to a design life of 2.2×10^{25} neutrons/m^2. The only difference in the material properties between 1×10^{25} and 2.2×10^{25} neutrons/m^2 is the increased shrinkage in the with-grain direction. If this can be accommodated, there is no other impediment. Similar results, although limited in size of data base, were also obtained on KFA grades ATR-2E, ATR-2E$_L$, and ASR-1RP and on POCO grade AXF-5Q.

We now come to the problem of greatest overall interest — the existence or nonexistence of a flux (or rate) effect. Such has been hypothesized for some years, although data to support the hypothesis is of some question and certainly not conclusive. The data plotted in Fig. 5.8 were measured on full-size blocks of TSX in the N-Reactor core and were superposed on the curves obtained in the current HFIR experiment. Within the temperature uncertainties (±25°C) and flux spectrum calculations (±10%), the data are identical. We conclude that there is no evidence over a flux ratio of 50 and that data based on the test reactor exposures may be used with confidence for power reactor design.

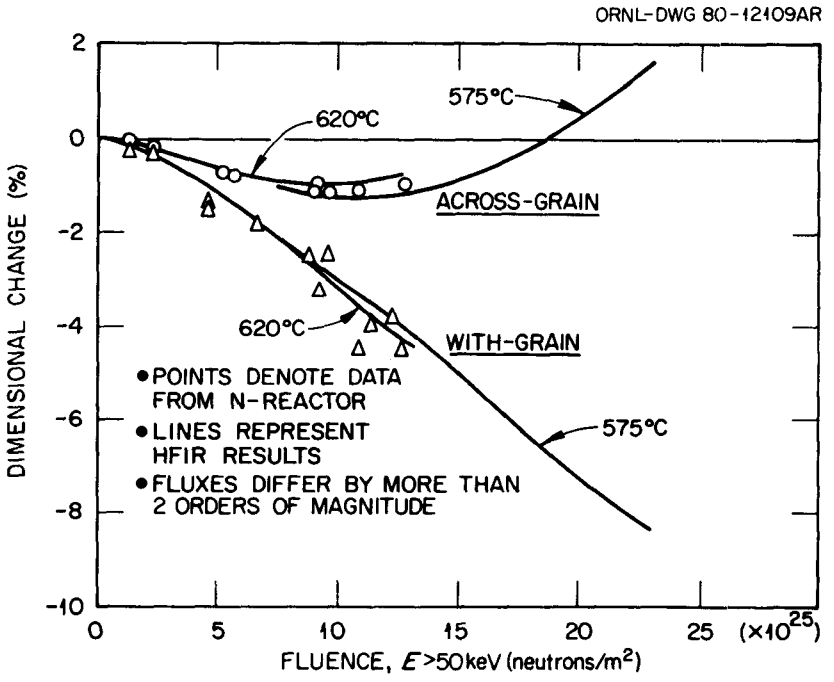

Fig. 5.8. Comparison of N-Reactor moderator block measurements with HFIR results.

5.2.2 Examination of German Reflector Graphites — C. R. Kennedy

The HFIR experiment HTK-4 is being conducted at 715°C to take advantage of an existing capsule design, to compare with early graphite studies under the Molten Salt Reactor Program involving dozens of graphite grades, and to tie in better the HFIR results with Petten irradiations normally conducted at 750°C. The samples contained in HTK-4 consist of graphite grades H451, POCO AXF, an advanced experimental graphite fabricated at ORNL, and a large number of specimens of German grades ATR-2E and ASR-2E. The latter two have been extensively studied at Petten. Included among these are grades ASR-2E/III and ATR-2E/II, which represent material from later production-scale fabrication runs.

The small blocks abstracted from billets by KFA and sent to ORNL have been nondestructively tested, and samples have been extracted. The preirradiation data are presented in Table 5.1. Agreement of the electrical resistance made in West Germany by voltage-drop methods and our eddy-current techniques is quite good. Of particular interest are the results of sample 81, where the normal rotational symmetry did not exist. This is not unusual in samples taken from the surface of extruded bars, as was sample 81. All of the remainder of the samples will be more like a molded texture, and the dimensional changes under irradiation should reflect this difference. The sonic moduli (ORNL) are observed to be slightly higher than the dynamic resonant values obtained in West Germany. This was also observed in past comparison of the values in other materials. The lack of symmetry in sample 81 was also reflected in the sonic moduli values.

5.3 GRAPHITE CORROSION STUDIES — W. P. Eatherly and R. P. Wichner

5.3.1 Corrosion Tests — C. D. Bopp, L. L. Fairchild, and R. P. Wichner

The experimental conditions and corrosion rates of our last 12 runs are shown in Table 5.2. In most cases, the corrosion rates determined by the carbon monoxide and carbon dioxide in the effluent gas flow and by the specimen weight loss were in good agreement. In those cases (runs 11, 14, and 21) in which the final corrosion rate was significantly higher than the overall run average, the corrosion rate during the last week of the

Table 5.1. Nondestructive evaluations of graphite for experiment HTK-4

Grade	Sample	Density, Mg/m^3		Electrical resistance, $\mu\Omega \cdot m$			Dynamic Young's modulus, GPa		
		FRG[a]	ORNL		FRG	ORNL		FRG	ORNL
ASR-2E/III	123	1.80	1.81	W/G[b]	8.00	8.07	W/G	10.70	10.96
				A/G[c]		9.70	A/G		9.99
	210	1.78	1.79	W/G	8.30	7.98	W/G	10.1	10.71
				A/G		10.17	A/G		9.82
	37	1.78	1.78	W/G		8.24	W/G		12.11
				A/G	10.50	10.15	A/G	7.62	8.66
	21	1.80	1.80	W/G		7.93	W/G		12.14
				A/G	10.00	9.76	A/G	8.39	8.96
ATR-2E/II	29	1.72	1.73	W/G	10.30	10.31	W/G	7.85	8.81
				A/G		11.81	A/G		8.53
	81	1.78	1.79	W/G	9.20	9.19	A/G	8.77	9.40
				A/G_θ		10.05	A/G_θ		9.09
				A/G_R		11.08	A/G_R		8.85
	41	1.77	1.78	W/G		9.18	W/G		9.56
				A/G	10.10	10.60	A/G	7.85	8.52
	45	1.77	1.77	W/G		9.10	W/G		9.53
				A/G	10.50	10.44	A/G	7.71	8.55

[a]Federal Republic of Germany.

[b]W/G = with grain.

[c]A/G = against grain.

Table 5.2. Conditions and corrosion rates for corrosion runs SP 9 to 16 and H451 19 to 22 (He flow = 50 cm^3/min)

Run	Material	Temperature (°C)	Rod diameter (cm)	Run time (h)	Impurity concentrations, vpm[a]				H_2/H_2O ratio	Rate of attack, mg/(cm^2·h)		Weight loss (%)
					H_2O	CO	CO_2	H_2		From CO + CO_2	From weight loss	
9	SP 2020[b]	1,000	1.27	336								
	Entire period				Small	7,000	90	7,400	>10	0.076	0.0700	4.3
	Last week				Small	7,000	70	7,400	>10			
10	SP 2020	1,000	1.90	504								
	Entire period				Small	6,700	140	7,100	>10	0.0487	0.0474	2.9
	Last week				Small	6,700	140	7,100	>10			
11	SP 2020	900	1.90	1248								
	Entire period				1,500	3,000	800	4,900	3	0.027	0.0269	4.0
	Last week				1,000	3,700	800	5,400	5	0.032		
12	SP 2020	1,000	1.90	506								
	Entire period				Small	5,800	300	6,600	>10	0.044	0.0433	2.7
	Last week				Small	6,100	260	6,800	>10			
13	SP 2020	1,000	1.27	336								
	Entire period				Small	16,700	760	17,500	>10	0.19	0.166	10.2
	Last week				Small	16,900	720	17,600	>10			
14	SP 2020	900	1.90	504								
	Entire period				4,500	8,200	2,000	12,800	3	0.072	0.0726	4.5
	Last week				3,300	10,000	1,900	14,000	4	0.084		
15	SP 2020	900	1.27	840								
	Entire period				600	4,000	820	5,800	10	0.051	0.0443	6.8
	Last week				600	4,200	830	5,800	10			
16	SP 2020	1,000	1.27	672								
	Entire period				Small	6,700	270	6,800	>10	0.074	0.0712	8.8
	Last week				Small	6,700	300	6,900	>10			
19	H451	1,000	1.90	336								
	Entire period				700	15,100	900	16,600	20	0.11	0.0775	3.3
	Last week				800	15,800	750	16,500	20			
20	H451	900	1.90	336								
	Entire period				7,400	8,890	570	9,900	1	0.067	0.0706	3.0
	Last week				7,400	8,890	580	9,900	1			
21	H451	900	2.54	1680								
	Entire period				1,000	4,800	600	5,100	5	0.029	0.0214	3.4
	Last week				Small	5,770	600	6,200	>10	0.034		
22	H451	1,000	2.54	1344								
	Entire period				Small	16,500	700	17,300	>10	0.092	0.0915	11.6
	Last week				Small	17,900	800	18,400	>10			

[a]vpm = volume parts per million.

[b]Heat-treated Stackpole 2020.

run is also provided in Table 5.2. The steam content of the corroding atmosphere was calculated as the difference between the inlet steam concentration and the amount consumed by the reactions $H_2O + C \quad CO + H_2$ and $H_2O + CO \rightarrow CO_2 + H_2$. The ratio of hydrogen-to-steam concentration in each run, where it can be unambiguously calculated, is lower than expected for an HTGR primary cooolant.

5.3.2 Catalytic Effects on Graphite Corrosion — R. P. Wichner

Because the transition metals (mainly iron and nickel) are catalytically active in the reduced form and evidently not as the oxide or carbide, it is important to determine the range of conditions in which the reduced form would be stable. This is particularly important when one attempts to carry over test data to reactor conditions. Usually, test data are acquired under accelerated corrosion conditions wherein the oxide form of the transition metal would more likely be the stable form (near the graphite surface at least) than under the HTGR primary circuit.

The question then arises as to whether or not the chemical form of iron or nickel may be expected to differ in the interior graphite regions from that in the surface. This possibility exists because the graphite exterior regions contain a more reducing gas composition in the pores than that existing in the interior. However, we must consider the possibility that the stable reduced form is the carbide, which would not be active catalytically.

Alkaline earths are virtually assured to exist as the oxide (SrO, BaO, and CaO) in any experiment designed to yield a reasonably large graphite corrosion rate. Therefore we must conclude that the observed catalytic activity of the alkaline earths results from the oxide. The question that must be explored is whether or not they would exist as oxides (hence retain their activity) under the more reducing conditions found in the HTGR primary circuit or in the interior graphite regions.

The regions of stability for the various species are illustrated in Fig. 5.9. The ordinate specifies the oxygen potential G_{O_2}, defined by $RT \ln P_{O_2}$. The temperature range experienced by test graphite and reactor core graphite is indicated on the abscissa.

ORNL-DWG 81-6993R

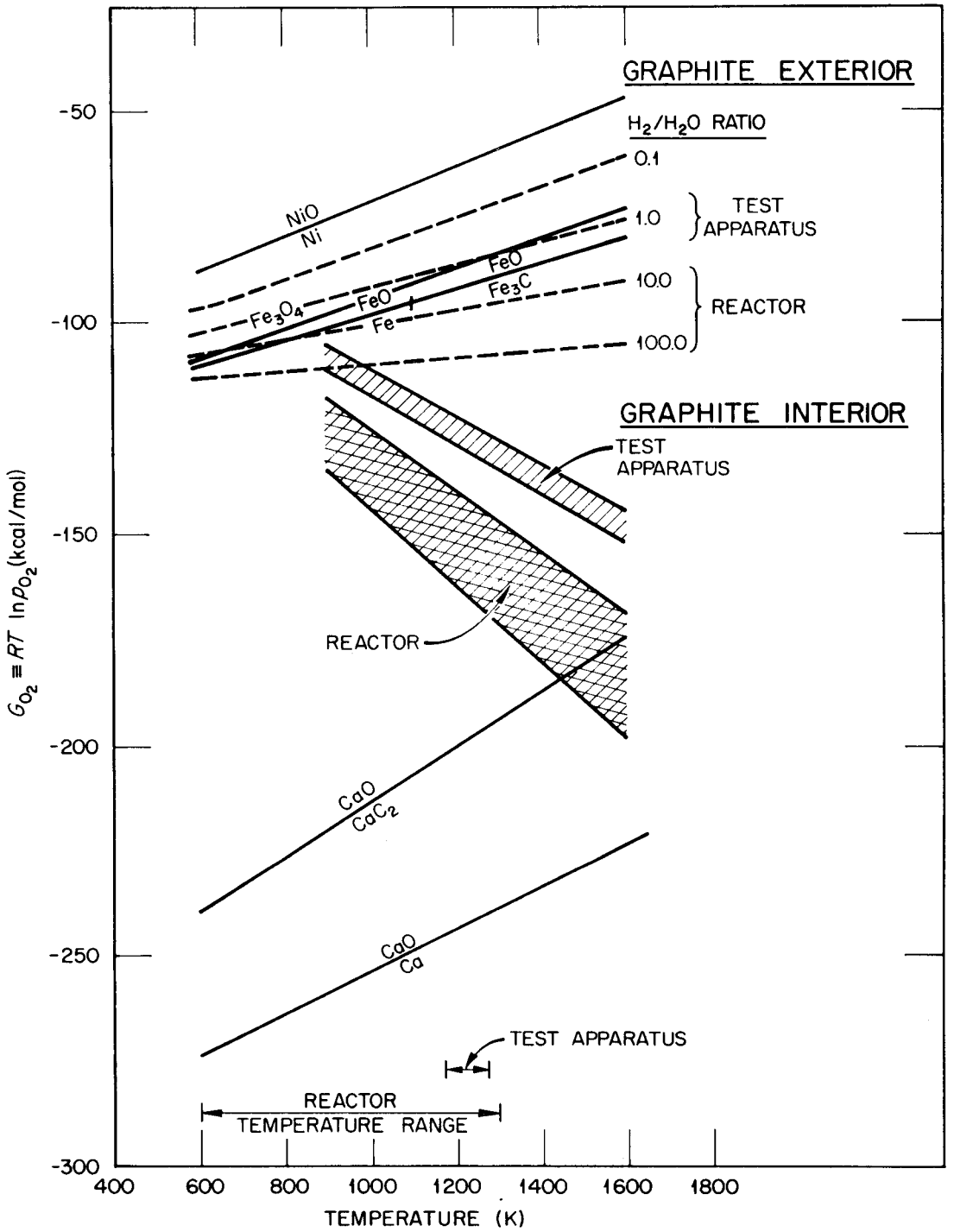

Fig. 5.9. Nickel, iron, and calcium transitions as functions of temperature and oxygen pressure.

The oxygen pressure in the vicinity of the exterior of a graphite specimen or core component is imposed by the gaseous environment, particularly the H_2/H_2O ratio. Parametric values of this ratio are listed at top right in Fig. 5.9, and the dependence of oxygen pressure as a function of temperature is shown by the associated dashed lines. As indicated in the figure, the H_2/H_2O ratio ranged between 0.4 and 4.0 in our corrosion apparatus, whereas HTGR primary systems are far more reducing under normal steady state conditions. The H_2/H_2O ratio averaged near 1000 in the Peach Bottom HTGR and from 200 to 500 in the Arbeitsgemeinschaft Versuchs-Reaktor.[9] (The Dragon reactor primary loop was more oxidizing, with an average H_2/H_2O ratio of ~10.) Gainey[9] indicates that the expected range of the H_2/H_2O ratio in future HTGRs is between 1 and 200. However, in view of past experience the higher end, from 10 to 200 would be more likely for normal steady operation.

The specimen interior will experience a far more reducing atmosphere. This was estimated by assuming that all the moisture in the exterior gas is converted to CO in the inner graphite regions. This simple procedure neglects both diffusion effects and CO_2 formation. Because the latter becomes significant below about 800 K, the shaded regions are not drawn below this temperature. The oxygen pressure was calculated from the equilibrium relation,

$$G_{O_2} = \Delta G^\circ(T) + 2RT \ln P_{CO} ,$$

where $\Delta G^\circ(T)$ is the standard free energy change for the reaction

$$2C + O_2 \rightarrow 2CO .$$

Values of $\Delta G^\circ(T)$ for the above and all subsequent chemical reactions were obtained from ref. 10. In our corrosion apparatus, the value of P_{CO} would range from about 8×10^3 to about 25×10^3 volume parts per million (vpm) in the specimen interior on the basis of complete conversion of H_2 to CO. The corresponding oxygen pressures are indicated by the shaded region. Oxygen pressures in the interior of a graphite member within the reactor are lower than for the test apparatus because there is far less total oxygen (H_2O, CO, and CO_2). The shaded region shown is based on a total range of 0.1 to 10 vpm total oxygen in the coolant, with complete conversion to CO within the graphite.

These estimates of internal graphite oxygen pressures are rough approximations only. The main purpose here is to portray our observation that conditions within the graphite pieces are more reducing than exterior conditions and to gain roughly some idea of the significance of this fact in the chemical alteration of active catalysts.

The oxygen potentials at which the various oxide to metal or carbide transitions occur are indicated by the labeled solid lines in Fig. 5.9.

The NiO/Ni transition occurs at higher oxygen potentials than existed in the gaseous environment of the test apparatus under the most highly oxidizing conditions (Fig. 5.9). Therefore, we would expect nickel to be in the metallic form in graphite for all reactor or test apparatus conditions.

All the iron transitions fall in the range of oxygen potentials experienced in the gaseous atmosphere of the test apparatus. In the most oxidizing runs, with the H_2/H_2O ratio of about 0.4, iron near the graphite surface probably exists as Fe_3O_4. The FeO to reduced form transition occurs at an H_2/H_2O ratio of about 2 at about 1300 K, but far more reducing conditions are required to effect the transition at lower temperatures. At 600 K, the FeO/Fe° transitions occur at an H_2/H_2O ratio of about 50.

Below 1100 K, Fe_3C is unstable (positive free energy of formation), and the reduced form is the metal. Above 1100 K, the free energy of formation of Fe_3C is negative, which means that it is the stable form in the presence of Fe° and C. Hence, above 1100 K the reduction of FeO goes to the carbide via

$$2FeO + 2/3C \rightarrow 2/3Fe_3C + O_2.$$

The reduction transition $FeO \rightarrow Fe_3C$ is thus thermodynamically predicted for temperatures above about 900 to 1000°C.

5.3.3 Electrical Conductivity as a Measure of Oxidation Gradients — C. R. Kennedy

The electrical conductivity of graphite is extremely sensitive to oxidation, because even a minor mass removal quickly interferes with the continuity of the material. The use of eddy-current techniques to examine

nondestructively graphite obviously lends itself to measurements on oxidized graphite in a particularly useful way: The skin depth of our single frequency probes (500 kHz) is of the order of 1 mm; hence, the measured conductivities are characteristic of a volume close to the exposed surface.

In the case of the right circular cylinders cut from extended rods and designed for compressive strength measurements, the oxidation occurs only from the curved surface. Hence, an eddy-current measurement on this surface determines the deterioration of the material directly exposed to the gas stream, whereas a measurement on the flat-end faces characterizes the interior material (Fig. 5.10). Only a minor correction is necessary for the change in coupling between a flat and curved surface to have a simple and direct estimate of the gross oxidation gradient generated in the material.

ORNL-DWG-81-6597

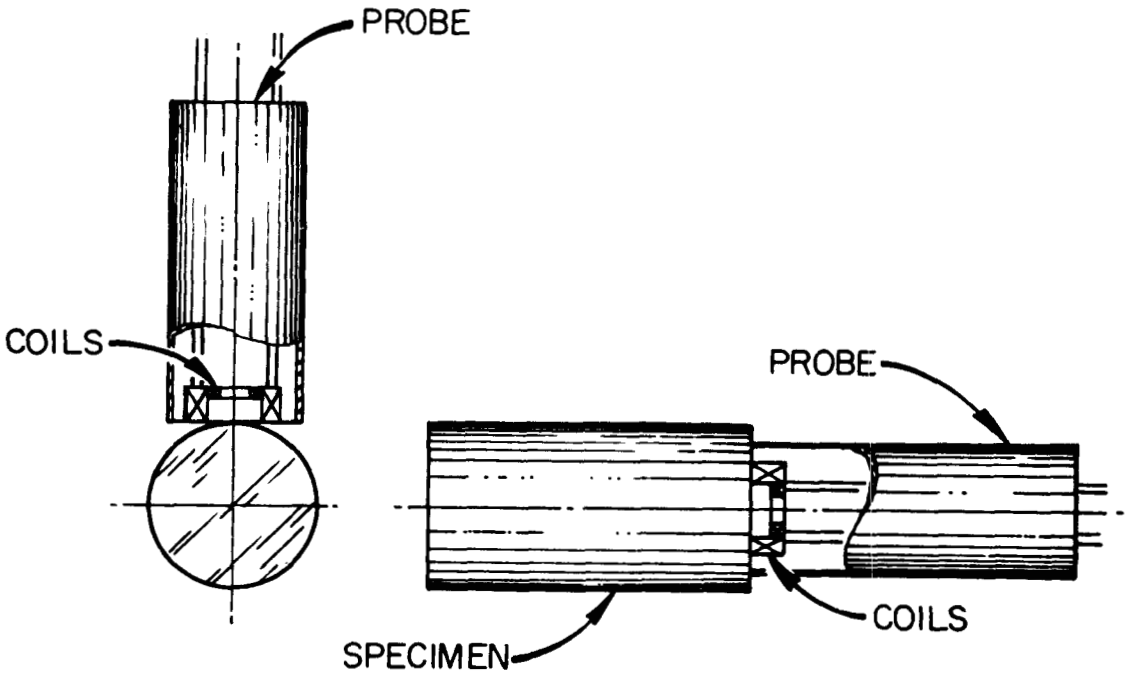

Fig. 5.10. Procedure used to measure eddy-current response of oxidized graphite cylindrical specimens.

In interpreting the eddy-current data, it must be kept in mind that the magnetic field of the probe coils senses an annular region of the order of a 3.6-mm outer radius and a 1-mm inner radius to a depth of about 2 mm.

Oxidized long rods of graphite grades H451 and Stackpole 2020 have been cut into short compressive strength specimens and eddy-current tested as described above. The results are presented in Figs. 5.11 through 5.15. The ordinate is the ratio of cylindrical surface to end surface conductivities, plotted with total porosity as the abscissa. The solid point at 17 to 18% porosity is the unoxidized material (controls) and, if different from unity, represents the anisotropy of the material. Values of the ratio below this control value obviously represent an expected density gradient from the exterior to the interior of the sample. Conversely, a higher value represents a more severe oxidation of the interior, that is,

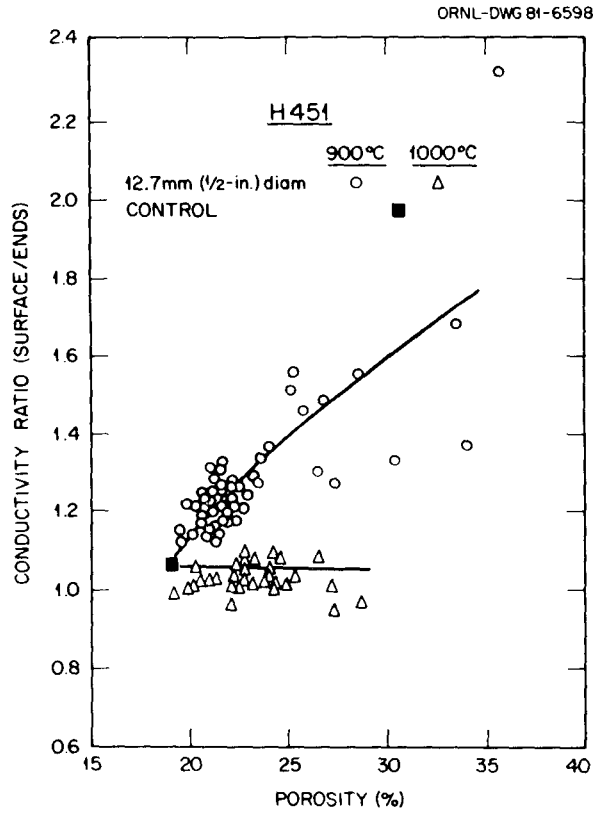

Fig. 5.11. Effect of oxidation on electrical resistivity of H451 graphite as determined by eddy-current techniques.

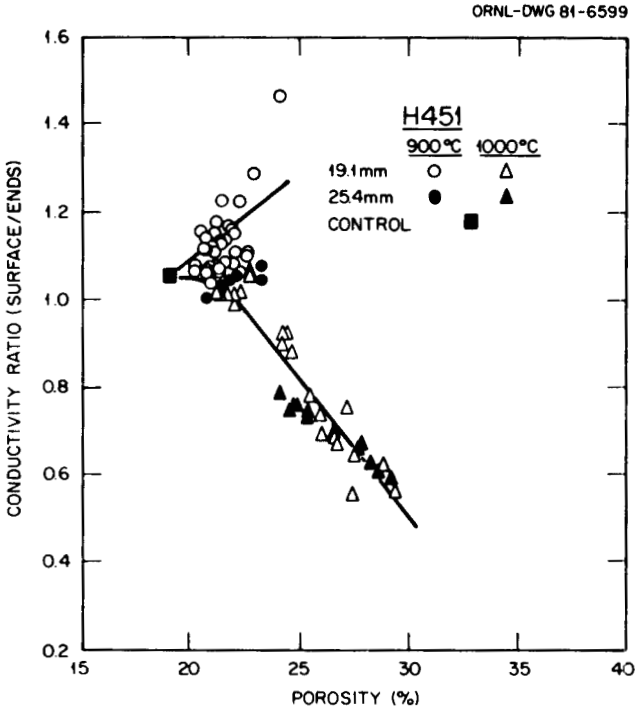

Fig. 5.12. Effect of oxidation on electrical resistivity of H451, continued.

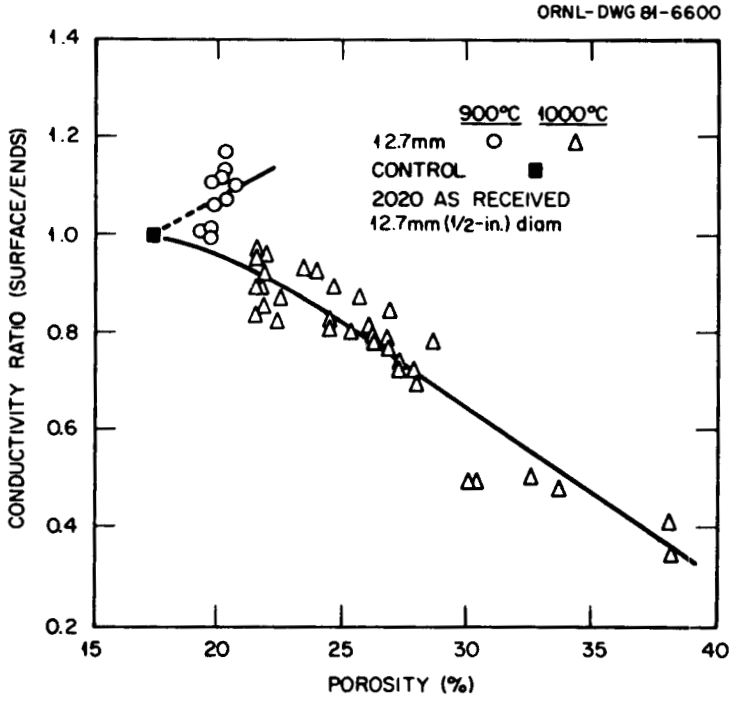

Fig. 5.13. Effect of oxidation on electrical resistivity of 2020 graphite as determined by eddy-current techniques.

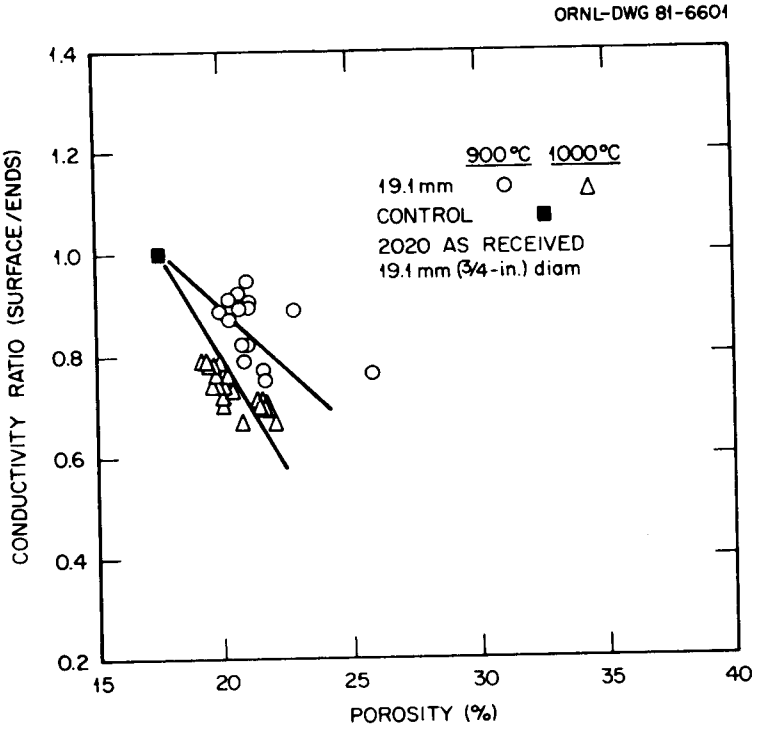

Fig. 5.14. Effect of oxidation on electrical resistivity of 2020 graphite, continued.

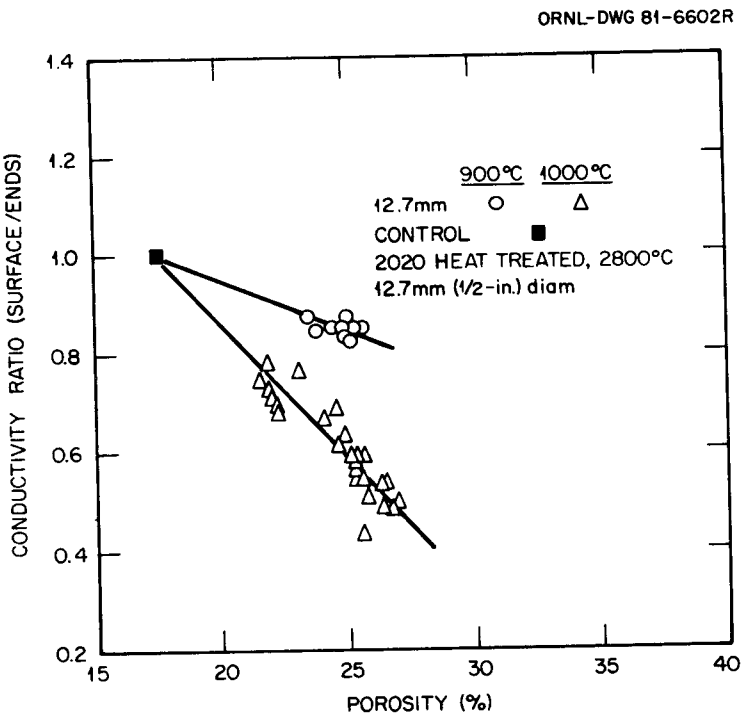

Fig. 5.15. Effect of oxidation on electrical resistivity of thermally purified 2020 graphite.

the so-called "inside-out" oxidation. Quite clearly, we have at our disposal a quick and inexpensive means to test and categorize large numbers of samples and thus to select a representative set of specimens for the elaborate radiographic density measurements.

Results for H451 graphite are given in Figs. 5.11 and 5.12 for the several cylinder diameters investigated. At 900°C the oxidation is obviously inside-out for the 12.7- and 19.0-mm-diam (0.5- and 0.75-in.) specimens. At 25.4 mm (1 in.) the oxidation appears to be uniform, although this result is clouded by the volume sensed by the eddy-current probe. A careful visual examination of radiographs failed, however, to show any indication of a gradient. At 1000°C the oxidation moved from uniform to normal "outside-in," with the "skin depth" saturating at the 19.0-mm-diam sample. This is further substantiated by the fact that all resistivities measured at the rod end positions are essentially equal to control value resistivity for all burnoffs.

Results on grade 2020 graphite are presented in Figs. 5.13 and 5.14. With the possible exception of one data set at 900°C and 2.5% burnoff, all samples show normal density gradients. Again, the more rapid decrease in the conductivity ratio with increasing diameter implies that the skin depth is saturating.

The characteristic pinhole oxidation of 2020 graphite previously reported has been associated with inclusions rich in calcium and perhaps iron. Heat-treating to 2800°C eliminates both the calcium and identifiable inclusions and the pinhole mode of oxidation. Data on the thermally purified 2020 are given in Fig. 5.15. Comparing this with Fig. 5.13, we see that the data suggest the oxidation in the more pure material to be less penetrating. The reason for this behavior is currently obscure.

These results do, however, allow several trends to be generalized:

- The expected reduction in penetration by increased oxidation temperature was observed.
- The expected reduction in penetration by finer grained, finer porosity, and less permeable graphites, such as 2020 compared with coarser grained H451, was observed.

- The maximum skin-depth effect at 1000°C obtained in this loop was with a 10-mm-diam rod. Increasing the rod diameter to 25.4 mm did not increase the skin-depth density gradient.
- Impurities as seen in the as-received 2020 demonstrated an increase in penetration at both 900 and 1000°C compared with the purified 2020 graphite.

5.3.4 Characterization of German Grade ASR—1RG — C. R. Kennedy

Grade ASR-1RG (FRG) is included as part of the oxidation test series under the U.S.—FRG Umbrella Agreement. This graphite is similar to grade ASR-1R except for its block size; the ASR-1RG block is 1200 mm in diameter by 900 mm long. Nondestructive evaluation indicates that the graphite is very uniform for such a large block. However, the structure is very coarse, and radiographs indicate a slight dispersion of high-Z impurities. Control brittle-ring and compression specimens have been tested.

Fracture results are compared in Table 5.3 with grades H451 and 2020. The fracture strength of ASR-1RG is lower than that of the other two graphites, as would be expected by the significantly larger defect structure indicated by the sonic attenuation.

Table 5.3. Comparison of unoxidized brittle-ring strength for grade ASR-1RG with grades H451 and 2020

Grade	Brittle-ring strength (MPa)	*C*-ring strength (MPa)	Sonic attenuation (dB/mm)	Young's modulus (GPa)
ASR-1RG	23.0	16.3	8.0	6.7
H451	27.0	19.5	3.9	7.4
2020	36.7	32.5	0.5	10.4

Selected compression specimens of grade ASR-1RG were evaluated for uniformity of the test block used for oxidation specimens. Twenty specimens were tested to yield: mean compressive strength — 45.7 MPa and

standard deviation — 1.43 MPa. Again ASR-1RG yields a lower strength than does H451 (50–60 MPa), as expected because of the very large defect structure. However, the very low variability in these results is interesting.

Brittle-ring specimens of German grade ASR-1RG have been oxidized at 900°C for two-, four-, and six-week periods. Compared with the 2.00 wt % loss for a two-week oxidation, the four- and six-week oxidations yielded 3.16 and 6.99 wt % losses, respectively. The oxidation pattern is given in Table 5.4.

Table 5.4. Weight loss of ASR-1RG specimens oxidized at 900°C

Block location	Weight loss, %		
	Two weeks	Four weeks	Six weeks
Inside	1.71 ± 0.25 (8)[a]	3.01 ± 0.25 (8)	6.79 ± 0.89 (9)
Middle	2.01 ± 0.26 (8)	3.34 ± 0.49 (8)	6.99 ± 0.66 (9)
Outside	2.24 ± 0.23 (9)	3.15 ± 0.43 (9)	7.23 ± 0.90 (7)
Average	2.00 ± 0.23 (25)	3.16 ± 0.41 (25)	6.99 ± 0.80 (25)

[a]Numbers in parentheses are numbers of specimens.

A trend of increased oxidation toward the outside of the block definitely occurs. The oxidation at six weeks was again somewhat larger than expected. The oxidation morphology of the longer four- and six-week specimens is of the cavity (pinhole) type demonstrated previously by as-received 2020. Radiographs of the oxidized specimens showed the characteristic catalytic type of oxidation, with low-density regions surrounding each impurity particle. The oxidation also tended to remove the obvious binder regions, with some slight gradient in density from the inside exposed diameter. The overall structure is very nonhomogeneous, even when compared with grade H451.

The brittle-ring test results on oxidized ASR-1RG are given in Fig. 5.16. A striking result of this test series is the relatively severe

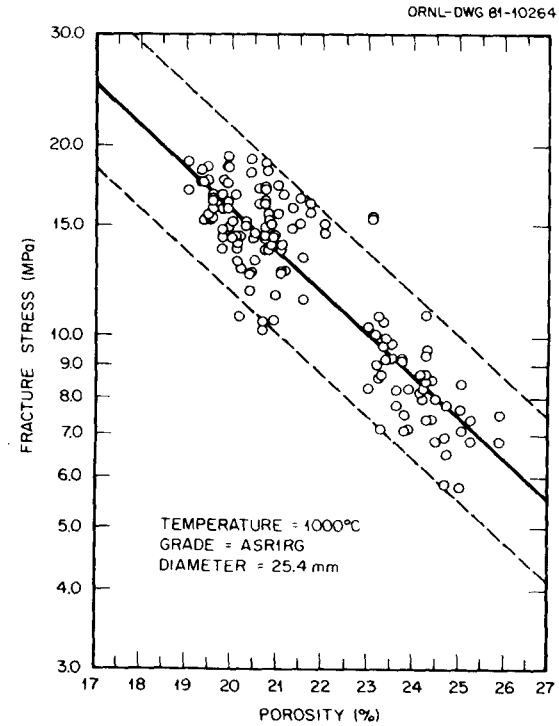

Fig. 5.16. O-ring (25.4-mm) fracture stress versus porosity for graphite grade ASR-1RG (dashed line is 95% confidence level).

decrease in strength at 10 wt % loss, in comparison with the other grades evaluated in Table 5.5. This loss may result from the defect size that is induced by oxidation becoming too large for the specimen size. Additional testing of larger specimens and compression testing are required to resolve the validity of this data.

Table 5.5. Strength retained after 10 wt % loss

Grade	Strength ratio
2020 (25.4 mm diam)	0.38
2020 (19 mm diam)	0.33
H451 (25.4 mm diam)	0.56
ASR-1RG (25.4 mm diam)	0.22

5.3.5 Mechanical Properties of Oxidized Grade 2020 — C. R. Kennedy

The particular lot of Stackpole grade 2020 graphite as received from the vendor was found to contain high concentrations of impurities, which control the oxidation morphology by catalysis. As indicated in our previous annual report,[11] heat treatment to 2800°C eliminates these concentrated impurities by vaporization. In this report, we summarize the quite different mechanical behavior of the as-received and the heat-treated graphites after oxidation under the conditions of our experiments. The compression testing results of the heat-treated 2020 control specimens were

	Compressive strength (MPa)	Fracture strain (%)
As-received graphite	85.7	2.81
Heat-treated (2800°C)	86.0	3.12

The heat treatment has not significantly altered the strength of the material; however, the graphite was softened and the fracture strain increased, as expected. This would imply a significant improvement in the overall toughness of the material.

Qualitative x-ray densitometry of the three graphites being studied (H451 and the two types of 2020) show rather marked contrasts. The as-received 2020 shows no evidence of any gradient in the dense material between the oxidized pockets (cavities) containing the concentrated impurities; that is, the oxidation is completely dominated by the catalytic reaction.[11] The H451, a high-purity graphite, also showed neither density gradient nor pitting at 1000°C, but showed inside-out oxidation at 900°C. For the purified 2020, the situation is even more complex: at 1000°C very sharp surface gradients were observed, but at 900°C a possible inside-out gradient appears to be superposed on the sharp surface gradient. Confirmation of these observations awaits quantitative densitometry, but even these superficial descriptions imply profound differences in mechanical property behavior.

As a first indication of these mechanical effects, the sonic attenuation is given in Fig. 5.17. The most attenuation (most scattering of the sonic wave) is seen in the as-received material with its large

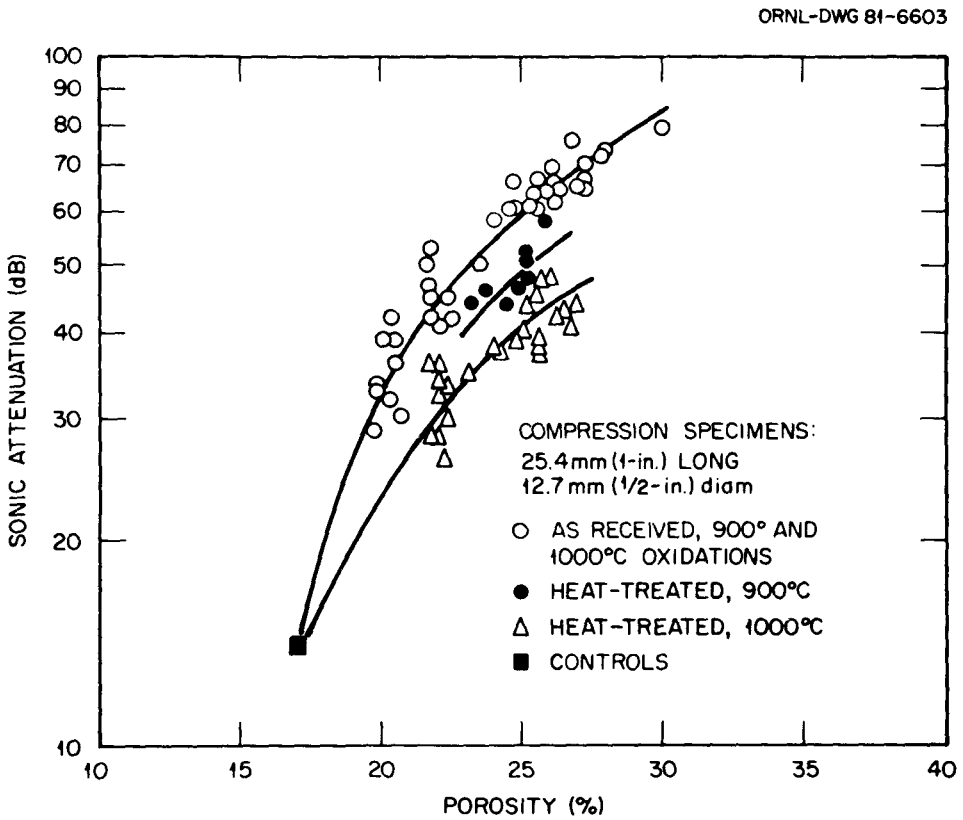

Fig. 5.17. Sonic attenuation measurements on oxidized specimens of as-received and heat-treated 2020 graphite.

oxidation-produced cavities, as expected. The scattering is large enough to mask any effect between the 900 and 1000°C oxidations. Heat treatment and elimination of the cavities reduce sonic attenuation for both the 900 and 1000°C samples. The rather surprising result is that, for the same porosity, the scattering is most reduced for the 1000°C-oxidized material.

Sonic velocities (Young's modulus) data for oxidized 2020 graphites are given in Fig. 5.18. The increase in average velocity at a given porosity for the 1000°C-oxidized purified material is perhaps expected because oxidation is confined to the surface. Conversely, the 900°C material shows a much decreased velocity, perhaps indicative of increased oxidation depth.

Because strength depends directly on modulus and inversely on flaw size, one might therefore expect the 1000°C purified material to have the

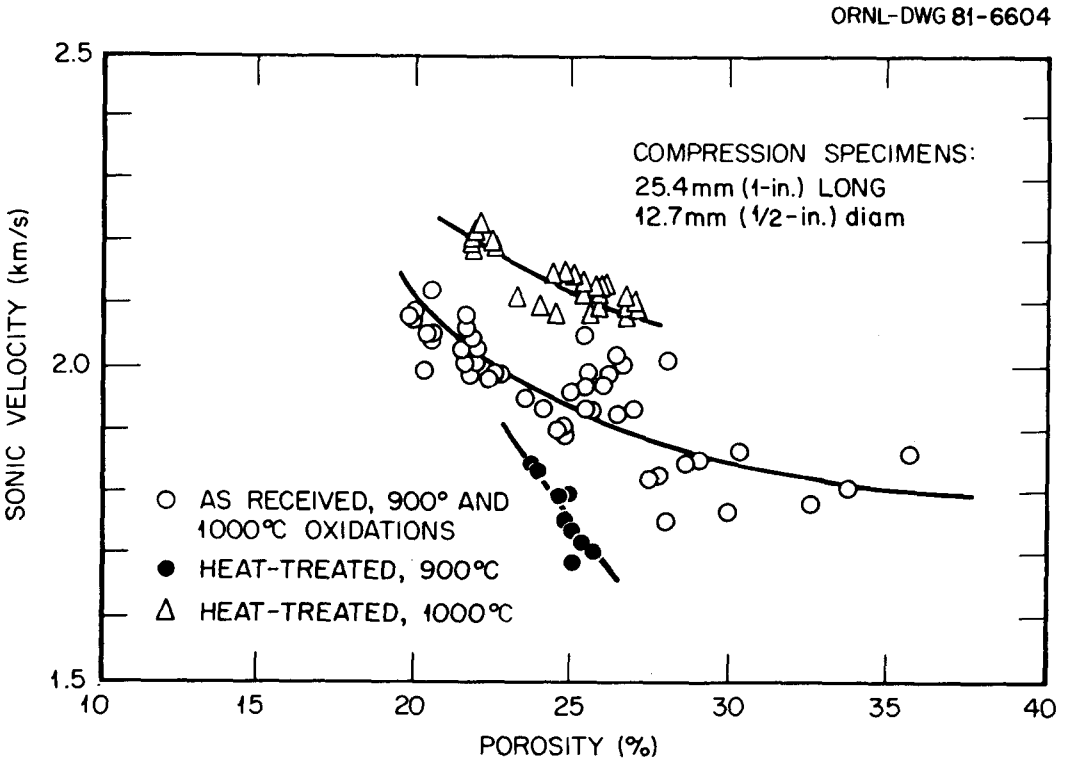

Fig. 5.18. Sonic velocity measurements on oxidized specimens of as-received and heat-treated 2020 graphite.

highest strength at a given porosity and the 900°C purified and the unpurified to be comparable. Such is the case, as shown in Fig. 5.19, but clearly the situation is quite complex because of the marked differences in microstructure and density gradients.

Tubular specimens of as-received 2020 graphite were oxidized in preparation for studies of the fracture-behavior at Aerospace Corporation. To simplify interpretation and modeling studies, it is most desirable for the specimens to be uniformly oxidized throughout their volume. For this reason, the samples were oxidized by R. E. Burnett at GA under conditions of $p(H_2)/p(H_2O) = 1$ at 900°C. To obtain significant changes in microstructure, oxidations of between 500 and 1000 h were required.

On return to ORNL, the oxidized tubes were machined into a number of 6-mm-thick (1/4-in.) brittle-ring samples. Preliminary results of eddy-current measurements of the three intact tubes are given in Fig. 5.20. The eddy-current response is shown as a function of position, and its average value for the entire tube, by a bar. A bar representing the

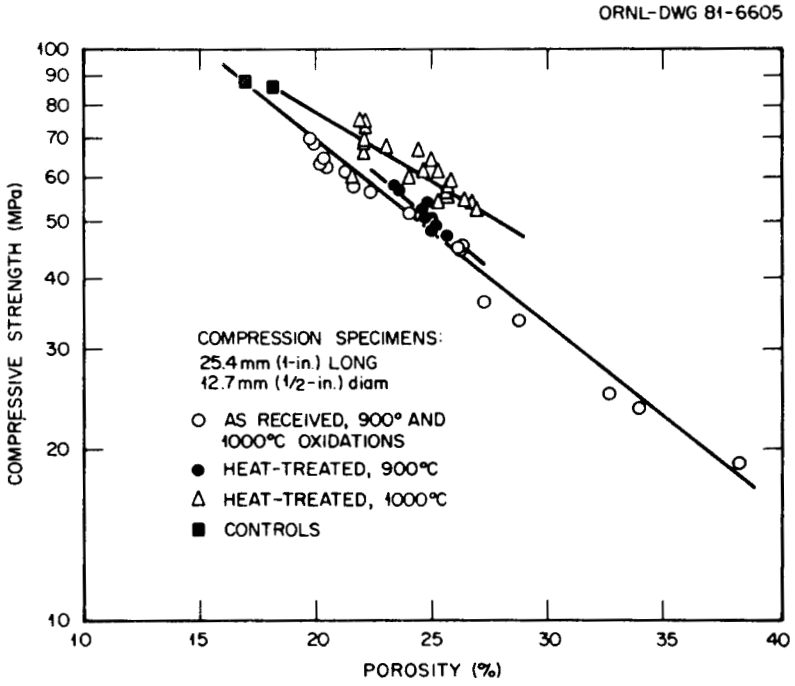

Fig. 5.19. Compressive strength loss caused by oxidation of both as-received and heat-treated 2020 graphite.

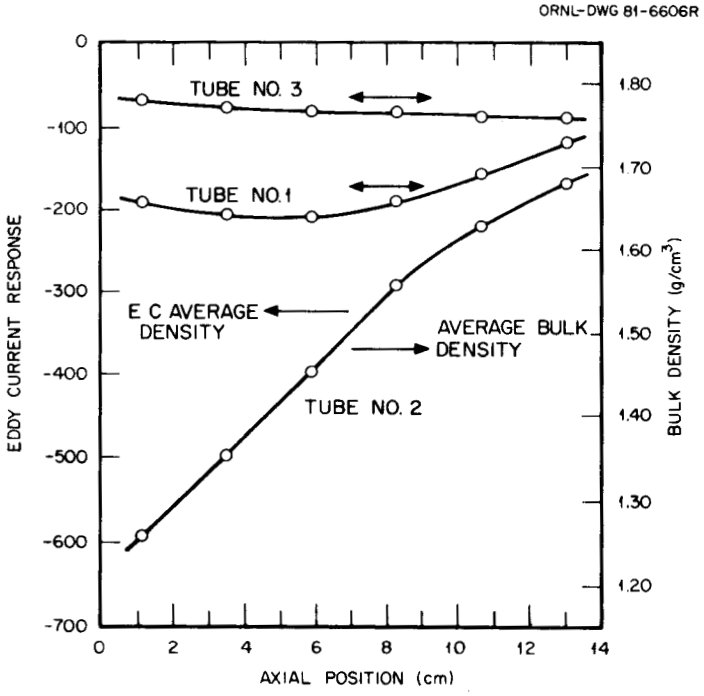

Fig. 5.20. Results of eddy-current testing on oxidized tubes of 2020 as-received graphite. Average eddy-current results are shown as bars and contrasted with the average bulk density.

average bulk density is also indicated. Because eddy-crrent response is a linear indicator of density for a given grade of graphite, the implication of Fig. 5.20 is of a definite axial gradient in density, particularly for the most highly oxidized tube 2.

The tubes were cut into specimens, and the detailed test results on a greatly expanded scale are shown in Fig. 5.21 for tube 1. Note the marked dependence of sonic attenuation, sonic velocity, and bulk density and eddy-current response. The axial gradients observed do not negate the use of these samples for the Aerospace work. The requirement of uniform oxidation is in the radial direction only; the axial variation will actually be an advantage.

Representative brittle-ring specimens made from the 10-mm tubes were sent to Aerospace for evaluation, and the remainder were tested at ORNL. The results of this test series are given in Fig. 5.22 as a fraction of porosity. The 10% burnoff strength is given in Table 5.5, compared with previous results for 25.4-mm rings. These results indicate very little difference in the strength loss between the two brittle-ring geometries, which gives additional credibility to the hypothesis that oxidation does

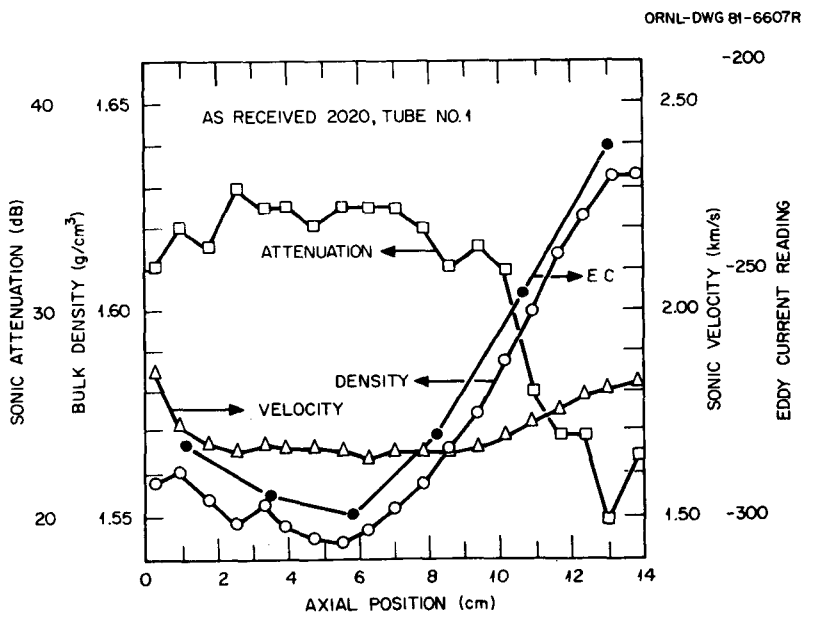

Fig. 5.21. Results of evaluating brittle-ring specimens made from oxidized tube 1.

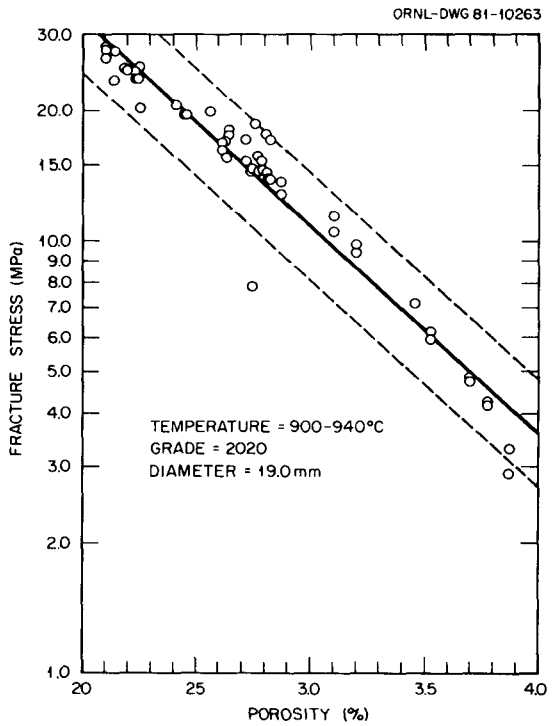

Fig. 5.22. O-ring (19-mm) fracture stress versus porosity for graphite grade 2020 (dashed line is 95% confidence level).

not alter the scaling factors resulting from the statistical nature of fracture. This will be examined in greater detail in the future.

5.3.6 BET Surface Area Measurements — J. D. Kintigh

Construction of the BET-type surface area apparatus is complete.[12] Surface areas are measured by gas adsorption. Adsorption of an inert gas on the surface of a solid material is carefully controlled and monitored. At the point at which a single monolayer of the gas covers the entire surface of the material, the surface area of the material can be calculated from the specific area of the adsorbate molecule or atom. The apparatus is also used to measure apparent density by using the helium gas displacement technique.

The apparatus (Fig. 5.23) used to measure surface areas determines the volume of gas adsorbed by measuring the pressure of the gas in a gas manifold of known volume and exposing the sample to the gas, which determines the pressure change. The manifold is defined by values

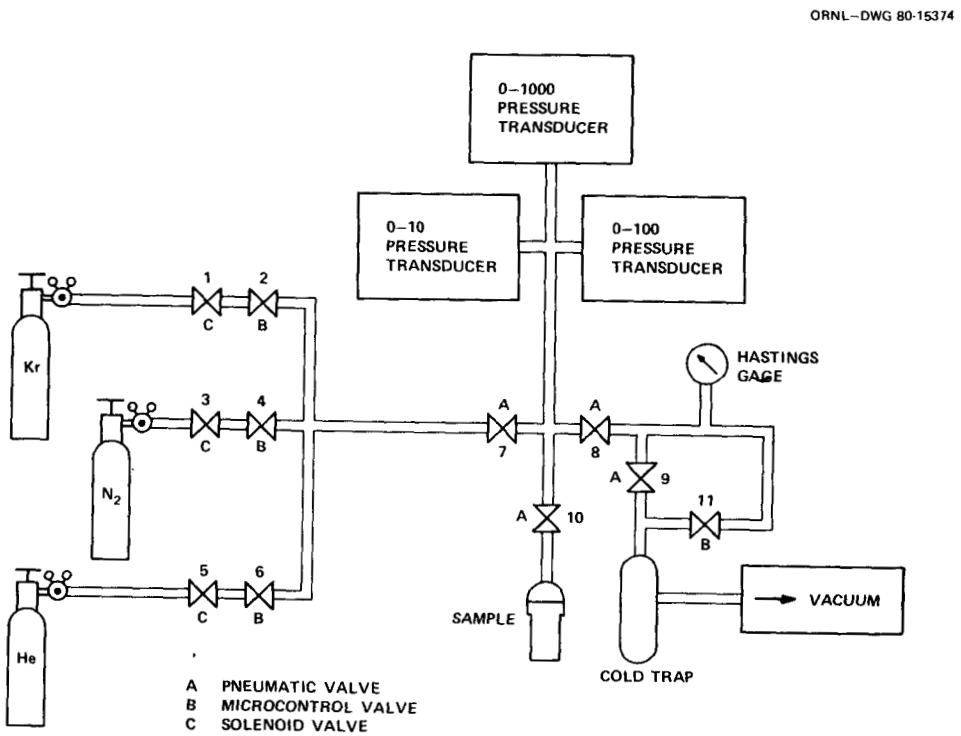

Fig. 5.23. Schematic of the BET apparatus.

7, 8, and 10. This change is compared with that of a nonadsorbed gas under the same circumstances, and the difference is attributed to adsorption of the gas on the sample.

The system is fully automated by using pneumatic valves for gas flow control and an MKS Barytron electronic pressure-monitoring system for reading the pressure. The entire system is controlled by a Hewlett-Packard 9835B desk-top computer. The computer, by monitoring the pressure, can control the amount of gas introduced to the gas manifold; thus, both adsorption and desorption isotherms can be measured. By using the computer clock, events can be timed, and overnight operation is possible. Because nitrogen gas is used in the adsorption, the sample is maintained at liquid nitrogen temperature by keeping the cell immersed in a liquid nitrogen bath. An automatic level control is used to maintain the liquid nitrogen in the bath at a constant level throughout the experiment. For powdered samples, valve 9 is closed and evacuation is controlled by microcontrol valve 11, which maintains the evacuation speed low enough to prevent blowing powder into the manifold.

In addition to the instrument control and data collection, the computer also stores the data on tape, calculates the surface area, and plots the adsorption isotherm.

The BET plots for solid samples of graphite were initially plagued by a premature onset of nonlinearity and even negative curvature, particularly for samples having a total surface area of less than 1 m^2. The source of this error in the BET surface area apparatus was located and corrected. This source is connected with the change in the apparent sample container volume as a result of the closing of its shutoff valve. Because of the nature of the measurement, this error cumulates in each succeeding measurement and must be corrected for.

The manifold was calibrated by gas displacement techniques using a gas bulb calibrated with mercury. The system measures areas with a precision of ±2% for samples of total surface greater than 5 m^2 but will measure surfaces as low as 0.5 m^2 with a precision of ±5%. The accuracy of the instrument has not yet been determined. Gas densities are measured with precision and accuracy of ±0.5% for samples with volumes greater than 2 cm^3 and of ±1% for samples with volumes as low as 0.2 cm^3.

Table 5.6 contains data for some representative samples of H451 and Stackpole 2020 graphites. Samples RA1 through RA5 and RB1 through RB5 were cylinders 2.54 cm (1 in.) long and 1.27 cm (1/2 in.) in diameter. Samples RA6 through RA10 and RB6 through RB10 were 1.27 cm (1/2 in.) long and 0.56 cm (7/32 in.) in diameter. The remainder of the samples were 0.635 cm (1/4 in.) long and 1.27 cm (1/2 in.) in diameter.

Figure 5.24 contains a BET plot of a representative sample. The plot is linear in the range of X (= p/p_o) between 0.05 and 0.35. The BET variables are

p = measurement pressure,

p_o = vapor pressure at liquification, and

V_a = equivalent gas volume of sorbed monolayer.

In brief, the precision of measurement per sample is superb, and the variability indicated in Table 5.6 can be attributed entirely to the material.

Table 5.6. Surface areas and helium densities of two HTGR graphites

Sample	Surface area (m^2/g)	Helium density (g/cm^3)
	H451 graphite	
RA1	0.66	2.04
RA2	1.01	2.06
RA3	0.90	2.06
RA4	1.06	2.06
RA5	1.01	2.05
RA6	0.82	2.04
RA7	1.06	2.03
RA8	1.31	2.07
RA9	0.89	2.12
RA10	0.89	2.09
HL3	0.95	2.06
HL6	0.85	2.13
M1	0.75	2.08
M2	0.71	2.05
H2	1.02	2.12
H4	1.06	2.07
Av	0.93 ± 0.16	2.07 ± 0.03
	Stackpole 2020 graphite	
RB1	0.34	2.01
RB2	0.33	2.02
RB3	0.43	2.05
RB4	0.41	2.01
RB5	0.46	2.02
RB6		2.03
RB7		2.03
RB8		2.02
RB9		2.02
RB10		2.03
SA1		2.06
SP1		2.03
Av	0.39 ± 0.06	2.03 ± 0.01

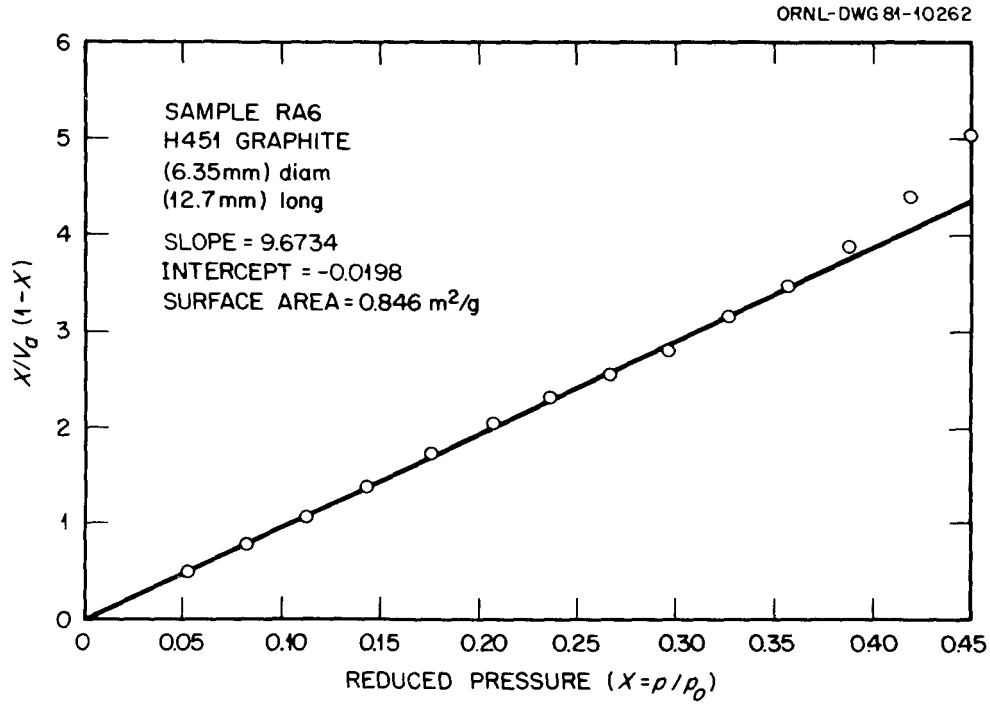

Fig. 5.24. Typical BET plot for graphite grade H451.

5.4 REFERENCES

1. W. P. Eatherly and J. A. Conlin, "Characterization and Standardization of Graphite," *HTGR Base-Technology Program Prog. Rep., Jan. 1, 1974–June 30, 1975*, ORNL-5108, pp. 475–84.
2. W. P. Eatherly and J. A. Conlin, "Characterization and Standardization of Graphite," *HTGR Base-Technology Program Prog. Rep., July 1, 1975–Dec. 31, 1976*, ORNL-5274, pp. 373–404.
3. R. L. Senn, W. H. Cook, J. A. Conlin, and W. P. Eatherly, *Design, Operation, and Initial Results from Capsule OC-1, the First of a Series of Graphite Creep Irradiation Experiments*, ORNL/TM-5798 (May 1977).
4. W. P. Eatherly and J. A. Conlin, "Characterization and Standardization of Graphite," *HTGR Base-Technology Program Annu. Prog. Rep., Dec. 31, 1977*, ORNL-5412, pp. 323 and 344.
5. Ibid., pp. 324 and 326.
6. W. P. Eatherly and J. A. Conlin, "HTGR Graphite Studies," *HTGR Base-Technology Program Annu. Prog. Rep., Dec. 31, 1979*, ORNL-5643, p. 241.

7. W. P. Eatherly and J. A. Conlin, "Characterization and Standardization of Graphite," *HTGR Base-Technology Program Annu. Prog. Rep., Dec. 31, 1977,* ORNL-5412, pp. 327 and 330.

8. W. P. Eatherly and J. A. Conlin, "HTGR Graphite Studies," *HTGR Base-Technology Program Annu. Prog. Rep., Dec. 31, 1979,* ORNL-5643, pp. 226–27.

9. B. W. Gainey, *An Evaluation of Carbon Deposition and Possible Consequences in the HTGR: A Review*, GA-A13982, General Atomic Company, San Diego, Calif. (July 1977).

10. J. F. Elliott and M. Gleiser, *Thermochemistry for Steelmaking*, vol. 1, Addison-Wesley, Reading, Mass., 1960.

11. W. P. Eatherly and J. A. Conlin, "HTGR Graphite Studies," *HTGR Base-Technology Program Annu. Prog. Rep., Dec. 31, 1979,* ORNL-5643, p. 10.

12. Ibid., p. 13.

6. HTR CORE EVALUATION

P. R. Kasten

A comparative evaluation was performed of pebble-bed and prismatic fuel configurations for HTGR cores. Basic studies carried out over a period of about six months involved specific relative evaluations and a review of the general information that was available. Because of time limitations, the evaluations were largely carried out by utilizing reference designs in comparing the two reactor concepts. Although not evident on the basis of the understanding developed during this study, design reoptimization of some of the specific parameters considered to be important here might influence the comparative results; such reoptimizations were not carried out.

The evaluation results obtained were those determined by ORNL; however, other participants also made significant contributions by providing information useful to this study. In particular, General Atomic Company (GA) provided information on design, thermal hydraulics, fission product behavior, safety studies, fuel cycle performance, maintenance requirements, and fuel reprocessing technology and costs. General Electric Company (GE) provided information on reactor availability, control, and design. Gas-cooled Reactor Associates (GCRA) provided utility perspectives on reactor maintenance and operations, and Management Analysis Company (MAC) provided the methodology for estimating the overall cost uncertainites of the two reactor concepts. We concluded that, on the basis of the results of this study, the United States should continue to develop the prismatic fueled HTGR.

The evaluation results have been reported;[1] an abstract of the report is given below:

> A comparative evaluation has been performed of the High Temperature Gas Cooled Reactor (HTGR) and the Federal Republic of Germany's Pebble Bed Reactor (PBR) for potential commercial applications in the U.S. The evaluation considered two reactor sizes [1000 and 3000 MW(t)] and three process applications (steam cycle, direct cycle, and process heat, with outlet coolant temperatures of 750, 850, and 950°C, respectively). The primary criterion for the comparison was the levelized (15-year) cost of producing electricity or process heat.

Emphasis was placed on the cost impact of differences between the prismatic-type HTGR core, which requires periodic refuelings during reactor shutdowns, and the pebble bed PBR core, which is refueled continuously during reactor operations. Detailed studies of key technical issues using reference HTGR and PBR designs revealed that two cost components contributing to the levelized power costs are higher for the PBR: capital costs and operation and maintenance costs. A third cost component, associated with nonavailability penalties, tended to be higher for the PBR except for the process heat application, for which there is a large uncertainty in the HTGR nonavailability penalty at the 950°C outlet coolant temperature. A fourth cost component, fuel cycle costs, is lower for the PBR but not sufficiently lower to offset the capital cost component. Thus, the HTGR appears to be slightly superior to the PBR in economic performance. Because of the advanced development of the HTGR concept, large HTGRs could also be commercialized in the United States with lower R&D costs and shorter lead times than could large PBRs. On the basis of these results, it is recommended that the U.S. gas-cooled thermal reactor program continue giving primary support to the HTGR. At the same time, the United States should maintain a cooperative PBR program with FRG, emphasizing work in the key areas of reactor control and instrumentation.

6.1 REFERENCES

1. P. R. Kasten et al., *Comparative Evaluation of Pebble-Bed and Prismatic-Fueled High-Temperature Gas-Cooled Reactors*, ORNL-5694 (January 1981).

7. HTR PHYSICS STUDIES

D. R. Vondy and D. E. Bartine

Development of the high-temperature reactor concept is supported by core physics analysis. Project objectives include high fuel utilization, high thermal efficiency, and a high-temperature source for process heat in a plant that is safe, can be controlled, and has competitive costs. The best core design, plant operating conditions, and mode of operation are determined from performance studies.

The major effort this year was in support of the pebble-bed and prismatic-fueled high-temperature reactor (HTR) assessment,[1] the physics effort being directed primarily toward the analysis of the pebble-bed concept. These studies also support the continuing effort by the General Electric Company (GE) to develop a U.S. pebble-bed design and contribute to the technical information exchange with the Federated Republic of Germany (FRG). In FY 1981, the emphasis shifted to supporting development of the prismatic core being designed by the General Atomic Company (GA).

7.1 HTR METHODS DEVELOPMENT

A computation system being used locally applies the diffusion theory approximation to neutron transport for generating core neutronics solutions.[2] The neutronics and exposure (burnup) capability has been developed under the U.S. Department of Energy (DOE) physics program, and additional capability has been incorporated under HTR project funding. Fuel management capability has been implemented under contract with the Technology for Energy Corporation.[3] Thermal hydraulics capability for the pebble-bed concept was integrated into the system, starting with a two-dimensional (2-D) code originated at the Los Alamos Scientific Laboratory.[4] This capability has been enhanced by ORNL to provide limited thermal hydraulic capability for treating the prismatic core.[5]

Further enhancements made to this computation system include the capability to assess stability against xenon-driven oscillation and treating temperature feedback effects. To produce the results necessary for establishing the inherent stabilizing force, general capability was

implemented for resolving the dominant neutronic harmonics problem. Indeed, for azimuthal symmetry, an *RZ* solution is possible, avoiding 3-D problems. Obtaining the spacial equilibrium ^{135}Xe poisoning effect simultaneously with solution of the neutronics problem was found to be crucial to avoid unrealistic neutron flux shifts during history calculations. Otherwise the exposure steps between neutronics solutions must be so short that computation costs are unacceptably high.

A related effort is the extension of the local double-heterogeneous, 1-D integral transport theory resonance shielding capability[6] to treat the fuel rod geometry of the prismatic core. Attempts to lower the computation costs of this method to an acceptable level for routine use have not been successful.

Methods development work continued. The cost of obtaining accurate 3-D neutronic solutions must be reduced, and certain enhancements to existing Monte Carlo neutronics capability are desirable. Cost calculations are being added to the fuel management capability. Three-dimensional thermal hydraulics and auxiliary analysis capability are required for adequate and reliable prismatic core performance analysis of HTRs.

7.2 PEBBLE-BED HTR CORE ANALYSIS

Results illustrating this analysis effort are presented in Table 7.1. The dependence of fuel temperature on certain design parameters and modes of operation are shown. Of special interest is the reduction in the high-energy flux exposure (and hence lower damage rate) of the pebble recycle. A special iterative procedure is used to produce such results for a critical core at equilibrium with continuous feed.

The behavior of the core against xenon-driven oscillation was found to be somewhat sensitive to the design and to its operation.[7] The neutron flux distribution and the natural restoring force for any perturbation depend on pebble control and control rod positioning.

Table 7.1. Effect of certain variables on core performance (one-dimensional, 1640 MW(t), C/HM[a] 325, core height 550 cm)

	Case				
	1	2	3	4	5
Number of pebbles passes through core	1	1	1	2	6
Average power density, W(t)/cm^3	8.43	5.62	5.62	5.62	5.62
Core discrete zones, subzones	36(0)	36(0)	18(0)	18(36)	18(108)
Core residence time, full power	2.10	3.15	3.15	3.15	3.15
Exposure, MW(t)-d/kg	102.4	103.0	103.1	103.6	104.0
Conversion ratio	0.579	0.598	0.610	0.635	0.657
Fissile feed, kg/d	1.325	1.242	1.211	1.155	1.102
Peak power density, pebble W(t)/cm^3	34.6	23.0	22.7	20.8	20.8
Fission product absorption fraction	0.1025	0.1022	0.1020	0.1061	0.1086
Fissile inventory, kg	472.6	653.1	640.5	655.6	644.1
Peak neutron flux, $>2 \times 10^5$ eV	14.6 + 13	9.8 + 13	9.8 + 13	7.0 + 13	5.6 + 13
Core pressure drop, kPa (atm)	157(1.55)	71.9(0.71)	71.9(0.71)	67.9(0.67)	64.8(0.64)
Temperature, coolant in 350°C, out 850°C:					
Coolant average	713	714	714	665	620
Peak HM	901	862	862	881	915
Peak pebble average HM	862	858	858	870	894
Core average HM	810	793	789	738	693
Power density, weighted mean	759	731	724	695	684
Pebble HM at core outlet	862	859	858	867	877
Temperature with 1.2 radial peaking factor (no crossflow):					
Coolant average	802	803	802	742	686
Peak HM	1014	986	985	1008	1050
Peak pebble average HM	987	982	981	996	1025
Core average	917	892	892	829	773
Power density weighted mean	851	809	809	775	761
Pebble HM at core outlet	987	982	981	996	1022

[a]HM = heavy metal.

[b]Core modeling discretization for neutronics and exposure; pebble recycle is modeled with subzones for individual exposure calculations.

Typical results are shown below for the core size where the stability bound occurs.

Design power density [W(t)/cm^3]	Size above which the core is unstable, MW(t)	
	Without temperature feedback	With temperature feedback
2.81	1660	2300
5.62	2500	3160
11.24	4240	5150

Control of a pebble-bed reactor was studied. No alternative to control rods for secondary shutdown capability that would produce wholly acceptable and desirable core characteristics was identified. Study of the core characteristics and demands expected on operation led us to conclude that the probability is high for some control rods to be inserted into the pebble bed during operation. For example, such would generally be necessary to provide the excess reactivity required for override and full restart capability, although fuel utilization would be degraded (neutron adsorption in control rods rather than fertile material). Sophisticated calculations of partial control rod insertion to demonstrate effects and to assess experimental results from Germany are still in progress.

7.3 PRISMATIC HTR CORE ANALYSIS

Only a small effort has gone into this analysis to date. We continue to study the performance of the core. Results of the elaborate GA analyses are available to us. Our own calculations allow us to understand the importance of, and requirements for, the use of burnable poison, selective fuel element repositioning, and coolant orificing to constrain fuel temperatures. The lack of a simple performance index of fuel temperatures and temperature peaking complicates assessment because the highest practical coolant outlet temperature may be desired for process heat application.

7.4 REFERENCES

1. P. R. Kasten et al., *Comparative Evaluation of Pebble-Bed and Prismatic-Fueled High-Temperature Gas-Cooled Reactors*, ORNL-5694 (January 1981).
2. D. R. Vondy et al., *A Computation System for Nuclear Reactor Core Analysis*, ORNL-5158 (April 1977).
3. T. W. Medlin et al., *Fuel Management Positioning and Accounting Module: FUELMANG*, ORNL-5718, to be published.
4. K. R. Stroh et al., *Thermal-Hydraulic Analysis Techniques for Axisymmetric Pebble-Bed Reactor Cores*, LA-UR-78-1765, Los Alamos Scientific Laboratory, Los Alamos, N.M. (1978).
5. D. R. Vondy, *PEBBLE, A Two-Dimensional Steady-State Pebble-Bed Reactor Thermal Hydraulics Code*, ORNL-5698, to be published.
6. R. M. Westfall, *The One-Dimensional Integral Transport Resonance Shielding Code ROLAIDS*, ORNL/CSD report, to be published.
7. D. R. Vondy, *Stability Analysis of the High-Temperature Thermal Pebble Bed Nuclear Reactor Concept*, ORNL/TM-7542 (February 1981).

8. HTR SHIELDING STUDIES

C. O. Slater

The HTR Shielding Program was initiated in FY 1981. Early efforts were directed toward (1) finding a suitable cross section set with which to calculate various shielding configurations and (2) planning a major shielding experiment so that the maximum desired information may be extracted from it.

As a first step in finding a suitable cross section set, we used two ORNL libraries to calculate an HTGR design problem. The results were compared with results obtained by General Atomic Company (GA) for the same problem. The ORNL libraries consisted of a 51-neutron-group set with four thermal groups and no upscattering and a 27-neutron-group set with 13 thermal groups and upscattering. The 51-group set was used in fast reactor analysis and thus placed little emphasis on the thermal energy range. The 27-group set, however, was designed specifically for thermal reactor applications; consequently, it has an abundance of thermal groups. In addition, several of the light elements in the 27-group library have scattering data that have been processed at several temperatures. For comparison, carbon cross sections at three different temperatures (293, 1000, and 1200 K) were selected for use in calculating the HTGR design problem. The different temperatures would affect mainly the flux spectrum in the thermal energy range and would change the upper energy boundary of the thermal range. The libraries for the three carbon temperatures selected were designated ORNL 27GP-1, ORNL 27GP-2, and ORNL 27GP-3.

The results showed reasonable agreement between the ORNL and GA fast- and intermediate-energy neutron fluxes except for (1) 50 to 70% higher ORNL fast fluxes in the prestressed concrete reactor vessel (PCRV) and (2) lower ORNL intermediate fluxes by factors of 2.3 (27 group) to 3.8 (51 group) in the permanent side reflector. The really big differences occurred in the thermal flux comparisons. A plot of the thermal fluxes calculated with the ORNL and GA libraries is shown in Fig. 8.1. The ORNL 51-group cross section set, without upscatter and with its low-temperature scattering kernel for carbon, obviously predicts grossly the thermal flux everywhere outside the core. The 27-group library with carbon processed

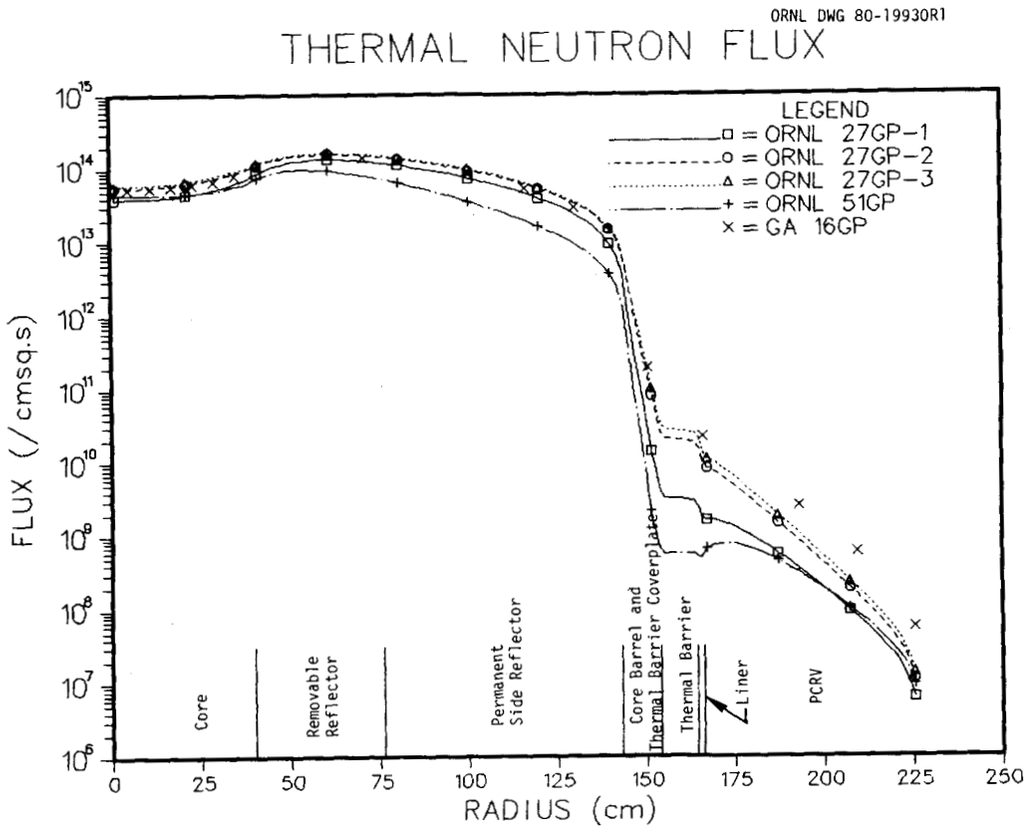

Fig. 8.1. Comparison of the thermal neutron flux (E < 2.38 eV) in the HTGR side region.

at 293 K and with upscatter (ORNL 27GP-1) is an improvement over the 51-group library, but it still gave results somewhat lower than GA's in the core and reflectors and substantially lower in the PCRV. The 27-group calculations with carbon at 1000 K (ORNL 27GP-2) and 1200 K (ORNL 27GP-3) gave thermal fluxes in excellent agreement with the GA results from the core through the permanent side reflector. Beyond the 11-cm-thick iron region representing the core barrel and thermal barrier cover plate, the thermal fluxes calculated with the latter two ORNL 27-group libraries and the GA library differ significantly. The three sets of results appear to coincide in the steep flux drop-off through the iron region. Because no carbon was included in the regions beyond the core barrel, it is possible that the carbon cross sections alone could not account for the discrepancies among the results obtained by using the two 27-group ORNL libraries and the GA library, although the difference in carbon temperatures did

influence a difference in the thermal flux in the PCRV as calculated with the ORNL libraries. Another theory is that, because the discrepancies occur following the iron region, differences between the ORNL and GA iron thermal cross sections could cause drastically different thermal flux spectra to emerge from the core barrel. This thermal flux incident on the PCRV greatly determines the thermal flux profile in the PCRV. Also in an ORNL-GA benchmark gas-cooled fast breeder reactor (GCFR) shielding calculation comparison,[1] large differences (factors of 1.5 to 2.0) were observed between GA and ORNL thermal fluxes following neutron transport through thick iron regions. The differences were attributed to differences in the cross section processing procedures. Because the GA calculation predated the benchmark comparison, it also used cross sections similar to those used in the benchmark. Thus, the differences observed between ORNL and GA results for this HTGR comparison could logically be expected. It was concluded that, although significant differences occurred in the results obtained by ORNL and GA with the various cross section libraries, the ORNL 27-group library with the appropriate choice of carbon temperature would be adequate for anlayzing the HTGR experiments.

Planning for the experiment was begun at a November 1980 meeting at GA. The reference design and general ideas of what the proposed experiment should include were discussed. Several milestones for the design, preanalysis, and fabrication of the experiment as well as the intermediate review stages were established. Design data were later received from GA, and efforts were begun to prepare the basic data needed for beginning the shielding analysis.

8.1 REFERENCES

1. C. A. Rouse et al., *Gas-Cooled Fast Breeder Reactor Shielding Benchmark Calculation*, GA-A14236, General Atomic Company, San Diego, Calif. (January 1977).

9. APPLICATION AND PROJECT ASSESSMENTS

P. R. Kasten

The application and project assessments contained here include three areas. The first involves dynamic modeling of heat transport systems; under study are the chemical heat pipe (CHP) and the molten salt (SALT) transport systems, combined with a high-temperature reactor (HTR). The HTR-CPH systems include the reactor; an intermediate-heat exchanger (IHX) that uses helium coolant, a reformer, a pipeline, and a pumping station; and a methanator. The HTR-SALT systems include the reactor; possibly an IHX; and a molten salt distribution system involving heat exchangers, pipes, pumps, and storage. The emphasis in this reporting period was on the CHP.

The second area concerns assessments of fossil conversion processes in which various processes are being studied to determine their appropriateness for HTR application. A screening process was carried out initially.

The third area involves project and priority assessments. The primary effort was on evaluating the relative economics of certain fossil conversion processes for producing liquid fuels and the cost of displacing liquid fuels with process heat; HTRs were considered to provide source energy in all cases.

9.1 HTR REFORMER AND PROCESS HEAT MODELING STUDIES

Work was performed in two areas: (1) defining and characterizing a CHP system on the basis of General Electric Company (GE) information and (2) dynamic modeling of process heat distribution systems, with the initial effort on CHP systems.

9.1.1 Characterization of Chemical Heat Pipe System — K. F. Wu

This initial effort was to evaluate the CHP concept proposed by GE for the application of HTRs to process heating. Among the HTR-CHP systems presented by GE,[1] we chose the reference case and its corresponding system with a multiple-feed evaporator (MFE) for evaluation of their thermal efficiencies. These two systems were chosen over the others presented for

two reasons: (1) available process information in the GE report is concentrated on the two systems and (2) a combination of these systems enables us not only to verify the material and energy balances of each process but also to ascertain whether or not a substantial improvement of the system efficiency can be achieved through the addition of an MFE to the reference system.

The data in the GE report on these two cases are scattered and inconsistent. Our first step in this effort was therefore to collect all available information in the GE report by constructing a flowsheet for each case. Figure 9.1 presents the reference system data, and Fig. 9.2 shows data for the corresponding system with an MFE. The chemical reaction in the above system is

$$CH_4 + H_2O(g) \rightleftharpoons CO + 3H_2 \ ,$$

with

$$\Delta H^\circ_{298\ K} = 206.2 \text{ kJ/mol} \ .$$

The reformer converts a methane-steam mixture into a mixture of carbon monoxide and hydrogen; the reverse reaction takes place in the methanator.

In addition to the flow diagrams, the only detailed information available concerns the reformer-side heat exchanger train of the system with MFE. Figure 9.3 gives details of this heat exchanger train and shows the interrelationships between the cooling and heating requirements. A simplified representation of this system is given in Fig. 9.4. For the heat exchanger train, the duties and the pressure drops for both shell and tube sides are given in Table 9.1.

After examining the information in Figs. 9.1 through 9.4 and Table 9.1, one easily concludes that the scattered data given on the two systems do not make it possible to verify even the energy balance of either system, not to mention checking the system efficiency improvement of one process over the other.

The reference system (without MFE) does not include data on pressure readings or on the interrelationships between the heating and cooling

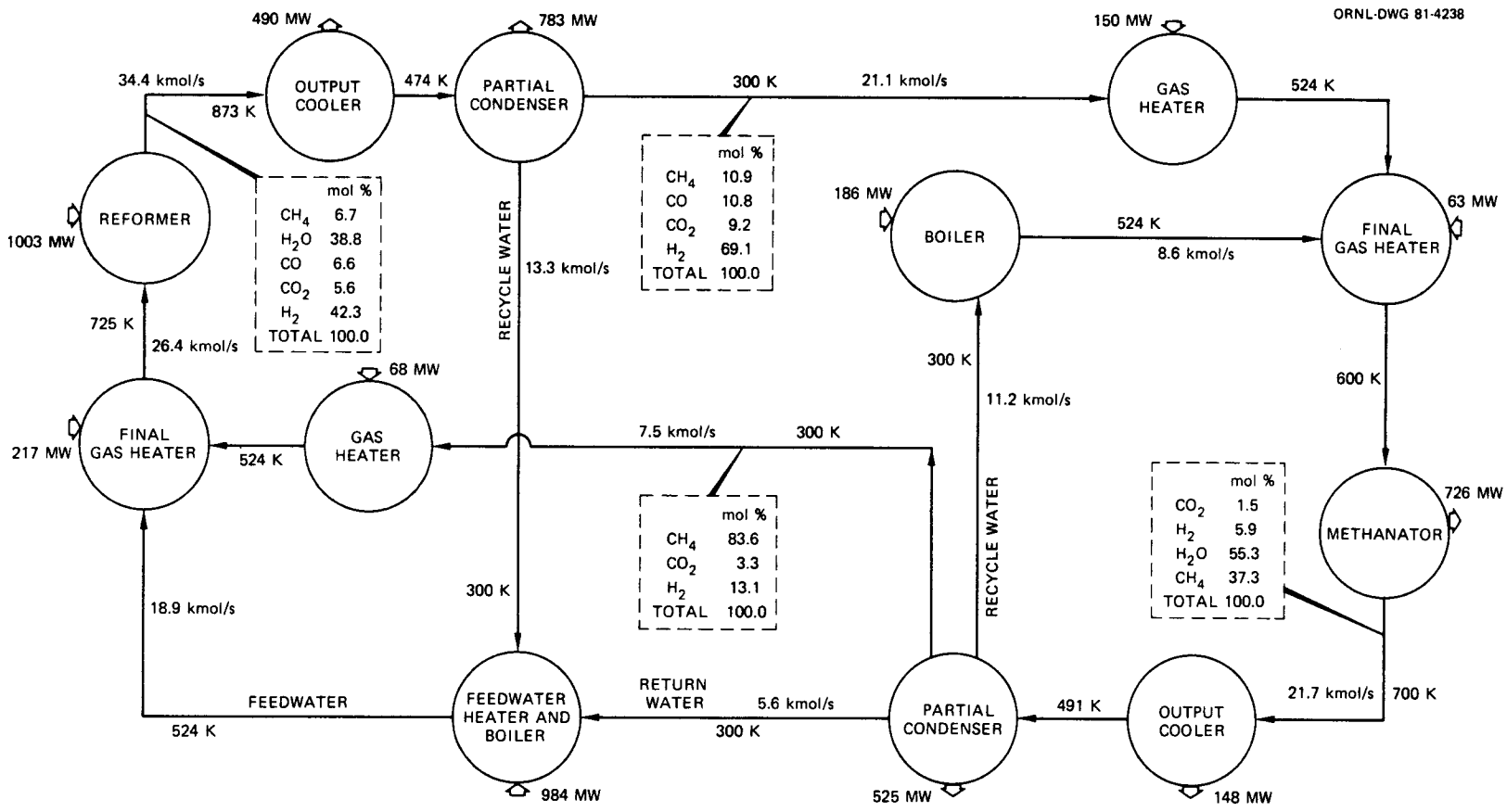

Fig. 9.1. Reference chemical heat pipe system.

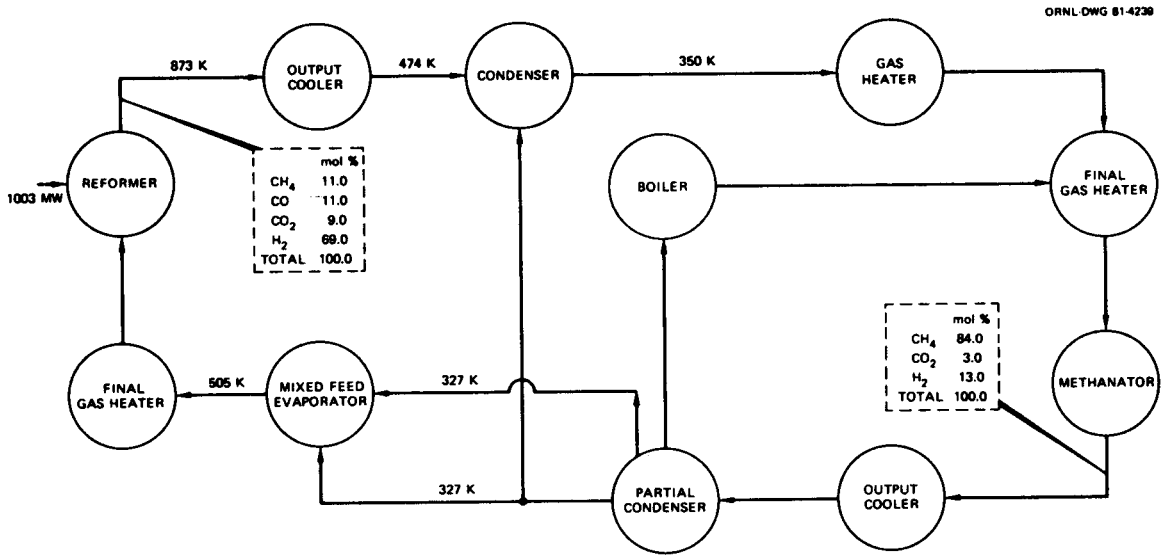

Fig. 9.2. Reference chemical heat pipe system with multiple feed evaporator.

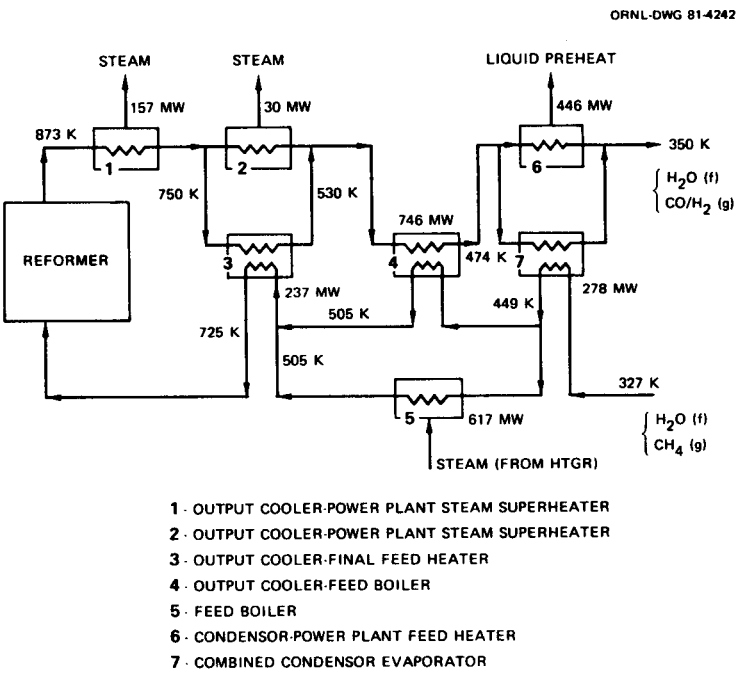

Fig. 9.3. Reformer-side heat exchanger train.

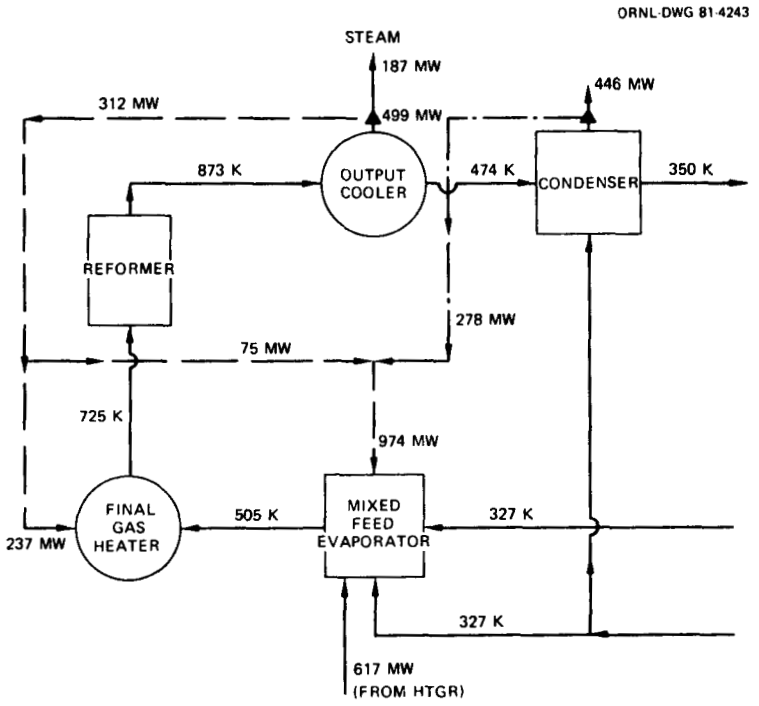

Fig. 9.4. Operating conditions for reformer chemical heat pipe system with multiple feed evaporator.

Table 9.1. Duties and pressure drops of the heat exchanger train (reformer side only) with multiple feed evaporator.

Heat exchanger	Duty (MW)	Pressure drop, kPa (psi)	
		Tube side	Shell side
1	157	0.7 (0.1)	0.7 (0.1)
2	30	9.9 (1.43)	55 (8)
3	237	6 (0.8)	110 (16)
4	75	0.6 (0.08)	52 (7.6)
5	617	0.7 (0.1)	104 (15.1)
6	446	0.7 (0.1)	74 (10.8)
7	278	22 (3.2)	20 (2.9)

duties of either the reformer or the methanator sides of the system. As a result of attempts to obtain these missing process pressure data through telephone conversations with persons involved with the GE HTGR-CHP report, we learned that the pressure drop across all process equipment had been assumed to be zero, although the report showed pressure drops for the reformer-side heat exchanger train of the system with MFE (Table 9.1). This finding implies that the reported fluid equilibrium compositions at various locations of the process are questionable.

Of the two systems being studied, more data are available on the system without MFE than on the one with MFE. In spite of the lack of complete information, we proceeded with mass and energy balances on the former system. The thermodynamic data base in Table 9.2 was the basis for the GE report and was therefore adopted for our study.

Table 9.2. General Atomic Company thermodynamic data base[a]

$$C_p = a + bT + cT^2$$

	$\Delta H_f^\circ(298)$ (J/mol)	$S^\circ(298)$ [J/(mol·K)]	a [J/(mol·K)]	b [J/(mol·K^2)]	c [J/(mol·K^3)]
CH_4	-74,850	186	14.14	74.91	-17.52
$H_2O(g)$	-241,830	189	28.83	13.74	-1.44
CO	-110,520	198	26.15	8.75	-1.92
CO_2	-139,510	214	28.66	35.70	-10.36
H_2	0	131	28.79	0.28	1.17

[a]$H_2O(l)$: ΔH of evaporation = 44,032 J/g; C_p = 75.35 J/(mol·K).

With all available data identified, we checked the system for conservation of mass. The inlet and outlet flow rates of CH_4, H_2O, CO, CO_2, and H_2 for the reformer, methanator, and partial condensers are tabulated in Table 9.3 for the reference case. Mass flow rate calculations show that, with the exception of the methanator and the methanator-side partial condenser, conservation of mass was achieved. For the partial condenser,

Table 9.3. Molar flow rates

Location	Flow rate, mol/s					
	CH_4	$H_2O(g)$	CO	CO_2	H_2	Total
Reformer exit	2,308	13,366	2,274	1,929	14,571	34,448
Reformer side partial condensor exit	2,301	13,334	2,280	1,942	14,589	34,446
Methanator-side final gas hector input	2,301	8,612	2,280	1,942	14,589	29,724
Methanator exit	8,082	11,983	0.0	325	1,278	21,668
Methanator-side partial condensor input	8,082	11,983	0.0	325	1,278	21,668
Reformer-side gas heater input	6,272	0.0	0.0	248	983	7,502
Reformer inlet	6,282	18,896	0.0	238	976	26,391

the input molar flow rate of H_2O amounts to 11,983 mol/s, and that of the outlet streams is 14,168 mol/s. Because no chemical reaction takes place in a partial condenser, we concluded that the mass (molar) flow rates given for the input and output streams of the methanator-side partial condenser are in error. This conclusion is further substantiated by the fact that molar flow rates of the constituents other than H_2O are also not conserved.

Following evaluation of the reference case mass balance, energy balance calculations were made for each piece of process equipment other than the methanator and the methanator-side partial condenser. Table 9.4 gives the equations used to evaluate enthalpy values of methane, steam, carbon monoxide, carbon dioxide, and hydrogen. The calculated values of these chemical species are tabulated in Table 9.5. From examining the results of Table 9.5, one can intuitively detect the wrong trend that the equations of Table 9.4 predict. With the exception of hydrogen, the enthalpy values decrease with increasing temperature rather than increasing as would be expected.

Table 9.4. Evaluation of enthalpy values (J/mol)[a,b]

CH_4:	$H_T = -74{,}850 + 14.14(T - 298) + 74.91(T^2 - 298^2) - 17.52(T^3 - 298^3)$
$H_2O(g)$:	$H_T = -241{,}830 + 28.83(T - 298) + 13.74(T^2 - 298^2) - 1.44(T^3 - 298^3)$
CO:	$H_T = -110{,}520 + 26.15(T - 298) + 8.75(T^2 - 298^2) - 1.92(T^3 - 298^3)$
CO_2:	$H_T = -393{,}510 + 28.66(T - 298) + 35.7(T^2 - 298^2) - 10.36(T^2 - 298^3)$
H_2:	$H_T = -28.79(T - 298) + 0.28(T^2 - 298^2) + 1.17(T^3 - 298^3)$

[a] T in K.

[b] Based on General Electric Company thermodymanic data.

Table 9.5. Tabulation of enthalpy values[a]

Temperature (K)	H_T, enthalpy, MJ/mol				
	CH_4	$H_2O(g)$	CO	CO_2	H_2
300	−9.38	−1.00	−1.13	−5.91	+0.63
474	−1,392	−113.6	−152.6	−824.7	−93.68
491	−1,599	−130.5	−175.2	−947.1	+107.6
524	−2,043	−166.8	−223.9	−1,210	+137.4
600	−3,300	−269.4	−361.6	−1,954	+221.8
700	−5,515	−450.5	−604.3	−3,265	+370.5
725	−6,180	−504.9	−677.1	3,659	+415.0
873	−11,143	−911.0	−1,221	−6,595	+747.7
1,100	−22,772	−1,863	−2,495	−13,475	+1,527

[a] Based on equations of Table 9.4.

The above results prompted us to compare the GE thermodynamic data base against the corresponding values taken from D. M. Himmelblau (Table 9.6) (ref. 2). We found that the coefficients b and c of Tables 9.2 and 9.6 were in error by several orders of magnitude. Because the equations in Table 9.6 were proven to be accurate, we modified the equations of Table 9.2 by multiplying the coefficients b and c by 10^{-3} and 10^{-6}, respectively, (Table 9.7). To substantiate these changes, enthalpy values of CH_4, $H_2O(g)$, CO, CO_2, and H_2 at various temperatures were tabulated in Tables 9.8 and 9.9, corresponding to the equations of Tables 9.6 and 9.7, respectively. The predicted enthalpy values of these two tables are extremely close; therefore, the corrections to the GE data base are reasonable.

Based on the revised enthalpy equations, the first energy balance calculations were made on the reformer. With the reformer inlet and exit temperatures at 725 and 873 K, respectively, the molar composition and

Table 9.6. Evaluation of enthalpy values (J/mol)[a,b]

$$C_p = a + bT + cT^2$$

CH_4	$H_T = 19.89(T - 298) + 2.736E\text{-}2(T^2 - 298^2) + 4.229E\text{-}6(T^3 - 298^3) - 2.75E\text{-}9(T^4 - 298^4)$
$H_2O(g)$	$H_T = 29.18(T - 298) + 0.725E\text{-}2(T^2 - 298^2) - 0.6741E\text{-}6(T^3 - 298^3)$
CO	$H_T = 26.15(T - 298) + 4.38E\text{-}2(T^2 - 298^2) - 0.64E\text{-}6(T^3 - 298^3)$
CO_2	$H_T = 26.77(T - 298) + 2.114E\text{-}2(T^2 - 298^2) - 4.752E\text{-}6(T^3 - 298^3)$
H_2	$H_T = 26.90(T - 298) + 0.2175E\text{-}2(T^2 - 298^2) - 0.1089E\text{-}6(T^3 - 298^3)$

[a]Based on data from D. M. Himmelblau, *Basic Principles and Calculations in Chemical Engineering*, 3d ed., Prentice Hall, Englewood Cliffs, N.J., 1974.

[b]T in K.

Table 9.7. Thermodynamic data base[a,b]

$$C_p = a + b \times 10^{-3}T + c \times 10^{-6}T^2$$

	$\Delta H_f^\circ(298)$ (J/mol)	S_{298}° [J/(mol·K)]	a [J/(mol·K)]	b [J/(mol·K^2)]	c [J/(mol·K^3)]
CH_4	−74,850	186	14.14	74.91	−17.52
$H_2O(g)$	−241,830	189	28.83	13.74	− 1.44
CO	−110,520	198	26.15	8.75	− 1.92
CO_2	−393,510	214	28.66	35.70	−10.36
H_2	0	131	28.79	0.28	1.17

[a]Revised General Electric Company data base.

[b]$H_2O(1)$: ΔH_{evap} = 44032 J/g; C_p = 75.35 J/(mol·K);
$\Delta H = a(T - 298) + (b \times 10^3/2)(T - 298^2) + (c \times 10^{-6}/3)(T^3 - 298^3)$.

Table 9.8. Tabulation of enthalpy values[a]

Temperature (K)	H_T, enthalpy MJ/mol				
	CH_4	$H_2O(g)$	CO	CO_2	H_2
300	−0.075	−0.242	−0.110	−0.393	+0.000
474	−0.067	−0.236	−0.100	−0.387	+0.005
491	−0.066	−0.235	−0.099	−0.386	+0.006
524	−0.065	−0.234	−0.097	−0.384	+0.007
600	−0.061	−0.231	−0.091	−0.381	+0.009
700	−0.055	−0.227	−0.083	−0.376	+0.012
725	−0.054	−0.226	−0.080	−0.375	+0.013
873	−0.044	−0.221	−0.066	−0.376	+0.017
1100	−0.027	−0.211	−0.041	−0.355	+0.024

[a]Based on equations of Table 9.6.

Table 9.9. Tabulation of enthalpy values[a]

Temperature (K)	H_T, enthalpy MJ/mol				
	CH_4	$H_2O(g)$	CO	CO_2	H_2
300	−0.075	−0.242	−0.110	−0.393	0.000
474	−0.064	−0.235	−0.105	−0.384	0.005
491	−0.062	−0.234	−0.104	−0.383	0.006
524	−0.060	−0.233	−0.103	−0.382	0.007
600	−0.054	−0.230	−0.101	−0.377	0.009
700	−0.045	−0.225	−0.097	−0.371	0.012
725	−0.042	−0.224	−0.096	−0.369	0.013
873	−0.027	−0.217	−0.091	−0.360	0.017
1100	+0.002	−0.205	−0.082	−0.344	0.025

[a]Based on equations of Table 9.7.

enthalpy values of each constituent are tabulated in Table 9.10. Using the molar flow rates given in Fig. 9.1, the rate of enthalpy input and output of the reformer are 4582 and 3617 MW, respectively. The net enthalpy transferred to the reformer is calculated to be 965 MW, which is within 4% of the GE value of 1003 MW. When the energy balance was calculated on the reformer-side output cooler, however, the difference between the input and output enthalpies of the output cooler (Tables 9.10 and 9.11) is 551 MW as opposed to the given value of 490 MW, a difference of more than 10%.

From these mass and energy balance calculations, we conclude:

- The mass flow rates to and from the methanator-side partial condenser are in error.
- The thermodynamic data base presented by GE is incorrect.
- The amounts of energy transferred between each component of the system under study and its environment are questionable.
- Detailed information on the interrelationships between cooling and heating duties of system components is needed for verification of system efficiency.

Table 9.10. Enthalpy values at locations before and after the reformer

Chemical species	Quantity (mol)	Enthalpy (MJ)	Temperature (K)
Before the reformer (725 K)[a]			
CH_4	0.962	−0.0404	725
$H_2O(g)$	2.925	−0.6552	725
CO	0	0	725
CO_2	0.038	−0.0140	725
H_2	0.151	+0.0020	725
TOTAL	4.076	−0.7076	
After the reformer (873 K)[b]			
CH_4	0.352	−0.0095	873
$H_2O(g)$	2.054	−0.4457	873
CO	0.349	−0.0318	873
CO_2	0.298	−0.1073	873
H_2	2.242	+0.0381	873
TOTAL	5.295	−0.5562	

[a]Specific enthalpy = −0.1736 MJ/mol.

[b]Specific enthalpy = −0.1050 MJ/mol.

Table 9.11. Enthalpy composition and energy values at output cooler exit at 474 K

Chemical species	Quantity (mol)	Enthalpy (MJ)	Temperature (K)
CH_4	0.352	−0.023	474
H_2O	2.054	−0.483	474
CO	0.349	−0.037	474
CO_2	0.289	−0.111	474
H_2	2.242	+0.011	474
TOTAL	5.295	−0.643	

To resolve the differences between our calculations and those of GE, a trip was made to the GE Advanced Reactor Systems Department (ARSD) at Sunnyvale, California, on October 15, 1980, to meet with personnel who prepared the GE report. As a result of this meeting, GE personnel at GE-ARSD agreed with our modification to their thermodynamic data base. They also revised the flow rates from the methanator to its output cooler and the partial condenser to the boiler (Fig. 9.1) from 78 and 31 Mg mol/h to 60 and 13 Mg mol/h, respectively. Based on the revised flow rates, we performed a quick check on the mass flow rate; our results showed that conservation of mass was achieved. The need for detailed interrelationships among process efficiency, heating, and cooling duties and failure to take full account of input energy for calculating system efficiencies were presented to GE personnel. They concurred with our disagreement on their efficiency definition and acknowledged that no detailed interrelationships between heating and cooling duties were available for the systems of our study.

General Electric has discontinued work on the two reference systems of its 1976 publication and, in cooperation with GA, has now adopted new HTR-CHP systems for its current study. No additional vital process information is therefore available that would enable us to check further GE's 1976 results or to make comparisons between the two reference systems. Thus, rather than continuing to review the old GE systems, we now plan to review current work by GA and GE and to determine how we can contribute further to their studies.

9.1.2. Process Heat Reactor Dynamics Studies — S. J. Ball, W. T. King, and J. A. Mullens

The purpose of the dynamic response studies task is to provide an independent evaluation of dynamics-related control and safety problems and to assist with future design optimization studies. Work on the modeling task began in August 1980 and initially concentrated on reformer HTR components and systems, including duplex-tube steam reformers, process gas systems, CHP pipeline dynamics, and methanator plant behavior. Subsequently, it was established that the economics of SALT heat-transport

systems are at least as attractive as are the CHP systems for some process heat applications, so the HTR-SALT systems are currently included in the scope of the work.

The close coupling of the HTR primary system (or IHX loop) with the steam-turbine, process gas, or other heat-transport systems presents unique plant control and safety system problems. The approach followed on this task is to make use of existing HTGR dynamics codes developed at ORNL under Nuclear Regulatory Commission (NRC) sponsorship for components common to both the steam cycle and process heat HTGRs. Existing simulations from the ORNL ORTAP code[3] that can be applied to the process heat designs include two alternative core models for the prismatic fuel design, a detailed once-through steam generator model, a detailed steam turbine plant model, and a steam-driven circulator model. New component models required for the process heat plants include IHXs, steam-methane reformers, process gas heat exchangers, CHP pipelines, methanators, and SALT transport systems.

9.1.2.1 Steam-Methane Reformer Simulation

An initial dynamic simulation of a duplex or double-wall steam methane reformer was developed by using the IBM Continuous System Modeling Program (CSMP) language. The heat transfer, pressure drop, physical property, and reaction kinetics algorithms were taken directly from the GE code DSR-1 (ref. 4). Some of the algorithms were simplified to make the simulation more efficient. For each model segment, the dynamic model includes an energy balance for each of the two reformer shell tubes and the pigtail, two energy balances for the catalyst, and the chemical reaction equations. The model currently uses a ten-axial-segment approximation; 20 segments would be the approximate upper limit for the program.

Since the original program was developed, we have improved the characterization of heat transfer between the process gas and catalyst. We have also investigated the sensitivity of the results to changes in various model parameters and to the use of different numerical integration schemes. The major difficulty with the dynamic modeling thus far is caused by the use of the methane rate equation in DSR-1. This equation

was derived from integral experiments and for steady state conditions and is not valid for calculating localized, dynamic methanation rates.

A topical report on the dynamics code is being prepared.

9.1.2.2 CHP Pipeline Dynamics

Modeling and simulation work was begun on a general-purpose computer code for the dynamics of long pipelines. An industry code, PIPETRAN-4, was acquired from the American Gas Association (AGA) and incorporated into the local IBM computers. PIPETRAN calculates the time domain responses of flow and pressure of compressible fluids in long pipelines for systems including storage tanks, compressers, junctions, and multiple users. The code was modified to create files containing time-dependent pressures and flows in a form convenient for reading and plotting. Scoping calculations of a variety of test configurations and transients were run for multiple reformer sources, 185-km-long (100-mile) pipelines, and several user-methanators. Inherent dynamic behavior was observed.

9.1.2.3 Methanator Simulation

We made a background study of the methanation process, with particular emphasis being applied to design features peculiar to CHP rather than to coal conversion process applications. We acquired a dynamic simulation code that had been developed specifically for coal conversion processes (DDS/2) by Lehigh University for the U.S. Department of Energy (DOE). Derivation of basic plant component models are being based on a DSS/2 companion report.[5]

9.2 HTR APPLICATION ASSESSMENTS OF FOSSIL CONVERSION PROCESSES — W. R. Gambill

The process evaluations reported here were conducted during the fourth quarter of 1980. A meeting was held at GE in Sunnyvale, California, on October 30–31, 1980, concerning HTGR process heat application studies. Past work by GE and by General Atomic Company (GA) on HTGR-heated steam-methane reformers was reviewed. The principal aspects of the review were on performance, optimization, safety, dynamics, control, and development needs. Preliminary program plans and economic ground rules were developed for the synfuel process applications studies.

A four-member Process Applications Working Group was formed to develop study criteria and to select processes for detailed consideration. Composed of R. E. Aronstein (Bechtel), W. R. Gambill (ORNL), R. N. Quade (GA), and I. N. Taylor (GE), the group held its first meeting at Bechtel in San Francisco on November 13, 1980. Before the meeting, ORNL provided the members with a set of basic flow diagrams for the major DOE coal conversion projects and a summary of relevant aspects of the Liquefaction Technology Assessment Survey (LTAS), an ongoing ORNL activity. The group shortened a list of 18 selection criteria to 7 for the initial process screening, from which 14 processes emerged: 4 for shale oil, 2 for direct coal liquefaction, 4 for coal gasification [substitute natural gas (SNG) product], and 4 for coal gasification (synthesis gas product).

Plans were made to meet again in San Diego on December 3–4, 1980, the first day at GA to apply final evaluation criteria to final process selection and the second day at Gas-Cooled Reactor Associates to present the results of the group's process screening studies. Before the December meeting, ORNL obtained:

- process data for the Institute of Gas Technology's Hytort process for producing syncrude by surface hydroretorting Eastern oil shales,
- process data for Westinghouse's fluidized-bed ash-agglomerating process for producing medium-Btu gas (MBG) from coal,
- the current status of Conoco's molten $ZnCl_2$ coal liquefaction process,
- the current status of Rockwell International's Rockgas molten salt (Na_2CO_3) coal gasification process, and
- the availability to the group of recent reports prepared for the Tennessee Valley Authority (TVA) on coal gasifiers for MBG production.

At the December meeting, the working group applied weighted process evaluation criteria to 17 processes and narrowed the set (with excellent internal agreement) to the following processes:

- coal gasification (to SNG) — Exxon catalytic coal gasification (ECCG),
- coal gasification (to syngas) — Texaco,
- coal liquefaction (direct) — Solvent Refined Coal-II (SRC-II), and
- oil shale retorting (surface) — Paraho-Indirect and Tosco-II.

These processes were considered to be representative of each of the major areas of opportunity. The ECCG process was selected for major emphasis during 1981.

Subsequent ORNL efforts involved a review of Bechtel's draft economic ground rules to be employed in later process comparisons, the tabulation of 47 literature references concerning the ECCG process, and an estimation of the distribution of the high-temperature heat requirements of this process. For a 0.092-m^3/s (50,000 bbl/d) (oil equivalent) plant, our preliminary conclusion was that the HTGR-process steam/cogeneration (PS/C) configuration could provide about 84% of the total process heat requirement and about 89% of the total primary energy requirement. This was in excellent agreement with GA's estimates for the ECCG process made later in December (82 and 89%, respectively). General Atomic's similar estimates for the SRC-II coal liquefaction and Paraho-Indirect oil shale retorting processes indicated that the HTGR-PS/C could provide only about 47 to 48% of the total primary energy needed.

9.3. PROJECT AND PRIORITY ASSESSMENTS — B. A. Worley

9.3.1 Objective

The objective of this task is to determine which of two strategies will be the most cost-effective for future development of the HTGR: (1) continued development of the HTGR for commercial applications requiring a reactor outlet-coolant temperature of approximately 750°C (steam-cycle electricity production and relatively low-temperature process heat applications) or (2) development of HTGR concepts that are capable of providing a high-temperature heat source, that is, outlet-coolant temperatures in the 850 to 950°C range, for advanced applications (high-temperature heat source to the reformer in coal liquefaction-gasification plants, CHPs, oil shale processing, etc).

9.3.2 Progress This Reporting Period

Six reactor applications were compared for total commercialization cost per barrel of crude oil equivalent produced and/or saved. One application represents the steam cycle HTGR with an outlet-coolant

temperature of 750°C, and five applications include the use of an HTGR with an outlet-coolant temperature of 850 to 950°C as a high-temperature heat source to a reformer.

Some promising applications were identified, and parametric studies were carried out to show the effects of changing (1) plant lifetime, (2) plant scheduling, (3) discount factor, (4) final year of comparison, (5) research and development (R&D) and first-of-a-kind (FOAK) costs, and (6) plant costs.

9.3.3 Summary of Analysis Results

The six plant applications, unit costs, and total commercialization cost for both product energy and crude oil saved/produced are listed in Table 9.12. The data show the HTGR steam cycle and HTGR reformer for oil shale processing to be more cost-effective than both CHP and coal liquefaction-gasification applications. However, the syncrude from oil shale needs further processing to be comparable with the other products.

9.3.4 Approach and Assumptions

The goal of this preliminary work was to summarize and compare the cost-effectiveness of HTGR applications for crude oil replacement. A schedule leading to full commercialization through 2025 was assumed in order to identify the total program cost, which includes basic R&D costs, additional FOAK plant developmental cost, and total plant costs. Information concerning capital investment, annual costs, annual production rates, and expected lifetimes of the six industrial applications were taken from ref. 6 with the exception of costs for the steam cycle cogeneration plant, which were taken from ref. 7.

The scheduling of plant construction was taken to be the same for all applications: one plant five years after the initial plant, one three years after the second plant, one two years after the third plant, and one each year thereafter through 2025. Startup of the initial commercial plant is assumed to take place in 1995 for the steam cycle application and in 2005 for the five higher temperature reformer applications.

All costs and benefits were discounted to 1981 by using a 0.07 discount factor; all cost data are in 1981 dollars. Future cost

Table 9.12. Cost-benefit of commercialization through year 2025 for six HTGR applications

Plant application	Cogeneration	Oil shale processing	Chemical heat pipe	Direct coal liquefaction	Coal hydrogasification	Indirect coal liquefaction
Major product	Electricity/ steam	Hydrotreated syncrude	Delivered heat	Synthetic crude liquids	Synthetic pipeline gas	Gasoline, synthetic gas, butanes, propanes
10^{16} J (10^{12} Btu) equivalent per year per plant	7.57 (71.8)	44.93 (426.0)	7.33 (69.5)	37.76 (358.0)	20.46 (194.0)	35.86 (340.0)
Operating period, years	30	20	20	20	20	20
First commercial reactor, year	1,995	2,005	2,005	2,005	2,005	2,005
Research and development cost[a]	400.0	600.0	600.0	600.0	600.0	600.0
Additional development cost for initial reactor[a]	400.0	600.0	600.0	600.0	600.0	600.0
Total investment cost per plant[a]	1,214.8	6,547.3	1,644.4	5,498.2	3,868.4	10,996.5
Annual cost per plant[a]	82.3	306.1	82.6	969.2	481.6	1.007.9
Total product cost						
\$/GJ (\$/MBtu)	3.16 (3.33)	2.76 (2.91)	4.70 (4.96)	4.79 (5.05)	5.22 (5.51)	7.21 (7.61)
\$/m^3 (\$ per equivalent bbl) crude oil	121.65 (19.34)	106.24 (16.89)	180.83 (28.75)	184.42 (29.32)	201.09 (31.97)	277.63 (44.14)
$10^3 m^3$ (10^4 bbl) crude oil/M\$	8,220 (51,706)	9,413 (59,207)	5,530 (34,783)	5,422 (34,106)	4,973 (31,279)	3,602 (22,655)

[a]Millions of 1981 dollars.

escalation was not included so that the cost-effectiveness of each application could be compared on the basis of perceived worth of product in 1981. Escalation of cost would not affect the relative comparison because all plants have similar cost components.

Plant construction periods were taken to be ten years. The plant operating lifetime for the five reformer applications is 20 years.[6]

This data is of a preliminary nature, and specific information needs refinement; however, the general trends were not affected by perturbations of the parameters.

9.3.5 Parametric Studies

9.3.5.1 Plant Lifetime

For the base case the steam cycle plant lifetime is 30 years, and that of the reformer plants is 20 years. The effect of extending the plant lifetimes to 40 years is summarized in Table 9.13. The relative order of the cost-effectiveness has not changed from the base case (Table 9.12), but oil shale process applications appear promising when compared with the steam cycle process heat at equal plant lifetimes.

Table 9.13. All plants with 40-year operating lifetimes

	$/GJ (million Btu)		$/1000 m^3 (barrels) of crude oil	
Steam cycle electricity process heat cogeneration	3.02	(3.19)	116.30	(18.49)
Oil shale processing	2.34	(2.47)	90.20	(14.34)
Chemical heat pipe	3.98	(4.20)	153.22	(24.36)
Direct coal liquefaction	4.37	(4.61)	168.25	(26.75)
Coal hydrogasification	4.67	(4.93)	179.70	(28.57)
Indirect coal liquefaction	6.35	(6.70)	244.42	(38.86)

Increasing the plant lifetime decreases the cost/product ratio because of the high initial capital cost investment. The capital/annual cost ratio affects the relative dropoff, but not as much as might be expected among the various applications, as shown in Fig. 9.5. Here the cost versus plant lifetime for the two applications with the highest and lowest capital/annual cost ratios are shown. Note that the dropoff in cost is similar. All other applications have cost dropoff rates between these two extremes.

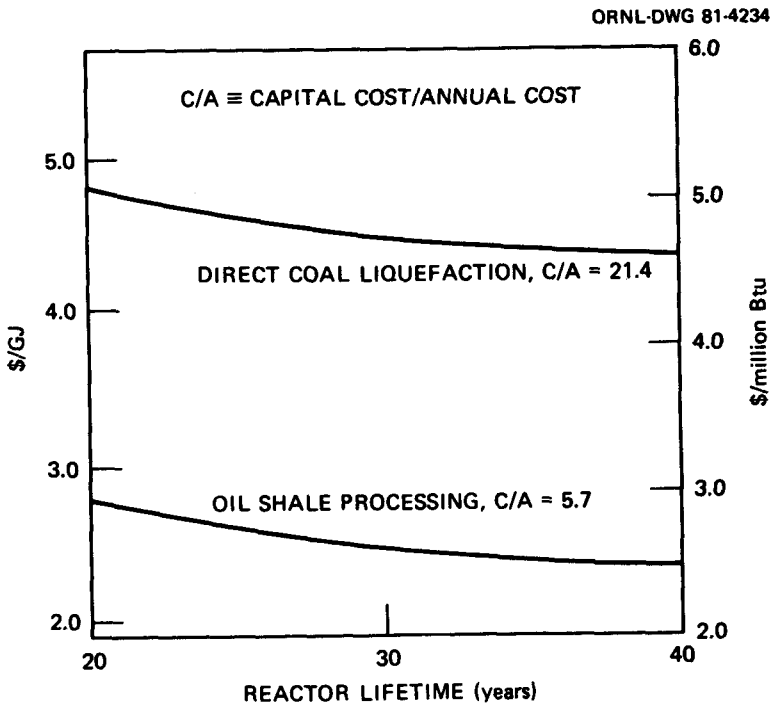

Fig. 9.5. Discounted total dollars per joule (million Btu) versus plant lifetime

9.3.5.2. Plant Scheduling

The effect of the initial commercialization date of each application was studied. The information illustrated in Fig. 9.6 is typical. Note that the total R&D expenditure was fixed as the initial reactor startup was delayed. The effect is that the cost/product ratio varies only slightly for applications with a higher capital and operating cost. As

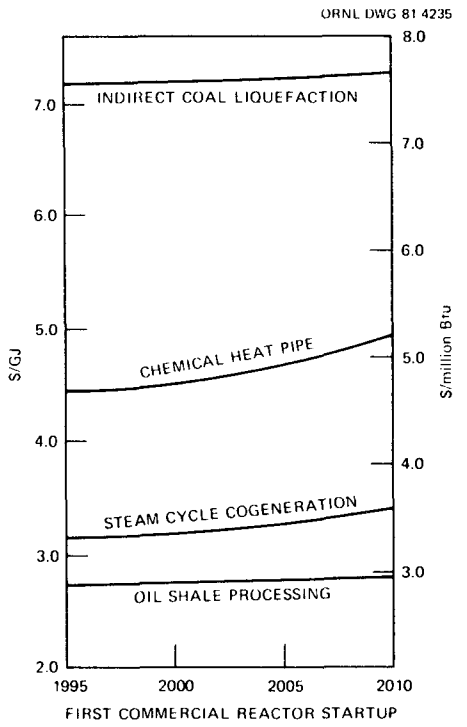

Fig. 9.6. Discounted total dollars per joule (million Btu) versus startup year of first commercial reactor.

shown in Fig. 9.6, the CHP and steam cycle cogeneration applications became slightly more costly from initial plant delay relative to the other, more capital cost-intensive, applications.

The effect of shortening the lag time between startup of plants subsequent to the initial plant for the base-case startup dates reduces the cost/product ratios as shown in Table 9.14. Note that this change reduces discounted total cost approximately the same amount as does moving up initial plant date for the reformer applications. Thus, the CHP application benefits most relative to other applications, but the cost reduction is small (4.8%).

9.3.5.3. Discount Factor

The discount factor was varied in order to determine its effect on the relative cost/product ratio among the various plant applications. The results are shown graphically in Fig. 9.7. The levelized cost of the CHP application is most sensitive to the discount factor. The cost of the

Table 9.14. Cost-product reduction from base case as a result of one plant startup per year after initial commercialization date

	$/GJ (million Btu)	Reduction from base case (%)
Steam cycle cogeneration	3.10 (3.27)	1.8
Oil shale processing	2.72 (2.87)	1.4
Chemical heat pipe	4.47 (4.72)	4.8
Direct coal liquefaction	4.75 (5.01)	0.8
Coal hydrogasification	5.15 (5.43)	1.5
Indirect coal liquefaction	7.17 (7.56)	0.7

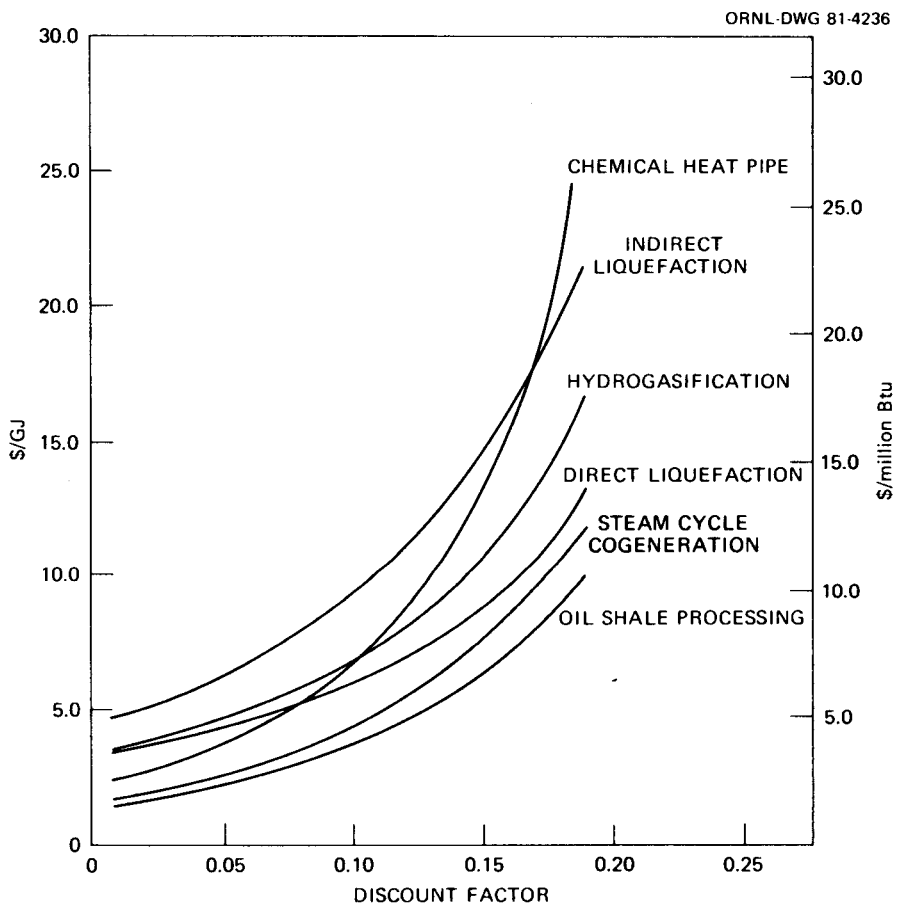

Fig. 9.7. Discounted total dollars per joule (million Btu) versus discount factor.

four capital-cost-intensive reformer applications vary with a change in the discount factor in approximately the same proportion. Finally, at low discount factors the oil shale processing, steam cycle electricity process heat cogeneration, and CHP applications have relatively lower discounted cost/product ratios; but at very high discount factors the direct coal liquefaction application, steam cycle-electricity production, and oil shale processing applications have the relatively lower cost/product ratios.

9.3.5.4. End Year of Comparison

When calculating the discounted cost/product ratio, comparison of various alternatives may depend on the choice of the year through which costs are to be discounted. For the plant commercialization schedules used in this study, the discounted dollars per joule (million Btu) versus the last year of anlaysis approaches its asymptotic value by 2025, as illustrated in Fig. 9.8. Note, however, that the relative merit of the CHP application changes if a cost/benefit ratio is to be evaluated before 2025.

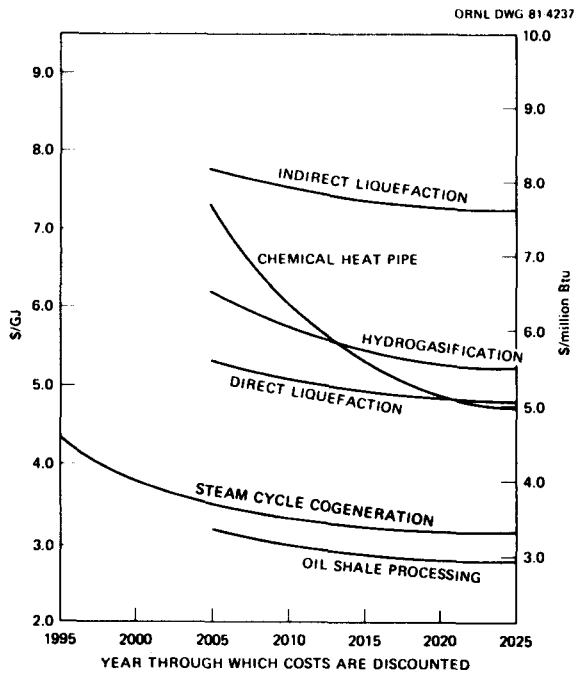

Fig. 9.8. Discounted total dollars per joule (million Btu) versus final year of discounting.

9.3.5.5. Research and Development and First-of-a-Kind Costs

Figure 9.6 shows that the total dollars per joule (million Btu) is less sensitive to initial commercialization time than might be expected. Shortening the time to initial commercialization by increasing R&D and FOAK expenditures might therefore not be cost-effective.

The results summarized in Table 9.15 illustrate the extreme situations of R&D and FOAK funding. First, suppose all R&D and FOAK of the steamer are applicable to higher temperature applications and that initial commercialization of the reformer applications begins in 1995 with zero R&D and FOAK costs. This scenario is the best possible, but, as shown in Table 9.15, even then none of the reformer applications except oil shale processing would be competitive with the steam cycle. The CHP application has the best relative gain.

Table 9.15. Effect of varying research and development and first-of-a-kind funds

	$/GJ (million Btu)		
	Base case (Table 9.1)	Zero R&D[a] and FOAK[b] costs, initial plant in 1995	R&D and FOAK costs tripled, initial plant in 1995
Steam cycle cogeneration	3.16 (3.33)		
Oil shale processing	2.76 (2.91)	2.68 (2.83)	2.83 (2.98)
Chemical heat pipe	4.70 (4.96)	4.21 (4.44)	5.10 (5.38)
Direct coal liquefaction	4.79 (5.05)	4.69 (4.95)	4.87 (5.14)
Coal hydrogasification	5.22 (5.51)	5.05 (5.33)	5.37 (5.66)
Indirect coal liquefaction	7.21 (7.61)	7.12 (7.51)	7.30 (7.70)

[a]R&D = research and development.

[b]FOAK = first of a kind.

On the other hand, if R&D and FOAK funds are tripled to bring about a 1995 commercialization date, the cost/benefit ratio of the reformer applications increases only slightly except for the CHP application.

9.3.5.6. Plant Costs

The capital and operating costs of the reformer applications were varied to identify the point at which they would have a levelized dollars per joule (million Btu) cost equal to cost of the steam cycle cogeneration base case. The results are summarized in Table 9.16.

Table 9.16. Change in reformer applications costs that result in levelized cost equal to steam cycle cost

	Change in capital and operating costs (%)
Oil shale processing	+17
Chemical heat pipe	−37
Direct coal liquefaction	−34
Coal hydrogasification	−42
Indirect coal liquefaction	−57

Note that the costs would have to decrease dramatically for the reformer applications to be competitive with the steam cycle plant costs; the exception is oil shale processing in which an increase of plant costs by 17% will result in a levelized dollars per joule (million Btu) equal to that of the steam cycle.

It should be noted that the syncrude produced from oil shale is not a comparable product to those considered in the other cases. Further treatment is required of the syncrude to give a comparable product, and the associated cost appears to be significant. Future studies will include estimates of the syncrude treatment costs.

9.4 REFERENCES

1. H. B. Vakail et al., *Closed-Loop Chemical Systems for Energy Storage and Transmission (Chemical Heat Pipe)*, General Electric Company, Schenectady, N.Y. (February 1978).
2. D. M. Himmelblau, *Basic Principles and Calculations in Chemical Engineering*, 3d ed., Prentice Hall, New York, 1974.
3. J. C. Cleveland et al., *ORTAP: A Nuclear Steam Supply System Simulation for the Dynamic Analysis of High-Temperature Gas-Cooled Reactor Transients*, ORNL/NUREG/TM-78 (September 1977).
4. D. J. Meyer and K. M. Parker, *DSR-1 Analytical Computer Program*, DSR 2841-6.1-(2), General Electric Company, Schenectady, N.Y. (January 1980).
5. William E. Schiesser et al., *Development of a Modular Software System for the Dynamic Simulation of Coal Conversion Plants*, FE-2338-14, U.S. Department of Energy (September 1979).
6. TRW, *High-Temperature Gas-Cooled Reactor (HTGR) Market Assessment*, TRW Assessment 97461-E002-RU-91, McLean, Va. (October 1979).
7. P. R. Kasten et al., *Comparative Evaluations of Pebble-Bed and Prismatic-Fueled High-Temperature Gas-Cooled Reactors*, ORNL-5694, (January 1981).

10. HTR CFTL STUDIES

J. P. Sanders

10.1 INTRODUCTION

Following the closeout of the Gas-Cooled Fast Breeder Program in FY 1980, the project staff of the Core Flow Test Loop was directed and funded by the U.S. Department of Energy (DOE) to evaluate the application of the loop to problem areas of design, performance, safety, or licensability of high-temperature reactors (HTRs). The aim of this study was to identify areas for evaluation both on the basis of (1) need or relative importance to the development of the HTR concept and (2) utilizating the particular attributes of the loop. For application to the HTR program, CFTL was used to designate the Component Flow Test Loop.

The characteristics of this loop that distinguish it from similar facilities available to the HTR program are its capability to circulate helium at HTR operating temperature and pressure and the potential for executing rapid and precisely controlled transients for both flow and power input. Another unusual attribute of the loop is the availability of a sophisticated data acquisition system (DAS) that is capable of collecting as many as 10,000 data points per second from 640 addressable channels.

In the application of the loop to evaluating HTR system components, a major feature of the site is an available reserve of electrical power. Transformers have been installed in the building that can supply 6.75 MW at required system voltages. Transformers are also installed just outside the building, which can supply 40 MW at 13,800 V. The local system provides power on either a maximum or continuous-use basis, which is not readily duplicated at other sites.

10.2 INITIAL SCOPE OF THE STUDIES

Initial study of areas having CFTL capabilities applicable to HTR development indicated that detailed consideration should be given to

- lifetime performance characteristics of the core support structure;
- performance of flow control devices in the primary loop;

- performance characteristics and structural response of heat exchange equipment such as (1) the primary steam generator, (2) the intermediate heat exchanger with an indirect cycle, (3) the core auxiliary heat exchanger, (4) the reformer in a primary or secondary loop, and (5) the methanator associated with the reformer;
- performance of the thermal barrier;
- effect of flow reversals on flow redistribution in the core resulting from natural convection effects; and
- adequacy of core designs to eliminate spacial flow-temperature oscillations.

In evaluating the range of tests for this overview, attention was given to the following restraints on the overall plan:

- primary consideration to be given to applications that would make maximum use of existing hardware and capabilities of the loop;
- overall plans to accommodate both near-term, short-range tests and also longer term tests that require a test model and extensive loop modifications;
- testing to be completed in a timely manner, enabling the results to feed into the design of the proposed demonstration plant;
- testing to be directed primarily toward those components that are generic to all applications of the HTR plant;
- preference to be given to evaluate experimentally those components that affect the system design in (1) safe operation, (2) reliability and availability, (3) uncertainty in design limits, and (4) optimization of performance;
- consideration to be given to other available test facilities and preference to be given to the specification of those tests for which the CFTL has characteristics that are more applicable to the test needs; and
- total needs of experimental evaluation of HTR components to be considered and those choices that can most easily be integrated into an overall test program to be made.

10.3 CORE SUPPORT PERFORMANCE TEST

On the basis of the foregoing considerations, a performance test for the proposed core support structure for the prismatic HTGR core was judged to have the most favorable attributes. Preliminary evaluation of the test requirements indicated that the flow range, power input, and available test bed volume closely match the capabilities of the Stage Alpha CFTL. Other hardware acquired for the CFTL but not installed in the Stage Alpha design was also judged to be suitable for use in fabricating an appropriate test vessel.

Requirements for the test were based on a study of the core support structure made at Oak Ridge and sponsored by the U.S. Energy Research and Development Administration (ERDA). The results of this study were summarized in a report[1] by Mechanics Research Inc. (MRI), a subcontractor. The major concern of this study was the structural interaction at the interface of the core support post and its seat.

As shown in Fig. 10.1, radii specified for the rounded end of the point differ from those for the face of the seat. This difference is necessary to allow movement in the core support structure of the prestressed concrete reactor vessel (PCRV) floor during the rise to operating temperature and during seismic events. Unfortunately, this design creates a limited area of contact and results in stress concentrations (Hertzian stresses).

The structural performance of the post and seat is also dependent on the corrosion (or burnoff) of the graphite by low concentrations of water vapor or other sources of oxygen in the circulating gas. Concerns about the correlations for the burnoff rate arose at the time of the MRI study. Subsequent studies (Chap. 5)[2,3] have also indicated uncertainty about the volumetric distribution of the burnoff effect. These tests with small specimens presented questions about whether the burnoff occurs mainly at the surface of the graphite, uniformly throughout the graphite piece, or perhaps even primarily on the interior of the specimen. The predictions do not account for the effects on the ultimate strength of the members as a function of burnoff.

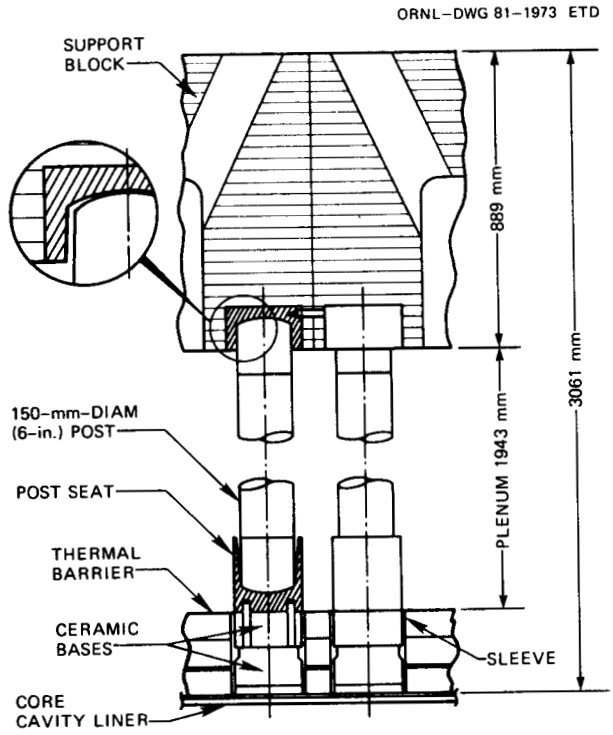

Fig. 10.1. Typical HTGR core support structure showing support blocks, posts, and post seats.

Because of concern about the rate and distribution of burnoff and the effect of burnoff on strength, ORNL previously recommended[4] evaluating performance of the core support post in a large-scale test under accelerated corrosion conditions. By relatively minor modifications of the CFTL, it now appears to be feasible to test a full-size segment of the core support structure. This test would incorporate the three types of graphite found in the support blocks, the post seats, and the support posts.

This assembly would be structurally loaded and tested under normal operating conditions, under conditions corresponding to the limits imposed by the operating technical specifications, and perhaps under certain accelerated corrosion conditions. This testing sequence, which might involve one or more test structures, was designated as the core support performance test (CSPT).

10.3.1 The Loop Configuration

The flowsheet for Stage Alpha CFTL (now designated as the Component Flow Test Loop for the HTR) is shown in Fig. 10.2. This represents the

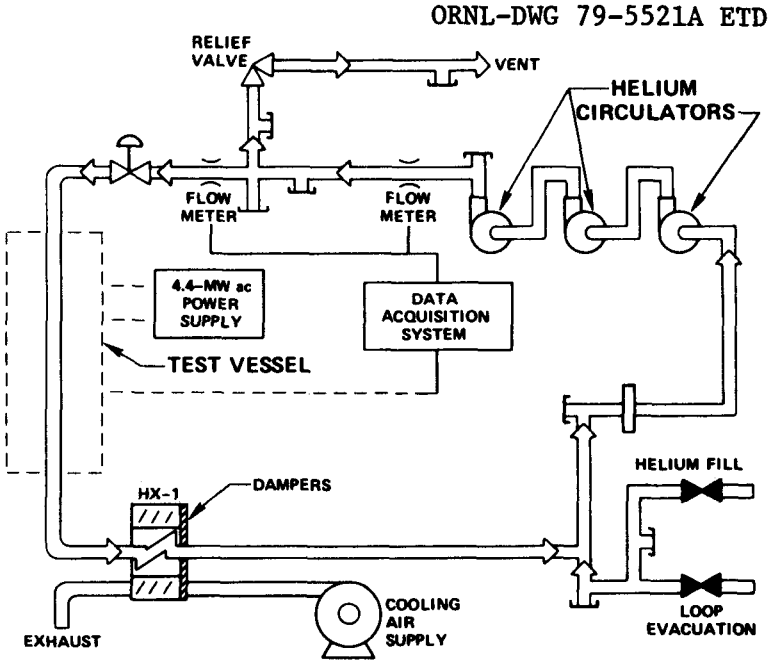

Fig. 10.2. Flow diagram for the Stage Alpha Component Flow Test Loop.

construction efforts that were included in the closeout efforts for the Gas-Cooled Fast Reactor (GCFR) Program. Significant features in comparison with requirements of the CSPT are (1) the test vessel was replaced with a section of 4-in. pipe, (2) the attemperation flow line was not installed, (3) the controller for the power supply had a maximum capacity of 0.4 MW, and (4) no signal leads were connected to the DAS.

A number of other components have been received but are neither installed nor connected in Stage Alpha. These components include (1) the parts for the test vessel, (2) two calibrated vortex shedding flow meters, (3) transformers to supply approximately 4.0 MW of additional power supply for the test section, (4) the cooling air supply for a secondary helium heat exchanger, and (5) a supply of components for the electrically heated rods that were to have been used to simulate the GCFR fuel rods.

An isometric drawing (Fig. 10.3) illustrates the relative locations of those loop components installed for Stage Alpha. An overall isometric drawing (Fig. 10.4) shows the relationship of the loop to ancillary equipment such as the power supply, the DAS, and the cooling air supply system for the helium heat exchangers. Additional equipment to provide cooling air for the transformers and the power controls is not shown in this figure.

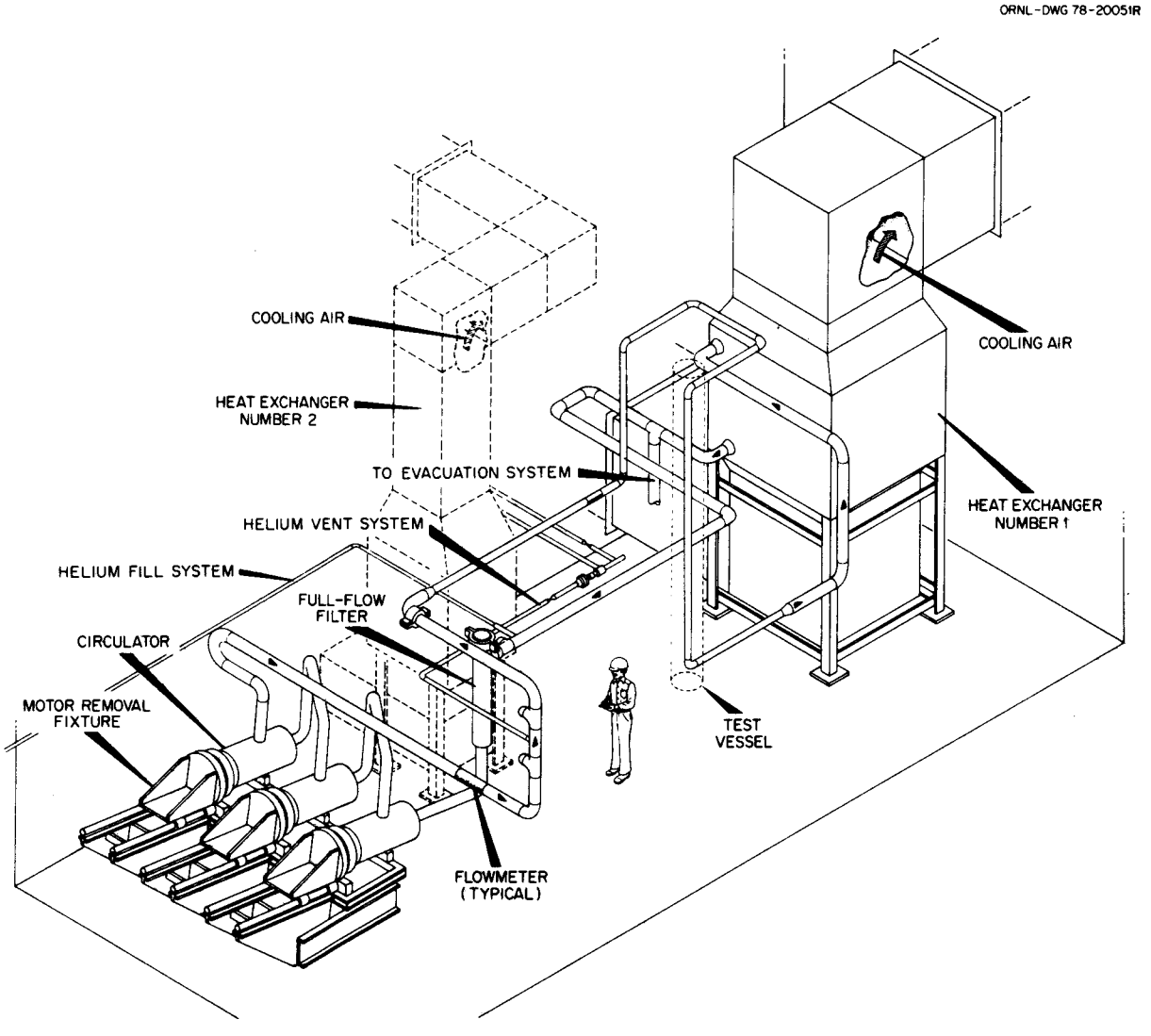

Fig. 10.3. Isometric drawing of the Stage Alpha Component Flow Test Loop.

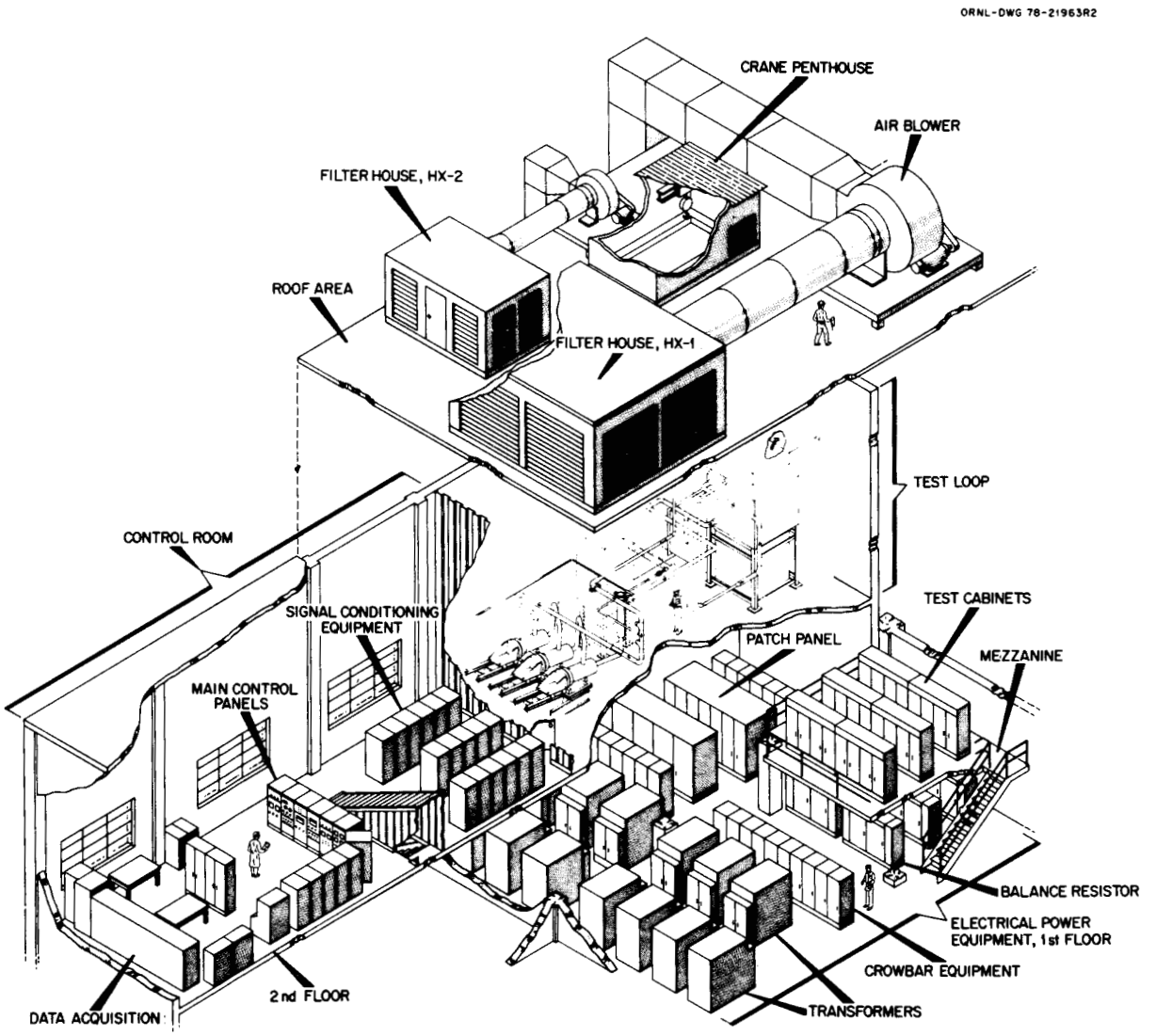

Fig. 10.4. Perspective of overall Component Flow Test Loop showing major items of ancillary equipment.

10.3.2 The CSPT Test Vessel

Preliminary requirements for the test indicate that an assembly of three graphite segments with diameters ranging from 150 to 225 mm (6 to 9 in.) would be exposed to a flow of helium at approximately 1000°C. The graphite assembly would be about 1 m (3 ft) in height. Such a test assembly could be placed in the proposed test vessel, for which parts had been acquired to test the GCFR fuel assembly mockup. This vessel consists of a straight segment of 16-in. pipe plus two blind Grayloc flanges to form the end closures.

Availability of these flanges is important to the timely fabrication of the test vessel. The Grayloc flanges required a delivery time of 21 months, which would be a critical time limitation if they were not available. Considerable discussion developed about allowable leak rates for these flanges, and the final action required ORNL to perform the leak testing. Although the vendor expressed reservations about the specification, tests on the closures indicated performance superior to ORNL requirements by a factor of 1000.

The proposed test vessel with the test structure in place is shown in Fig. 10.5. To test the graphite structure at a temperature of 1000°C, the helium must be heated to this temperature just upstream from the graphite test assembly.

10.3.3 Loop Limitations

The metal pressure boundary of the test vessel and piping has a maximum operating temperature of 600°C at the design pressure of 11.8 MPa (1715 psia). To limit the temperature of this boundary, we plan to divert part of the inlet helium for attemperation flow around the test assembly. This attemperation flow will be mixed with the outlet helium from the test assembly to produce a mixed mean temperature of 600°C or less.

An air-cooled heat exchanger is installed in the loop just downstream from the test vessel, as shown in Fig. 10.2. This unit will remove the heat added in the heater bundle and reduce the gas temperature to the maximum allowable temperature for the helium circulators. The original design criteria for the CFTL circulators specified a maximum allowable temperature of 345°C (650°F), based on the thermal limit of the electrical insulation in the motor windings. Initial testing of the prototype

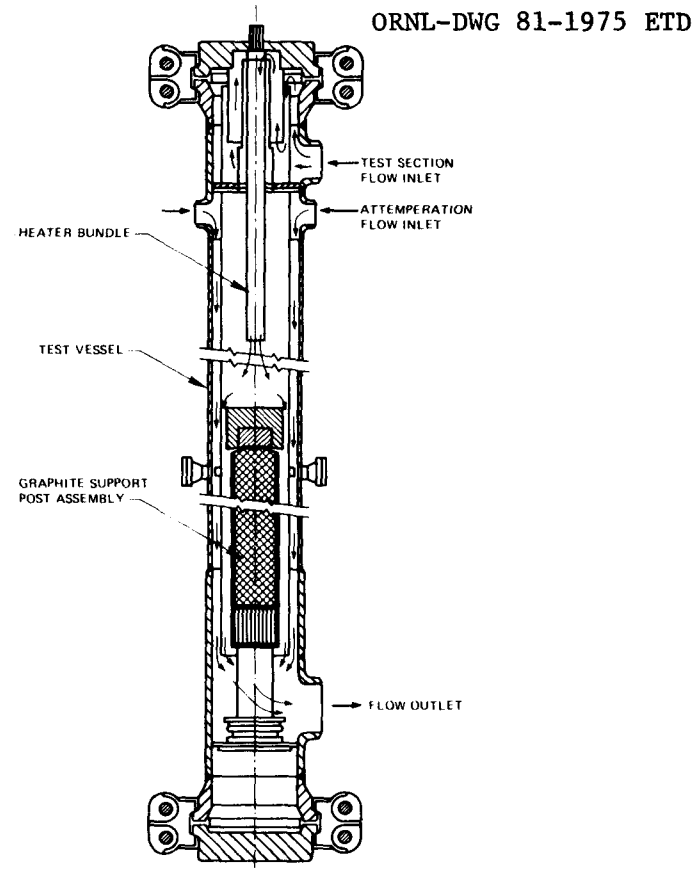

Fig. 10.5. Schematic of test vessel for the proposed core support performance test.

circulator indicated that the motor cooling capacity maintained a significantly lower temperature in the windings than that in the MTI design calcualtions. Testing of the circulator by MTI was extended to establish a maximum allowable operating gas temperature of 450°C (850°F).

10.3.4 Test Assembly

The proposed test assembly (Fig. 10.6) shows three types of graphite, representing the support block, the post seat, and the post. Limitations of space within the test vessel prevented duplication of the actual geometry of the post seat, but the important features for performance of the structure are included. The maximum diameter of the test assembly has been specified as 225 mm (~9 in.) to accommodate specifications for the support posts, which have ranged from 15 to 23 cm (6 to 9 in.) in the designs being developed by the General Atomic Company (GA).

ORNL-DWG 81-1974 ETD

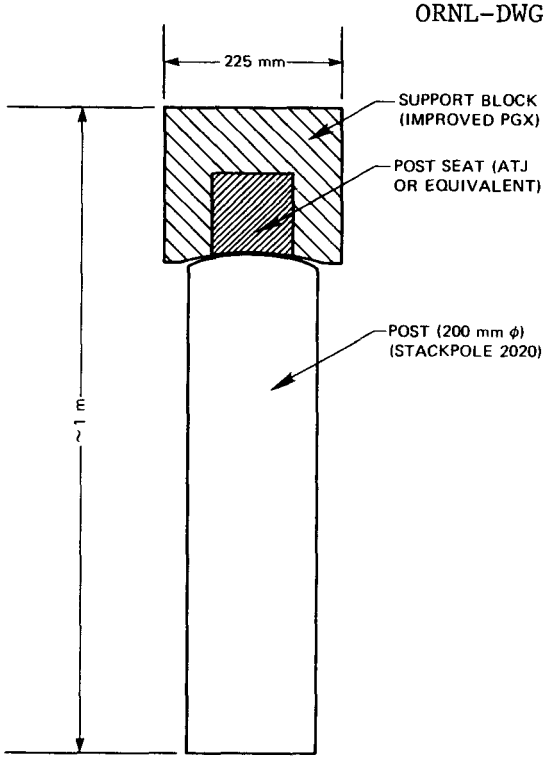

Fig. 10.6. Representative drawing for the proposed test piece for the core support performance test.

The graphite segment that represents the post will be about 200 mm (8 in.) in diameter. Within the space available in the test vessel, these dimensions can be adjusted to obtain the desired flows over the surfaces of the test pieces.

10.3.5 Operating Limitations

The major operating limit that will impact the design and performance of the test assembly is capacity of the circulator. At the initial operating conditions[5] for the circulator [10.3 MPa (1500 psia) and 350°C (660°F)], the available head of the three circulators in series was 73 kJ/kg [552 kPa (85.5 psi) at 10.6 MPa (1540 psia) and 600°C (1100°F)]. At a system pressure of 5.38 MPa (780 psia) for the HTR design, the head will be 73 kJ/kg (44.6 psi). The initial mass flow was 3.2 kg/s (7 lb/s) at 10.3 MPa; at 5.38 MPa this flow will be 1.6 kg/s (3.6 lb/s) because the circulators can be considered constant volumetric flow units over this range of conditions.

This mass flow will be divided into the test assembly flow and the attemperation flow. The ratio of flow in these two streams will dictate the power requirement of the heater. The geometry of the test assembly will establish the heat and mass transfer coefficients at the surface of the graphite pieces and the pressure drop through this section.

10.4 EVALUATION OF PARAMETERS AT THE TEST ASSEMBLY — J. C. Conklin

A parameter study was performed to evaluate the capability of the CFTL to provide the flow of high-temperature helium in the proposed test of the HTR core support structure. We assumed that temperatures of about 1000°C (1850°F) would be required at the test piece and that velocities and flow characteristics around the piece would be typical of the lower plenum design conditions.

The following parameters were considered for flow past a 0.225-m-diam, 1-m-long cylindrical test structure:

- shroud diameters of 0.28, 0.30, and 0.32 m;
- helium flow ranging from 0.2 to 1.6 kg/s; and
- heat rates to helium of 0.5, 1.0, 1.5, and 2.0 MW.

Figure 10.7 indicates the outlet temperature from the heater (just upstream from the test piece) as a function of the helium flow and the heater power. A helium inlet temperature of 350°C (660°F) is assumed. For a flow of 0.5 kg/s through the test assembly, a heater power in the range of 1.0 to 1.5 MW is required.

Figure 10.8 shows that, for this same range of flows, Reynolds numbers in excess of 20,000 are obtained for all three of the outer shrouds considered. Figure 10.9 indicates that the helium velocity past the test piece in this range of flows will be at least 3 m/s, even for the largest shroud diameter.

These calculations indicate that, for a flow range that is well within the capacity of the CFTL circulators, appropriate flow conditions can be produced at a test piece having the geometries indicated. The calculations also indicate that a controlled power supply of approximately 1.5 MW will be needed. Although this power is available from the installed transformers for the Stage Alpha CFTL configurations, additional controls for about 1.0 MW will be needed.

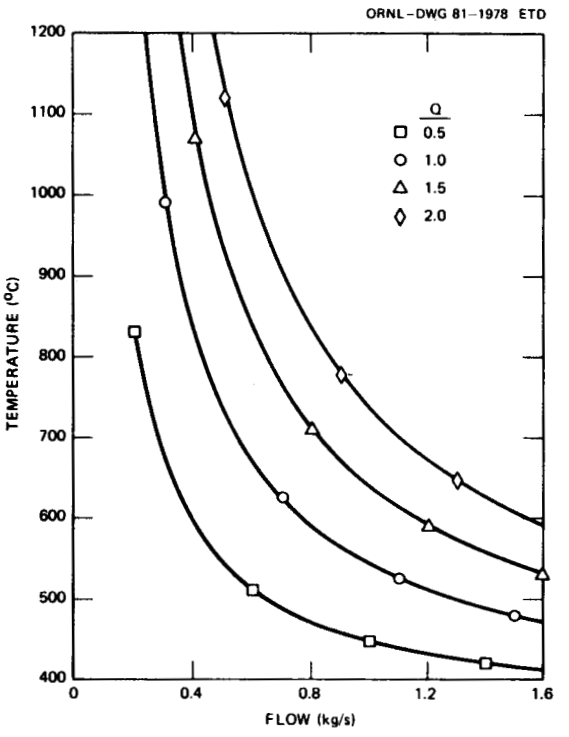

Fig. 10.7. Outlet temperature from the heater section for the core support performance test as a function of flow in the section and heater power.

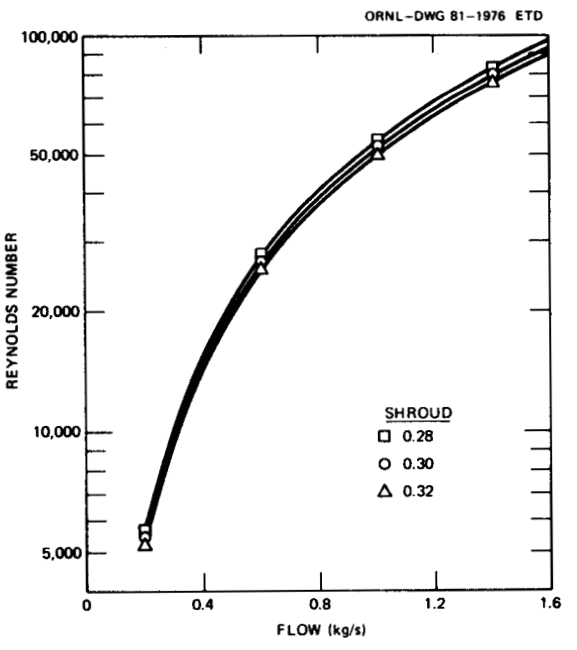

Fig. 10.8. Reynolds number at the surface of the test piece as a function of the flow and outer shroud diameter.

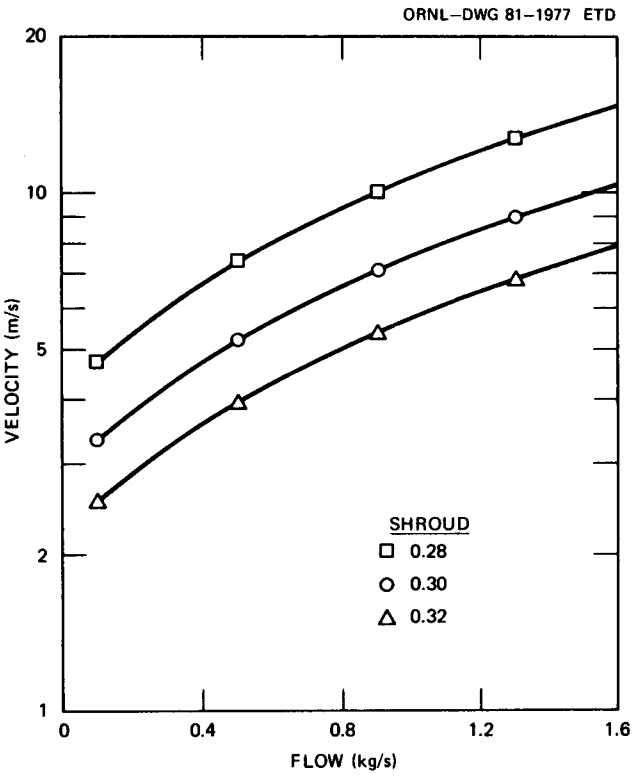

Fig. 10.9. Velocity at the surface of the test piece as a function of flow and outer shroud diameter.

10.5 IMPURITY MEASUREMENT AND CONTROL

The Stage Alpha CFTL and the test vessel provide the basic requirements for the performance test of the HTGR core support structure. Stage Alpha impurity measurements can be performed by off-line analysis of batch samples. Impurity control can be accomplished by using helium venting and makeup. The loop can be modified for continuous on-line impurity monitoring, purification, and injection. Such a modification was originally designed and included in the total design for the CFTL; however, the required components were deleted from the construction plans for Stage Alpha.

10.6 TESTING OF HEAT EXCHANGE EQUIPMENT

As tests following those for the core support structure, we considered evaluating critical performance characteristics of the heat

exchange equipment in the HTR. Vital questions to be answered in tests adapted to the CFTL concern flow distribution and pressure loss in the equipment, surface heat transfer characteristics, and temperature distributions and related stresses during transient operation. Items of equipment included the intermediate heat exchanger (IHX), which is generic for all indirect cycle HTR designs; steam generator characteristics that differ significantly from the Fort St. Vrain design; the core auxilliary heat exchanger (CAHE); and a reformer and its associated methanator unit.

10.6.1 Intermediate Heat Exchanger

A representative section of an IHX was considered to determine the adequacy of materials and structural design, to obtain the heat exchange data and related correlations, and to assist in optimizing the design of this component. The IHX was studied as the first large component to be tested because it is generic to all advanced HTR designs that use indirect cycles. In addition, it is representative of a group of components of similar design such as steam generators, reformers, and recuperators. In developing various applications of the HTR, the IHX will be required for the high-temperature process heat or reformer application. The lack of certainty for heat transfer and flow data for helium in heat exchangers at the Reynolds numbers and geometries proposed for the IHX requires overdesign and affects the cost of other components such as the PCRV. Optimizing the design of helium heat exchangers should be very cost-effective.

Lack of performance characteristics of materials, tubesheet structures, and tube support plate structures requires scale testing of the design before its installation in an HTR. Performance reliability of these parts for the lifetime of the component is vital to its licensability, and this information can be gathered only through realistic testing.

10.6.1.1 Objectives

The objectives of the IHX testing are

- to explore and determine the adequacy and reliability of the HTR heat exchanger design under normal operating conditions and under off-design conditions including transients, cycling, and depressurizations;

- to gather systematic heat transfer and flow data that can be used to optimize HTR heat exchanger designs for normal and off-normal conditions;
- to test large sections of the intermediate heat exchanger with prototypical dimensions to confirm the material behavior; and
- to determine failure modes of the IHX and their consequences, their detectability, and the associated maintenance requirements.

10.6.1.2 Method

Sections of an IHX with prototypical dimensions will be provided with temperature, stress, vibrational, and acoustic sensors. The sections will be operated in the CFTL with circulating helium at various pressures, temperatures, and coolant impurity levels. Flow, temperature, and pressure cycling and transients as well as impurity levels will be controlled. The data acquired will be analyzed to confirm and improve design and performance characteristics. Some design parameters such as tube diameter and tube pitch will be varied to assist the selection of optimum design features.

10.6.1.3 Test Configuration

The IHX is a heat exchanger with helium flow on both sides of the tube walls. Several loop configurations are possible; the choice will depend on the size of the test section or model and the energy requirements for testing. Two configurations are shown schematically in Figs. 10.10 and 10.11. For those tests in which an inlet temperature to the IHX of greater than 450°C is required, a preheater is needed to increase the allowable outlet temperature from the CFTL circulators. The design of these circulators limits their operation to this maximum gas temperature. Attemperation flow will be required in many tests to reduce the temperature of the helium leaving the IHX to about 600°C to protect the large heat sink.

10.6.1.3.1 Dual loop. In this arrangement, shown in Fig. 10.10, the IHX is installed with two independent loops. The main loop will use the large heat sink and requires a preheater. A bypass flow will bring the discharge gas to the loop thermal limits. The secondary loop will use one of the circulators and the small heat sink to reduce temperatures to

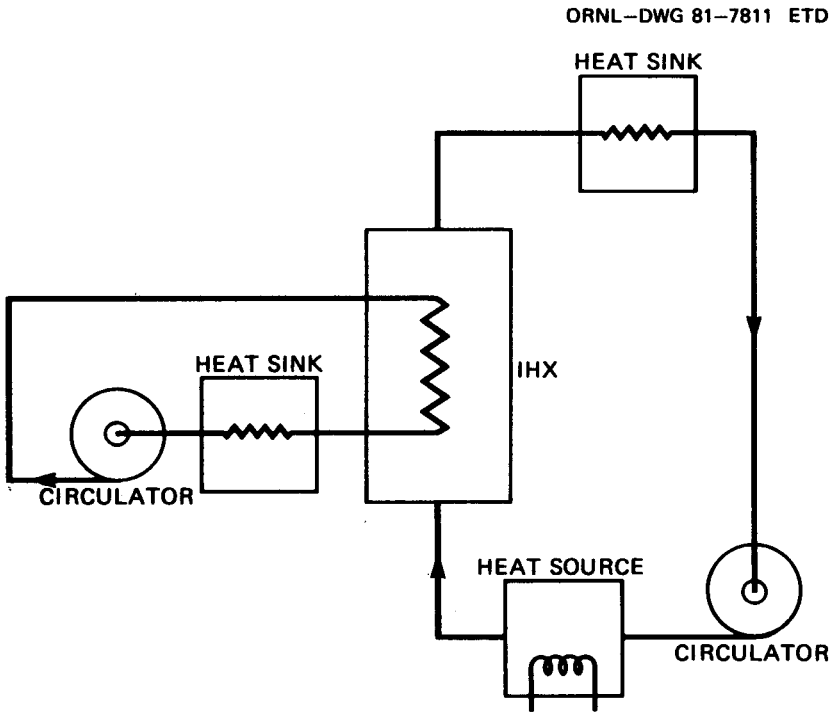

Fig. 10.10. Component Flow Test Loop dual loop configuration.

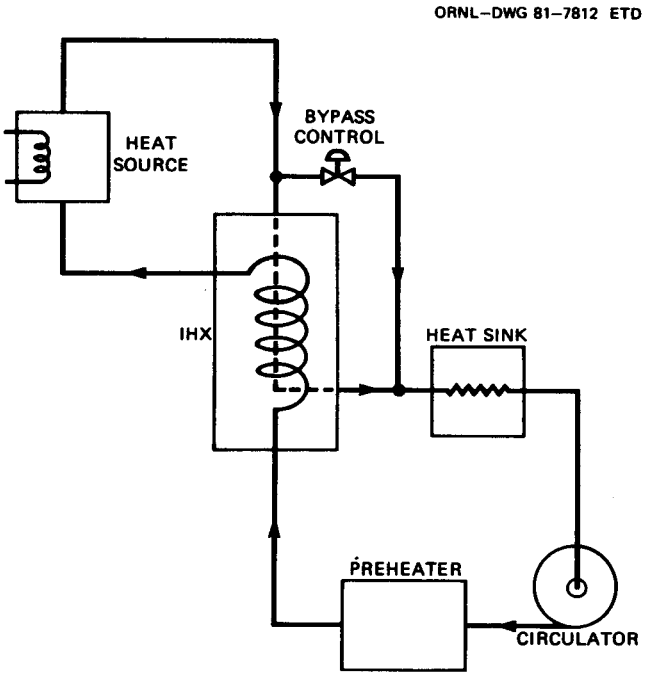

Fig. 10.11. Component Flow Test Loop "figure eight" loop configuration.

one of the circulators and the small heat sink to reduce temperatures to the operating range of the circulator. The advantages of this arrangement are that flow, pressure, and temperature conditions in each loop can be varied independently. The secondary coolant can be varied to include other gases. The disadvantages of this arrangement are that it requires two separate sets of circulators and additional components and controls and that it is relatively expensive. Also, the total size of the test apparatus is limited by the number of circulators, the power supply, and the heat sink.

10.6.1.3.2 Figure eight. In the "figure eight" installation shown in Fig. 10.11, the same helium flows through both sides of the IHX. The helium from the circulators is preheated to the temperature required for the inlet to the IHX primary side. At the exit of the primary side, a heat source increases the temperature of the helium before entering the secondary side of the IHX. At the exit of the IHX, the secondary flow of helium is mixed with attemperation flow to reduce the temperature as necessary to protect the heat sink.

The power load of the heaters and the duty of the heat sink are approximately equal for steady state operation. The actual duty of the IHX may be as much as 10 times the duty of the ancillary units for the figure eight arrangement. Thus, the figure eight arrangement permits the testing of larger units and requires fewer modifications of the loop than the dual loop arrangement. However, in the figure eight arrangement, the pressure of both sides, and to some extent the temperatures, are interrelated. The pressure difference of the two sides of the IHX is limited by the available head of the ciruclators. Flow transients on either the primary or secondary sides can be represented through the use of bypass streams. Other transients, cycling, and depressurizations are limited by the combined dynamics of the system.

10.6.1.4 Scheduling

A preliminary schedule was developed for the completion of the Stage Alpha loop and its modification for the CSPT. The period required for testing a series of CSPT assemblies will provide sufficient time to design the following test, acquire the needed equipment and test component, and make the necessary installations. This schedule will permit the testing

of the heat exchange equipment in 1985 at the earliest. Such a schedule will be contingent on adequate funding and appropriate progress in the HTR program.

10.6.2 Steam Generator

A significant amount of testing was performed on developing the steam generators for the Fort St. Vrain design; however, significant changes have been made in the basic concept for the unit for large HTRs. The reheater unit has been eliminated, the helium flow path has been changed, and the superheater section is considerably different. Subsequent testing will be required before construction of large HTR steam cycle plants.

Testing a steam generator module requires design, procurement, and fabrication of a dual cycle CFTL similar to that in the flow sheet given in Fig. 10.10. An appropriate feedwater system and a condenser will replace the circulator and heat sink in the secondary cycle.

10.6.3 Core Auxiliary Heat Exchanger

The CAHE also requires experimental verification of its performance. No similar unit was installed in the Fort St. Vrain plant; the main steam generators were flooded to serve this purpose. Also, the design of the CAHE bundle has been modified significantly since the detailed design of the Fulton and Delmarva plants. The bundle now consists of reentrant (bayonet) tubes located at the lower face of the PCRV.

Because of the significance of the performance of this unit to the safety of the reactor, detailed experimentation of anticipated operating conditions will be required. Because the duty of this unit is relatively low compared with that of the steam generator, it is within the scope of the CFTL to test a full-size unit at design loads.

10.6.4 Reformer and Methanator

Testing of the reformer, which has been proposed as an application for HTRs, will also require a dual loop arrangement similar to that shown in Fig. 10.10. For this evaluation, the secondary loop will circulate the makeup and effluent gas for the reformer. This loop can be operated as an open loop or as a closed loop containing the methanator. In addition to

the heat transfer and flow characteristics of the heat transfer surfaces, information is needed about the performance of the catalyst when operated at simulated HTR conditions. In particular, the ability of the methanator cycle to perform when subjected to the normal transients created by HTR operation must be investigated before this process can be incorporated into a demonstration facility.

This type of study is a long-range possibliity for application of the CFTL.

10.7 OTHER PRIMARY LOOP COMPONENTS

Several other components of the primary loop of an HTR can be tested in the CFTL. Each of these applications requires construction of a relatively large test vessel in the existing loop.

10.7.1 Thermal Barrier

Because of the vital function of the thermal barrier that protects the PCRV liner from the hot gases in the primary loop, several aspects of the design and performance of these components should be tested in the CFTL. To represent the actual geometry of the barrier, relatively large test vessels are required. The tests of the insulation include the structural performance of (1) the class A and class B cover sheets at the limiting helium temperatures and (2) the liners for the cross ducts connecting the lower plenum to the steam generator cavities. Evaluation of the performance as a function of time at temperature will be required.

Such testing is within the capability of the CFTL if it is assumed that large "flow blockers" can be placed in the vessel to create the required velocities at the surface of the test piece.

10.7.2 Intracore Components

The need for preoperational flow testing of the central core cavity components has been emphasized by the flow oscillations encountered in the initial operational phases of the Fort St. Vrain reactor plant. In addition to the evaluation of conditions at normal operating ranges, it

is important to evaluate the flow and thermal response for severe accident sequences that follow the loss of forced convection cooling and a coincident reactor trip. Tests should evaluate the conditions following this incident in which low convective flows are imposed at varying intervals. Such tests are vital to establishing the potential for removal of afterheat by use of a natural convection flow.

The above tests involve a large test vessel with a distributed internal heat source. Because of the necessity to represent a large number of flow channels at differing powers, an apporpriately scaled model of the core can be selected. The resources for this test are available at the CFTL site.

10.8 CONCLUSIONS

Based on a preliminary evaluation of the attributes of the CFTL loop and the development needs of commercial HTR plants, we concluded that the optimum choice for an initial test is an evaluation of the performance of the core support structure. This test exposes a series of test pieces of typical dimensions under a compressive load to conditions encountered at the HTR core outlet. The concentration of impurities (mainly water vapor) will be increased so that the corrosion of the support during its 30-year design lifetime would be represented in a six-month test.

While this testing is in progress, detailed evaluation of subsequent tests will be made. Based on results of this study, the requirements for the subsequent test can be established and the design of loop modifications, followed by procurement and installation of equipment, will proceed.

10.9 REFERENCES

1. D. W. MacKenzie, *HTGR Core Support Structure Reliability Study, Final Report,* MRI-2801-02, Mechanics Research Inc., Los Angeles, Calif. (July 1975).
2. C. Velasquez et al., *Effect of Steam Oxidation on the Strength and Elastic Modulus of Graphite H451,* GA-A14657, General Atomic Company, San Diego, Calif. (December 1979).

3. F. J. Homan and P. R. Kasten, *HTGR Base-Technology Program Annu. Prog. Rep., Dec. 31, 1979,* ORNL-5643, chap. 1.

4. P. R. Kasten et al., *Planning Guide for HTGR Safety and Safety-Related Research and Development,* ORNL-4968 (May 1974), chap. 10, p. 23; chap. 13, pp. 10 and 14–19.

5. W. R. Huntley and A. G. Grindell, *System Design Description for GCFR-Core Flow Test Loop,* ORNL/TM-7455 (December 1980), pp. 39–42.

GAS-COOLED REACTOR PROGRAMS

JANUARY 1, 1981

PAUL R. KASTEN,* DIRECTOR CMO
JUNE L. ZACHARY, SECRETARY CMO

FINANCE OFFICER
M. J. ROSE FM

DIVISION MANAGERS AND COORDINATORS
D. E. BARTINE * EP
F. J. HOMAN* MC
R. E. MacPHERSON ET
A. P. MALINAUSKAS CT
D. J. NAUS* ET

HTGR BASE TECHNOLOGY PROGRAM
F. J. HOMAN* MC
PROGRAM MANAGER

PCRV DEVELOPMENT
D. J. NAUS* ET
J. R. DOUGAN* ET
C. B. OLAND ET
G. C. ROBINSON* ET
C. C. HURTT ET
R. SMITH, JR.* ET

HTGR STRUCTURAL MATERIALS STUDIES
P. L. RITTENHOUSE MC
R. L. BEATTY MC
D. O. HOBSON MC
H. INOUYE MC
J. F. KING MC
R. J. LAUF* MC
K. C. LIU MC
C. J. LONG† MC
H. E. McCOY MC
R. K. NANSTAD MC
J. P. STRIZAK MC
R. W. SWINDEMAN MC
K. W. BOLING MC
E. BOLLING MC
J. C. FELTNER MC
J. L. GRIFFITH MC
W. C. HAWKINS MC
J. D. HUDSON MC
P. J. JONES MC
H. KEATING MC
B. McNABB MC
E. D. PATTON MC
L. T. RATCLIFF MC
R. W. REED MC
J. W. SHAW MC
R. L. SWAIN MC
B. C. WILLIAMS MC

GA IRRADIATION SERVICES
J. A. CONLIN* ET
R. L. SENN* ET
I. SIMAN-TOV ET
E. D. CLEMMER ET
C. A. WALLACE ET
T. H. WYNN ET

HTGR GRAPHITE DEVELOPMENT
W. P. EATHERLY* MC
C. R. KENNEDY MC
D. B. FIELDEN MC
F. P. JEFFERS MC
J. A. CONLIN* ET
R. L. SENN* ET
R. P. WICHNER* CT
C. D. BOPP CT
L. L. FAIRCHILD CT

HTGR CHEMISTRY STUDIES
R. P. WICHNER* CT
R. A. LORENZ CT
R. B. BRIGGS§ CT
R. CAUSEY§ CT
O. K. TALLENT CT
P. C. ARWOOD CT
R. L. TOWNS CT

FUELED GRAPHITE DEVELOPMENT
F. J. HOMAN* MC
M. J. KANIA MC
R. J. LAUF* MC
T. B. LINDEMER CT
R. L. PEARSON CT
D. P. STINTON MC
T. N. TIEGS MC
W. H. ELLIOTT MC
T. J. HENSON MC
S. S. RAWLSTON MC
E. L. RYAN MC
L. G. SHRADER MC
R. L. WHITE MC

HTR APPLICATION AND PROJECT ASSESSMENTS
P. R. KASTEN* CMO
S. J. BALL* IC
J. C. CONKLIN* ET
W. R. GAMBILL CT
R. M. HARRINGTON* IC
W. T. KING* IC
W. C. STODDART E
B. A. WORLEY* EP
K. F. WU E

HTR PHYSICS AND SHIELDING
D. E. BARTINE* EP

HTR PHYSICS STUDIES
D. R. VONDY EP
J. P. RENIER CS
J. S. TANG CS
B. A. WORLEY* EP

HTR SHIELDING STUDIES
C. O. SLATER EP
S. N. CRAMER* EP
L. R. WILLIAMS* EP

HTR COMPONENT FLOW TEST LOOP
J. P. SANDERS* ET
A. G. GRINDELL* ET
W. R. CLARK* E
N. D. ROBERTS* E
C. W. COLLINS* E
J. C. CONKLIN* ET
W. P. EATHERLY* MC
P. G. HERNDON* IC
E. M. LEES* ET
R. W. McCULLOCH* ET
C. A. MILLS* ET
H. C. YOUNG* ET

GAS-COOLED FAST REACTOR PROGRAM
P. R. KASTEN* CMO
MANAGER

PRESSURE VESSELS AND CLOSURES
D. J. NAUS* ET
J. R. DOUGAN* ET
G. C. ROBINSON* ET
R. SMITH, JR.* ET

SHIELDING STUDIES
D. T. INGERSOLL EP
S. N. CRAMER* EP
M. B. EMMETT CS
F. J. MUCKENTHALER EP
L. R. WILLIAMS* EP

CORE FLOW TEST LOOP
J. P. SANDERS* ET
A. G. GRINDELL* ET
R. L. ANDERSON IC
S. P. BAKER IC
S. J. BALL* IC
R. B. BIGGS E
W. R. CLARK* E
N. D. ROBERTS* E
C. W. COLLINS* E
J. C. CONKLIN* ET
K. J. CROSS IC
F. R. GIBSON IC
R. E. HARPER IC
P. G. HERNDON* IC
S. A. HODGE ET
W. R. NELSON ET
C. F. HOLLOWAY ET
T. L. HUDSON ET
E. M. LEES* ET
R. W. McCULLOCH* ET
R. E. DIAL ET
W. R. FINNEL ET
J. R. McGUFFEY QA
C. A. MILLS* ET
J. E. SMITH ET
R. W. TUCKER IC
H. C. YOUNG* ET

HTGR SAFETY STUDIES FOR NRC–RSR
S. J. BALL* IC
PROGRAM MANAGER

SYSTEM RESPONSE AND SAFETY ANALYSIS
S. J. BALL* IC
J. C. CONKLIN* ET
R. M. HARRINGTON* IC

*DUAL CAPACITY
†SPECIAL ASSIGNMENT TO KFA-JULICH, FRG
§CONSULTANT

CMO	CENTRAL MANAGEMENT OFFICES
CS	COMPUTER SCIENCES
CT	CHEMICAL TECHNOLOGY DIVISION
E	ENGINEERING
EP	ENGINEERING PHYSICS DIVISION
ET	ENGINEERING TECHNOLOGY DIVISION
IC	INSTRUMENTATION AND CONTROLS DIVISION
MC	METALS AND CERAMICS DIVISION
QA	QUALITY ASSURANCE AND INSPECTION

ORNL-5753
Distribution
Category UC-77

INTERNAL DISTRIBUTION

1–2. Central Research Library
3. Document Reference Section
4–6. Laboratory Records Department
7. Laboratory Records, ORNL RC
8. Patent Office
9. S. M. Babcock
10. S. J. Ball
11. M. K. Booker
12. I. H. Brogden
13. A. J. Caputo
14. R. E. Clausing
15. C. W. Collins
16. J. C. Conklin
17. J. A. Conlin
18. R. G. Donnelly
19. J. R. Dougan
20. W. P. Eatherly
21. Uri Gat
22. R. W. Glass
23. A. G. Grindell
24. R. E. Helms
25. R. F. Hibbs
26–29. M. R. Hill
30–34. F. J. Homan
35. D. O. Hobson
36. J. R. Horton
37. H. Inouye
38. D. R. Johnson
39. M. J. Kania
40–54. P. R. Kasten
55. J. F. King
56. W. J. Lackey
57. C. E. Lamb
58. R. J. Lauf
59. E. H. Lee
60. T. B. Lindemer
61. C. J. Long
62. A. P. Malinauskas
63. P. J. Maziasz
64. H. E. McCoy Jr.
65. R. K. Nanstad
66. D. J. Naus
67. R. E. Norman
68. C. B. Oland
69. R. L. Pearson
70. H. Postma
71. P. L. Rittenhouse
72. G. C. Robinson
73. J. R. Sanders
74. A. C. Schaffhauser
75. R. L. Senn
76. G. M. Slaughter
77. I. Spiewak
78. D. P. Stinton
79. J. P. Strizak
80. T. N. Tiegs
81. D. R. Vondy
82. G. C. Wei
83. S. K. Whatley
84. B. A. Worley
85. H. C. Young

EXTERNAL DISTRIBUTION

86–87. DOE, HIGH TEMPERATURE REACTOR PROGRAM, Washington, DC 20545

J. E. Fox
G. A. Newby

88. DOE, OFFICE OF NUCLEAR POWER SYSTEMS, Washington, DC 20545

Director

89. DOE, SAN-SAN DIEGO, 110 West A Street, Suite 460, San Diego, CA 92101

Manager

90–91. DOE, OAK RIDGE OPERATIONS OFFICE, P. O. Box E, Oak Ridge, TN 37830

Office of Assistant Manager for Research and Development
Director, Nuclear Research and Development Division

92–242. DOE, TECHNICAL INFORMATION CENTER, P. O. Box 62, Oak Ridge, TN 37830

For distribution as shown in TID-4500 Distribution Category, UC-77 (Gas-Cooled Reactor Technology)

☆U.S. GOVERNMENT PRINTING OFFICE: 1981-740-062/156